INVESTIGATIONS ON THE CHARACTERIZATION OF ION IMPLANTED HEXAGONAL BORON NITRIDE

By

Emily Aradi

A thesis submitted to the Faculty of Science, University of the Witwatersrand, Johannesburg, in fulfilment of the requirements for the degree of Doctor of Philosophy.

Johannesburg, 2014.

Declaration

I declare that this thesis is my own, unaided work. It is being submitted for the degree of Doctor of Philosophy in the University of the Witwatersrand, Johannesburg. It has not been submitted before for any degree or examination in any other university.

(Signature of candidate)

27 day of October 2014

Abstract

Boron nitride (BN) in its cubic form (cubic boron nitride (c-BN)) is one of the known superhard materials with superior mechanical, chemical and electronic properties. These properties have made it an excellent material in many modern industrial and electronic applications and as such, extensive research grounds have been developed for over half a decade now with the aim of finding alternative ways to synthesize it.

The work presented in this thesis was inspired by the fact that defects introduced into the hexagonal form of boron nitride (h-BN) under certain conditions can lead to a change in its local structure and hence the formation of the cubic BN symmetry.

The work focused on the introduction of different ions which included helium, lithium, boron, nitrogen and argon into h-BN, by the ion implantation process, in order to promote a defect-induced phase change to the cubic symmetry and possibly to other BN polymorphs. We introduced these ions at different fluences (number of ions per unit area) and energies so as to investigate the best conditions that will influence the lowest activation energy that will in turn favour the c-BN formation. The resulting thin hard layer could be an excellent sub-surface treatment.

All the samples used were high quality polycrystalline and single crystal h-BN, obtained from various manufacturers. The fluence range used was from 1×10^{13} ions/cm^2 to 5×10^{16} ions/cm^2, with energy ranging from 40 keV to 150 keV. This energy and fluence choice was inspired by previous research that had been done at higher energies (MeV range) and recommended that low energy (keV range) and fluence could induce similar change.

To investigate these effects, various analysis techniques were employed. The major techniques involved optical vibrational methods using Raman Spectroscopy

(RS) and Fourier Transform Infrared Spectroscopy (FTIR) carried out on the samples before and after implantation. Other techniques used included Glancing Incidence X-ray Diffraction (GIXRD), Transmission Electron Microscopy (TEM), and Energy Dispersive X-ray Spectroscopy (EDS).

Raman and FTIR measurements showed the introduction of new phonon and vibrational modes in the samples after implantation. The position, size and broadening suggested that they originated from a symmetry attributed to nano-structured cubic BN (nc-BN). The nature and extent of the nc-BN features was very dependent on the implantation parameters with different atomic mass ions each having an optimum fluence with regards to the intensities of the Raman and FTIR signal associated with them. Glancing incidence X-ray diffraction showed new diffraction patterns whose angles corresponded to the cubic and rhombohedral BN symmetries. The linewidths of these peaks were used to estimate the crystal size, which were in the nanoscale range, hence complementing the results obtained by optical spectroscopy.

The High-Angle Annular Dark-field Scanning Transmission Electron microscopy (HAADF-STEM) analyses showed regions with low contrast within the implanted region, suggesting that there were regions within the implanted layer that contained dense structures which were attributed to the cubic BN symmetry.

Computer simulations using the Stopping and Range of Ions in Matter (SRIM) programme were performed to understand the events that take place during the interaction of the ions with h-BN. Phonon confinement model calculations were also performed to understand the nature of peaks forming after implantation with an aim of support Raman measurements and to estimate the size of the nc-BN domains.

With these complementary analyses, it was concluded that indeed implantation is an effective method of creating nanocrystalline c-BN under less extreme conditions of pressure and temperature.

To my parents, mr and mrs Aradi. You are the best parents in the whole world!

Acknowledgements

The past few years have been the most challenging yet the most eye opening and exciting years of my academic life. I would never have made it on my own and so I am very grateful to everyone who has made it possible for me to successfully complete my degree.

I would like to express my sincere gratitude to my supervisors Prof. Trevor Derry and Dr. Mervin Naidoo who have constantly been available throughout the course of my studies. Their expertise, encouragement, and support were extremely motivational. This work was made possible through their guidance, wisdom, foresight and never ending supervision. I also extend so much gratitude to Prof. John Carter, the head of the School of Physics, for always believing in me in so many ways.

Many thanks to the iThemba LABS Gauteng, for allowing me to use the ion implanter facility throughout the course of my studies. I am grateful to Dr. Rudolph Erasmus who has always been available to help me carry out all the Raman Spectroscopy analyses. Many thanks to Dr. Ronald Machaka, from whose work I formed the basis of this research and who helped me with the theoretical section of the work. I am also grateful to my collaborator Prof. Basil Julies from the University of the Western Cape and Prof. Alexander Ziegler from the Microscopy Unit-Wits for guiding and training me on how to use the Transmission Electron Microscope. A big thank you to Dr. Daniel Wamwangi and Prof. Dave Billing for their help with X-ray diffraction measurements and Mildred Airo for FTIR measurements. Much appreciation to Dr. Charles Levitt who assisted me with sample preparation.

I would also like to thank my mentors and former supervisors, Dr. Nicholas Makau, Prof. George Amolo and Dr. Zack Mapelu from The University of Eldoret, Kenya, who gave me the right guidance and a better start towards my career. They

have also constantly checked my work providing necessary corrections, advice and suggestion, despite their busy schedule and the fact that they are far away in Kenya.

The financial support of the DST-NRF Centre of Excellence in Strong Materials (CoE-SM) towards this research is highly acknowledged. The financial assistance from Wits Postgraduate Merit Award and Bradlow post-graduate award, and the School of Physics, Wits University is also highly appreciated.

My beloved parents Mr and Mrs Aradi, my siblings Catherine, Shiller, Sylviah and Hillary and my love Kennedy have been my source of strength. They always encourage me to go for what I believe in and to be the best that I can be in everything. Above all, their unconditional love has made me a better person.

Much gratitude to my colleagues, Dr. Emmanuel Nshingabigwi, Isaac Motochi, Anna Kozakiewicz, and George Manyali, from the University of the Witwatersrand, Cecil Moro from University of Pretoria, and Enoch from Moi University's Computational Physics and Materials Science Group. Their assistance and encouragement was overwhelming.

Thanks to all my friends Indrah, Mr and Mrs Misoi, Tabither, Loreen, Kuda, Moshe, Bridget, Marie Chantel, just to mention a few, who always made me have a good laugh away from my busy research work. Their friendship is highly appreciated as they have made me a better person, both academically and socially.

Above all I thank the Almighty God for His guidance, protection and never ending favour. He has given me the most important gift of life and good health and ensured that my work is a great success. Thank you God!

Contents

List of Figures

List of Tables

List of Symbols and Abbreviations.

The following are the symbols and acronyms used in this thesis.

B	Boron
C	Carbon
Li	Lithium
N	Nitrogen
O	Oxygen
H^+	Hydrogen ions
He^+	Helium ions
$GaAs$	Gallium arsenide
GaN	Gallium nitride
SiC	Silicon carbide
GaN	Gallium nitride
BN	Boron nitride
$\alpha - BN$	Amorphous boron nitride
c-BN	Cubic boron nitride
E-BN	Explosive boron nitride
h-BN	Hexagonal boron nitride
r-BN	Rhombohedral boron nitride
t-BN	Turbostratic boron nitride
w-BN	Wurtzite boron nitride
EEL	Electronic Energy Loss
NEL	Nuclear Energy Loss
bcc	Body centered cubic
fcc	Face centered cubic

InN	Indium Nitride
TiC	Titanium Carbide
TiN	Titanium Nitride
GPa	Giga Pascal
eV	Electron volts
keV	Kilo electron volts
MeV	Mega electron volts
GeV	Giga electron volts
MOSFET	Metal Oxide Semiconductor Field Effect Transistor
HP-STP'S	High Pressure Structural Phase Transitions
HTHP	High Temperature High Pressure
IBAD	Ion Induced Beam Assisted Deposition
CVD	Chemical Vapour deposition
PVD	Physical Vapour deposition
WC	Tungsten carbide
RS	Raman Spectroscopy
EELS	Electronic Energy Loss Spectroscopy
EDS/EDX	Energy Dispersive Xray Spectroscopy
FTIR	Fourier Transform Infrared Spectroscopy
HRTEM	High Resolution Transmission Electron Microscopy
HAADF	High Angular Annuler Dark Field
TEM	Transmission Electron Microscopy
SBS	Surface Brillouin Scattering
GIXRD	Glancing Incidence X-Ray Diffraction
XRD	X-Ray diffraction

Chapter 1

Introduction

1.1 Motivation

The search for materials with unique properties continues unabated due to the ever increasing demand, especially in the modern high temperature-high frequency microelectronic device fabrication, optical device fabrication, coating materials for heavy duty machines, the abrasive subsector and the beauty and fashion industries. It is no longer feasible to satisfy these increasing industrial requirements using the already known natural materials (which are becoming overly scarce with time) and hence the need for modifying the already existing ones, or creating new ones with more superior properties than the existing ones.

Diamond has been widely used over the years for most of the above mentioned applications, and as such, the possibility of synthesizing new materials with ultra-hardness and other superior properties similar to, or even better than diamond has become of great interest to physicists, chemists and the entire community of material scientists. Over the years, this search has indicated that to synthesize stable materials which have hardness greater than that of diamond is a great challenge. Research is therefore being focused on the synthesis of materials with phases that are almost as hard as diamond, but with possibly other qualities that will be

superior to diamond in other respect.

The superior properties of cubic boron nitride (c-BN) including super hardness (second after diamond), high thermal conductivity and high melting point [1, 2, 3, 4] makes it useful for the above mentioned applications. Cubic BN has been found to surpass some of the properties exhibited by diamond. These include the oxidation (1200 ^{o}C) and phase transformation temperatures (1500 ^{o}C) of c-BN which are much higher than those of diamond at 600 ^{o}C and 1400 ^{o}C respectively [2, 3]. It is chemically inert against molten ferrous materials, whereas diamond reacts with them to form iron carbides. Moreover, c-BN is a potentially semiconducting material superior to diamond and other group III-V semiconductors such as gallium arsenide (GaAs), gallium nitride (GaN) and indium nitride (InN)[4, 5] because it has a wider band gap, with moderately shallow n-type (with B, Si and S) and p-type (with Be and Mg) dopants. A shallow n-type dopant is still problematic in diamond [6].

These and many more extreme properties of c-BN (discussed in detail in Chapter three) have prompted material scientists to carry out extensive research on the development and synthesis of novel structures of the c-BN phase to cater for the before mentioned applications. The study on the synthesis and characterization of c-BN started in late 1950s [7]. To date, c-BN has been synthesized industrially for commercial use in large quantities as powder, with sizes ranging from sub-micron to millimeter by high temperature high pressure (HTHP) method, initially developed by Wentorf Jr in 1956 [7, 8].

The severe nature of the HTHP method, particularly with regard to the extreme pressure and temperature conditions and the limited size of c-BN grains produced prohibit many attractive potential applications of c-BN [2, 4, 9]. This has become

a major motivating factor for thin film synthesis of *c*-BN using vapour deposition techniques. Researchers have also been prompted to explore the role of defects in the structural transformation of BN together with the thermodynamic processes involved [10, 11, 12]. There have been many first principle theoretical studies for this structural phase transformation. Recent theoretical research and study carried out by T. E. Mosuang and J. E. Lowther [13], on the "Influence of Defects in Affecting Transformation of *h*-BN to *c*-BN", using the *ab initio* Local Density Approach (LDA), suggested that a subtle change in the thermal behavior of *h*-BN, in the presence of strain deformation due to defects could lead to a phase transformation to the cubic form [13].

Experimentally, ion bombardment has been found to strongly influence the thin film growth, with defect production of *c*-BN occurring immediately upon ion impact [1]. In their research, Machaka *et al* demonstrated that by introducing helium ions into *h*-BN at the energy of 200 keV and fluence of 1×10^{17} ions/cm^2, using the ion implantation process [14]. The study suggested that ions with larger atomic masses than helium could promote a *c*-BN to *h*-BN phase transition at lower energies and ion fluences.

1.2 Statement of the Problem

Synthesis of *c*-BN has been found to have great economic benefits, since it is a hard material and has some superior properties as compared to those of diamond and other materials as outlined previously and in later chapters. On the other hand, *h*-BN also possesses excellent physicochemical properties. The production of a thin film *c*-BN on *h*-BN surface and subsurface would have advantages in combining the properties of both materials.

Irradiation of soft h-BN with protons or alpha particles has been predicted and shown to introduce phonon vibrational changes in h-BN to nanostructures related to the ultrahard c-BN symmetry at high energies and at high fluences. Presently the mechanisms for the h-BN structural modifications with respect to controlling the different implantation parameters have not been studied. More research therefore needs to be carried out with regards to varying different parameters and especially the ion mass by using heavier ion species such as, Li, B, C, N and O, the ion fluence and with different energies in order to establish the optimum or critical conditions for the occurrence of these c-BN nanostructures.

1.3 Research Objectives

The aim of this work is to determine the effect of radiation damage through ion implantation in h-BN with the anticipation of inducing a possible structural change to the ultrahard cubic boron nitride nanoparticles and/or possibly other phases of boron nitride.

It aims at determining the physical parameters that control the nc-BN occurrence and to establishing the relationship and trend of these parameters with regards to how they influence the h-BN to c-BN structural modifications and to what extent the irradiation end products are generated. The parameters that are investigated include the ion mass (by the varying the incident ions such as helium, lithium, boron, nitrogen and argon), the ion fluence which is the number of ions implanted per unit area, and the ion energy.

The effect of varying the implantation temperature and annealing after implantation will also be investigated, with implantation temperatures ranging from liquid nitrogen to about 400 ^{o}C and annealing up to 400 ^{o}C.

1.4 Thesis outline

This work is organized in the following way:

Chapter Two gives an overview of ion implantation, starting with ion-solid interaction information, the theory and physics of ion implantation, stopping power mechanisms and the resultant disruption of the pre-existing lattice structure. The chapter ends with details on the computer simulations by Stopping and Range of Ions in Matter (SRIM2008) with regards to events that take place during ion implantation of boron nitride such as the stopping power, the range of implants and the damage densities.

Chapter Three gives a general view on boron nitride, its structure, synthesis and the different forms or phases of its existence. It focuses on the properties and applications of the *h*-BN and *c*-BN phases, ending with information on the different synthesis methods for the *c*-BN.

Chapter Four describes the experimental details and the characterization mechanisms used in this work. It gives details on the instrumentation and principles of operation for the apparatus used, samples and sample preparation techniques and the overall experimental procedures carried out on the prepared samples.

Chapter Five presents the results obtained from experiments and their discussions thereafter. The first section is on the results obtained from Raman Spectroscopy (RS) followed by Fourier Transform Infrared Spectroscopy, Glancing Incident X-ray Diffraction, Energy Dispersive X-ray spectroscopy and finally Transmission Electron Microscopy (conventional TEM, high resolution TEM and HAADF-STEM).

Chapter Six focuses on the theoretical calculation and analyses on the Raman results using the Phonon confinement model.

Finally Chapter Seven gives the conclusions and recommendations from the work.

Appendix A1 shows photographs of the different instruments used in the experiments, Appendix A2 gives a list of publications from this work and Appendix A3 gives a list of conferences attended to present this work.

Chapter 2

Ion-Solid Interactions

2.1 Introduction

The science of energetic particles, emitted from a radioactive material, was discovered in the early 20^{th} century. Research by Ernest Rutherford showed that alpha particles can be easily stopped in matter while gamma rays penetrate deeper into matter before being stopped. This led to a great deal of interest by other scientists, including J. J. Thompson and Niels Bohr who designed experiments to show how these particles penetrate, slow down and finally settle/stop in matter and hence unveiling the physics of ion-solid interaction [15, 16].

Ion-solid interactions is a field of materials science that involves the acceleration of charged particles into a solid material. The development and advancement of ion beam technology has been ongoing for over half a century to the state of the art well known in the present age. Before the discovery of nuclear fission in 1939, the theoretical, computational and experimental advancement in this field were both few and essentially academic.

Today, a fully developed science of ion-solid interactions belongs both to well established academic and research techniques in materials science, which is used for various commercial applications, especially in the field of semiconductor physics

[17, 18].

Ion-solid interactions processes, also known as ion beam processes, involve among others, substrate sputtering, Ion Beam Assisted Deposition (IBAD), ion beam mixing, ion implantation and ion induced phase transformations [19].

Ion beams have been used extensively in Nuclear Physics, where the interaction with detector material enables not only the identification of the unknown particle and its properties, but also played a special role in the establishment and evolution of Atomic Physics, for example in the development of atomic or nuclear power. Ion implantation is important in the semiconductor device manufacturing industry, to introduce a wide range of dopants into semiconducting materials, such as silicon (Si), germanium (Ge), gallium nitride (GaN) and gallium arsenide (GaAs).

Other applications of ion-solid interactions include fusion power generation, Laser Isotope Separation plasma processing (LIS) and controlled fusion [18]. Heavy ion beams have also been used in cancer therapy with heavy ion treatment of deep seated cancer being more effective and at the same time less destructive for benign tissues than the conventional proton therapy [20].

High fluence irradiation of nitrogen or chromium ions has been seen as an essential way in corrosion protection of metals. Nitrogen ion implantation assists in formation of a highly resistive nitride surface layer that withstands tribological load much longer [17]. Materials can also be sterilized by ion irradiation [19].

With regards to this thesis, ion irradiation has also been used quite extensively in ion induced phase transition of hard materials from a soft phase. A good example is the phase transformation from graphite to diamond and h-BN to c-BN [17, 19].

2.2 Fundamentals of Ion-Solid Interactions

In general, ion-solid interaction is a physical/atomic process resulting from the collision of energetic ions with a solid material [21]. When a high energy particle is incident on a material's surface it may cause sputtering and degradation of the surface. The resultant processes involve elastic and inelastic scattering of the projectile ions, penetration of the projectiles into the solid and the emission of electrons and atoms from the surface of the solid material. The passage of the accelerated ions in the solid and the subsequent slowing down process leaves along its way both extended and isolated defects (displacement of the atoms leading to a vacancy or by settling on the interstitial site of the lattice of the material). This displacement of atoms and the resultant defect cascade leads to a volumetric strain that in turn changes the chemical, electrical, physical and optical properties of the target material [19, 22]. Figure 2.1 below shows a schematic illustration of the ion-solid interaction process.

The surface of the solid plays a participatory role in all the material's interactions with its external environment e.g. friction, oxidation and wear among others. Ion-solid interactions techniques are therefore important since they aim at modifying the surface and sub-surface characteristics of the given material making them resistant to these possible harsh external interactions.

All ion-solid interactions processes are energy dependent. At high energies (>1 MeV) processes such as nuclear reactions and emission of high energy radiation (Bremsstrahlung and Cherenkov radiation) take place as the ion penetrates the solid [23, 24]. The generation of phonons leads to local heating of the target material, charge exchange and the emission of other secondary particles such as Auger electrons. For the purpose of this work, which is based in the keV energy

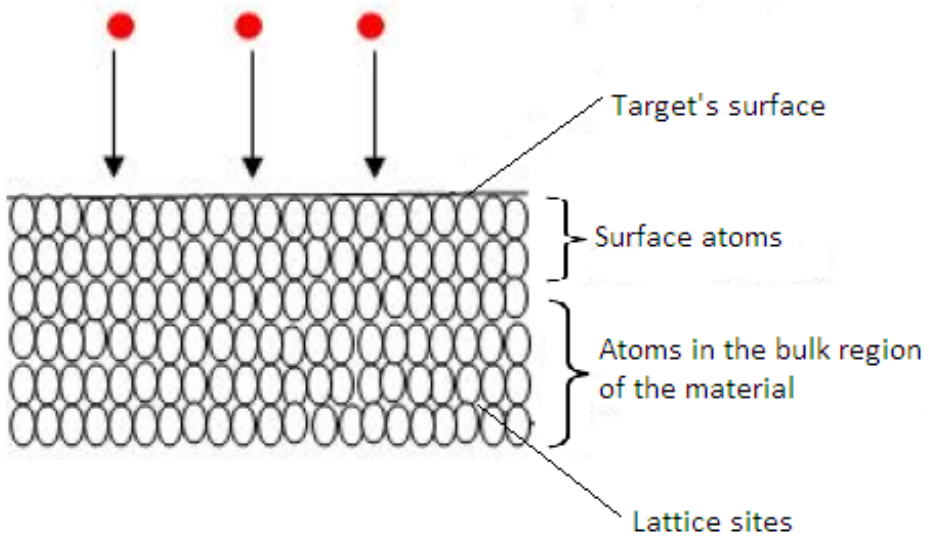

Figure 2.1: *Crystal lattice for a target material before irradiation with energetic ions.*

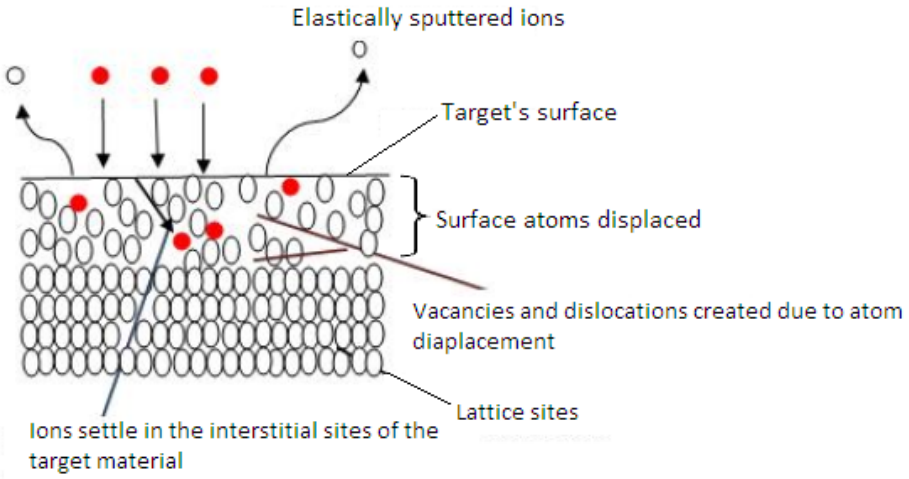

Figure 2.2: *An illustration of the possible interactions that take place during ion beam bombardment (IBB) in the ion- solid interaction process.*

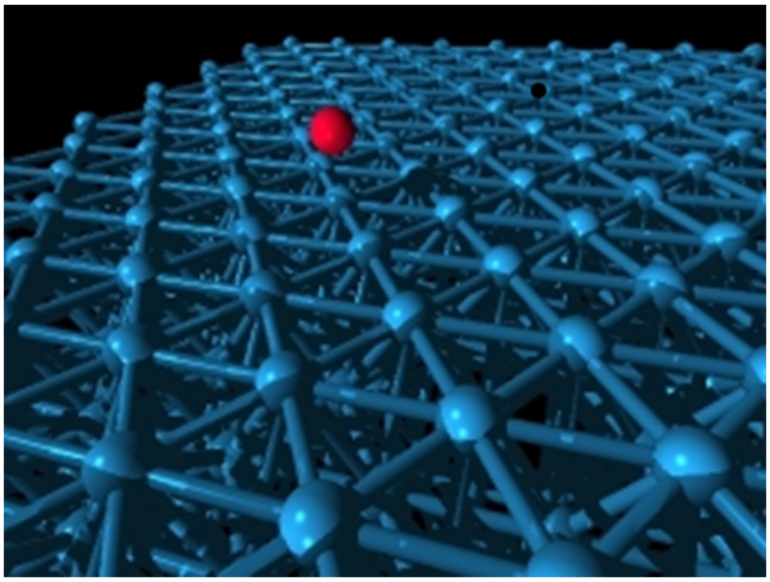

Figure 2.3: *Photographic representation of the ion-solid interaction process. The red sphere represents an energetic ion while the blue spheres represent the atoms in the target material [22].*

regime, high energy processes such as nuclear reactions do not occur and therefore will not be discussed further.

Ion beams are the basic requirement for performing any ion-solid interactions experiment and therefore a readily available and reliable source is needed. There are various common producers for these ions, including, using radioactive atomic sources yielding alpha particles or fission fragments. An example of this is the exploitation of the nuclear reaction using neutrons from a reactor, emitting protons, tritons, among others, depending on the type of the material.

Ions can also be produced by the bombardment of swift heavy ions (SHI) [17, 22], onto a specific target, using various types of nuclear reactions such as fission reactions. Sporadically arriving cosmic rays can be used to obtain or produce particles with very high energies.

Currently, the most convenient way of obtaining charged particles with sufficient fluence in a wide energy range from keV to MeV is to produce them in a particle

accelerator with an appropriate ion source [17].

2.3 Ion Implantation

2.3.1 Introduction

Ion implantation process is a harsh, non-equilibrium and powerful ion beam modification technique which involves the acceleration of energetic charged particles/ions (usually in keV to MeV ranges) into the subsurface layer of a solid material. In their stopping process, these ions interact with the atoms in the shallow regions of the host material's matrix, resulting in the creation of point and extended defects. It is the added ions (which become neutral), their interaction with the host atoms and the resultant defects that are consequently responsible for the modification of the physical, chemical, electrical and optical characteristics or properties of surface and subsurface layers of solid state materials [14, 19, 25, 26].

Ion implantation has successfully been used to modify controllably the various properties of different materials because it possesses numerous advantages compared to other surface modification techniques such as coating, diffusion and oxidation [27, 28]. Ion implantation enables selective alteration to the material without necessarily altering the bulk of the material i.e. the implantation depth can be controlled. It is possible to control the ion concentration to be used for implantation into a given material by changing the energy and the ion fluence, hence a precise choice for the energy and fluence can develop a desired impurity profile beneath the surface. The choice of the implant is not limited by the conventional rule of solubility and so any ion may be used for implantation in any substrate [23, 25].

Ion implantation is a low temperature process, as such there is no change on

the size of the material due to thermal alterations and hence minimal surface degradation. The dimensions of the material are also retained since it is not a coating process. Ion implantation processes are carried out in particle accelerators that are able to produce isotopically pure beams, selected by a mass analyzing magnet, so there is minimum or no contamination to the substrate or the material to be implanted [25, 27].

The major problem involving ion implantation is that, many atoms in the target material are displaced, causing radiation damage which may be undesirable especially in semiconductor modification. This damage can in most conventional materials like silicon and germanium be annealed away by thermal treatment. The damage may however be beneficial for altering the properties of other materials as is the case in this thesis.

2.3.2 The Theory of Ion Implantation

When an energetic ion impinges upon the surface of condensed matter, it experiences a series of inelastic and elastic collisions with the atoms which lie along its path. This results in loss of kinetic energy of the projectile and excitation of the solid material as well as momentum transfer between the interacting bodies [29, 30].

The energy loss is dependent on the incident energy and the atomic mass of the projectile ion, as well as the atomic mass and binding energy of the target material. Energy loss (with distance) determines the final penetration depth of the projectile into the solid and the amount of disorder that is created in the material's lattice [31, 32].

The energy lost by the projectile as it goes through the solid is determined

by the "*stopping power*", defined as the energy transfer per unit path length of a particle along its trajectory [17, 14, 26, 31, 29, 33], and denoted as:

$$S(E) = -\frac{dE}{dx} \tag{2.3.1}$$

The sign of the stopping power is negative to indicate an *energy loss* change along the path length.

If the maximum possible energy transfer in the course of a collision event is T_{max} and there are N_{ions} target atoms per unit volume, then the stopping power is given as:

$$-\frac{dE}{dx} = -N_i ons \int T_{max} d\varepsilon \tag{2.3.2}$$

where $d\varepsilon$ the differential implanted cross section by the trajectory. N_{ions} is also referred to as the implant density. If expressed as the atomic density, then N_{ions} can be approximated as a Gaussian range distribution as predicted by Lindhart, Scharff and Schiott [34], and is given as:

$$N(x) = \frac{\varphi}{\Delta R_p \sqrt{2\pi}} \exp\left[-\frac{(x - R_p)^2}{2(\Delta R_p)^2}\right] \tag{2.3.3}$$

where φ is the ion fluence, ΔR_p is the standard deviation for the mean projected range (projected range straggle) which defines the peak position measured from the target's surface,R_p the mean perpendicular penetration depth also known as the projected range and x the ion depth of penetration [32, 35].

There are two main processes that contribute to the energy loss mechanism. They are, **the electronic stopping power** denoted as $S_e(E)$, also known as the inelastic energy loss mechanism, and **the nuclear stopping power** denoted as $S_n(E)$, also known as the elastic energy loss mechanism, based on the energy regime

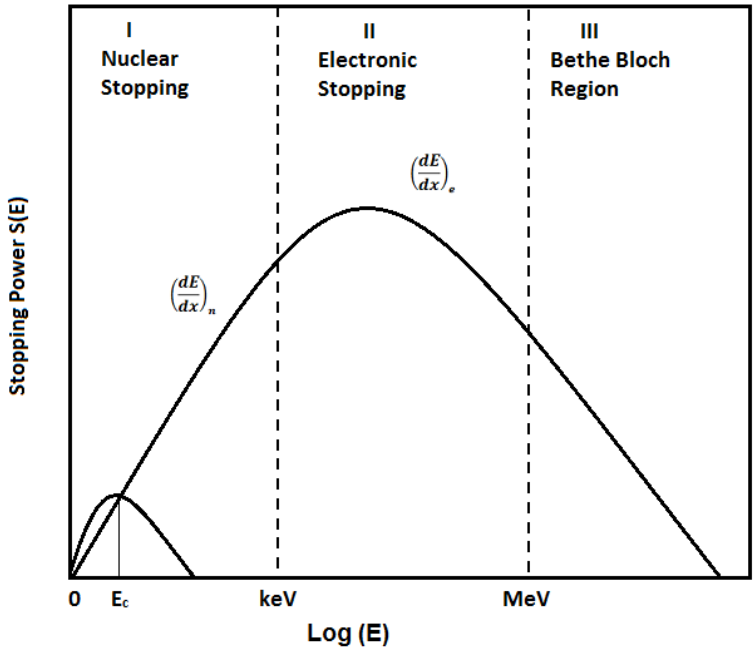

Figure 2.4: *Typical dependence of the and electronic and nuclear stopping of ion in matter with respect to energy (plotted logarithmically). E_c is defined as the energy below which nuclear and electronic stopping are comparable [36].*

where they are dominant [18, 27, 29, 33],

When the ion's velocity is high at the beginning of its impinging path into the material, electronic stopping is primarily responsible for the energy loss of the ion in the solid. As the ion penetrates further into the solid, its speed is reduced, as a result the nuclear stopping increases and eventually form the major part of the energy loss mechanism. The stopping process responsible for the most damage in the material depends on the incident ion species, the implantation energy and the target material's mass (as will be seen in the discussions for boron nitride).

The total stopping power is therefore given as the arithmetic sum for the electronic stopping, the nuclear stopping and energy losses due to radiative processes[1] [37] given as:

[1]such as Bremsstrahlung and Cherenkov Radiation

$$S(E) = S_e(E) + S_n(E) + S_r(E) \tag{2.3.4}$$

The energy loss *$S_r(E)$* due to radiative processes is small and can therefore be neglected. The units for *$S(E)$* can be eV/cm/atom among other several units given in literature. Figure 2.4 shows the schematic illustration of how electronic and nuclear energy losses contribute to the stopping process with respect to energy.

2.3.3 The Electronic Energy Loss

The electronic energy loss (EEL) mechanism/electronic stopping involves the interaction between the incident ion and electrons of the host material [33]. It occurs as a result of the elastic collision between the bound electrons in the medium/ target material and the incident projectile ion moving through it leading to ionization and excitation of the atoms.[38].

As the ion interacts with the electron cloud of the target atoms, it experiences a *"viscous drag"* causing it to slow down until the nuclear process dominates. Since electronic stopping is associated with high energy and velocity regimes for the incident ion, there is less interaction with the target nuclei at this stage. Therefore the damage in terms of the target atom displacement is minimal in the electronic stopping regime [19, 39].

The relationship between the electronic stopping power *$S_e(E)$* of the material and the incident ion energy was developed by Lindhard and Scharff [34, 40] and is given as:

$$S_e(E) = \frac{8\pi e^2 a_o}{\varepsilon_o} \frac{z_1 z_2}{(z_1^{\frac{2}{3}} + z_2^{\frac{2}{3}})^{\frac{3}{2}}} \left[\frac{E}{E_o}\right]^{\frac{1}{2}} \tag{2.3.5}$$

Where a_o is the Bohr Radius, E the current energy of the ion, E_o the Bohr's

energy, e the electronic charge and z_1 and z_2 the ion and target's atomic numbers respectively. From this relationship, the electronic stopping power $S_e(E)$ varies directly as the square root of energy of the incident ion, given as:

$$S_e(E)\alpha E^{\frac{1}{2}} \tag{2.3.6}$$

Electronic stopping in this regime occurs typically in energy regions ranging from 100 keV to 10 MeV. For relativistic projectile energies E >10 MeV, the electronic stopping is described by the Bethe-Bloch formalism [41, 42]. The electronic stopping decreases when moving towards higher energies in the in the Bethe- Bloch region. This is due to the fact that the higher the velocity of the incident ion, the less time it has to interact with each target atom it encounters [43]. In this work all energies are in the keV region therefore the Bethe Bloch formulation does not apply.

2.3.4 The Nuclear Energy Loss

The nuclear energy loss (NEL) mechanism, also known as the nuclear stopping process, is the energy loss process that involves the interactions of the incident ions with the nuclei of the host material. It occurs as a result of scattering of the projectile ions by the screened nuclear potential of the of the target atoms, also known as Rutherford Scattering [29, 37, 38].

As the ions slow down, reaching low energy regimes, electronic stopping decreases and now nuclear stopping begins to dominate the stopping process as shown in figure 2.4. In the nuclear stopping process, the ions experience elastic collisions with the atoms of the target as they penetrate through the solid, dislodging many

of these atoms from their equilibrium positions [26]. It is in this region that maximum damage usually occurs. Nuclear energy loss dominates at low ion energies (typically below 10 keV for light ions in boron nitride). It is given as:

$$S_n(E) = N\frac{\pi^2}{2}E^{-2}a\left[\frac{z_1 z_2 m_1}{m_1 + m_2}\right] \tag{2.3.7}$$

where N is the atomic concentration, a the lattice parameter, z_1 and z_2 are the ion and target's atomic numbers respectively, and m_1 and m_2 the atomic masses for ion and target respectively [44]. From this equation, nuclear stopping has an inverse square relationship with the energy of incident ion i.e.

$$S_n(E)\alpha E^{-2} \tag{2.3.8}$$

When all the atoms' energy in the system fall below the threshold displacement energy E_d, no further damage cascade is produced and as a result nuclear stopping ceases. The total amount of energy deposited by nuclear collision is called the *Nuclear Displacement Energy* [39, 45]

2.3.5 Ion Range

As the incident ion travels into the solid matrix, it does not move in a straight line to its end of range position as it encounters multiple collisions with the substrate's atoms. The implanted range *R(E)*, therefore defines the total integrated distance the ion travels through the solid before coming to rest [29, 26, 32, 38]. It is given as,

$$R(E) = \int \frac{dE}{S_n(E) + S_e(E)} \tag{2.3.9}$$

where $\mathrm{S}_n(E)$ and $\mathrm{S}_e(E)$ are the nuclear and electronic stopping powers respectively.

The projected range defines the net perpendicular peak position measured from the target's surface or in other words the mean penetration depth relative to the surface. Because of the statistics of the process, not all the ions reach the same depth and the ion distribution obtained after implantation can be approximated by a gaussian distribution being characterized by mean projected range R_p and the straggling $\Delta R_p(E)$ (see equation 2.3.3)[29, 43].

The probability function describing the implantation depth distribution is often approximated to be Gaussian for relatively low ion concentration and in the absence of crystallographic channelling effects [19] . In this case, the largest number of ions will be located at R_p and ΔR_p is $R_p/2.35$. The range of distribution however deviates from this Gaussian profile for high fluences and where there is crystallographic ion channelling (see channelling next section) [29, 38, 43].

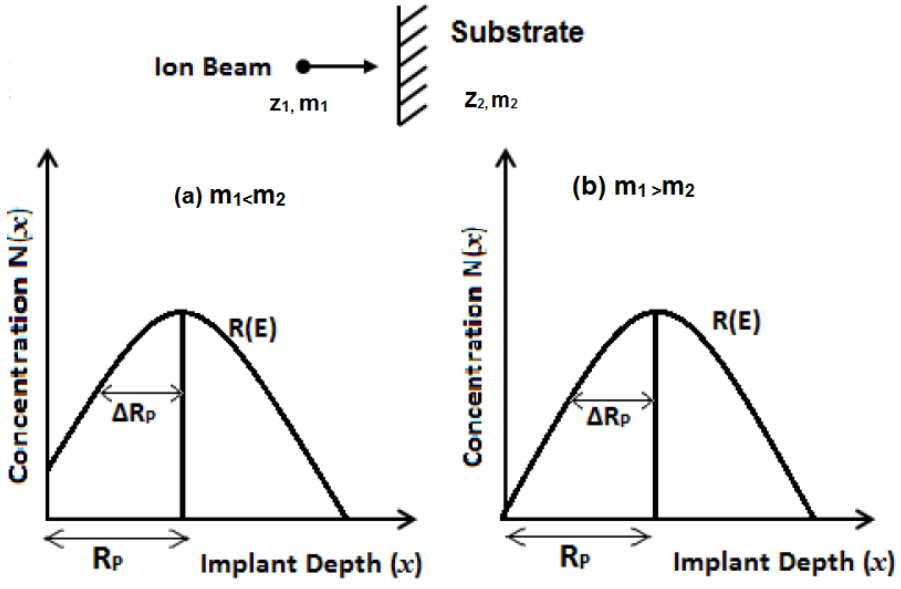

Figure 2.5: *Depth distribution of implanted ions in a target where;* ***(a)*** *the ion mass m_1 is less than the mass m_2 of the substrate ($m_1<m_2$)* ***(b)*** *the ion mass m_1 is greater than the mass m_2 for the substrate ($m_1>m_2$)* [43]. The mean depth R_p depends only on m_1 and E_1 whereas $\Delta R_p/R_p$ depends on the ratio of m_1 and m_2.

Figure 2.5 shows the variation of $R(E)$, $R_p(E)$ and $\Delta R_p(E)$. The mean depth

R_P depends on the ion mass m_1 and the incident energy E_1, whereas the relative width ΔR_P of the distribution depends on the ratio between ion mass and mass of substrate [29, 43]. The concentration *N(x)* is the implant density given in equation (2.3.3).

2.3.6 The Ion Channelling Effect

All ion-solid interaction processes (energy-loss mechanisms, Rutherford scattering, nuclear reaction) have cross sections which depend on the impact parameter of the collision with the target atom [42, 45]. When the target material is isotropic and homogeneous, the impact parameter distribution

$$\vartheta(b) \approx 2\pi b \tag{2.3.10}$$

does not depend on the target and the relative orientation of the beam's direction, therefore both the projectiles and the target atoms move chaotically with respect to each other.

If the target material is monocrystalline (single crystal), the distribution of the impact parameters strongly depends on the relative orientation of the target atoms with respect to the incoming beam. This dependence of the ion's penetration on the crystal orientation is known as "*The Channelling Effect*" [14, 46, 47]. The effect takes place when the angle between beam direction and crystal axis is lower than a critical angle which depends on the crystal structure of the material and mass and energy of the incoming ions

In the channelling effect, the ions incident upon a crystal along a symmetry axis or plane, suffer a series of small-angle scattering that steer them by a succession of low energy-loss event into the open channels between the rows/planes of the lattice

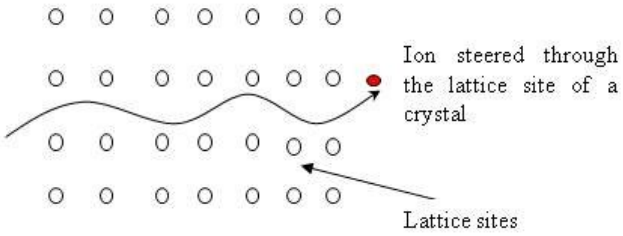

Figure 2.6: *Schematic representation of the channelling effect in a monocrystalline material. (Oscillations of the channelled trajectory occur with wavelengths typically several hundred thousand times the lattice spacing)* [46].

atoms and thus penetrate deeper into the crystal than in other directions [28], as shown in figure 2.6. The channelled incident ions do not get close to the lattice site, where they would experience large angular scattering. This implies that in highly symmetric crystals, the ion comes to rest much deeper into the bulk of the material when they enter along a crystallographic plane. To avoid this effect, the incident ions are directed into these materials at an angle about 7^o in the planes of the lattice atoms, which is grater than the critical angle for h-BN (2-3^o) at 150 keV.

2.3.7 Lattice and Lattice Disorder

As the ion slows down and comes to rest within the target's lattice, it makes many collisions with the lattice atoms, breaking their chemical bonds and displacing them from their lattice sites. The disruption of the preexisting lattice atomic arrangement is known as the *Radiation Damage*. All the atomic collisions initiated by a single ion are known as a *Collision Cascade* [36]. For radiation damage to occur, the incident energy of the ion should be greater than the displacement energy E_d the target atom of the materia/lattice. This causes a phenomenon known as a

Displacement Spike or the *Prompt Stage* [48].

The atoms that are displaced by an incident ion are known as the *primary knock-on atoms* or PKAs. These displaced atoms further displace other atoms, referred to as *secondary and tertiary knock-on atoms*, in the target material and the net result is the production of a highly disordered region near the end of range of the implanted ion [19, 29]. The total amount of disorder and the distribution in depth is dependent on the ion species, the total ion fluence, the incident ion's energy, the temperature of the material and the channelling effect.

Typical defects created include point defects such as vacancies and interstitials. The agglomeration of the point defects forms complexes, generally referred to as *extended defects* which include dislocation loops, grain boundaries, clusters and voids (gaseous inclusions) [32]. Due to these collisions, the atoms in the ion's path are in thermal motion and at high temperatures. The heat created will spread and be reduced in the crystal by conduction, in a phenomenon is known as *Thermal Spikes* which lasts for about 1 ns [49]. If the lattice temperature is high enough, many of these defects will relax by thermally activated migration in the *relaxation phase* of the collision cascade . When the incident ion's energy is less than the displacement energy E_d of the target atoms, the ion is no longer capable of ejecting the target nuclei from their lattice sites [50, 51]. This is the the energy which has to be transferred to a lattice atom for obtaining a stable pair of one vacancy and one interstitial atom (Frenkel pair) as shown in figure 2.7.

It should be noted that radiation damage does not necessarily have adverse effects on the properties of the material. These created defects are in fact responsible for changes in the chemical, physical, optical and electrical properties of materials which in many cases are beneficial. Annealing, a thermal treatment technique, is

normally carried out after implantation of the material in order to repair the radiation damage and trap dopant atoms on substitutional site in case of semiconductor applications. A schematic representation of the collision cascade is shown in figure 2.7.

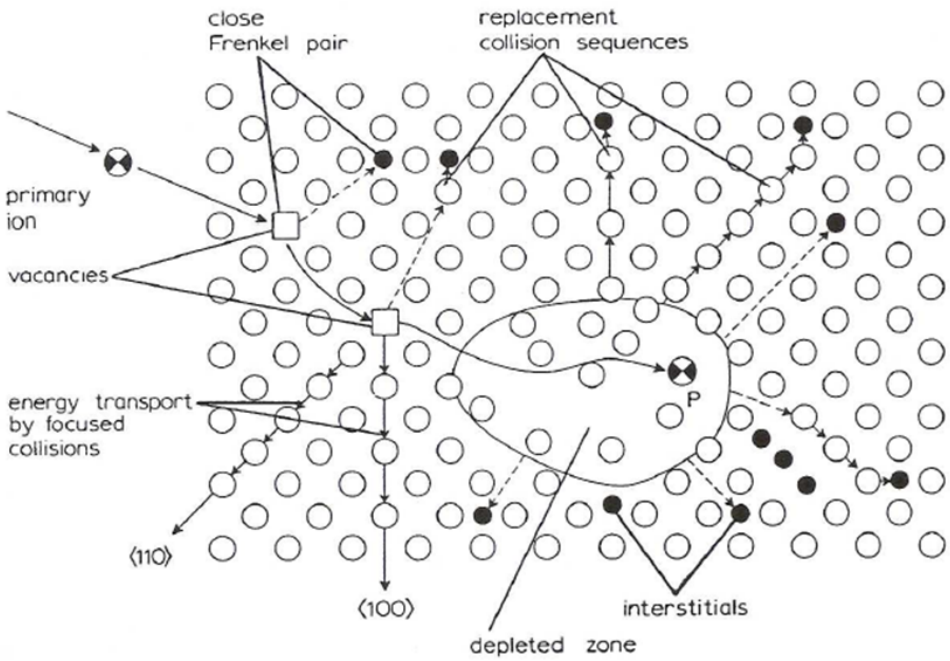

Figure 2.7: *A schematic representation of the collision cascade process showing the collision cascade and focused collision sequences extending beyond the main cascade regime* [49].

2.4 Radiation damage in boron nitride

2.4.1 Stopping and Range of Ions in Matter (SRIM) Simulations

After understanding the theory of ion implantation, it was necessary to know the effect it produces in the material (h-BN) used in this study, at a much higher

level of accuracy. To understand the phenomena that take place during *h*-BN ion implantation with different ions, computer simulations were carried out using the SRIM (Stopping and Range of Ions in Matter) programme, a later version of TRIM (Transport and Range of Ions in Matter). It is a Monte Carlo computer simulation method that predicts the range and distribution of damage that occur during the interactions of energetic ions with a given target material.

It was developed by James F. Ziegler and Jochen P. Biersack around 1983, since then, it has been revised every 5 years [52]. This program uses several physical approximations like the Binary Collision Approximation (BCA), interpolation of the measured stopping powers, and random selection of collisions, to obtain various computational calculations with high efficiency and accuracy [53, 54]. It was used in this work to carry out the respective calculations on BN before the actual experiment.

The SRIM-2008 version was used in this work to perform calculations in order to determine the depth distribution and collision details of the implanted ions and of the energy deposited in electronic and nuclear interaction in the *h*-BN material. Using this program, calculations for different ion beams including helium, lithium, boron, nitrogen and argon were performed on a layer of *h*-BN at different ion energies and fluence in order to establish the relationship of these parameters (energy and ion mass) with the damage caused as ions come to stop/settle within the *h*-BN matrix.

The simulations were done at various energies for the different ions that were used in the actual experiment, implanted into *h*-BN with a density of 2.27g/cm^3. The displacement energies used in these calculations were 19 eV for boron and 23 eV for nitrogen.

Figure 2.8 below shows an example of SRIM output. Figure 2.8(a) is known as the collision event plot which is given as the number of vacancies produced per ion and unit length as a function of depth. This plot can be used to determine the estimated damage density when the value of the peak of the plot is multiplied by the fluence used in the actual experiment. Figure 2.8(b) shows the ion range in terms of the proportion of the implanted atoms against the target depth.

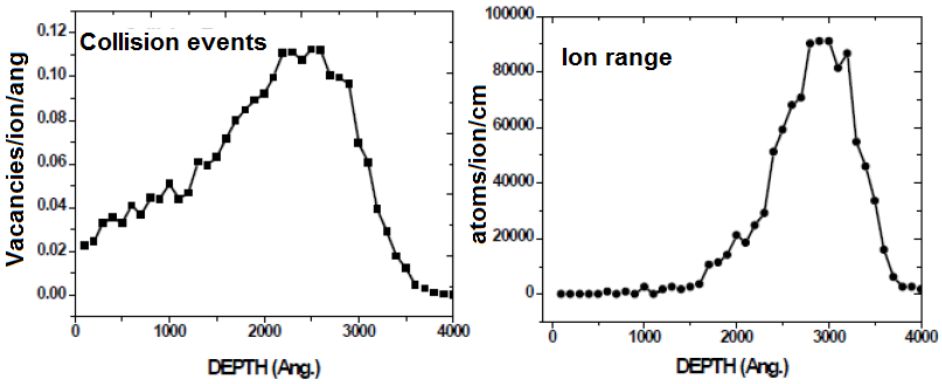

Figure 2.8: *An example of SRIM output at 150 keV showing (a) the collision events and (b) the ion distribution as boron ions come to rest within the h-BN matrix.*

Ion Mass dependence

Figure 2.9 represents the relationship between the vacancies created per angstrom-ion and the penetration depth for the different ions. The total displacements includes the sum of the number of vacancies created in the sample's matrix by the implanted ions and vacancies created by the recoils (the vacancies created by the recoils are normally more than those created by the incident ions). All the simulations were carried out at a constant energy of 150 keV (which was used in the experiment) to realize the maximum depth of the damage at the same energy for the different ions. This relationship compares total atomic displacements generated into the target material and the depth of distribution of different ion species (which

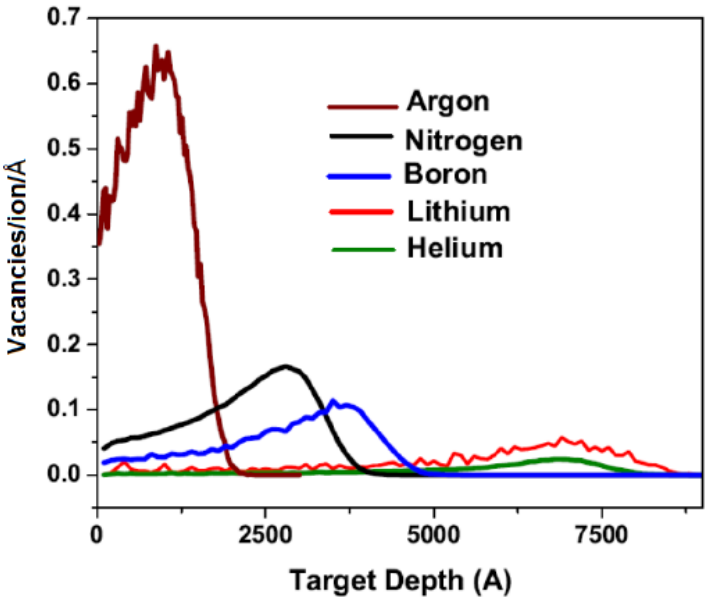

Figure 2.9: *SRIM simulation for the number of primary atom displacements (vacancies) per ion and unit length (Å) versus depth for argon, nitrogen, boron, lithium and helium ions species implanted into h-BN at 150 keV.*

were used in the actual experiment) implanted into h-BN in order to demonstrate the effect of varying the incident ion mass.

It is observed the all the accelerated ions came to rest and are embedded within shallow depths, creating a damaged region which is $< 1\mu$m below the surface of the host h-BN material.

From figure2.9 it is observed that the integrated number of vacancies/ion and unit length increases with increasing ion mass, since argon had the highest integrated number of displacements followed by nitrogen, boron, lithium and finally helium. This implies that more damage is generated by heavier ions at the same energy as compared to lighter ions. The heavy ions are more likely to knock off more of the substrate's atoms during their stopping process as compared to the light ions which interact less with the substrate atoms in their stopping process.

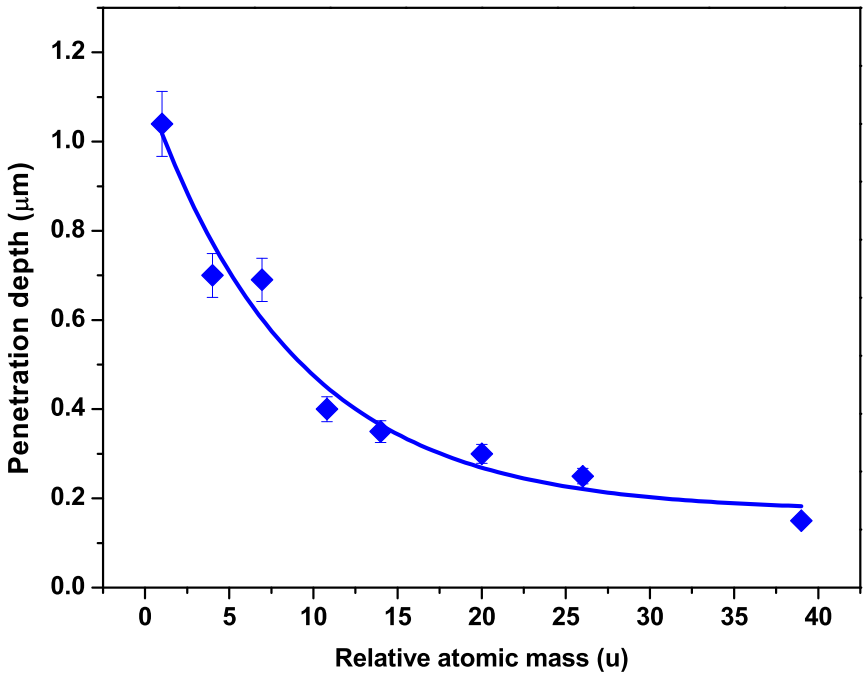

Figure 2.10: *Relationship between the ion penetration depth and the relative atomic mass for different ions implanted into h-BN. All simulations were carried out at 150 keV.*

It is also observed that lighter ions penetrate deeper into the substrate as compared to the heavier ones. Helium penetrated a depth of 0.75 μm and an end of range depth/maximum depth of 0.87 μm, lithium penetrated to a slightly higher projected range of 0.80 μm and end of range depth of 0.94 μm. Helium and lithium had almost similar values due to the fact that they have almost similar atomic masses. Boron penetrated closer to the surface at 0.4 μm and 0.50 μm for projected range and end of range depths respectively. Nitrogen and argon had a penetration depth of 0.35 μm and 0.13 μm respectively. The ion's penetration ability depends on its atomic mass, as such, heavier ions are bound to be stopped faster with the atoms of the target material as compared to their lighter counterparts and as such will settle closer to the surface. This is shown in figure 2.10 together with data for hydrogen, neon and aluminium.

When the mean number of vacancies/ion/$\mathring{A}$ for damage distribution is multiplied by the fluence over the entire region, it gives the damage density/vacancy concentration ρ in the material [55] i. e.

$$\rho = Meanvacancies/ion/\mathring{A}) \times fluence(ions/cm^2) \tag{2.4.1}$$

with ρ having units of vacancies/cm^3. Taking an example of boron with the number of vacancies per ion per unit length= 0.036 vacancies/(10 $^{-8}$ cm-ion) at a fluence of 5×10^{14} ions/cm^2, which is the optimum fluence that was obtained in the actual experiment, then its damage concentration in h-BN will be,

$$\rho = 0.036vac/10^{-8}cm - ion) \times (5 \times 10^{14}(ions/cm^2) \tag{2.4.2}$$

$$\rho = 1.8 \times 10^{21}vac/cm^3 \tag{2.4.3}$$

Table 2.1: *Some of SRIM input and output conditions for boron implantation in h-BN. All the calculations were performed at the energy of 150 keV and the damage density calculated for the different ions at optimum fluences.*

Ion species	Ion fluence (ions /cm^2)	Optimum Range (μm)	Projected Straggle (μm)	Mean Vacancy per ion per unit length	Vacancy Concentration (x10^{21}Atoms /cm^3)
Argon	1×10^{13}	0.09	0.03	0.68	20
Nitrogen	1×10^{14}	0.28	0.04	0.128	3.1
Boron	5×10^{14}	0.35	0.05	0.036	2.4
Lithium	1×10^{15}	0.69	0.10	0.017	1.8
Helium	5×10^{15}	0.70	0.07	0.006	1.3

A summary of all the parameters obtained from SRIM is shown in table 3.4. All the simulations were carried out at 150 keV and at the mean number of vacancies/ion and unit length. The implantation density was calculated at a different

optimum fluences that were obtained in the actual experiment. From this data, it is observed that the almost equal damage concentration is obtained for the different ions at optimum fluence. As such there is a uniform dependence of the damage density independent of the ion used. Similar trends have also been seen in implantation of other substrates e.g. in gallium nitride (GaN) [56].

Ion Energy dependence

Figure 2.11 shows the energy dependence of the vacancy distribution and target depth for the different ions used in h-BN ion implantation. The simulations were done for energies between 40 and 150 keV which was the energy range used in the actual experiment.

From these SRIM calculations, it is observed that the implant depth is localized to depths just below the surface and as the energy increases the implanted region is buried more into the sub-surface regions of the substrate. The depth distribution also depends on the ion mass, with the lighter ions penetrating more below the surface than the heavier ones at the same energies. Integrating the number of vacancies over the entire range for each ion, the number is observed to increase with increasing energy for all the ions with the highest number of vacancy introduced by argon at the highest energy. The energy variation is normally important in situations where a uniformly implanted layer from the surface is required. In this case a multiple implantation sequence is employed where implantation is done on the same sample at different energies and fluence fractions [32].

An important observation is also with respect to the damage distribution with mass and energy. Helium at 150 keV, for example, has the implanted layer buried about 0.9 μm into the substrate with minimal interference/interaction with the

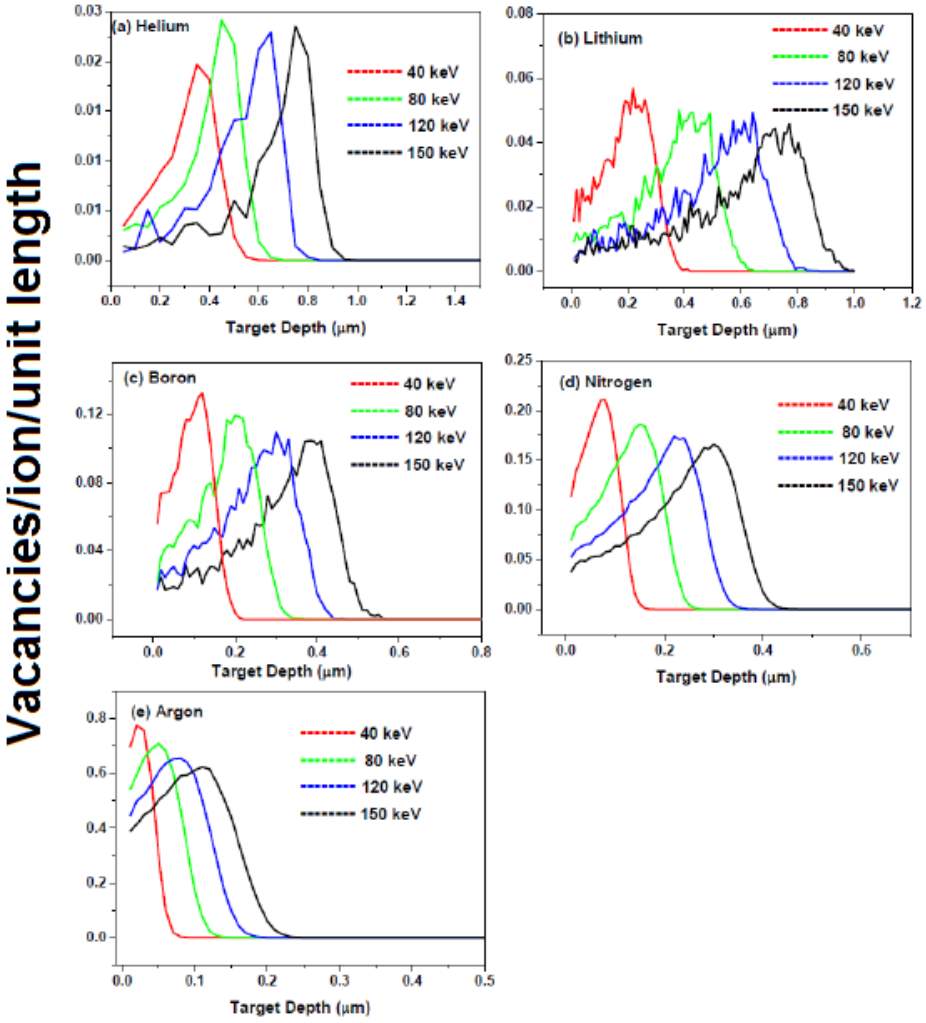

Figure 2.11: *SRIM simulations for h-BN implanted with different ions in energy range of 40 keV to 150 keV for (a) Helium, (b) lithium (c) boron, (d) Nitrogen and (e) Argon.*

surface atoms. On the other hand, argon at the same energy has a damage distribution extending from the surface up to the end of range of the implant about 0.2 μm (the trend is the same for the intermediate ions used). This knowledge is important in material modifications where top-most surface modifications are best achieved by heavy ion implantation at low energies while the sub-surface modification are best implemented by light ion implantation at high energies. Figure 2.12 gives a summary on how varying the incident energy affects the penetration depth for each ion.

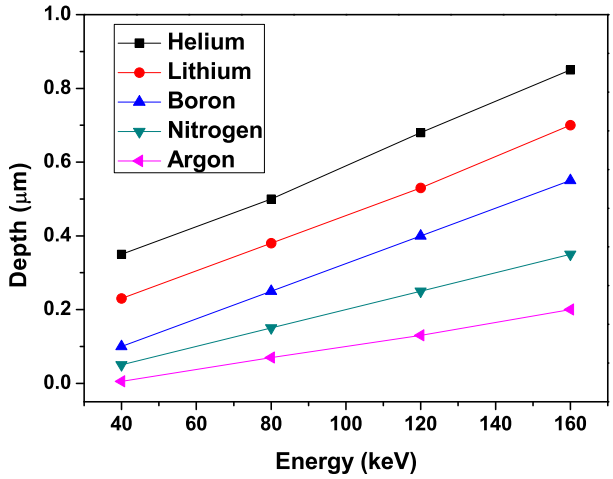

Figure 2.12: *A summary of the relationship between the penetration depth vs implant energy for the different ions.*

Stopping power in boron nitride

Since the energy regime used in this simulation was up to 150 keV, it is essential to study the stopping process across this energy regime for the different ions as they settle within the *h*-BN matrix. Calculations were carried out to establish the dominant stopping process responsible for the maximum damage exhibited by the different ions as they lose their energy from 150 keV to the lowest energy possible which is 0.1 keV in SRIM.

Figure 2.13 shows the SRIM simulations for *h*-BN implanted with different ions where each graph shows how the different ions exhibit different energy loss regimes as they settle within the substrate's matrix.

Figure 2.13 (a) shows the stopping power-energy relationship for helium implanted into *h*-BN. The electronic stopping is the dominant stopping process for helium at higher energies, with nuclear stopping having its maximum at a very low energy of 0.7 keV. This implies that only when the ion's energy has reduced to 0.7 keV does nuclear stopping become the dominant stopping process. In practice

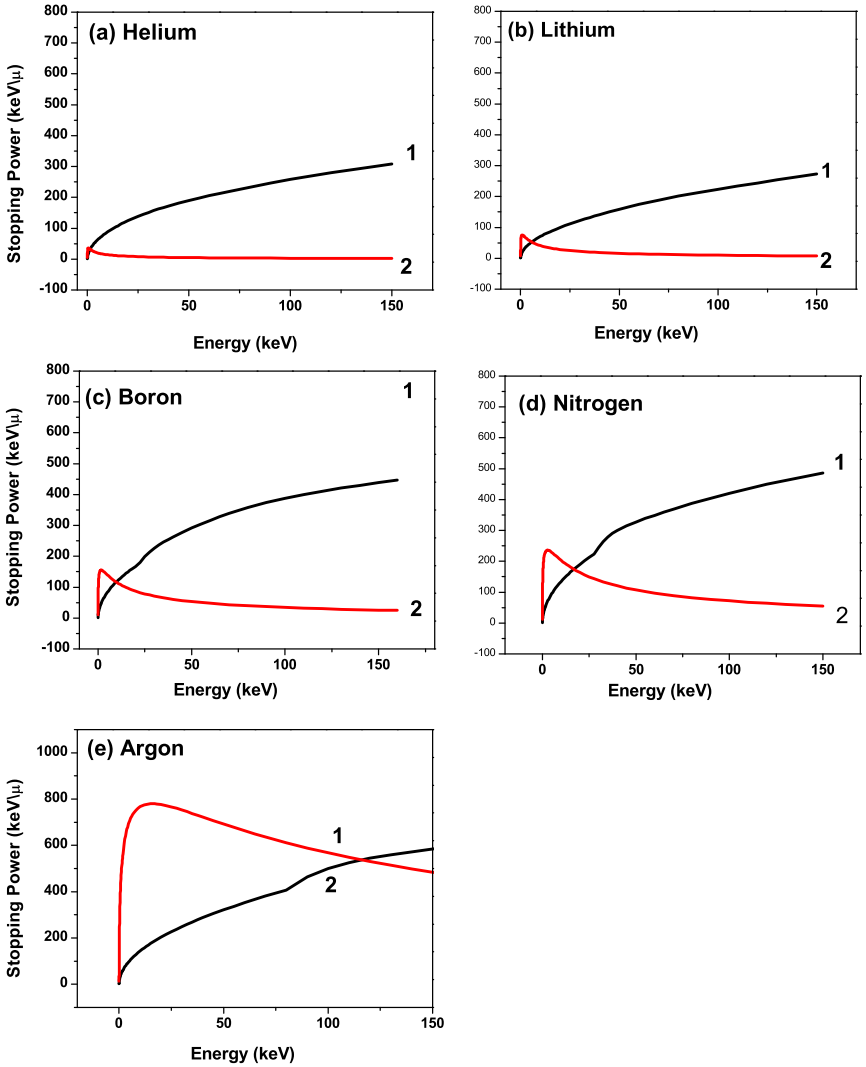

Figure 2.13: *SRIM simulations for h-BN implanted with different ions in energy range of 0.1 keV to 150 keV. The figure is a schematic illustration of how the (1) electronic and (2) nuclear stopping contribute to the stopping power with respective energies for the different ions.*

helium being a light ion, at high energy has less interaction with the nuclei of atoms in the substrate, interacting mostly with the electrons and hence making electronic stopping the major process when the implanted ions are at high energy.

Helium and lithium ions have very close atomic masses and therefore will have almost similar stopping power regimes. Figure 2.13 (b) represent the relationship of the stopping power and the energy for lithium ions with the nuclear stopping being dominant and maximum at 0.8 keV.

Figure 2.13 (c) and (d) are the SRIM simulations for the stopping power against

the energy for boron and nitrogen ions respectively. The behavior is similar as that observed in lithium and helium where the electronic stopping dominates the stopping process in both cases at high energies and the nuclear stopping becomes dominant at when the ions have lost most of their energy in the low energy regimes. Nuclear stopping is maximum at 1.6 keV for boron and 2.5 keV for nitrogen.

Figure 2.13 (e) represents the SRIM calculation for argon ions. This was the heaviest ion that was used in this work. The stopping power versus energy plot for this ion is different as compared to all the other ions. Unlike for the light ions, where electronic stopping is dominant for most of the stopping process, for argon the nuclear stopping is the most dominant process. The electronic stopping is dominant from the time of implantation at 150 keV, and as the ions loose their energy to 120 keV, the nuclear stopping begins to dominate the stopping process attaining a maximum at 15 keV.

In summary, the stopping process depends on the mass of the incident ion in the same matrix. Most light ions, at high energy, interact primarily with the electrons of the host material's atoms and interact more with the nuclei only when the ions have lost a sufficiently large amount of energy and their velocity reduced. For the heavy ions, they are slowed much faster and therefore lose their energy faster in the electronic stopping process. This increases the probability of interacting with the the nuclei of the substrate's atoms hence making nuclear stopping dominant.

It is noted that for light ions, when electronic stopping is dominant, the nuclear stopping is not completely zero, but has very low value of energy per micron. Also noted, unlike in the light ions where the nuclear stopping is very small when electronic stopping is dominant, for heavier and larger implanted ions like argon both stopping processes are high for the energy regime used in this work.

Chapter 3

Boron Nitride

3.1 Structure, Properties and Applications

3.1.1 Introduction

Boron nitride is an important inorganic compound with the chemical formula BN. A BN unit cell consists of boron (B) and nitrogen (N) atoms in equal proportions. These atoms straddle carbon (C) in the periodic table hence making BN isoelectronic to carbon. It therefore has the tendency of forming compounds that are isostructural (with similar structures) to those of carbon [57, 58].

Five crystalline phases in BN exists, namely: hexagonal boron nitride (h-BN), cubic boron nitride (c-BN), wurtzite boron nitride (w-BN), rhombohedral boron nitride (r-BN) and rocksalt boron nitride (RS-BN) [57, 59, 60, 61, 62]. The crystal structures for BN are shown in figure 3.1. Cubic BN and w-BN structures are the dense and harder phases of BN made up of 4 strong covalent σ-bonds with sp^3 hybridization, similar to that found in cubic diamond and hexagonal diamond (lonsdaleite) respectively. Hexagonal BN and the high pressure modification r-BN phases have the graphite-like structure, in which flat hexagonal sheets with sp^2 hybridization (π-bonds) are layered by different stacking sequences on top of each other [57, 60, 63].

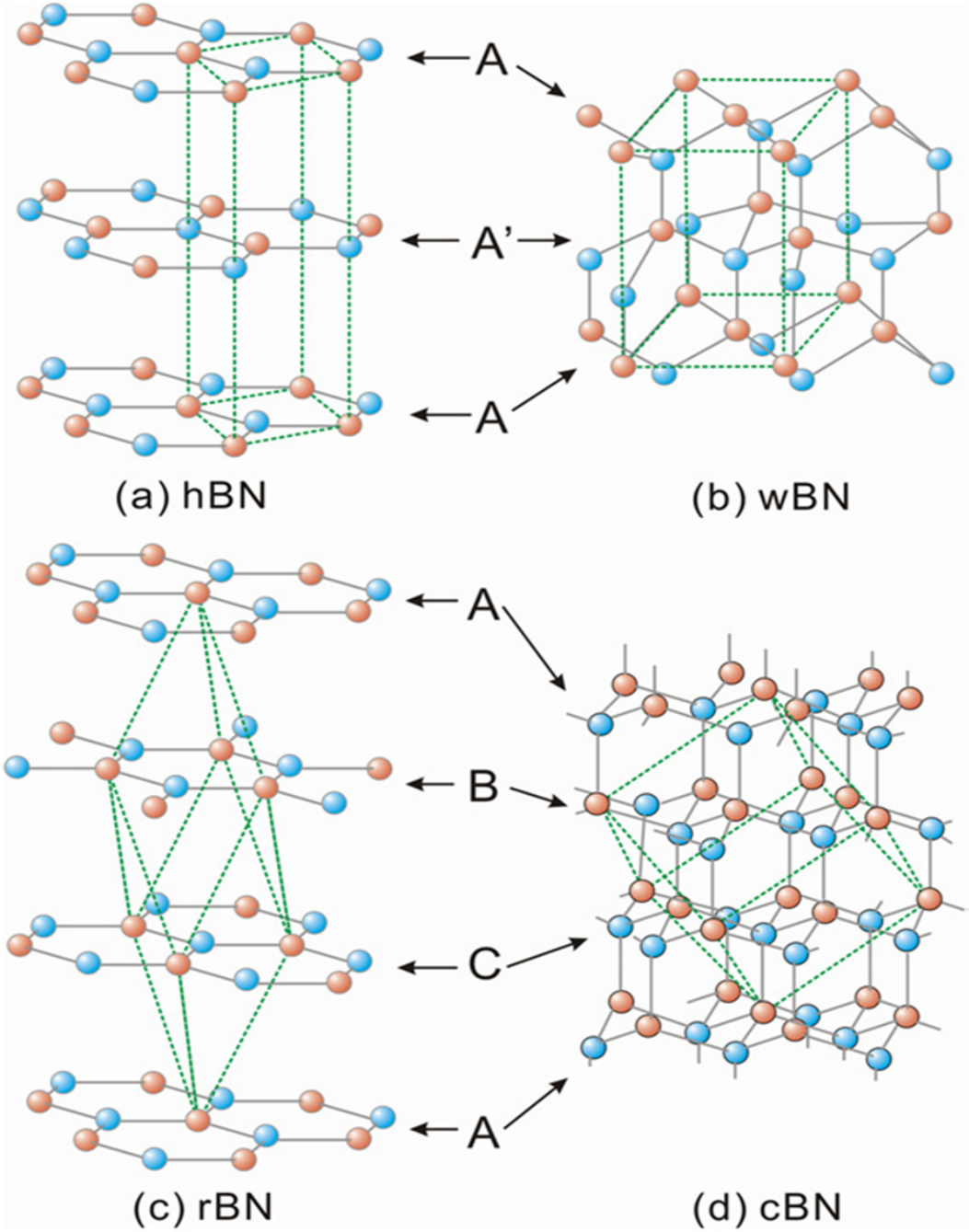

Figure 3.1: *Crystal structures for the different polymorphs of BN. The blue spheres represent the nitrogen atoms while the orange ones represents the boron atoms. The unit cell indicating the stacking sequence is shown by green dotted lines. AA'A represents the stalking sequence for h-BN and w-BN while ABCA represents the staking sequence for r-BN and c-BN* [2].

Table 3.1: *Position of boron and nitrogen atoms for the various phases of boron nitride. A common feature to all the BN polymorphs is the location of B and N nearest neighbour in alternate positions* [64].

Phase	Atomic position
h-BN	B (0,0,0), $(\frac{2}{3}, \frac{1}{3}, \frac{1}{2})$ N $(\frac{2}{3}, \frac{1}{3}, 0)$, $(0,0, \frac{1}{2})$
r-BN	B (0,0,0), $(\frac{2}{3}, \frac{1}{3}, \frac{1}{3})$, $(\frac{1}{2}, \frac{2}{3}, \frac{2}{3})$ N $(\frac{2}{3}, \frac{1}{3}, 0)$, $(0, \frac{1}{2}, \frac{1}{2})$, $(0,0, \frac{2}{3})$
c-BN	B (0,0,0), $(\frac{1}{2}, \frac{1}{2}, 0)$, $(0, \frac{1}{2}, \frac{1}{2})$, $(\frac{1}{2}, 0, \frac{1}{2})$ N $(\frac{1}{4}, \frac{1}{4}, \frac{1}{4})$, $(\frac{3}{4}, \frac{3}{4}, \frac{1}{4})$, $(\frac{1}{4}, \frac{1}{4}, \frac{3}{4})$, $(\frac{3}{4}, \frac{1}{4}, \frac{3}{4})$,
w-BN	B (0,0,0), $(\frac{1}{3}, \frac{2}{3}, \frac{1}{2})$ N $(0,0, \frac{3}{8})$, $(\frac{1}{3}, \frac{2}{3}, \frac{3}{8})$

The c-BN and h-BN structures are the stable phases of the boron nitride at ambient conditions hence they have many applications as compared to w-BN, r-BN and rock salt structures which are the metastable phases at standard temperature-pressure conditions. The structural parameters shown in table 3.1 and table 3.2.

Occasionally observed is the explosive boron nitride (e-BN) [60, 61] between the low density and high density BN. It contains equal amounts of sp^2 and sp^3 covalent bonds, where nitrogen and boron atoms are placed parallel to the strongly deformed hexagons [67].

There also exist two non-crystalline forms of boron nitride, which are turbostratic boron nitride (t-BN) and amorphous boron nitride α-BN/(a-BN) [2, 64, 65]. In turbostratic boron nitride, the stacking of the sp^2 layers is random, and the layers are rotated randomly along the c-axis. It is similar to h-BN but the order in the direction of the c-axis is disturbed in such a way that each hexagonal layer is twisted in a random way against its neighbour's layers. The stacking produces

Table 3.2: *Structural and cohesive properties of the various phases of boron nitride. ΔE is the energy difference with respect to the cohesive energy of the* c*-BN structure* [65, 66].

Phase	a(Å)	c(Å)	d(Å)	Space group	Bulk modulus (GPa)	Volume /atom (Å)	Δ E(eV) /atom
h-BN	2.504	6.66	1.446	$P6_3/mmc$	36.5	8.747	0.055
r-BN	2.318	9.99	1.450	R_3m	32.8	8.693	0.052
c-BN	3.615	-	1.560	$F_{43}m$	400	5.797	0.000
w-BN	2.551	4.21	1.576	$P6_3mc$	395	5.813	0.011
Rock Salt BN	3.474	-	-	F_m3_m	410	5.244	1.244

a broad and diffuse X-ray diffraction pattern that is distinct from h-BN and r-BN [68, 69], since it has a larger interplanar spacing by 15 percent than the basal planes of these ordered phases.

Amorphous BN is the most disordered phase of BN, characterized by an atomic level structural disorder, which has a non-detectable order on the microscopic level [2, 70]. It is usually difficult to distinguish between the t-BN and the α-BN using X-ray diffraction patterns and spectroscopy, therefore best analyzed by electron microscopy. The α-BN is used in the manufacture of semiconductor devices for example MOSFETs [71].

3.1.2 Synthesis of Boron Nitride

The synthesis of boron nitride has been made possible by the fact that boron and nitrogen have almost equal atomic radii. It has been produced by a nitridation or ammonolysis process of boron oxide at elevated temperatures of 1000 ^{o}C [72, 73, 74].

These industrial processes are based on two reactions: either by melting boron oxide with ammonia, or melting boric acid or alkaline borate with urea, guanine, melamine[1], or a suitable organic nitrogen compound in nitrogen atmosphere [73, 75, 76].

The synthesis reaction involving ammonia and boric acid is given as

$$3B(OH)_{3(s)} + 3NH_{3(g)} \rightarrow 3B(NH_2)_{(s)} + 6H_2O_{(l)} \tag{3.1.1}$$

Upon heating to temperatures of about 1000 ^{o}C, one obtains,

$$B(NH)_{2(s)} \rightarrow 2NH_{3(g)} + BN_{(s)} \tag{3.1.2}$$

The combustion of the boron nitride powder in nitrogen plasma at 5500 ^{o}C yields the h-BN used for lubricants and tones. Hexagonal-BN can also be obtained by hot-pressing the BN powder using boron oxide as a sintering agent with subsequent machining [77].

The other BN phases have been produced from hexagonal BN as a starting material. Wurtzite BN, with polytype 2H, has been synthesized from h-BN by high pressure structural phase transition (HP-SPT'S) [78, 79, 80]. It is obtained via high pressure or dynamic shock method applied to h-BN at temperature ranges of 300 - 2500 ^{o}C under static pressure of 11.5 - 13.0 GPa, in the presence of a Fe, Ni or Mg catalyst. Lian *et al* [81] also reported that w-BN can be obtained from h-BN at relatively hypothermal condition of 300 ^{o}C at a much lower pressure of 12 MPa. Wurtzite BN is known to be a superabrasive material harder than diamond [82], with Vickers hardness of up to 117 GPa. Its applications has however been limited because it is metastable at ambient conditions.

[1] An organic base and a trimer of cyanide with a 1, 3, 5,-triazine skeleton

Rhombohedral BN with polytype 3R is formed transitionally during the h-BN to c-BN phase transformation, at temperatures of 1600 ^{o}C and a total gas pressure of 400 GPa on the h-BN substrate [83, 84]. Ishii *et al* [85] also reported that heating h-BN in sufficient amount of oxygen up to temperatures between 1700 and 2000 ^{o}C in nitrogen atmosphere yielded a r-BN crystal system.

A phase transformation from the c-BN to RS-BN has been shown to be possible. This stems from the theoretical work of Cui et al [86] on the first-principle study of zinc-blende to rock salt transition of BN, where it was concluded that structural transformation from c-BN to RS-BN is found to occur at pressures between 550 and 1088 GPa. Rocksalt BN is also formed from the w-BN under very high pressure [58].

Amorphous BN is produced by chemical vapour deposition of B-trichloroborazine (BCl_3NH_3) with caesium metal as a catalyst, or of N_2/NH_3 with ZrB_2 [87, 88]. This amorphous product can be converted into t-BN phase upon heating to temperatures of 1100 ^{o}C [89]. Cubic BN is synthesized using various methods which will be discussed in details in section 3.4.

3.1.3 The Phase Diagram of Boron Nitride

Phase diagrams are the primary visualizing tools in materials science because they allow one to predict and interpret changes in the composition of a material from one phase to another. As a result, phase diagrams have been proven to provide an immense understanding of how a material forms microstructures within itself [90].

An understanding of the thermodynamic stability of a material can lay a foundation to ascertain the kinetic processes that take place during its synthesis. It is well known that the Gibbs free energy is an adaptable measure that determines the

stability of a state in the phase transformations among competing phases [90, 91].

Thermodynamically, the phase transformation is prompted by the difference in the free energy. The Gibbs free energy (G) can be expressed as a function of both pressure and the Helmholtz free energy (F) given as [91, 92]

$$G=F+PV \tag{3.1.3}$$

here P is the pressure of the system, V is the volume and F is the Helmholtz free energy which depends on temperature, and is given by,

$$F= U-TS \tag{3.1.4}$$

where U is the internal energy of the system, T is the temperature and S is the entropy.

The most important phases of BN are c-BN and h-BN since they are the stable forms under ambient conditions as mentioned earlier. Under a given condition of pressure and temperature, c-BN and h-BN can coexist, but only one of the phases is stable, with minimal free energy, while the other is metastable [65, 92, 91]. The cubic and the hexagonal phases are found to coexist at the point where the Gibbs free energy is zero [93].

The first phase diagram for BN was reported by Bundy and Wentorf in 1963 [67, 94]. Over recent years, this equilibrium phase diagram of BN has been under constant modification. The generally accepted version was proposed by Corrigan and Bundy in 1975 [95, 96] based on several research works concerning the equilibrium line between graphite and diamond [90]. This phase diagram is shown in figure 3.2 [97].

It shows that c-BN is thermodynamically stable up to temperatures of 1600

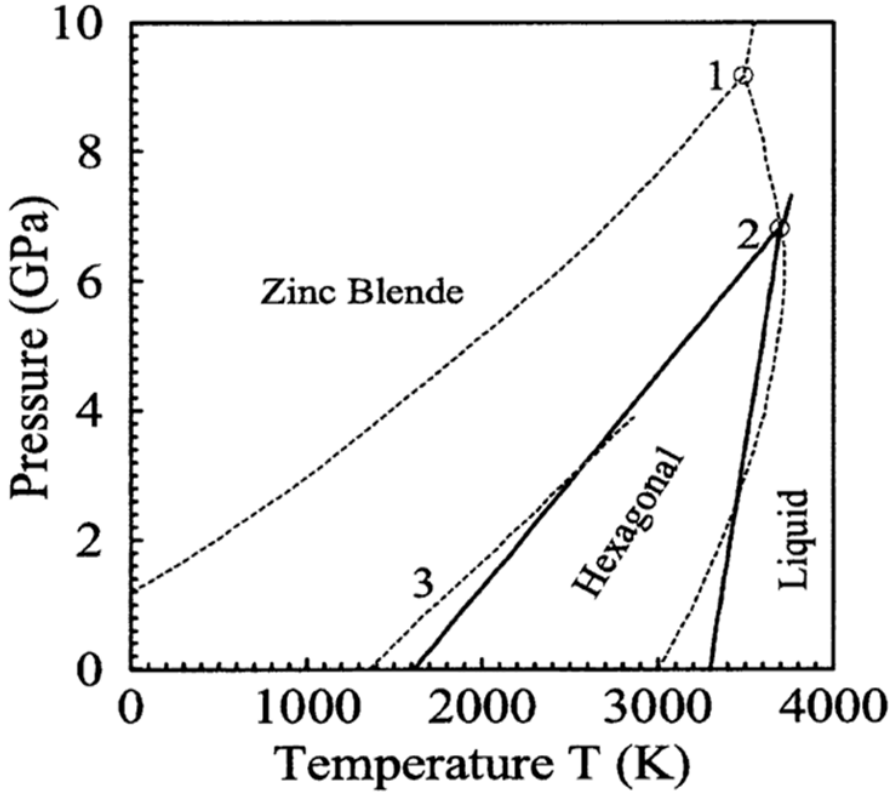

Figure 3.2: *The generally accepted phase diagram for boron nitride. (Dash line is the phase diagram as proposed by Corrigan and Bundy [96] and the continuous line is the phase diagram according to Wentorf [98]).*

K, and since it has a low molar volume it is characterized by a wide region of thermodynamic stability at high pressures [89]. It also shows that h-BN is thermodynamically stable at high temperatures [65, 70, 99]. The phase diagram for BN is strikingly different from that of carbon where in contrast to c-BN being the stable phase, diamond is the metastable phase under ambient thermo-baric conditions [2, 100]. The knowledge of the phase diagram for BN is therefore important in the synthesis of c-BN and the other BN phases.

3.2 Hexagonal Boron Nitride

Hexagonal boron nitride (h-BN) is one of the most important and widely used form of boron nitride and therefore forms the basis of many industrial applications [68, 87]. It is transparent when in single crystal form and appears as a white solid when pressed as shown in figure 3.3. It has similar structure and bonding as that found in graphite, hence often referred to as "white graphite" [2, 101, 102].

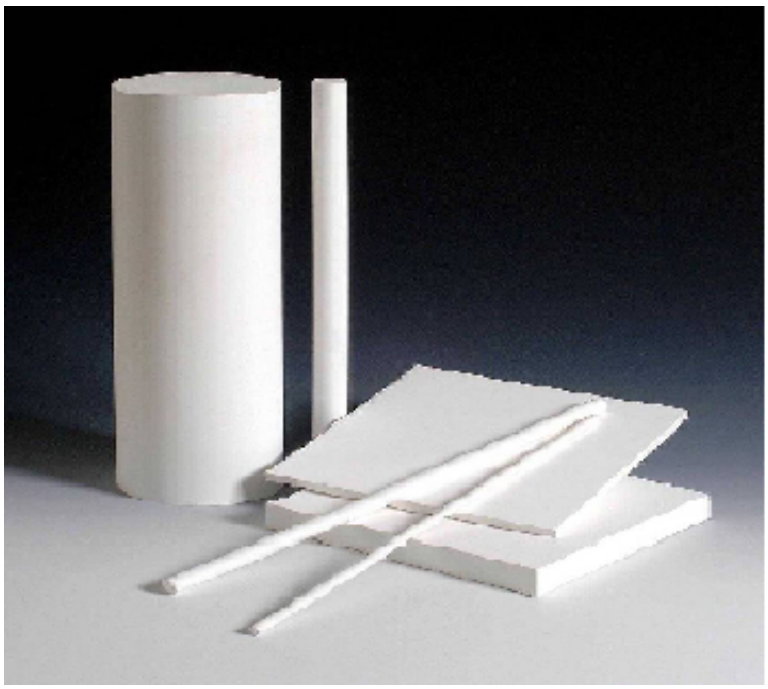

Figure 3.3: *A photograph of hexagonal boron nitride rods and sheets obtained from GoodFellow UK Ceramic company website.*

Hexagonal BN (h-BN also g-BN) is a light material with a density of 2.27g/cm^3. It is made of hexagonal rings which form basal planes, with every boron atom bonded to three nitrogen atoms in the same plane and vice versa [101, 103]. Each layer in a plane consists of flat or nearly flat network of regular B_3N_3 hexagons [104, 105, 106]. These hexagon layers are arranged into AA'AA' stacking sequence

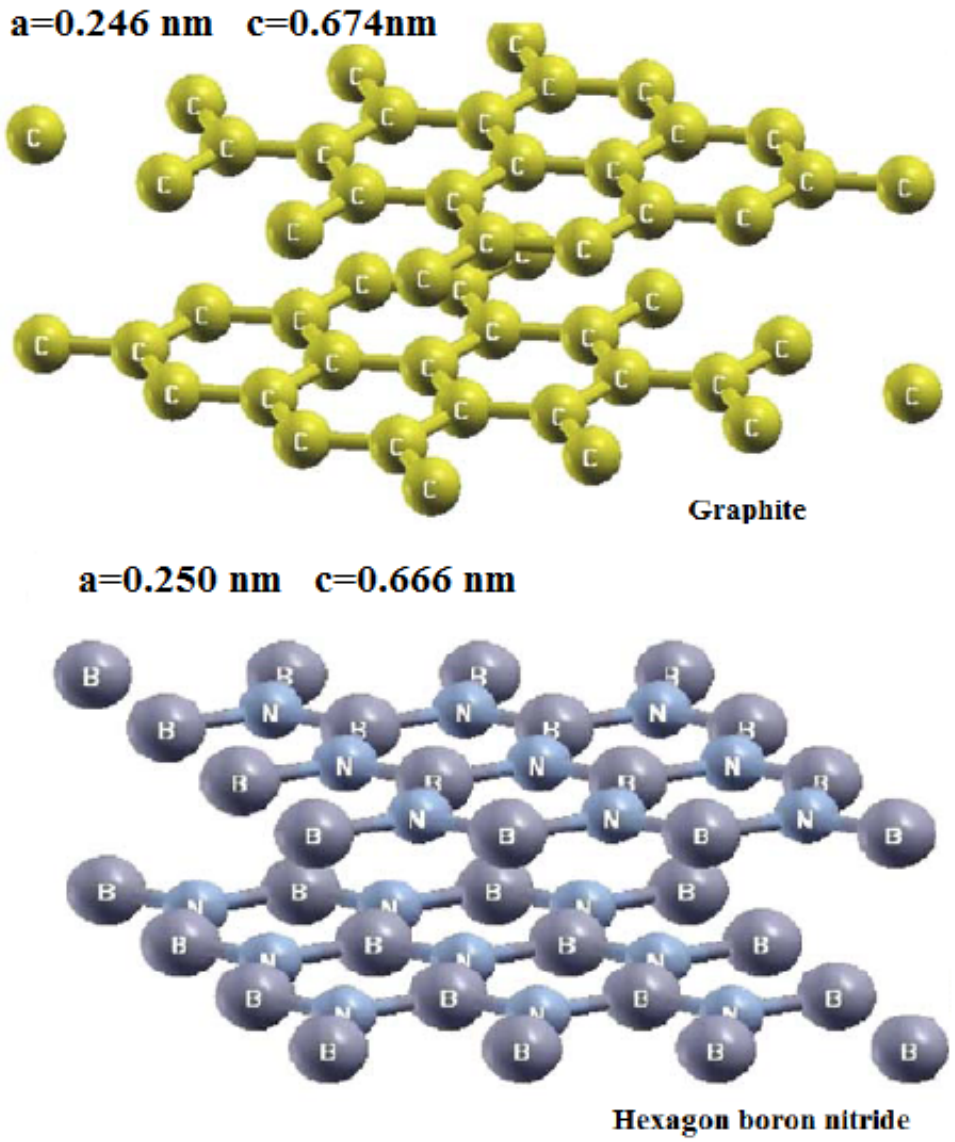

Figure 3.4: *Comparison between the structures of graphite and hexagonal boron nitride* [102, 103].

(see fig 3.1), where there is a 180^o rotation in the atomic arrangement of every alternate layer, different from that of hexagonal graphite which is the ABAB stacking sequence in which the hexagonal sheets are attached directly above each other but with each successive layer rotated by 30^o as shown in figure 3.4 [64, 70, 104].

The strong directional bonding between the adjacent coplanar atoms shows charge delocalization. The in-plane atoms are bonded by localized sp^2 hybridization, while the out of plane layers are bonded by the delocalized weak π-orbitals, with electrons in the π-orbital localized closer towards the N-atom than to the B-atoms. This characteristic makes h-BN to be an electrical insulator. Depending on the atomic radii assumed for each atom, the N atom gains 1-3 electrons to its three neighboring boron atoms [64, 101, 104]. The interplanar layer bonding is weak with no directional bonds present and is a mixture of van der Waals bonding and ionic attraction between the oppositely charged ions in the adjacent planes [103, 106].

The stacking pattern of h-BN can lead to the production of a diamond-like structure by direct compression along the c-axis as well as splitting the basal planes. This splitting leads to strong chemical bond formation between the (0002) planes and finally a tetrahedral coordination can be induced. This process is known as *the puckering mechanism* [70, 103].

Great interest has been directed towards h-BN due to its fascinating properties. Most of these properties are exhibited due to the strongly anisotropic character (directional dependence) of h-BN [103]. It is a good insulator, commonly used in vacuum technology, X-ray lithography masks and in thin film form for microelectronic device fabrication [102, 63]. It has a high melting point (>3000 ^{o}C) and is an excellent thermal conductor, therefore quite useful as an additive to various

types of heat radiation materials [73, 101].

Because of its weak interplanar layer bonding, h-BN is a soft material which has become a popular wear-resistant dry lubricant. The ease of sliding between basal planes makes it a great solid lubricant [101, 107] for reducing wear and friction. it can therefore be added to other solid/liquid lubricants for machining processes.

Hexagonal BN is a very inert refractory material to molten metal and salts hence, commonly used for crucibles in vacuum evaporating technologies and as a mould release agent [11, 108]. It is also a non wetting material and therefore used widely in glass manufacturing [11].

3.3 Cubic Boron Nitride

Cubic boron nitride (c-BN) represents itself as one of the simplest and most interesting group III-V compounds [104, 109, 110]. Pure c-BN is transparent or amber in colour, with different colours occurring with introduction of defects or excess boron or nitrogen. (Figure 3.6 is an example of c-BN with excess nitrogen). It crystallizes into the zinc blende (sphalerite) structure with a cubic unit cell which closely resembles the structure of diamond as shown in figure 3.5. Its space group is changed from the centrosymmetric Fd_{3m} of diamond to the non-centrosymmetric $\mathrm{F}_{43}\mathrm{m}$ group in c-BN [65, 104, 111].

The c-BN structure is composed of two interpenetrating face centred cubic (FCC) sublattices, each containing only one type of atoms and shifted over one quarter (1/4) of the lattice along the diagonal direction [113]. It is bonded through strong sp^3 hybridization (σ- bond), with each boron atom tetrahedrally coordinated to four neighboring nitrogen atoms, and vice-versa. These atoms are arranged in a three layered (ABCABC...) stacking sequence as shown in figure 3.1 [64, 70].

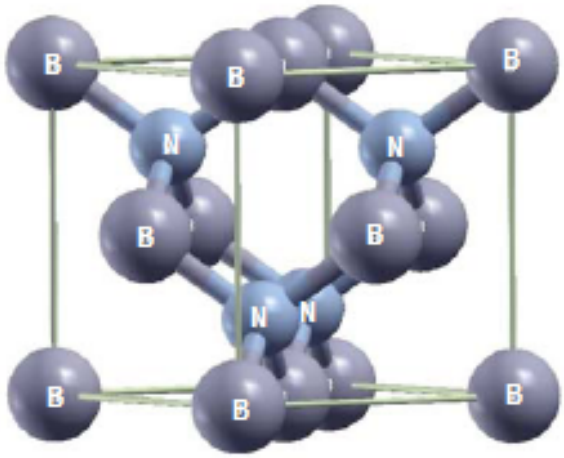

Figure 3.5: *The structure of c-BN* [103].

Figure 3.6: *Photograph representation of c-BN. (a) is the amber, semi-blocky c-BN, with and irregular crystal morphology and (b) is the golden coloured c-BN with a blocky morphology* [112].

Detailed studies of charge deformation densities from X-ray diffraction show that a formal charge transfer of 0.46 electrons occurs from boron towards the nitrogen as expected from their respective electro-negativities, and 0.36 electrons are transferred from nitrogen to boron [110, 113]. The bond in *c*-BN is covalent and partially ionic, thus making the structure electrostatically favoured [109].

Due to its structure and bonding, *c*-BN exhibits excellent properties which make it very important in mechanical, optical, chemical, thermal and electrical applications.

The large charge accumulation between atoms and the high density strong covalent bonds with a short B-N bond length of 1.57Å are responsible for the extreme hardness in*c*-BN [109, 114]. It exhibits hardness values of between 73 and 75 GPa, second only to diamond's 115 GPa [104, 115, 116, 117], hence it is classified as a "superhard" material. A comparison of the hardness of c-BN with other superhard materials is shown in table 3.3 This extreme hardness makes *c*-BN an important material for various industrial applications. Some of these applications include, as powder for abrasive processes (i.e. with a wheel setup) and as a sintered ceramic for sawing, cutting, drilling or crushing purposes. Sintered *c*-BN in particular is inserted in high speed machining equipment for hardened steel, chilled cast iron, carbides and nickel or cobalt based superalloys [9, 67, 70]. Borazon, commercially produced *c*-BN, is the only material that can scratch diamond and is therefore used in diamond cutting applications [92, 94, 118].

Cubic boron nitride has a low value of molar volume, and it therefore has high thermodynamic stability at high pressures, for instance, it has a high melting point (3000 ^{o}C) and high thermal conductivity (13 $\mathrm{Wcm^{-1}K^{-1}}$), second to diamond (4000 ^{o}C and 20 $\mathrm{Wcm^{-1}K^{-1}}$) respectively. It also has a low a dielectric constant

Table 3.3: *Comparison of the Vickers hardness and fracture toughness of common superhard materials* [119, 120].

Material	Vickers Hardness (GPa)	Fracture toughness $(MPam)^{1/2}$
Diamond	115	5.3
Cubic BN	75	6.3
Cubic BC_2N	72	4.5
Cubic BC_5	71	9.5
B_4C	38	3.5
ReB_2	48	

of 7.1 making it useful in high-temperature high-frequency microelectronic device fabrication [2, 94, 121, 122].

It is essentially a semiconducting material superior to other group III-V semiconductors. For instance, it is the lightest known group III-V compound with the widest indirect band gap (E_g= 6.0-6.5 eV) of all semiconductor [9, 67, 123]. It also has a large refractive index (n $_{c-BN}$=2.17), and a high transparency in a wide region of the electromagnetic spectrum, including the infrared, the visible light and the ultra violet regions. This makes it applicable in the fabrication of opto-electronics and electron emitting devices [102, 117, 124].

Cubic BN can be doped as both *n*-type and *p*-type semiconductor, making it superior to diamond whose shallow *n*-type semiconductivity is still problematic [122]. Beryllium and magnesium form the most ideal shallow *p*-type dopants for *c*-BN with activation energies of 0.23 and 0.3 eV respectively, while Zn and Si dopant make an ideal shallow *n*-type dopant with activation energies of 0.1 and 0.3 eV respectively [125]. This makes it useful in high speed electronic applications [62, 65, 102, 126], for example in the creation of a p-n junction diode having a portion of its emission spectrum in the UV region [22, 127]. μ^2

It also surpasses diamond in some chemical and electrical properties, one of

Table 3.4: *A summary comparison of the physiochemical properties of cubic boron nitride and diamond* [72, 90, 92].

	c-BN	Diamond
Structural properties		
Structure	Cubic F_{43m}	Cubic F_{d3m}
Unit cell parameter (Å)	a=3.615	a=3.567
Interatomic distance(Å)	d=1.57	d=1.54
Density(g/cm^3)	3.48	3.52
Chemical Properties		
Doping elements	B, Be, S, Si, Al	B, P
Reaction with Fe Materials	Inert	Forms (Fe_3C_2)
Mechanical Properties		
Hardness (kgmm^{-2})	4500	9000
Knoop hardness (Gpa)	73	115
Bulk modulus (GPa)	847	1141
Thermal Properties		
Conductivity (Wcm^{-1}K^{-1})	13	20
Expansion (^{o}C $^{-1}$)	4.8	3.5
Oxygen stability (^{o}C)	1200	600
Phase change temp. (^{o}C)	1500	1400
Melting Point (^{o}C)	2967	3726
Breakdown field (MV cm^{-1})	8	3.1
Optical Properties		
Refractive index	2.117	2.417
Band gap(indirect)(eV)	6.1-6.5	5.47
Electrical Properties		
Resistivity (Ωm)	10^{10}	10^{16}
Dielectric constant	7.1	5.50

these being with respect to oxygen stability. The *c*-BN's oxidation (1200 ^{o}C) and phase change temperatures (1500 ^{o}C) are much higher than those of diamond (600 ^{o}C and 1400 ^{o}C) [2, 57]. This is due to the formation of a B_2O_3 protective layer in air that prevents further oxidation. Cubic BN shows high chemical inertness with molten ferrous materials even at high temperatures up to 1500-1600 ^{o}C, whereas diamond readily forms iron carbide (Fe_3C_2) in the presence of these materials. This property makes *c*-BN very important in coatings and tribological applications where ferrous materials are concerned [59, 61, 74, 124]. Other properties of *c*-BN with respect to diamond and *c*-BN are given in Table 3.4.

3.4 Synthesis of Cubic Boron Nitride

The excellent properties exhibited by *c*-BN leading to its enormous potential application have prompted scientists to research on ways of synthesizing it. This research has been ongoing for the past half a century after its discovery in the late 1950's. To date, *c*-BN has been commercially synthesized in large quantities as powder and as thin films.

Owing to the fact that *c*-BN has similar structure, properties, technological evolution and application as those of diamond and as discussed earlier, most developments in its synthesis evolved from synthesis methods for diamond. Various methods reported below have been successfully used in the formation of *c*-BN as powder and as thin films.

3.4.1 High pressure High Temperature (HPHT) Synthesis

The first successful synthesis of *c*-BN was by the high pressure high temperature (HTHP) method which was discovered in 1957 after being used in the preparation

of diamond from the graphite as shown in figure 3.7.

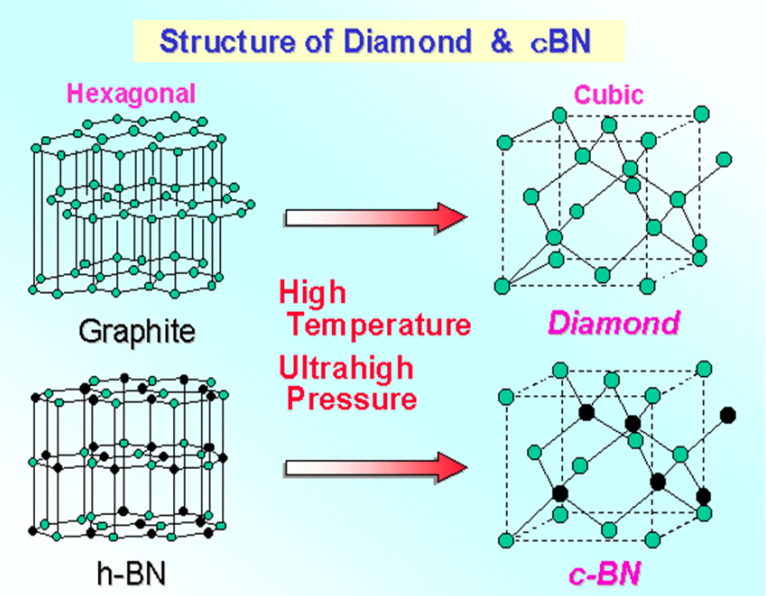

Figure 3.7: *Conditions of high temperature and ultra-high pressures are required to convert the hexagonal (graphite and h-BN) to the cubic (diamond and c-BN) structures* [128, 129].

As shown in equation 3.1.3 and 3.1.4, for high pressure high temperature systems, the Gibbs free energy determines the stability of the system is given as

$$G = U + PV - TS, \tag{3.4.1}$$

where U is the internal energy of the system, P the pressure, V the volume, T the temperature and S the entropy of the system. Equation 3.4.1 shows that as pressure and temperature increase, the phases with lower molar volume are favoured even if they have high internal energy. In connection to our system, high pressure and high temperature applied to the low dimensional BN modification, i.e. hexagonal BN reduces the Gibbs free energy leading to a reduction in its molar volume and hence structural modification to the cubic form [87, 66].

Hexagonal BN is thermodynamically stable over a wide region as seen from

figure 3.2, it therefore has a high activation energy barrier. The high temperature ($\sim$ 2000 K) used in this method leads to melting of the *h*-BN system and the subsequent emergence of a liquid phase, which abruptly decreases this activation barrier and lowers the parameters for *c*-BN production [87, 100]. The high pressure ($\sim$12 GPa) used causes the breaking of the sp^2 bonds in *h*-BN and a subsequent sp^3 bond reconstruction for the *c*-BN phase [100].

High pressure high temperature synthesis of *c*-BN includes two processes; the direct synthesis and the use of multicomponent/flux precursors (catalysts) synthesis.

Direct conversion of pure *h*-BN to *c*-BN was performed by Bundy and Wentorf [91, 128, 130], in 1963 when they were able to produce *c*-BN crystallites with sizes of $\sim 1\mu$m at high pressures of 12 GPa at 2000 K. At lower threshold pressure of 11 GPa, the synthesis temperature range was 3000 - 4000 K [67, 98]. It was later reported by Wakatsuki *et al* [131] that direct conversion at even lower pressures of 6 GPa is possible at temperature ranges of 1470-2720 K.

A study by Ichinose *et al* [132] and a recent study by Will *et al* [113] show that the degree of crystallinity of *h*-BN used as a starting material influences the thermodynamic conditions for *c*-BN formation. Ichinose *et al* showed that poorly crystalline *h*-BN can be converted to *c*-BN at 6 GPa with temperatures of 1470 K. Will *et al* showed that using amorphous BN as a starting material reduced the thermo-baric conditions to 2.5 GPa at 2000 K. The HPHT phase transformation process is also highly dependent on other parameters such as the grain size, defect concentration and the purity of the starting material [60, 95].

The second HPHT method, which involves the use of flux precursors (catalysts) is the major method used in commercial and large scale production of *c*-BN [60,

133]. It involves the use of a multicomponent system which significantly reduces the thermo-baric conditions. In this process, *h*-BN is dissolved into the flux precursor to form a eutectic composition. When moderately high temperature and pressure are applied to this system, *c*-BN crystallites proceed as a precipitate [67].

Different precursors have been used to enhance this transformation. Molten alkali and alkaline earth metals, in particular lithium, magnesium and calcium metals have been used. They react with *h*-BN to form corresponding nitrides (Li_3N, Mg_3N_2, and Ca_3N_2) and an elemental boron or borate. The metal nitride then reacts partially with *h*-BN and because of the difference in solubilities of the hexagonal and cubic phases, *c*-BN crystallizes [67, 101].

Alkali and alkaline earth metal nitrides have also been used as flux precursors. They include Li_3N, Mg_3N_2 and Ca_3N_2. For Mg_3N_2 as a solvent, the lowest synthesis parameters were found to be 4.7 GPa and 1670 K. For Ca_3N_2 the parameters were 6.5 GPa and 1670 K and for Li_3N the parameters were 6 GPa at 1823 K [101, 132, 134, 135].

The third group of precursors includes alkali and alkaline earth metal fluoronitrides which are Li_3NF, Mg_3N_2F, and Ca_3N_2F. The lowest synthesis parameters were found to be similar to those of metal nitrides but the *c*-BN conversion rate was much faster [67, 124].

Water has also been used as a flux precursor when combined with additives such as boron oxide to form boric acid. Boric acid in the presence of *h*-BN produces *c*-BN at the low thermo-baric conditions of 6 GPa and 1100-1300 K or 5 Gpa at 1770 K, which is the lowest thermo-baric condition obtained compared to all precursors used in *c*-BN production [101, 134, 136]. Other flux precursors that have been used in *c*-BN synthesis include silicon, silicon nitride or silicon alloys as well as

mixtures containing aluminium [118], where *c*-BN was produced at pressures of 5.2 GPa and temperatures of 2000 K. Figure 3.8 is a phase diagram showing the formation regions of *c*-BN by direct synthesis and using different precursors.

Despite being successfully used as a method of *c*-BN synthesis, HPHT poses in itself some disadvantages. The severe nature of the HPHT method and the limited size of *c*-BN produced prohibit many attractive potential applications of *c*-BN. This method also requires very expensive machinery hence it is not cost effective. This has led to a major motivation for thin film synthesis of *c*-BN [2].

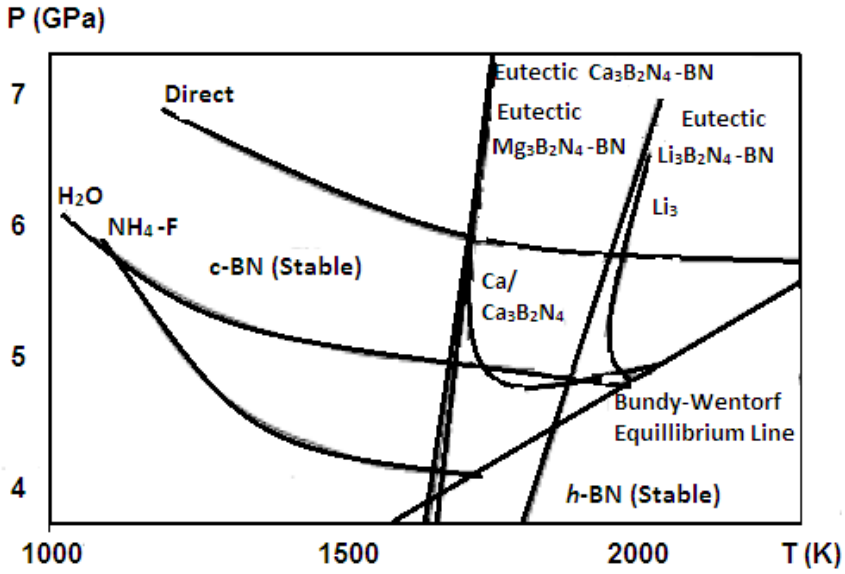

Figure 3.8: *The formation regions for c-BN by direct synthesis and using flux precursors or non-catalytic processes* [118].

3.4.2 Ion Beam Assisted Deposition (IBAD)Synthesis methods

Ion Beam Assisted Deposition (IBAD) has been used as an alternative method of synthesizing *c*-BN at relatively low pressure and temperature conditions [137, 138]. This technique involves the use of high voltage, bias sputtering or ion beam

bombardment applied on the *h*-BN substrate [139]. Low energy ranges of 0-1000 eV are used to produce high compressive stress (up to 10 GPa) in the *h*-BN substrate enhancing the phase transformation to the cubic form [2, 140].

IBAD is generally a combination of various physical processes which include Physical Vapour deposition (PVD), Chemical Vapour Deposition (CVD) [78], Radio-Frequency Sputtering among others [70, 139, 141, 142, 143].

Physical Vapour deposition (PVD) was first recognized by Weissmantel *et al* [143, 144]. The process involves the transfer of materials at an atomic level, where the raw materials are solid precursors [138]. Ion induced nucleation of *c*-BN on the *h*-BN basal layer is employed, where boron is thermally evaporated on to the *h*-BN substrate and simultaneously bombarded with nitrogen and argon ions from a given source [144].

The ion bombardment causes nitrogen and boron interstitials in *h*-BN material and the boron atoms to be driven into the lattice by the argon ions. The interstitial atoms condense to create inserted Ab-planes in *h*-BN, leading to an increase in the local density and hence alterations to the cubic phase [137, 145, 146].

PVD includes various processes. Those that have been successfully used in *c*-BN synthesis include plasma deposition, Ion Plating PVD, Pulsed Laser Ablation PVD, mass selected ion deposition, ball milling, and magnetron sputter PVD [2, 146, 147].

The chemical vapour deposition (CVD) processes involves the deposition of solid materials from a gaseous phase [142, 148]. The synthesis procedure is similar to that of PVD, except that gaseous precursors are used instead of solid ones used in PVD [64]. The various gaseous precursors used in CVD include; B_2H_6, BH_3NH_3, H_2, F and trimethyl borazol [2, 148, 149]. These reagents are often deposited on *h*-BN substrate with temperature ranges of 100-1000 ^oC [150]. Ion bombardment

of the substrate plays an essential role in the formation of the cubic phase of boron nitride.

The CVD processes used in *c*-BN production include: Radio-Frequency plasma CVD, Laser CVD, Jet Plasma CVD and microwave plasma CVD/ Cyclotron Microwave plasma CVD (which produces a thick *c*-BN film) [149, 150, 151, 152].

For both PVD and CVD, studies show that ion bombardment with energy ranging from 60-1000 eV is essential for *c*-BN nucleation. Above 1000 eV ion bombardment induces strong re-sputtering and no film is deposited [153]. It is however reported that deposition at low energies leads to *c*-BN growth with reduced stress and improved crystallinity [152].

3.4.3 Ion Implantation method

Ion Implantation involves the use of energetic ions E >1000 eV on a target in order to change its properties or to create new materials. It has successfully been used in the transformation of the *h*-BN to *c*-BN phase.

Investigation by T. E. Mosuang and J. E Lowther [13] using the *ab-initio* Local Density Approximation for simple defects, such as C, O, B and N, predicted that these defects induced in *h*-BN could facilitate a low activation energy from hexagonal to a cubic boron nitride phase transformation.

An examination of the "Core Level Photoabsorption Study of Defects and Metastable Bonding Configuration in Boron Nitride", carried out by Jimenez *et al* [11] reported that point defects (nitrogen vacancies in the hexagonal bonding of BN, nitrogen interstitials and boron clustering,) created during ion bombardment of *h*-BN with argon ions at 2 keV, and with fluences of 2×10^{17} ions/cm^2 led to the formation of a significant proportion of the sp^3 bonding characteristic found in

c-BN.

The formation of *c*-BN by ion implantation is also reported by Hu *et al* [154]. In this study, *c*-BN was synthesized by nitrogen ion implantation. Boron films were used as implantation target on a Si (100) substrate. Nitrogen ions at 30 keV were used as implantation ions at fluences of 1×10^{17} - 2×10^{18} ions/cm^2. Pure *c*-BN was obtained at a fluence of 2×10^{18} ions/cm^2. During this *c*-BN synthesis, several other BN phases such as *t*-BN, *w*-BN and $B_{25}N$ were obtained at fluence of 6×10^{17} ions/cm^2 [154].

Machaka *et al* used ion implantation as a technique of introducing H^+ and He^+ ions at energies of 200 keV-1.2 MeV at fluences of order 10^{16} - 10^{17} ions/cm^2 to introduce defects into *h*-BN [1]. Results from Raman spectroscopy showed that indeed He^+ induced *h*-BN to *c*-BN symmetry change [14]. Traces of the rhombohedral (*r*-BN) were observed at fluence of 1×10^{16} ions/cm^2 and 1.2 Mev energy during this transformation.

From this research, it was suggested that other ions, heavier than helium, such as Li, B, N and Ar could also induce this phase transformation at much lower energies and ion fluences, which forms the basis of work herein.

The work presented here focuses on the optimization of the implantation conditions for a possible *h*-BN - *c*-BN symmetry change by varying various parameters such as the ion mass (by varying the ion species), ion fluence, incident ion energy and implantation temperature, followed by analyses using various characterization techniques to establish the changes that occur as a result of implantation and varying this parameters.

Chapter 4

Experimental Methods

4.1 Introduction

This chapter entails a detailed view on the experimental and characterization instruments used in this work. It gives a detailed overlook on the sample types, their preparations and the experimental procedures carried out on them and finally the characterization procedures.

In order to achieve the objectives of this work, suitable samples were chosen. Ion beams from appropriate sources, with different energies and ion fluences were also selected. The results obtained from these experiments are recorded in the subsequent chapter.

4.2 Experimental instruments

This section gives details of the instrumentation and principle of operation of the apparatus used in this work. The experimental apparatus used include the Diamond Wire Saw used for sample preparation, the 200-20A2F Ion Implanter used for ion implantation, the Raman Spectroscopy system, The Fourier Transform Infrared Spectroscope, the Transmission Electron Microscope system (TEM and HRTEM)

and Glancing Incidence X-ray Diffraction systems (GIXRD) used for characterization.

4.2.1 Diamond Wire Saw

The Well Model 3032 precision horizontal Diamond Wire saw was used to cut all the h-BN samples used in this work. Figure 4.1 shows a photograph of the 3032 diamond wire saw model, located at the School of Physics, University of the Witwatersrand.

The Model 3032 model cuts samples with the wire travelling horizontally across the sample. It uses particularly thin diameter wire (ranging from 0.06 to 0.3 mm) which cuts by the abrasion process. A single strand of the wire is roughened by impregnating it with abrasive compounds such as borazon or diamond beads (and spacers) [155, 156]. The Model 3032 affords the operator the option of positioning the sample inside the loop of the wire thereby allowing for accurate positioning prior to the cutting, and viewing of the sample during the cutting process. Pressure against the wire is accomplished by attaching the sample holder to a counterbalanced arm that uses weights to establish and maintain the proper amount of force throughout the entire cutting or slicing process [157].

A microscope is normally mounted on the saw so that accurate positioning of the diamond wire can be readily accomplished and to watch the cut or slice while in progress. A special sample holder is designed in such a way as to position the wire to rotates to and fro on the sample through a 360^o turn. As a result, proper orientation of the cutting axis is achieved [156].

Two standard micrometers are supplied on this machine: one for accurate positioning of the sample and the other for setting the depth of a slice or cut. The

cutting process involves a high generation of heat on the wire, therefore the saw is always cooled or lubricated using oil, distilled water or other commercial coolants [155]. An adjustable electrical motor unit with an end-switch automatically shuts off the signal when the desired depth of cut is obtained

Figure 4.1: *Photograph of the 3032-model diamond wire saw (From the series Well Model 3032 diamond saw catalogue).*

4.2.2 The Ion Implanter

The Varian-Extrion 200-20A2F ion implanter was used to carry out all the implantations in this work. This facility is located at the iThemba LABS (Gauteng), formerly known as the Schonland Research Institute for Nuclear Sciences, at the University of the Witwatersrand, Johannesburg.

This discussion involves the instrumentation of the ion implanter and the mode of operation of the different parts as provided from manuals of the supplier of the 200-20A2F ion implanter together with other references.

Instrumentation

A typical 200-20A2F ion implanter consists of five major parts or systems, which include: the ion source, the mass analyzer magnet, the electrostatic accelerating tube, the beam manipulating system (consisting of a horizontal and vertical beam electrostatic lenses) and the end station. All these systems operate under high vacuum for sustainable plasma generation and transportation of the ion beams from the source to the processing chamber. Figure 4.3 shows a block diagram of the 200-20A2F ion implanter [35, 158].

The Ion Source

The ion source is a plasma generator, from which different ion beams can be extracted. The 200-20A2F ion implanter makes use of the Freeman Arc Discharge ion source because it can provide ion beams from most species (ranging from solids to gaseous material) [35]. It comprises seven different parts: the gaseous ion source chamber, the vaporizer, the gas feed system, extraction electrodes, a cooling system, a vacuum system and a 23 keV bias power supply.

Ion beams to be used for implantation can be generated from either a gaseous or a solid source. Beam formation from a gas (e.g. helium) occurs by feeding the gas into the ion source chamber. The ion source chamber contains a tungsten rod "filament" which is heated to white hot by a high filament current ($\approx$160 A) to produce electrons through thermionic emission. These electrons collide with the specific gas molecules, ionizing the gas to create a plasma.

Formation of beams from solid elements involved the in-situ chlorination, where the solid element is placed in a crucible within the chamber. The high temperature in the chamber causes vaporization of the lithium metal which combines with

carbon tetrachloride (CCl_4) gas to form lithium chloride (LiCl) in vapour form which collide with the electrons from the filament to produce different ions. The ions produced from a feed-through are dissociated and ionized in the arc chamber then accelerated from the ion source by a 23 kV extraction potential towards the analyzer magnet [158]. An extra 2 kV electrode assists in focusing the beam.

Figure 4.2: *A photograph of the freeman ion source of the 200-20A2F Ion Implanter (photo taken at iThemba LABS Gauteng).*

The Mass Analyzer Magnet

Various ion species can be produced in the ion source but only a specific beam is required to carry out the ion implantation process. The analyzer magnet is therefore used to select the desired ion species. As the beam of ions enter the analyzing magnet from the ion source, the light ions strike the inner wall and the heavier ions strike the outer wall of the magnet. Only the ions that have equal electromagnetic and centripetal forces are allowed to pass through the slit to the next section [158, 159]. This is known as the filtering process and it is achieved by

mass analysis selection of the incoming beam. In this process the mass analyzing magnet separates different ionic species according to their charge to mass (q/m) ratio, by passing them through a narrow resolving aperture.

The 200-20A2F model uses a 90^o mass analyzing magnet to do the resolution of the stream of ions coming from the ion source and obtain a low impurity level in the desired ion beam. For an ion with charge q, accelerated by a potential V and moving with velocity υ, the conservation of energy relation will be given as,

$$qV = \frac{m\upsilon^2}{2} \tag{4.2.1}$$

Since the ion will experience a magnetic force equal to the centripetal force as it travels in through the 90^o path, then

$$q\upsilon B = \frac{m\upsilon^2}{R} \tag{4.2.2}$$

It then follows that the charge to mass ratio for the ions will be,

$$\frac{q}{m} = \frac{2V}{B^2R^2} \tag{4.2.3}$$

with R being the critical orbit of radius of aperture for the ions as they move through a circular path and proceed to the accelerating tube and B is the magnetic field. In addition to the mass resolution, the analyzing magnet also acts as a converging lens to the desired beam on the resolution aperture and thus focuses the ion beam towards the accelerating tube [35, 65, 160].

The Accelerating Tube

The accelerating tube enables the ion beams to attain the energy required for implantation. After separation of the ions in the analyzer magnet section, the

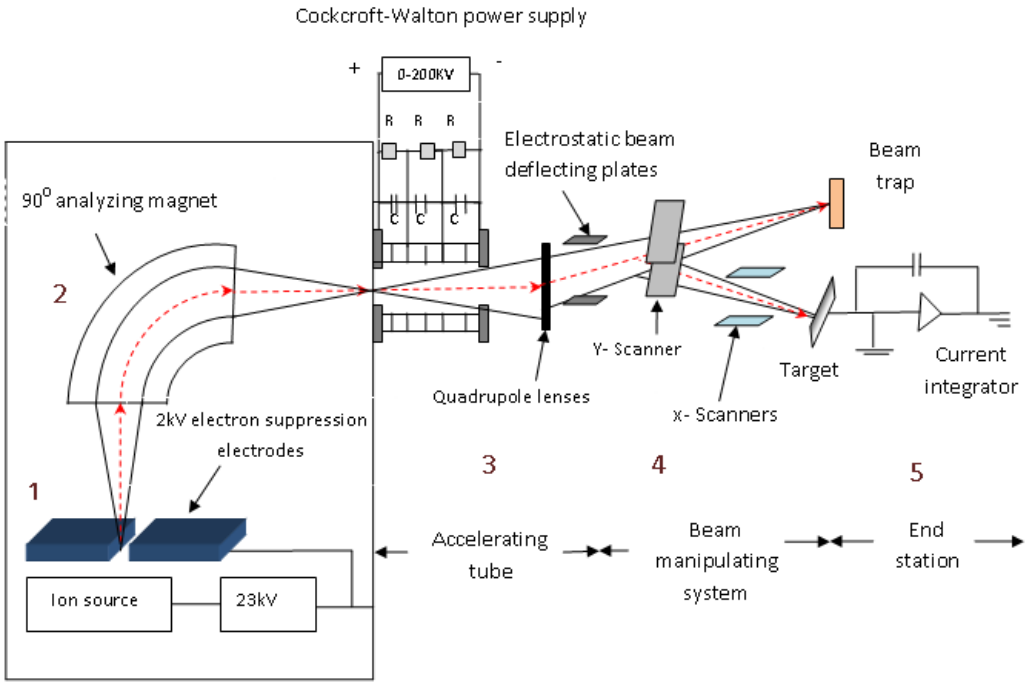

Figure 4.3: *Block diagram for the 200-20A2F ion implanter.*

beam enters the acceleration stage with an energy of 25 kV. The acceleration tube contains electrodes which operate in three modes depending on the required implantation energy, i.e. the drift mode, the post accel mode and the post deccel mode.

The drift mode of operation refers to the operation where the ion beam's energy remains unchanged after leaving the analyzing magnet. The post accel mode refers to the mode of operation in which the ion beam's energy is increased after leaving the analyzing magnet. This energy ranges from 25-180 keV. The post decel mode is the operation mode in which the ion beam energy is reduced after leaving the analyzing magnet and these energy ranges are 0-7 keV [161, 162].

The implanter is equipped with a high frequency Cockcroft-Walton power supply used to maintain the high voltage terminal at accelerating potential. The physical components that make up the acceleration tube all have round edges to

combat the arcing effect from the electric field concentration at sharp points [160].

Beam Manipulation System

It is necessary for the beam to be uniformly distributed onto the substrate to ensure proper implantation. This is done by the beam manipulating system. The system makes use of electrostatic fields to direct the ion beam on to the target as well as ensuring uniform surface implantation of the sample [161, 163, 164]

Following acceleration, the beam is focused by an electrostatic quadrupole triplet lens which applies transverse forces to maintain a small beam radius about the main beam axis (other implanters also use magnetic lenses) [162, 160, 163]. The ion beam tends to lose its shape as a result of rapid expansion due to its space charge (blow up effect). This is because at low propagation energies the ions are exposed to one another for much longer, resulting to significant mutual repulsion of the individual ions in the beam, causing the beam shape to diverge away from the beam's main axis.

The beam then passes through two sets of beam scanning electrostatic plates, that is the x and y scanners, that sweep the beam across the sample to provide a homogeneous fluence such that the beam is scanned in both x and y directions by separate voltages with triangular waveforms applied at the deflection plates. The available scanning frequencies, whose ratios are varied, are unsynchronized to prevent path retracing. A beam current integrator, located at the control console, measures the fluence to be implanted in the sample and closes the beam gate i. e. deflects the beam aside using the y-plate when the desired fluence level is reached. The x plates carry a deflection bias voltage to remove any neutral ions created in the beam, because these are undeflected and strike the tube wall. Only when the ion beam is actually required for implantation is it deflected onto the target

chamber [161, 164].

The End Station

After the beam has been scanned, it is directed to the end station where the ion implantation process takes place. The end station contains a target holder, where the samples to be implanted are mounted. The implantation process often causes a considerable phonon generation as a result of the stopping mechanism, leading to a considerable temperature rise in the target sample and therefore requires an active cooling mechanism. The active temperature control system makes use of a heater and liquid nitrogen to maintain the implantation temperature at a particular value. The end station also measures the implant fluence and minimizes fluence error. This implant fluence control is carried out using Faraday cups which expels secondary electrons to avoid the current multiplication effect [26, 159].

The design has four corner cups and the main cup at the centre, all designed with a 500 V bias electron suppression voltage at the entrance of each faraday assembly. As a result, an electrostatic field is set up in such a way that it prevents slow moving secondary electrons from leaving the Faraday cups entrance without inhibiting the passage of the high energy ion beam. The corner cups gives a measure of the current reaching the substrate i.e. it is an indirect measurement of current on the sample (which is harder to measure accurately) using the area of the corner cups to calculate the fluence on the sample [26, 160, 164]. The current signal from the four cups is integrated over the entire duration of implantation to get the desired fluence.

The vacuum system

The main purpose for a vacuum system in the implanted is to increase the mean free path inside the machine to several metres (according to kinetic theory) so that the ion can travel all the way to the end station. Another purpose is to combat problems that may occur due to the intense electromagnetic field associated with ion extraction and selection processes [165, 166]. The ion implantation process is associated with a variety of highly reactive and corrosive materials. For instance some gases used in the ion source for plasma generation such as boron trifluoride (BF_3), in the presence of water vapour react to form hydrofluoric acid (HF) which is a corrosive liquid.

A high vacuum system is therefore required to ensure that the ion implantation is a clean process. To ensure this, a number of pumps are used to pump pressures down to the ranges of 10^{-6} mbars and below. Each section of the implanter has a specialized pump to reduce the pressure to the required amount [167]. To ensure vacuum to the required pressure ranging from 10^{-4} to 10^{-6} mbars, a combination of oil-sealed diffusion pumps are used. Other typical pumps used in an ion implanter include rotary pumps, Turbo pumps and Cryo pumps. High vacuum pumps have to be backed up by other mechanical pumps which can exhaust to the atmosphere.

4.2.3 Summary of the Principle of Operation of the Ion Implanter

The basic function of the ion implanter is to generate a stream of electrostatically charged particles of a specific atomic mass, accelerate them and direct them to the target sample.

The ion implanter generates plasma in the ion source. A stream of positively

charged ions is then extracted by electrostatic means and subsequently accelerated towards an analyzing magnet which steers the ion beams through a 90^o bend implanting unwanted ions on the wall liner of the magnet and focusing ions of the desired q/m ratio through the resolving aperture into the acceleration tube. The accelerating tube further boosts the acceleration of the ion beams to the desired beam energy.

The beam then passes though an array of electrostatic plates that deflect and scan it. A 7^o offset voltage is fixed on the x-scan plater and deflects the charged beam onto the target. This further eliminated residual neutral particles so that the correct fluence is calculated by the current integrator.

4.2.4 Raman Spectroscopy System

This section will provide a description of the Raman Spectroscopy system located in the Raman and Luminescence laboratory at the University of the Witwatersrand. The system consists of an argon-ion laser used in the excitation of the source, the Jobin-Yvon T64000 Raman triple grating spectrograph, and an optical microscope with a movable stage. A camera is attached to the microscope and the micrometer movement of the stage enables the study of the specimen at various positions.

Introduction

The inelastic scattering of light by matter was first observed by Sir C. V. Raman in 1928. He observed that a minute fraction of the incident light was shifted from its original wavelength after interacting with a liquid under observation. When a material is illuminated, some light will be transmitted, some will be absorbed and a very small fraction will be scattered. The scattering is a result of inhomogeneities in the material such as molecular vibrations and defects. Most of the scattered

light will be scattered elastically, that is the frequency and energy of the incident and the scattered light will be the same. This scattering process is called *Rayleigh scattering*. An even smaller fraction of the scattered light, typically about 10^{-7}, will be inelastically scattered. This scattering process is known as the *Raman effect*. The incident light radiation undergoes an energy change. The difference between the incident light energy E_{inc} and the energy of the Raman scattered light is equal to the energy involved in changing the molecules vibrational state from v_i to v_j and the energy difference is called the *Raman shift*. In other words the shift in frequency of the incident light is due to the interaction of the photons of light with the phonons (vibrations and rotations of the molecules) in the material being investigated.

Raman Effect

Raman scattering is basically concerned with lattice dynamics. It can be treated in two ways, either classically or quantum mechanically. The classical mechanic details are given in detail in [168]

The From a quantum mechanical perspective, the Raman effect can be considered, in principle, as a lightmatter interaction where the incident photon interacts with the phonon in matter. The phonons can either be vibrational, rotational modes or a combination of both. The basis of this treatment comes from the understanding that the electronic, vibrational and rotational states of a molecule are considered to be quantized.The direct transition from one vibrational (or rotational) state v_n to another v_{n+1} gives rise to an IR spectrum and the direct transition from any state n to the virtual state and relaxation back to that state gives rise to the Rayleigh scattering, this process has a large crosssection. Raman

scattering can arise as a result of a change in the vibrational or rotational or electronic energy states of a molecule in a vibrational state to a virtual state and the subsequent relaxation transition to another vibrational or rotational state almost simultaneously. The molecule can either gain or lose energy in the *anti-Stokes* and *Stokes* process respectively. The progression of the transition is governed by the quantum mechanical selection rules.

The scattering process is viewed as the creation and annihilation of vibrational excitations (phonons) by photons and the resultant Raman frequency shift equals the frequency of the phonon created or annihilated. It is perceivable that since the Raman effect is a two photon process, the permitted transitions are; for a vibrational transition $v = 1 \leftarrow 0$ (Stokes transition) and $v = 1 \rightarrow 0$ (anti-Stokes transition), hence the overall vibrational transitions obeys the $\Delta\ v = \pm 1$ selection rule. For rotational transitions, 'each rotational' 'photon' transition obeys the $\Delta\ v = \pm 1$ transition, therefore it follows that the overall transition obeys $\Delta\ v = 0, \pm 2$, since this process is a two photon process where $\Delta\ v = \pm 2$ corresponds to Rayleigh scattering, $\Delta\ J = 2$ to Stokes scattering $\Delta\ J = -2$ to an antiStokes scattering transition. Where J is the total angular momentum quantum number and J is the vibrational quantum number.

The Argon-Ion Laser

Raman spectroscopy is a form of vibrational spectroscopy based on inelastic Raman scattering which requires an intense and monochromatic source of light. This light may be obtained from laser sources or from mercury lamps with appropriate filters [169, 170, 171].

The argon-ion laser was used in this work. Laser light was produced by amplification of radiative electronic transition of the ionized states of inert gas atoms

[172]. In order to produce the laser beam, argon gas, contained in a sealed cylinder known as a plasma tube at low pressures, is used. The cylinder also contains two electrodes with intense electric discharge. The electrons produced by these electrodes collide with the neutral argon gas particles creating plasma which is at a highly excited state as seen in figure 4.4 [173, 174].

This excited state has a short lifetime so the ions decay non-radioactively to a $4p$ orbital level. This level has a longer lifetime hence allows buildup of ions, creating a condition known as population inversion. At this stage, there are more ions in the higher level as compared to the ground state. This population inversion is necessary for lasing operation.

The ions in the 4p orbital then decay into the $4s$ orbital either spontaneously or by stimulation of a photon of equivalent energy. This transition is radiative and a photon of wavelength

$$\lambda = \frac{hc}{E} \tag{4.2.4}$$

is emitted where h is the Plank's constant, c the speed of light and E the separation energy between the states [175].

Light released through stimulated emission in the plasma tube is stored in an optical cavity. One end of the optical cavity has a reflective mirror with 100% reflectivity and another end is a mirror with reflectivity slightly less than 100%. The emitted photon moves back and forth between these mirrors and in the process, more atoms are stimulated to produce photons. A small percentage of photons manages to pass through the output mirror and makes up the laser output [174].

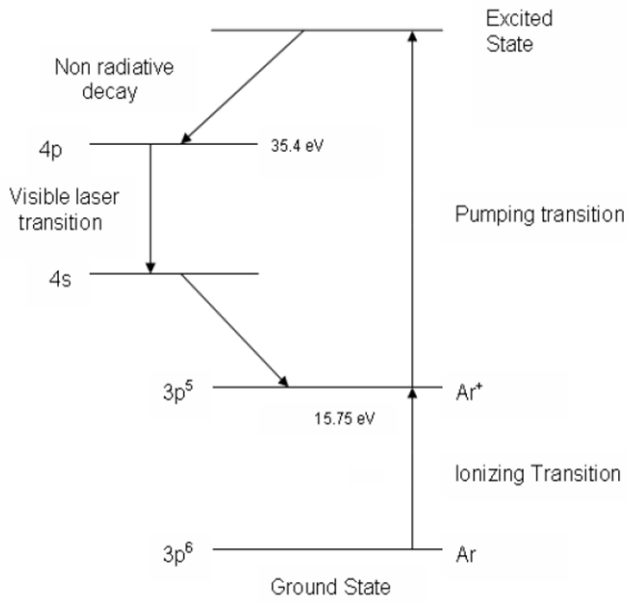

Figure 4.4: *Stages involved in the production of Ar^+ laser(From Operational Manual for Spectra Physics 2020/2025 ion laser).*

The Raman Spectrograph

The Jobin-Yvon T64000 spectrometer was used in this research. It is a triple monochromator dispersive system shown in figure 4.5. Laser light is directed into the spectrometer using an Olympus *BX40* microscope attached to the spectrograph. Scattered light from the sample returns through the microscope into the spectrometer where it is processed.

This processing involves the single spectrograph mode in which light is directed to a holographic notch filter, which suppresses the elastic scattered light but allows the Raman scattered light to pass through. The transmitted light then passes through an entrance slit and falls on the grating where it is dispersed [176].

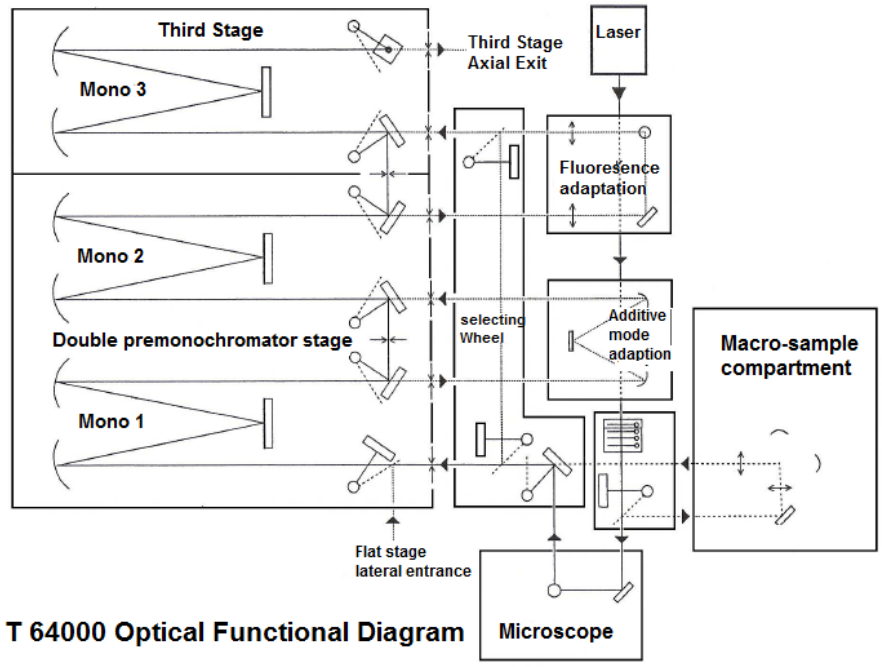

Figure 4.5: *Schematic diagram of the Raman Spectrograph showing the beam path. (From the Instruction Manual for the Jobin-Yvon T64000 Raman Spectrograph).*

The light dispersed by grating falls on the Charge Coupled Device (CCD) detector, which detects the scattered light and produces a spectrum. The CCD comprises 1024-256 pixels with each pixel being a silicon photosensor. When scattered radiation falls on the pixels, photoelectrons are produced in numbers proportional to the intensity of radiation. To provide the best performance to the spectrometer, the CCD is cooled by liquid nitrogen to 140 K. The CCD offers rapid analysis of the spectrum and is ideal for most analytical purposes [177].

In the coupled configuration, a monochromator has the capability of measuring Raman signals of very low intensity in a broadband vibration/rotation with high resolution [26, 176, 178].

The output from the detector is analyzed on a computer using Labspec scientific software supplied by Jobin-Yvon. The spectrum can be saved in form of data or

text file which can be exported to a spreadsheet for analysis using the Origin8 Pro software.

4.2.5 Transmission Electron Microscopy

Electron Interaction with Matter

An electron microscope is an instrument that is able to resolve an image of an object to nano-meter dimension by the use of electrons. Electrons gained major attraction in the development of transmission microscopy since they are smaller than the atom and therefore were thought theoretically and seen experimentally to be able to resolve images at the atomic level [179] because the de Broglie wavelength of electrons is far less than that of light.

The resolving power of an electron microscope is defined as the separation distance between two detailed objects. For an incoherent beam of electrons, the resolving power is given by,

$$\rho = \frac{0.16\lambda}{\mu \sin \beta} \tag{4.2.5}$$

where λ is the wavelength of the electron, μ the refractive index of the viewing medium, β the maximum angle between the incident and the deflected beam in the limit of lens aberrations.

A summary of electron-solid interactions are shown in figure 4.6 When an electron at energies usually in keV is accelerated onto a material, it interacts with the electrons and nuclei of the target material. The accelerated electrons upon hitting the material may be scattered elastically or inelastically, or may remain undeviated when the material is sufficiently thin. Elastic scattering is due to the interaction of the electron with the electrostatic potential of the nuclei of the atom. Here

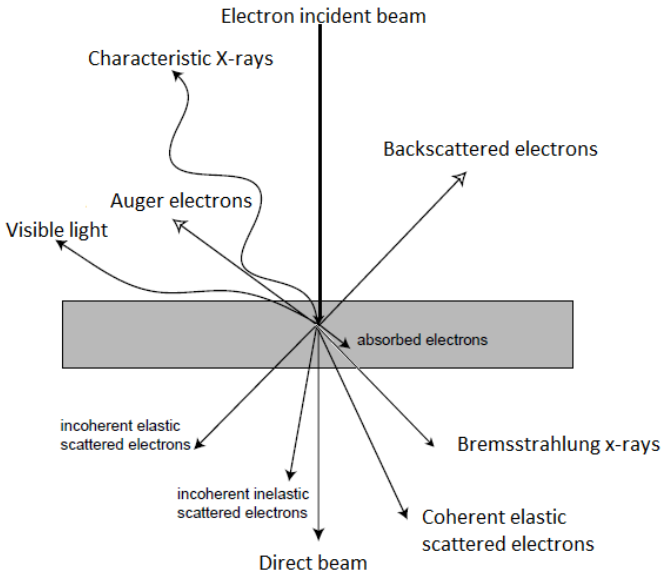

Figure 4.6: *Electron interaction with matter processes* [179].

there is no energy loss but only a change in the direction of the interacting electrons. In inelastic scattering, the energy of the incident electron is transferred to the atom/specimen causing an excitation of the bound electrons from the electrons of the lattice leading to heating or radiation damage of the specimen [180, 181].

These excitations lead to different signals that give details on the composition and structure of the sample. The processes that occur due to electrons hitting the surface i.e backscattering, secondary electron, Auger electrons and visible light are used in Scanning Electron Microscopy analysis of materials. The processes that occur due to the electron penetrating and being transmitted i. e. inelastic and elastic scattering are the ones used for TEM analysis of the material. Analysis with this technique requires the specimen to be electron transparent, usually less than 100 nm thick.

TEM Instrumentation

The electron microscope has several parts on which its mode of operation depends. It is subdivided into the following sections: the electron gun, the illuminating stage, the objective lenses (with an electron transparent sample immersed in the electromagnetic field), the magnification and projection system with several electromagnetic lenses, a detector, photographic cameras, and a Charge-Coupled Device (CCD) camera. Figure 4.7 shows some major parts of the TEM system and the schematic mode of its operation.

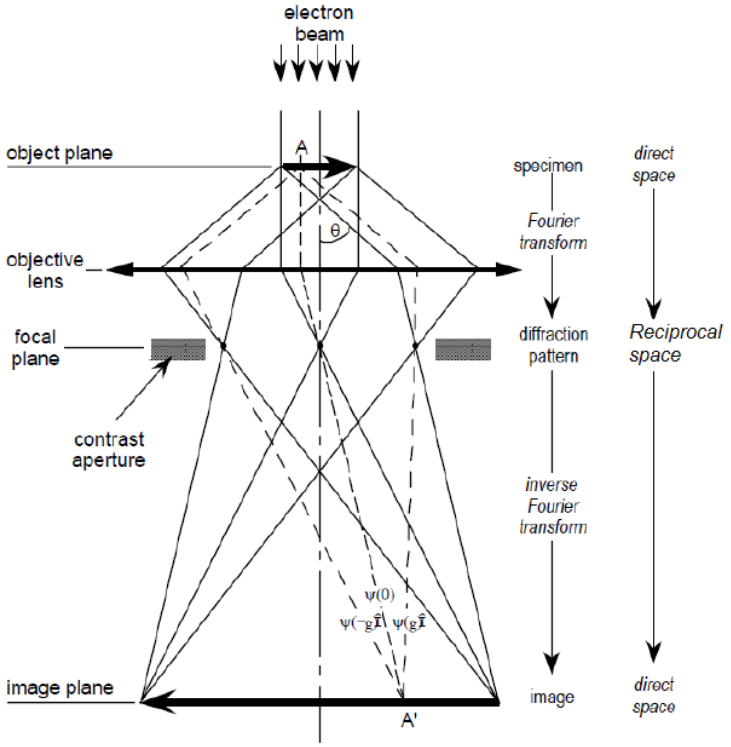

Figure 4.7: *Major parts of and electron microscope and the schematic mode of operation* [179].

The Electron Gun

This is where the electrons are produced. The electrons are mainly generated by the thermionic emission, which uses tungsten or Lanthanum Hexaboride (LaB6)

filament, or the field electron emission processes. The beam of electrons produced is then accelerated towards the microscope's magnet by a positive anode.

The electromagnetic lens system

The beam of electrons is then manipulated and focused by electromagnetic lenses and metal apertures. The system allows electrons within a small energy range to pass through so that the electron beam will have a well defined energy. Magnetic lenses which are circular electromagnets, act like optical lenses which focuses the beam of electrons. The metal apertures, which are thin discs with small holes with diameters between 20 nm and 100 nm, are used to restrict the unwanted electrons before hitting the sample/specimen. Sample holders are located on a platforms equipped with a mechanical arm for holding the sample and controlling its position.

The Imaging System

The imaging system consists of a photographic and CCD cameras, a set of electromagnetic lens system and a screen for viewing the sample's image. The electromagnetic system consists of two lens systems, one for re-focusing the electrons after passing through the specimen and the other for enlarging image and projecting it onto the screen. The screen is made up of a phosphor-fluorescent plates which glows when hit by the electrons. The images form in a similar manner as in photography.

The TEM system has other systems that are vital to its operation. It requires a high voltage system to accelerate electrons to energies usually 80 to 300 keV.

Electrons require a high vacuum ranging from $\approx 10^{-7}$ to 10^{-12} mbar in order to travel typically a distance of 1-2 m of the TEM column, therefore, TEM is

equipped with a high vacuum system. To maintain the high vacuum the system is equipped with several pumps e.g. roughing pumps, diffusion pumps, getter ion pumps, turbomolecular pumps with manual and automatic valves [182].

Due to the high voltage used in TEM, lot of heat is generated, therefore the lens coils which carry several amperes of currents require a cooling system. The TEM system is normally automated in such a way that the cooling system is interlocked with other systems so that the microscope does not overheat if there is insufficient cooling. Deionized water is mostly used as a coolant.

When the electrons hit the solid material, X-rays are produced by the bremsstrahlung radiation process. As a result, all the areas where the X-rays may be generated are covered with a double shield: the first one is an aluminium shield which converts all the electron's kinetic energy into low energy X-rays and the second shield is made of a high atomic number material such as lead which absorbs the low energy X-ray photons preventing them from reaching the operator. The viewing window is also made of a special lead containing glass to absorb X-rays. The radiation shield contributes significantly to the weight of the microscope, with thicker shields for high energy TEM [180, 182].

The TEM also contains other systems such as the Energy Dispersive X-ray Analyzer (EDS), Electron Energy Loss Spectroscope (EEL), scanning attachments, detectors and image energy filters. The EDS spectroscopy is used in the analysis of materials by using characteristic X-rays generated by the material after interaction with electrons.

In this study we used the Field Emission TEM (the Tecnai F20) system equipped with EDS, and a HAADF-STEM (High Angle Annular Dark Field Scanning TEM) detectors. The TEM system is interfaced with a PC containing the Field Emission

and Ion Technology (FEI) Quanta software for all the data display and collection.

4.2.6 TEM working principles

TEM works like a slide projector. A beam of electrons is passed though an electron transparent specimen. The pattern formed by the specimen's image only allows a certain part of the beam of electrons to pass through, thus the transmitted beam replicates the pattern of the specimen when falling on the screen. In TEM, the transmission of the electrons is highly dependent on the properties of the material being examined. These properties include the density, porosity, composition and crystallinity.

Other techniques used in this work such as Fourier Transform Infrared spectroscopy (FTIR) and High Annular Angle Dark Field (HAADF-STEM) will be discussed briefly in the next chapter

4.3 Experimental Procedures

4.3.1 Sample and sample preparation

Hexagonal BN samples were used as substrates throughout this experiment. These samples were were supplied by Goodfellow Cambridge Company Limited, England and HQ graphene ceramic company, Netherlands. Three forms of *h*-BN samples were used: the first two sets of *h*-BN samples used were in the form of hot-pressed polycrystalline powder, generally synthesized by the reaction of boric acid and urea followed by sintering using boron oxide and subsequent machining (a detailed explanation is given in Chapter 3, Section 3.1.2).

The first polycrystalline sample was a 50 mm long, and 15 mm-diameter white rod, weighing 16.1 g, and with 99.9% purity. The main sample preparation involved

slicing and polishing of the samples. Slicing was carried out using the diamond wire saw. An appropriate sample holder was designed at the School of Physics Workshop in such a way as to fit in the diamond wire saw and to hold the sample firmly in place during the cutting process.

The samples were cut into 25 pieces, each with 2 mm thickness. This was accomplished using the vernier scale on the wire saw, attached to the knob of the sample holder. Since *h*-BN is a soft material, the cutting speed of the saw was reduced to 3 rotations per second to minimize any damage on the sample during the cutting process.

After cutting/slicing, the samples were polished mechanically using a P1200 sandpaper with average particle size of 15.3 μm, with final polish done using either diamond paste with 0.5 μm particle size or alpha micro polish alumina gel with particle size of 0.3 μm. The paste and gel were used since they are non corrosive and ensure a smooth finish on the surface of the sample. The polished samples were then cleaned using methanol. After the sample preparation the samples were analyzed using various analysis techniques before implantation.

The second set of polycrystalline samples were *h*-BN sheets with dimensions of 5 mm by 5 mm with 0.2 mm thickness. These samples were easier to prepare especially for FTIR and TEM analysis compared to the rods. The sample preparation involved cutting the sample to thickness of 0.1 mm, using a diamond wire saw followed by mechanical polishing using diamond paste.

The third set of samples were *h*-BN single crystals with 1 mm$\times$1 mm surface area and thickness of 100 μm. The main sample preparation on these samples was using Focused Ion Beam Sectioning for TEM which is discussed in Chapter 5.

4.3.2 Ion implantation experiments

All the implantations were carried out using the Varian 200-20A2F ion implanter at high vacuum conditions with most implantations being carried out at room temperature, and a few at liquid nitrogen and at high temperatures of 200 ^{o}C and 400 ^{o}C. Different ions including helium, lithium, boron, nitrogen and argon ions were chosen for the implantation, at various fluences and the implantation energies.

Ion Production and Acceleration

Helium, nitrogen and argon gases were used for helium, nitrogen and argon ions respectively. For boron ions, boron trifluoride gas (BF_3) was used and B^+ and F^+ were produced. The analyzer magnet was used to select the desired ion to be used for implantation.

To produce lithium ion beams, lithium metal was used. Lithium metal is usually very reactive, hence it is normally stored under oil to prevent reaction with air. The lithium metal is cut into a rice grain sized piece and placed in the arc chamber. The high temperatures created by hot tungsten filament inside the arc chamber vaporizes the Li metal. The Li vapour then combines with CCl_4 to form LiCl vapour which then collides with electrons produced by thermionic emission from the hot tungsten filament to form lithium ion beams.

The ions produced were accelerated to energies ranging from 40-150 keV and implanted at fluences ranging from 1×10^{13} ions/cm^2 to 5×10^{16} ions/cm^2.

The surface area of the rod sample was large such that the sample could be implanted with different fluences. This was achieved as follows: the sample holder was designed so that an externally controlled mask in front of the sample could be lowered. The first implant was 1×10^{14} ions/cm^2 over the entire surface of the sample.

The mask was then lowered by 3 mm, and a fluence of 1×10^{14} ions/cm^2 implanted over the remaining area, now having a total fluence of 2×10^{14} ions/cm^2. The mask was lowered by a further 3 mm and a fluence of 2×10^{14} ions/cm^2 implanted on the remaining surface which now had a total fluence of 4×10^{14} ions/cm^2. In the last step the mask was lowered again by 3mm and an additional 4×10^{14} ions/cm^2 implanted on the remaining surface so that the forth region had a total of 8×10^{14} ions/cm^2. The sample then had four regions implanted with different fluences i.e. 1×10^{14} ions/cm^2, 2×10^{14} ions/cm^2, 4×10^{14} ions/cm^2 and 8×10^{14} ions/cm^2. We referred to this as sample 1.

Further, the second rod sample was implanted in a similar manner. The sample had a minimum fluence of 1×10^{15} ions/cm^2 and a maximum of 8×10^{15} ions/cm^2. For the third rod sample, the entire sample was implanted with a fluence of 5×10^{16} ions/cm^2. The polycrystalline sheets and the single crystal samples were implanted with different individual fluence from 1×10^{14} ions/cm^2 to 1×10^{16} ions/cm^2 because of their small sizes.

Raman characterization and GIXRD were carried out on these implanted samples since these techniques are nondestructive and require no elaborate sample preparation. For FTIR, further mechanical polishing was done for the polycrystalline samples before analysis because the infrared penetration depends on the sample thickness (the thicker the sample the lower the transmission), with all polishing done on the unimplanted surface and implantation performed on the originally hot pressed unpolished surface of the sample. Focused Ion Beam sectioning (FIB) was further done on samples used for TEM analyses (see Chapter 5).

The implantation experiments were also conducted by varying the implantation energies. The different energies used were 150 keV, 120 keV, 80 keV and 40

keV. To investigate the effect of varying implantation temperature, some samples were implanted at different temperatures from liquid nitrogen to 400 ^{o}. These implantations were carried out at an optimum fluence obtained for boron implants, and analyzed using the various techniques. Some of the implanted samples were annealed at temperatures ranging from 50 ^{o}C to 400 ^{o}C and analyzed by Raman spectroscopy.

4.3.3 Raman Analysis

Raman scattering was carried out on the samples for characterization before and after implantation. The 514.5 nm argon ion laser excitation line, the 488 nm Ar ion laser and the 244 nm UV lasers were used for the Raman analysis, under ambient conditions. Parallel polarization configuration(light wave in which the vibrations occur in a single plane) of the incident laser light of power 20 mW was used where individual light waves are aligned parallel to each other. In order to focus the beam, an optical microscope with different magnifications (20×, 50× and 100×objective) was used. A 1800 groove/mm grating and a nitrogen cooled CCD was used to analyze the scattered light.

The spectrometer was operated in the micro-Raman modes, with the measurements done on a microscopic stage where light with a spot size of 1 μm in diameter focused on the sample surface.

The first set of micro-Raman measurements were carried out on the unimplanted sample. The mappings were carried out over a 500×500 μm square area on 25×25 points for the polycrystalline samples and over a 500 μm line for the single crystal samples. Subsequent Raman experiments were carried out on the samples implanted with boron, lithium, helium, nitrogen and argon ions. The same area of

500×500 μm (25×25 points) and 25 points over a 500 μm line for the single crystal samples were used for all the implanted samples. The final set of Raman measurements were carried out on samples implanted at different implant energies ranging from 40 keV to 160 keV. Prestik was used to hold the polycrystalline samples on the X-Y stage in order to keep them in position during the 'Jacking' movements of the stage.

The output from the detector was analyzed by an interfaced PC using spectromax software supplied by Jobin-Yvon in graphical form. The software was also used to control all functions of the spectrometer which include moving the monochromator, changing the modes and intermediate slits between the gratings among others. The data obtained from the software was stored as text file data and the Origin8 Pro program used to export the data for further analysis.

4.3.4 TEM Sample and sample Preparation

The most important consideration in the TEM studies of material is the ability of the materials to be electron transparent. This implies that the material should have a thickness ranging between 10 nm and 100 nm. There are several methods of preparing samples for TEM analysis. They include the Focused Ion Beam (FIB) technique, mechanical polishing and ion milling, jet electropolishing and powder suspension among others, depending on the type of the material to be analyzed. In our current work we mainly used FIB techniques in preparing our sample.

Chapter 5

Results and Discussions

This chapter describes the results obtained from all the experimental work in the preceding chapter.

Raman spectroscopy was the major characterization technique used in this work. Various analyses will be discussed herein including results for the unimplanted h-BN samples and for samples implanted with the individual ions (boron, lithium, helium, nitrogen and argon) with variation of the ion fluences, energies, laser parameters and the effect of annealing for the different ions.

The next section will be on the analyses and discussions for Fourier Transform Infrared spectroscopy (FTIR) characterization followed by Glancing incidence X-ray Diffraction (GIXRD) and finally Conventional and High resolution Transmission Electron Microscopy (TEM). Other minor subsections including the Energy Dispersive X-ray Diffraction Spectroscopy (EDS), Scanning Transmission Electron Microscopy (STEM) and Scanning Electron Microscopy (SEM), will also be discussed briefly in this chapter.

Conclusions and recommendations from these results are recorded in the subsequent chapter.

5.1 Raman Spectroscopy Results

Micro-Raman spectroscopy is a useful method of characterization that can be used to gain information from the crystal's surface and sub-surface. It is sensitive enough to detect vibrations and changes in stoichiometry of a given material.

Raman results are presented as a plot of the Raman intensity (with units of counts per second) as a function of the frequency shift/wavenumber from the incident radiation, which is the Raman shift (with units of cm^{-1}). Most of the data presented in this section are for smoothed data. Because of background fluorescence, the spectra may have a noisy/irregular signal and therefore some important signals may not be well interpreted. As such an "adjacent averaging" method in Origin Program was used to get a cleaned/smoothed signal.

5.2 *c*-BN powder

Due to the difference between the bonding nature of *c*-BN and *h*-BN, it is expected that they will have different Raman vibrational modes. In contrast to *h*-BN, the space group $F_{43}m$ of *c*-BN allows only T_2 vibrational modes to be active in Raman. The Raman signal for bulk *c*-BN therefore normally exhibits two vibrational modes i.e. the Longitudinal Optical mode (LO) which occurs at 1305 cm^{-1} and the Transverse Optical mode (TO) which occurs at 1056 cm^{-1} for pure samples. The bonding in *c*-BN, i.e. being covalent and slightly ionic and its functional sp^3 groups, are responsible for the presence of these two modes [2].

The existence of these modes in terms of the frequency position, linewidth and intensity are highly dependent on the crystal orientation, the crystal size and the the defect density within the *c*-BN samples. Based on the selection rules and the Spatial Correlation Model [183] (discussed in chapter 6), bulk *c*-BN with micron

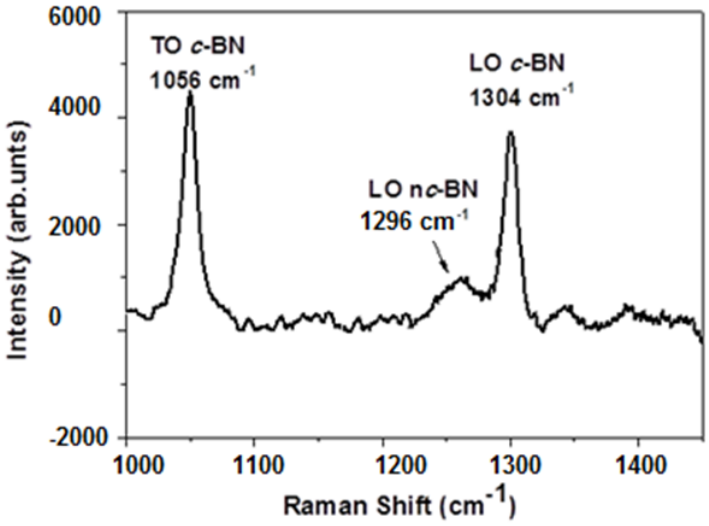

Figure 5.1: *Raman measurements for the c-BN powder.*

sized crystals will exhibit both modes. As the crystal size decreases, the Raman intensity of the TO mode decreases and eventually vanishes when the *c*-BN under investigation is of nano-size crystals, leaving an unstructured LO peak visible. The nature of the LO peak also depends on factors mentioned above. A broad and asymmetrical peak with a shift to low wavenumber indicates that the *c*-BN is of nanosized crystal nature [184].

Figure 5.1 shows the Raman signal for a *c*-BN powder sample that was provided by Element Six. It exhibits two vibrational modes: the longitudinal optical (LO) phonon mode which is observed at 1304 cm^{-1} and the transverse optical (TO) phonon modes observed at 1056 cm^{-1}, with similar results also reported by Hidetochi *et al* [185]. The LO and TO mode peaks have linewidth of 28 and 33 cm^{-1} respectively. Together with these two peaks, there occurs a broad unstructured feature at 1296 cm^{-1}, with a linewidth of 80 cm^{-1}. According to the selection rule for *c*-BN crystal symmetry, we attribute this peak to the LO mode for the nanocrystalline *c*-BN present in the sample.

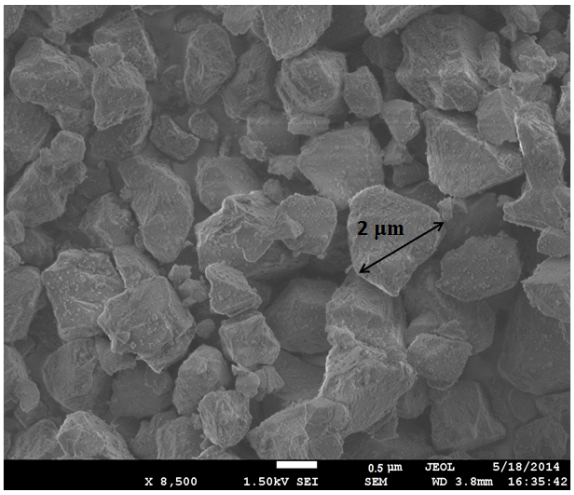

Figure 5.2: *A SEM micrograph for c-BN powder showing the larger micron sized crystals.*

From this Raman analysis, it is evident that the *c*-BN sample contained both micron and nano sized crystals. To establish this, Scanning Electron Microscopy (SEM) measurements were carried out on this sample. Figure 5.2 represent the SEM micrograph for the *c*-BN sample. The image shows that the sample contains crystals with approximate sizes of between 1 μm and 1.5 μm. Figure 5.3 is the SEM micrograph for the *c*-BN sample showing crystal sizes of between 80 - 100 nm. To obtain these smaller crystals from the micron sized ones, the sample was mixed with methanol as a solvent, the sonicated for 20 minutes and filtered with a filter paper. The filtered mixture was then separated using a centrifuge located in the School of Chemistry, University of the Witwatersrand.

The Raman spectroscopy of the other BN phases has not been studied at length. In summary *w*-BN and *r*-BN have Raman bands at 1000 cm^{-1} and 790 cm^{-1} respectively [14]. Amorphous BN has a Raman band near the *h*-BN mode and it appears as a broad and continuous peak of *h*-BN. The Raman spectroscopy study for the different BN phases will be used to give a comparison for *h*-BN spectra after implantation.

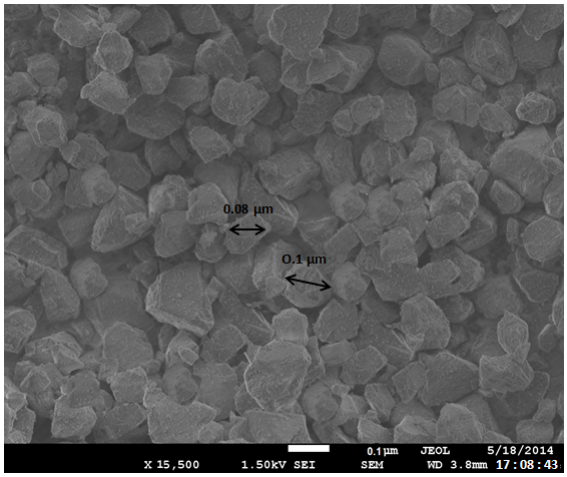

Figure 5.3: *A SEM micrograph for c-BN powder showing the smaller crystallites after centrifugation.*

5.3 Unimplanted *h*-BN Samples

Introduction

Raman spectroscopy was carried out on pristine/virgin polycrystalline and single crystal h-BN samples with measurements collected in a backscattering geometry. The spectrometer was calibrated using silicon wafer (100) as a standard sample to check for linearity and repeatability of the intensity. These were used as control samples which were to be compared to all the samples analyzed after implantation.

Generally, the normal optical vibration phonon modes of h-BN with space group $P6_3/mmc$ is expected to be at the Brillouin zone centre given as;

$$\Gamma = 2B_{lg} + A_{2u} + E_{lu} + 2E_{2g} \tag{5.3.1}$$

The term $2B_{lg}$ in equation 5.3.1 represents the phonon mode that is optically inactive, and it is therefore absent in any optical vibrational spectrum. The terms A_{2u} and E_{lu} represent the phonon vibrational modes that are active in infrared, corresponding to the out-of-plane B-N-B stretching and in-plane B-N bending of

boron nitride respectively, therefore they will also not be expected in the visible Raman spectrum [103]. The last term of the equation (E_{2g}) represents the Raman active mode which normally exhibits two vibrational centres. These symmetry centres are as a result of in-plane and out-of-plane atomic displacement of the boron and nitrogen atoms [186].

The first normal mode frequency of the vibrational centre appears at around 1366.1 cm^{-1}. It represents the high frequency vibrational Raman mode, and it is the characteristic B-N bond stretching vibrations within the basal planes. The second centre appears at around 51.8 cm^{-1}. It represents the low frequency mode, also known as the *"rigid-layer shear mode"*, and is characterized by the layer shearing vibration between the basal layers [187]. We therefore expect Raman peaks to occur at 1366 cm^{-1} and 52 cm^{-1} in the spectrum of the unimplanted *h*-BN sample.

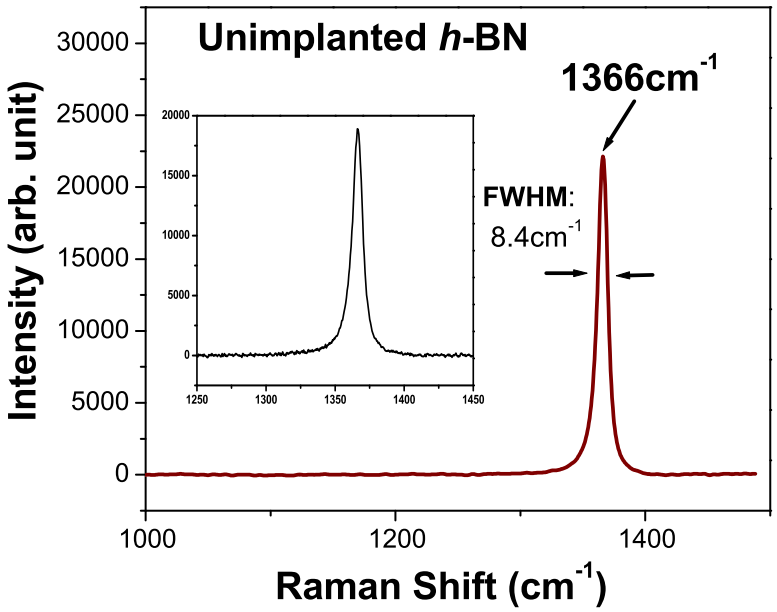

Figure 5.4: *Raman spectroscopy measurements for the unimplanted polycrystalline h-BN sheets. Inset is the spectrum for polycrystalline h-BN rod sample.*

Prior to implantation, scans from Raman spectroscopy were performed on polycrystalline and single crystal *h*-BN samples. These were used for subsequent comparison with, and as a reference to the spectra obtained for the samples after implantation throughout this work. Figure 5.4 shows the point-to-point Raman mapping of the virgin polycrystalline *h*-BN sheet sample analyzed using a Lorentzian peak fit. The inset is the spectrum for the polycrystalline rod sample. The Raman measurements were carried out at room temperature, using the green 514 nm line of argon ion laser. The laser beam was located to map 25 different points on 500 $\times$ 500 μm area matrix on the surface of the sample. The laser power used was 20 mW with a 1 μm laser spot size.

Approximately 1 μm penetration depth below the sample surface was sampled using the 514 nm Ar line (2.14 eV). The laser penetration depth p is given as the inverse of the absorption coefficient (α), i.e. $p = \alpha^{-1}$. This is the average depth that a photon travels through a material before being absorbed. The absorption coefficient α is given as

$$\alpha = \frac{4\pi k}{\lambda} \tag{5.3.2}$$

Where λ is the wavelength of the photon and k the extinction coefficient $\approx$ 0.041 for *h*-BN [122].

Discussion

The sheet sample spectrum shows a Lorentzian peak at 1366 cm^{-1} which exhibits an intensity of 22,500 counts per second and a linewidth/full width at half maximum (FWHM) of 8.4 cm^{-1}. The FWHM is the measure of crystallinity and stress of a material, with narrow FWHM values indicating the material is of high crystallinity and low stress. Based on the normal mode for BN, this feature represents the sp^2

hybridized planar bonding to which has been attributed the high frequency mode for h-BN with low internal stresses.

The low frequency E_{2g} shear mode for h-BN which normally occurs at 51.8 cm^{-1} was not observed in this spectrum due to the Raman Shift cut off for wavenumbers less than 400 cm^{-1} by the notch filter used in the Raman Spectroscope. The polycrystalline rod samples also showed closely similar results, with the peak's position at 1366.1 cm^{-1}, FWHM of 8.5 cm^{-1} and an intensity of 19,500 counts/s. No other modes were observed in both spectra.

Since the unimplanted Raman spectra only showed the Lorentzian features at 1366 cm^{-1}, it implies that the two polycrystalline starting samples were h-BN with no impurities and compared to microcrystals with high crystal quality. The main focus will be on any changes that occur to the h-BN spectra after implantation and their variation with different implantation parameters such as the incident ions, ion fluences and the incident ion energies. The behavior of the h-BN peaks' characteristics including the peak positions, the peak's intensities and the full width at half maximum (FWHM) will be of major interest.

5.4 Boron Ion Implantation

The μ-Raman spectra in this section were obtained for different h-BN samples implanted with boron ions. Different parameters were varied including the ion fluence, the implanting energy, and the annealing effect. The Raman laser parameters such as the wavelength and the objective lens magnification were also varied.

5.4.1 Polycrystalline *h*-BN Sheets

Varying the fluence

The polycrystalline *h*-BN sheet samples were implanted at an energy of 150 keV and with fluences ranging from 1×10^{14} ions/cm^2 to 5×10^{16} ions/cm^2. All the implantations were carried out at room temperature.

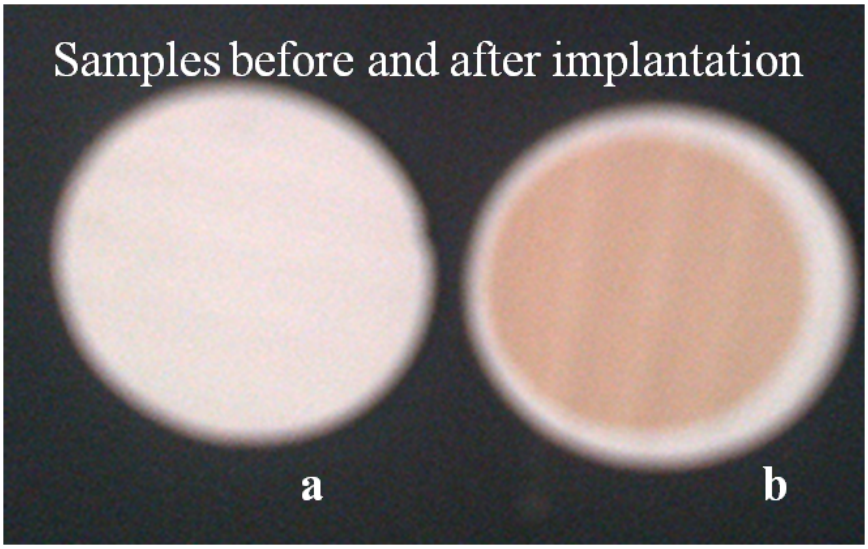

Figure 5.5: *A photograph for h-BN polycrystalline samples (a) before and (b) after implantation as shown for the rod sample.*

Figure 5.5 is a photographic representation of the difference between the unimplanted and implanted samples. One of the most obvious changes observed on the implanted *h*-BN samples's surface is the colour change from white to amber-brown colour. The hue of the implanted samples were dependent on the different implantation parameters. For instance, with respect to the fluence, samples implanted with higher fluence were observed to be darker as compared to the samples implanted with lower fluences.

It was also dependent on the implantation energy where higher energy implanted samples were darker as compared to those implanted at low energies for

the same fluence. The higher mass implanted samples also indicated a darker hue as compared to those implanted with lower mass ions for similar energies and fluences. No other colour changes were observed on the samples after varying the implantation temperature or after annealing. This indicated that the colour change was only isolated to the implantation and the resulting radiation damage. The implantation depth is quite shallow as compared to the penetration depth of Raman laser light as such the colour does not interfere with the Raman signal.

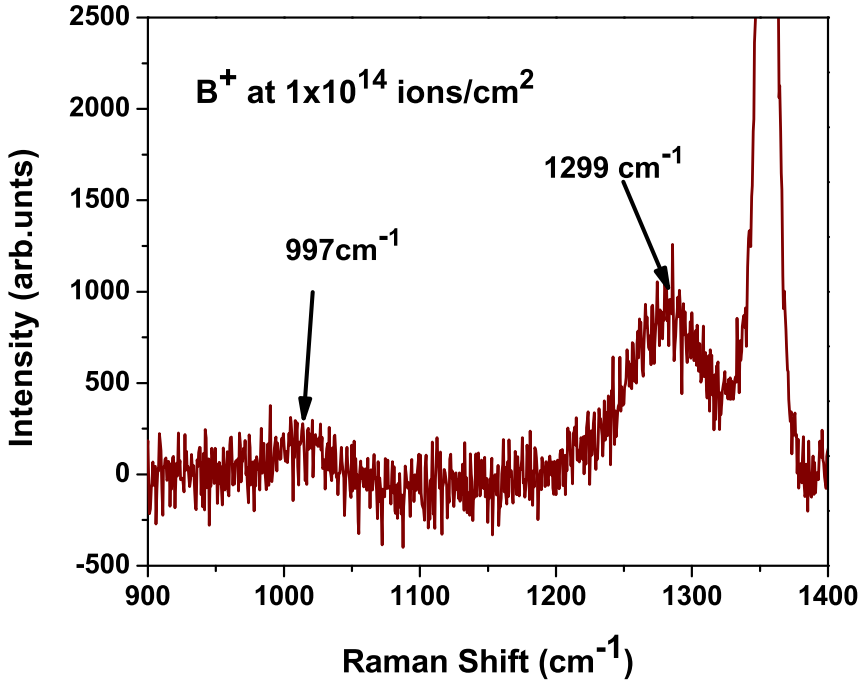

Figure 5.6: *Raman measurements for h-BN sheet samples implanted at $1\times10^{14} ions/cm^2$ and an energy of 150 keV (unsmoothed data).*

Figure 5.6 represents the Raman spectrum for the sample that was implanted with boron ions at the energy of 150 keV with the fluence of 1×10^{14} ions/cm^2. This was the lowest fluence used for all the boron implants. The measurements were taken on three different areas with an average of twenty five points (25), over a 0.5×0.5 mm square area, scanned on the sample's surface. Each scan was carried out over a period of 20 minutes, implying that for each single point, measurements

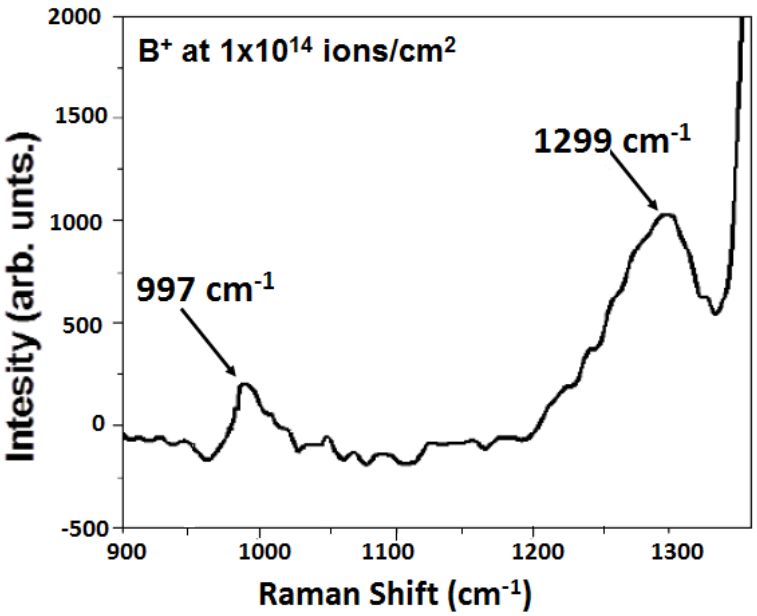

Figure 5.7: *Raman measurements for h-BN sheet samples implanted at 1×10* ^{14}*ions/cm*^{2} *centred around the region of interest.*

were carried out for 48 seconds to increase the count statistics. Figure 5.7 is the spectrum centred at the region of interest, to view clearly the additional features of the spectrum after implantation.

The data in figure 5.6 and 5.7 was fitted using Lorentzian and Gaussian peak functions to determine the integrated peak intensity of each peak. From this fitting, the *h*-BN peak which was present in the unimplanted sample was predominantly retained and was observed at the frequency of 1366.5 cm^{-1}. The peak had a wider FWHM of 9 cm^{-1} as compared to the unimplanted *h*-BN sample's spectrum in figure 5.4. The peak's intensity (intensity is in arbitrary units) was also observed to decrease from 22,500 counts to 20,000 counts.

Since Raman laser light can focus down to 1μm on the sample surface, the presence of the Lorentzian peak at 1366.5 cm^{-1} is an indication that the bulk of the material was still predominantly *h*-BN. The defects that were created after

implantation were localized on the subsurface, less than 1 μm below the surface. For most of the implants, the range of the Raman scattering volume was much larger than the implanted range, and it is therefore not possible to correlate the intensity of the h-BN peak relative to the implanted volume and broadening. For higher fluences the impact on the principal h-BN peak after implantation was more observable.

In addition to the Lorentzian peak at 1366.5 cm^{-1}, there are two new broad peaks appearing in the spectrum, which were not present in the unimplanted spectrum. The first peak is centred at 1299 cm^{-1} with a relatively low intensity of 1032 counts, as compared to the h-BN peak and a linewidth of 77 cm^{-1}. The second peak has a much lower intensity and is centred at 997 cm^{-1} as seen from figure 5.7.

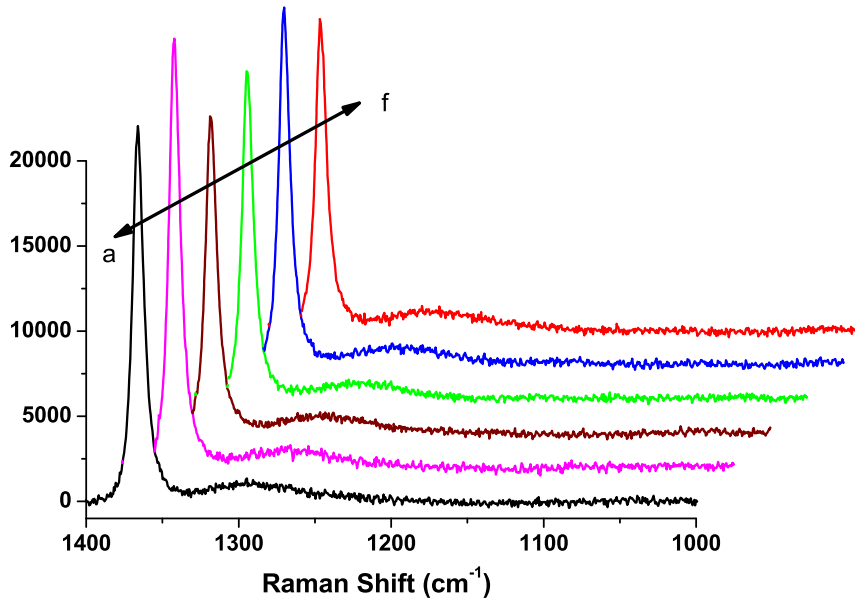

Figure 5.8: *Raman measurements for h-BN sheet samples implanted at 1×10* ^{14} *ions/cm*^{2} *measured at different points across a 0.5×0. 5 mm area.*

Figure 5.8 shows the Raman spectra for the sample measured at six random points across the h-BN implanted surface over an area of 0.5×0.5 mm. The spectra have been offset in order to show a clear distinction for the different spectra. The

spectra shows the presence of the new peaks for all the points investigated.

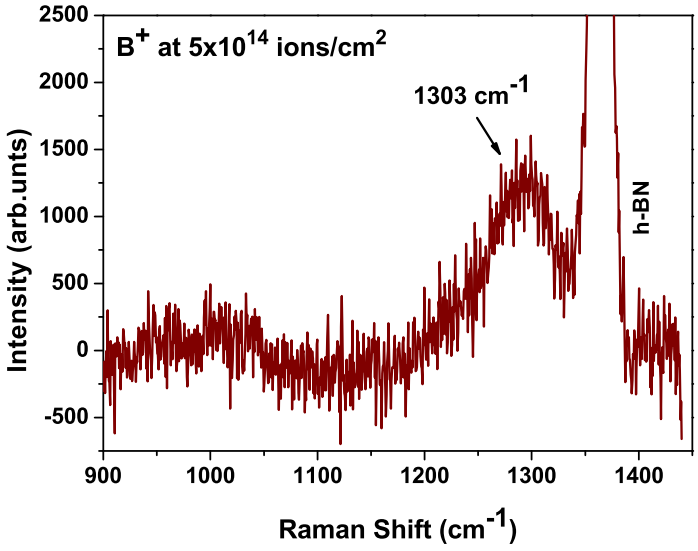

Figure 5.9: *Raman measurements for h-BN sheet samples implanted with boron at* 5×10^{14} *ions/cm*^{2}*.(Unsmoothed data)*

Figure 5.9, 5.10 and 5.11 represent the spectrum for samples implanted with boron at 5×10^{14} ions/cm^2, with figure 5.9 being the spectrum centred around the region of interest. These measurements were also carried out on twenty five different points over a 0.5 mm$\times$ 0.5 mm square area with similar time intervals as for the previous measurements. Figure 5.11 represents the spectra for measurements taken from eleven random points chosen from the 0.25 mm^2 area.

From these spectra, the *h*-BN peak was still predominant, but its intensity was further reduced to 18,700 counts. Its position is at a wavenumber of 1366.6 cm^{-1} as compared to the principal *h*-BN peak at 1366.0 cm^{-1}, a linewidth of 10 cm^{-1}. There are new features also appearing in the spectrum. At the region of interest as shown in figure 5.10, the broad features were more apparent with the first feature located at 1025 cm^{-1}, and the second at 1303 cm^{-1}. The intensities of these peaks are higher as compared to the intensities of spectrum in figures 5.6 and 5.7, for the

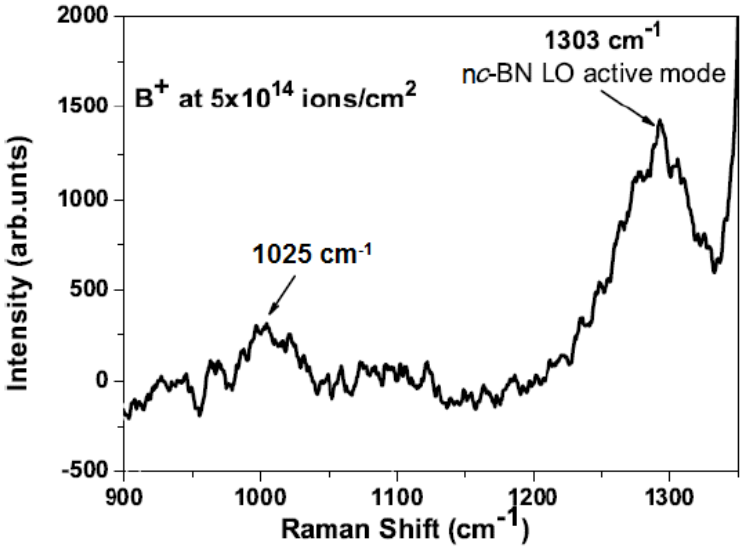

Figure 5.10: *Raman measurements for h-BN sheet samples implanted with boron at 5×10^{14} ions/cm^2 centred around the region of interest.*

lower fluence of 1×10^{14} ions/cm^2.

It is also observed that the Gaussian feature at 1303 cm^{-1} has a lower frequency shift (1 cm^{-1}) as compared to one for low fluence in figure 5.7 which had a 5 cm^{-1} frequency shift with reference to the position of the *c*-BN nanopowder LO peak at 1296 cm^{-1} in figure 5.1, with a further reduced FWHM of 56 cm^{-1}. The intensity of this feature is increased by 800 counts as compared to the intensity of the samples implanted by 1×10^{14} ions/cm^2.

The spectrum for samples implanted with higher fluences is given in figure 5.12. The *h*-BN Lorentzian peak drastically reduced with increasing ion fluence as observed in the spectra, with intensity decreasing with larger margins at the highest fluence. The broad Gaussian LO *c*-BN peaks are observed at 1300 cm^{-1}, 1292 cm^{-1}, 1287 cm^{-1} and 1276 cm^{-1} for the respective fluences. These peaks also reduced in intensity with increasing fluence and at higher fluences starting at 1×10^{16} ions/cm^2 and the peak had the lowest intensity at 5×10^{16} ions/cm^2 of all

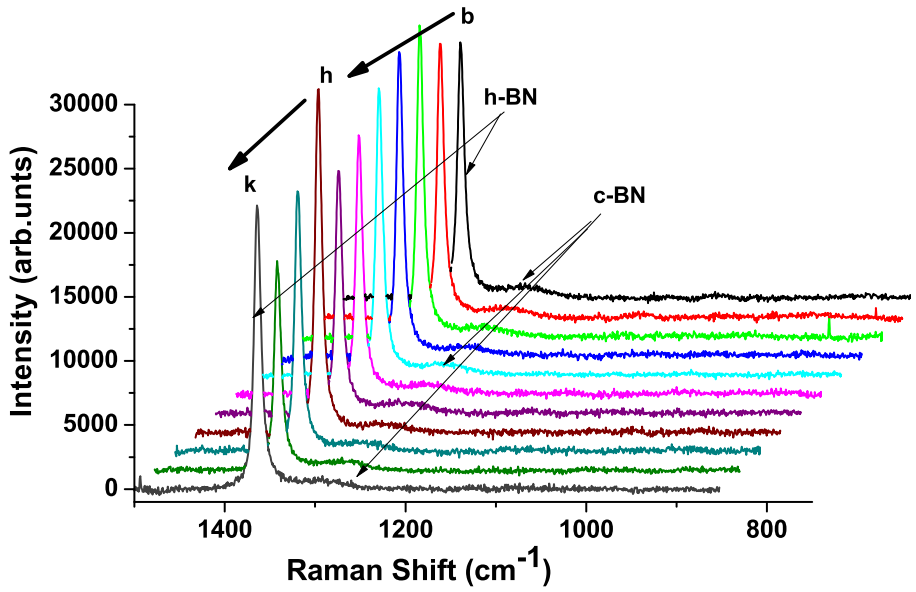

Figure 5.11: *Raman measurements at eleven different points across implanted area for h-BN sheet sample implanted at 150 keV and fluence of* 5×10^{14} *ions/cm*^{2}.

the implanted samples.

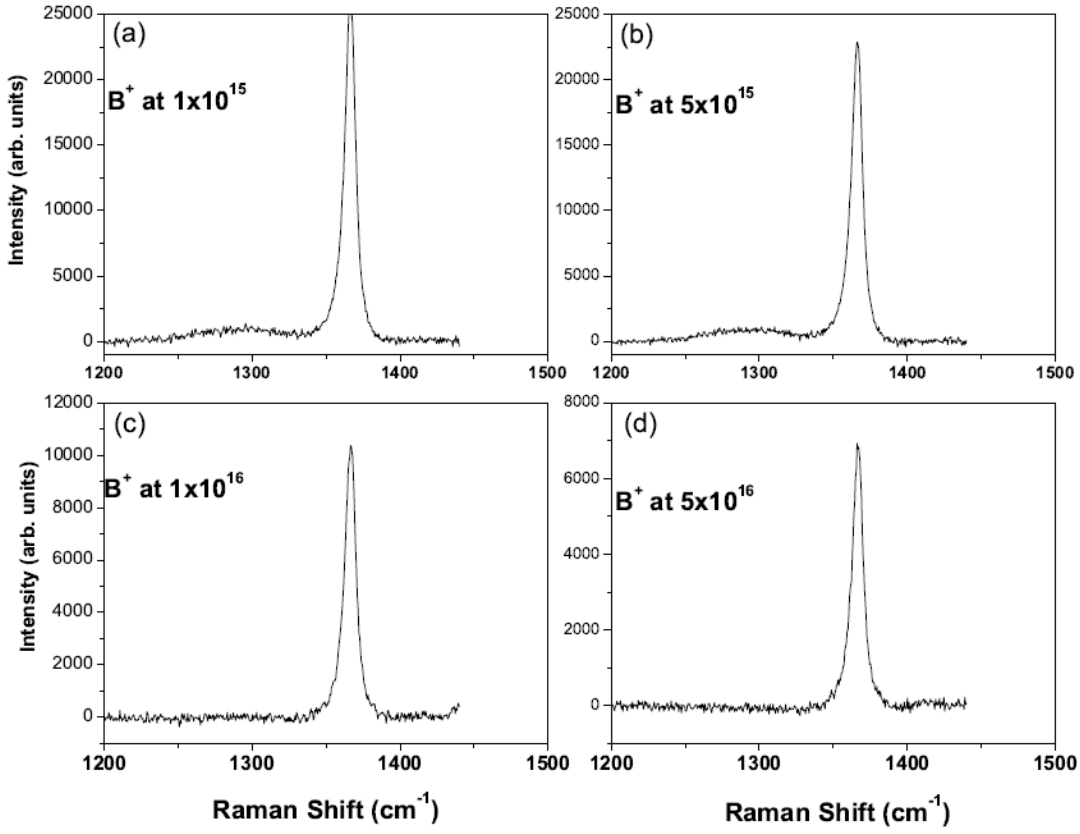

Figure 5.12: *Raman measurements for h-BN sheet samples implanted higher boron fluences (a) at 1×10^{15} ions/cm^2(b) at 5×10^{15} ions/cm^2, (c)1×10^{16} ions/cm^2, (d) 5×10^{16} ions/cm^2, all at an energy of 150 keV.*

Discussion

After implantation the principal h-BN high frequency vibration symmetry mode peaks are predominantly observed in the spectra. SRIM simulations in figure 2.9 show that for boron implantation at 150 keV the range of implantation is 0.4 μm. The Raman signal can probe the sample up to a penetration depth of 1 μm, which means that it is able to penetrate beyond the end of range of implantation for boron implantation. A significant portion of the Raman scattering therefore emerges from the unimplanted region beyond the end of range of the implantation and damage profile where the bulk of the sample is purely h-BN.

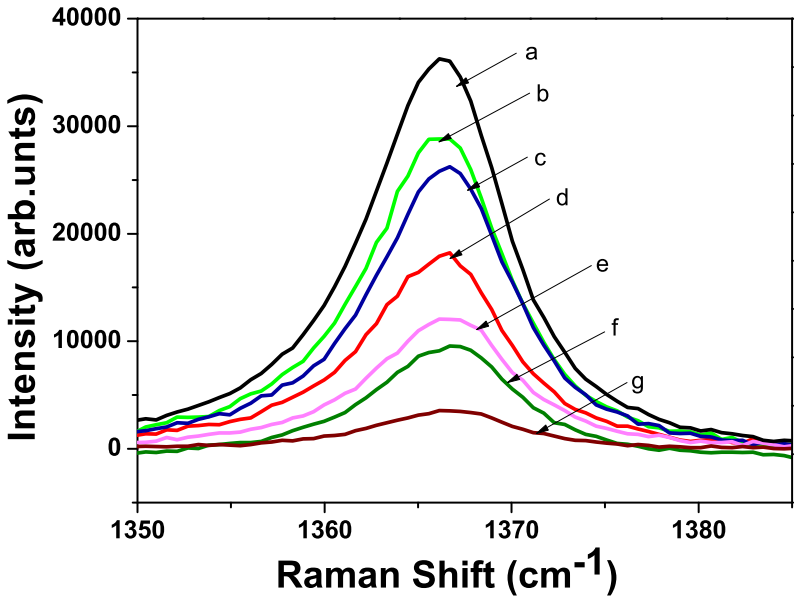

Figure 5.13: *Raman spectra for principal h-BN peak for (a) unimplanted sample, (b) implanted with 1×10^{14} ions/cm^2 (c) at 5×10^{14} ions/cm^2 (d) 1×10^{15} ions/cm^2 (e) at 5×10^{15} ions/cm^2, (f)1×10^{16} ions/cm^2, (g) 5×10^{16} ions/cm^2, all at an energy of 150 keV.*

Figure 5.13 shows the variation of the Raman spectra for h-BN high vibrational Raman mode with the implantation fluence. The peaks' intensities decreases with

increasing fluence. Its linewidth also increases slightly with the implantation fluence. There is also a slight upshift in the frequency of the peak with increasing fluence from 1366.1 cm^{-1} in the unimplanted to 1366.3 cm^{-1}, 1366.5 cm^{-1}, 1366.7 cm^{-1}, 1367.0 cm^{-1}, and 1367.2 cm^{-1} for the respective fluences. In an ideal crystal the Raman frequency will be measured at its theoretical position which is seen in the unimplanted spectrum. With implantation, the crystal is subjected to stress generated due radiation damage created by implanted ions and its general introduction into the sample's matrix, as such the phonons within the lattice are subsequently affected causing the phonon frequency to shift. Erasmus *et al* [188] in their study have shown that a high wavenumber shift indicates that the crystal has undergone a compressive stress. We have observed a shift to higher wavenumbers which we attributed to residual compressional stress caused within the crystal lattice. The residual stress was attributed to the effect of induced defect density in the sample due to ion bombardment which distorted the pre-existing lattice. This effect has been shown theoretically to induce phase transformations of *h*-BN to other BN phases [13].

The new peaks appearing in the implanted samples for wavenumbers between 1289 cm^{-1} and 1303 cm^{-1} correspond to the LO phonon mode for nanocrystalline *c*-BN (n*c*-BN) that occurs at 1296 cm^{-1} (figure 5.1) therefore we attribute the peaks to the presence of *c*-BN structure in the implanted sample.

Theory and experiments have shown that the presence of defects introduced into *h*-BN matrix may lead to a symmetry change to the cubic form [13, 189]. The changes that occur in *h*-BN to the creation of the *c*-BN symmetry in this work are proposed to occur due to the accumulation of point defects introduced during ion implantation. As the energetic ions are introduced into the *h*-BN matrix, they

enter the lattice sites of the material colliding with the atoms and displacing them from their equilibrium position creating either a vacancy or by temporarily settling in the interstitial site within the interplanar space of the material hence causing a large defect concentration. The concentration of defects and the distortion of the lattice sites create high stress/strain level in *h*-BN. These midplane defects and the subsequent volumetric stress they cause are known to induce a significant amount of buckling and breaking of the weak van der Waal bonds within the *h*-BN planes. The progressive buckling of the weak van Der Waal bonds and stretching the bond of the basal B_3N_3 honeycomb hexagon increases the bond length and as a result the local density of the material increases.

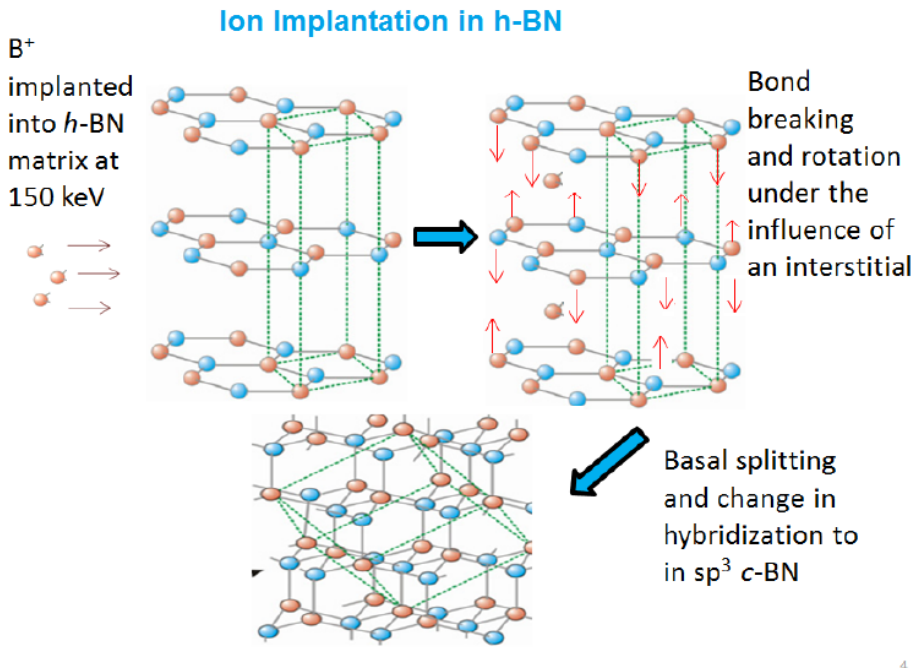

Figure 5.14: *Schematic representation of the processes that take place during ion implantation of h-BN*

As the interplanar bonds break, there occur changes in the electron density in the interatomic and interlayer spaces. The electron density between the boron atom

and the nitrogen atom in adjacent layers increases, decreasing local interlayer spacing and lowering the formation energy. The B_3N_3 honeycomb buckles into a cubic chair configuration that favours a nonplanar steric covalent bond reconstruction of the atoms in the adjacent planes. The bonding network is now tetrahedral and 3-dimensional with an sp^3 hybridization which results into a change in symmetry of the material to the high density *c*-BN whose phonon vibrations are detected by Raman as shown in spectra after implantation. Similar cases have also been seen in the transformation of graphite to diamond [190]. A schematic representation of the processes that occur during ion implantation of *h*-BN is shown in figure 5.14.

The nature and extent of the LO-*c*-BN feature seen after implantation is however different from the microcrystallite *c*-BN, in that, the features are observed to have a characteristic asymmetric line broadening, a shift to lower wavenumber and a low intensity. Similar characteristics have been observed in semiconductors and in diamond with nanocrystal size [191, 192]. A careful observation of the spectrum does not show any feature at or near the TO phonon mode mode for *c*-BN. Similar occurrence have been observed by [184, 193] for nanocrystalline *c*-BN where no TO mode for was observed. We therefore attribute the nature of the *c*-BN symmetry formed to be nanostructural.

Parayanthal and Pollak developed a Spatial Correlation Model (SCM) to explain these changes in the Raman spectra [183]. This model is based on the variation of the shape, size and position of Raman peak with changing crystal size. In an ideal infinite crystal, phonons near the center of the Brillouin zone *(q=0)* give rise to the Raman spectrum because of the conservation of momentum between the phonons and the incident scattered light. The Raman peaks here have a symmetric Gaussian distribution with a fairly narrow FWHM and high intensities. When the

crystal size of the material reduces to nano-scale, there occurs an uncertainty in the phonon momentum allowing phonons with $q \neq 0$ to contribute to the Raman spectrum. The resulting Raman features have an asymmetric broadening of the linewidth, a shift in the frequency and a reduced intensity. The SCM is discussed in detail in Chapter 6.

We therefore conclude that boron ion implantation induces a structural change of *h*-BN to nano-regions associated to the *c*-BN symmetry, with the changes originating from the presence of defects introduced as interplane interstitial and the associated stress.

Generally observed in all the spectra are the high intensities of *h*-BN peaks as compared with the *c*-BN peaks. It is well known that *c*-BN has an indirect band gap with values between 6-6.5 eV. The resonant frequency for materials with wide indirect band gaps generally have a low light absorption property because of the additional phonons necessary for the optical transition in the scattering process, as such it will experience a low Raman scattering cross-section and hence a low intensity. Normally the Raman Gaussian signal for *c*-BN is almost 1000 times less than of *h*-BN which has a direct band of E_g=5.8 eV hence it is more visible [194, 122, 195] in case of a mixed phased sample.

Another factor that may explain the low intensity of the signal is the fact that we expect most of the Raman signal to originate from *h*-BN since Raman probes the sample up to a depth of 1 μm. It is expected that all the changes occurring in the *h*-BN material are localized within the implanted region, which constitutes a very small thickness with respect to the volume probed by the laser. Only a small sub-surface layer of the material approximately 0.4 μm for boron (0.7 μm for He and Li) interacts with the ions (from SRIM calculations the implantation density

is within a small volume).

Together with the *c*-BN symmetry phonon modes, new peaks are observed in the lower wavenumbers as outlined above. According to the theoretical calculations for *w*-BN [196], its phonon vibration normally occurs at wavenumbers between 930 and 1015 cm^{-1} which represents the the E_2 mode for the Raman signal, but no symmetry assignment has been made due to the random orientation of *w*-BN crystallite reported in [73, 197]. The *w*-BN phase has been observed as an intermediate phase that forms during the transformation of *h*-BN to *c*-BN. Comparing these to the modes observed in the present work, they coincide well with frequency shifts seen in the implanted spectra. It could therefore be suggested that the additional features occurring in figures 5.7 and 5.10 at 997 cm^{-1} and 1025 cm^{-1} respectively might be attributed to a possible wurtzite symmetry of boron nitride (*w*-BN). Analysis carried out with other techniques in Sections 5.8 and 5.9 however did not show any suggestion of a wurtzite BN symmetry.

These peaks (at 997 cm^{-1} and 1025 cm^{-1}) are only observed in samples that are implanted with boron ions and therefore only isolated to B implantation (as will be seen in the subsequent subsections for implantation with other ions i.e. He and Li), as such more investigations were carried out to determine another possible origin for these peaks. Boron has a tendency of forming clusters when in excess in some materials [198]. A detailed Raman study on boron-rich crystals shows that there are Raman phonon modes that occur at similar wavenumbers or frequency shifts as observed in the implanted samples. These have been observed to overlap the Raman doublet associated with total symmetrical vibration commonly found in the spectra for boron and boron rich solids [197, 199]. It is therefore possible that these peaks are as a result of boron clusters in the crystal, although the fluences

used in these implantations are small compared to the atomic density of h-BN.

It should be noted that these peaks are almost 200 cm^{-1} away from the LO c-BN peaks therefore we cannot attribute them to the Raman mode for c-BN structures at 1300 cm^{-1}. We do not associate these peaks to the TO mode either. The TO c-BN mode is only observed in bulk c-BN with particle size of over 200 nm and according to calculations, simulations and TEM analysis, it is highly unlikely that these Raman vibrations are from bulk/microcrystal c-BN. As discussed earlier, the TO and LO modes for nc-BN merge into a single broad asymmetrical peak at, or very close to the LO mode when the particle size is reduced to nanoscale.

There was also a small peak visible in some spectra at about 1175 cm^{-1}, which is due to the calibration mercury Raman line.

Table 5.1: *A summary of the nc-BN peak characteristics for h-BN sheet samples implanted with boron ions at 150 keV.*

Fluence (ions/cm^2)	Peak position (cm^{-1})	FWHM (cm^{-1})	$I_G I_L$ peaks (cm^{-1})	Additional
1.0x10^{14}	1299	77	0.045	997
5.0x10^{14}	1303	35	0.062	1000
1.0x10^{15}	1301	68	0.032	1025
5.0x10^{15}	1292	91	0.020	1256
1.0x10^{16}	1287	106	0.012	-

All the peaks obtained were analyzed as a Lorentzian fit for the principal h-BN peak and as Gaussian fit for the peak occurring after implantation for the different fluences. From this, table 5.1 was constructed to give a summary that compares peak details for Raman scattering measurements for the polycrystalline sheet h-BN samples. The table also shows the additional peaks occurring in the spectra.

To give a clear comparison for the effect of varying the ion fluence with the Raman peak intensities of the nc-BN LO mode peak, a graph of the Raman intensity

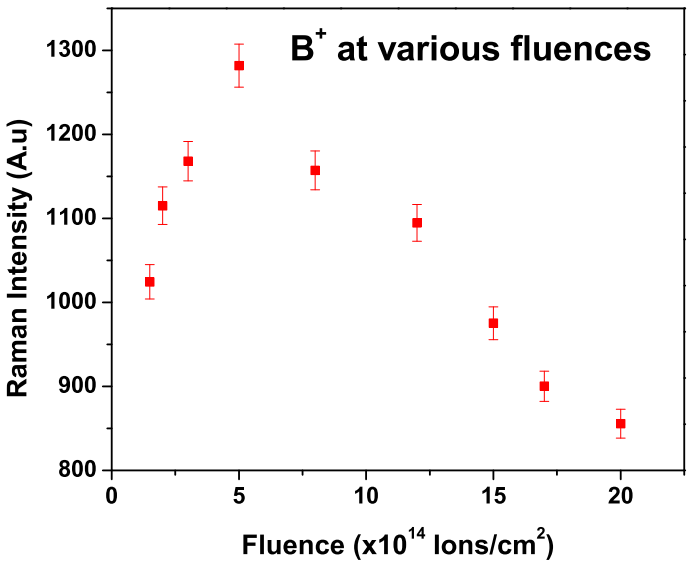

Figure 5.15: *Relationship between the Raman peak intensity for the Gaussian fit and the ion fluence for samples implanted with boron ions at 150 keV for the nc-BN peak .*

as a function of fluence was plotted as shown in figure 5.15. For each spectrum, data points for the peak intensities were obtained from the position of the highest intensity after fitting the data using a Gaussian fit.

From figure 5.15, there is a clear dependence of the intensity with the ion fluence, and hence the n*c*-BN formation is dependent on the fluence. It is observed that the peak intensity increases with an increasing ion fluence up to 5×10^{14} ions/cm^2, then it reduces with a further increase in the fluence. Comparing the intensities for the lower fluences with the higher ones, the lowest fluence gives a higher intensity than the highest fluence used (5×10^{16} ions/cm^2) which exhibits the lowest intensity of all.

The plausible explanation for this behaviour is, at low fluence, there is sufficient accumulation of defect induced stress to cause buckling up of the hexagonal plane and subsequent bond reconstruction initiates sp^3 structural formation of the cubic

nanostructure. With increasing fluence, more defects are introduced into the material, leading to an increase in the bond breaking and subsequent reconstruction to the cubic symmetry until an optimum is obtained. Above this optimum value, the higher fluence leads to more radiation damage, increasing the compressive stress in the material. At this point excess stress levels in the film reduced the n*c*-BN Raman signal or the high damage density exceeded the *c*-BN formation threshold and as such no signal was observed.

From this study the optimum fluence for all boron implants in the *h*-BN was obtained as 5×10^{14} ions/cm^2. The linewidth also decreases with increasing fluence, reaching its narrowest value at 5×10^{14} ions/cm^2, above which it begins to increase. This implies that the extent to which this new mode occurs is fluence dependent. Generally observed is the broadening of the linewidth and a peak intensity reduction for the *h*-BN peak with increasing fluence.

Energy Dependence of the LO c-BN Peak for B implants

The energy dependence on the frequency, intensity and the linewidth for implanted *h*-BN sheet samples were studied herein in order to determine how varying the energy affects the formation of the sp^3 symmetry with all the other parameters held constant. The samples were implanted with boron ions at the optimum fluence of 5×10^{14} ions/cm^2. The implant energy was varied from 40 keV to 150 keV. This was carried out to determine how the implant energy affects the nature and extent of the new peak formed.

Before the actual experiment, SRIM simulations were carried out to establish the damage density and the penetration depth of the ions at various energies. Figure 5.16 represents the SRIM simulations for *h*-BN samples implanted with boron ions from 1 keV to 150 keV. Figure 5.16 shows an increase in the projected range

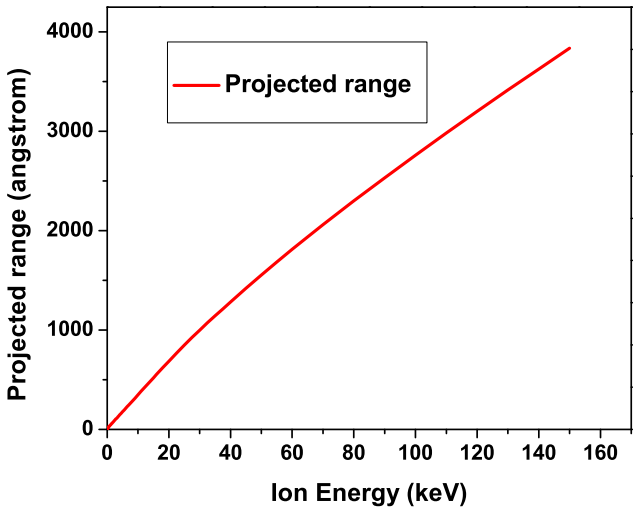

Figure 5.16: *SRIM simulations showing the relationship between the projected range and the ion energy for h-BN sheets implanted with boron ions from 1 keV to 150 keV.*

for the ions with increasing energies. At 40, 80, 120 and 150 keV, the penetration depths were approximately 0.1μm, 0.2μm, 0.3μm and 0.4 μm respectively. The slope remains rather constant and so the range of implantation increases almost linearly with increasing energy. The the integral damage concentration also increases with an increase in energy within our experimental energy range.

Figure 5.17 shows the Raman spectra for the samples implanted with the different energies with the spectra centrered around the region of interest. Broad peaks were observed exclusively on the implanted samples, which are absent in the unimplanted samples. The peaks have the characteristic asymmetric broadening characteristic of n*c*-BN. There is also a downshift in the frequency at with increasing energies.

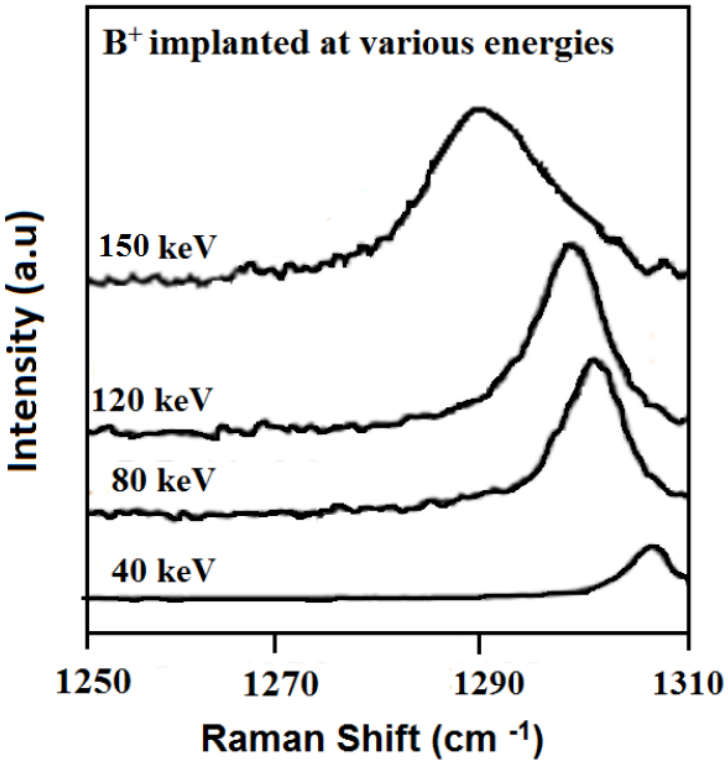

Figure 5.17: *Raman spectra for h-BN sheets samples implanted with boron ions at various energies at a constant fluence of* 5×10^{14} *ions/cm*^{2}.

Discussion

Figure 5.18 shows a summary of the relationship of the implant energy with respect to the normalized (with respect to the intensity of the *h*-BN principal peak $I_{Lorentzian}$) LO n*c*-BN Gaussian peak intensity and the linewidth. The normalized intensity and the linewidth are observed to increase with increasing energy.

Simulations with SRIM shows that with increasing energy, the implanted layer is buried deeper below the crystal surface as seen in figure 5.16. The integrated damage density increases with increasing energy seen in Chapter 2 and as a result the induced stress also increases with increasing energy and will be dependent on how far the implanted layer is below the surface. The peak broadening and increase in the normalized intensity therefore is stress related. At low energy there is a low

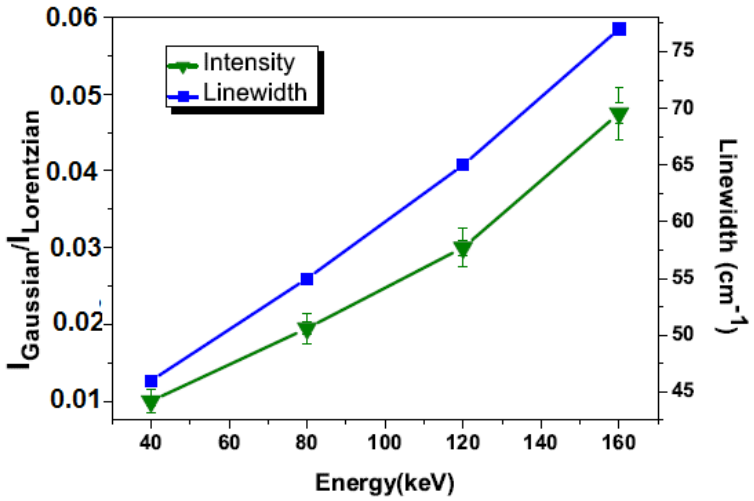

Figure 5.18: *Relationship of the normalized (with respect to the intensity of the unimplanted sample) c-BN peak intensity and linewidth as functions of energy for samples implanted with boron ions at* 5×10^{14} *ions/cm*^{2}

defect concentration and hence insufficient stress build up that is able to initiate the n*c*-BN symmetry formation, which agrees well with the SRIM calculations.

As the energy increases the critical stress build-up is achieved and as such, the LO Raman active modes are able to be detected until the highest percentage n*c*-BN amount is achieved. If this is the case then the observed broadening of the vibrational band is possibly from the n*c*-BN crystallites created in the electronic stopping region when the ions have a high energy. When the ions energy decreases, the nuclear stopping becomes dominant and the Raman modes for n*c*-BN observed may have been formed as a result of nuclear stopping, suggesting that both processes are responsible for n*c*-BN formation also observed by [200, 201].

Incident Laser Energy Dependance

Due to the nature of *c*-BN, i.e. the wide band gap, it has been seen that its Raman scattering efficiency is quite low as compared to that of *h*-BN. As such, different

Raman laser lines were used to determine the relationship between the Raman laser energy and the corresponding n*c*-BN LO peak intensity, linewidth and frequency shift.

To accomplish this, the samples that were implanted with boron ions at 150 keV and the optimum fluence of 5×10^{14} ions/cm^2 were analyzed by three different Raman lines i.e. the green 514 nm Ar^+, the blue 488 nm Ar^+ and the ultra violet (UV) 244 nm Raman lines to determine which of the three laser lines was the most effective in detecting and analyzing the n*c*-BN structure in the implanted sample.

Visible Raman

Figure 5.19 represents the Raman spectrum for the n*c*-BN LO peak analyzed by the 514 nm, 488 nm and the 700 nm lines. All the scans were taken at the same sample at the same point.

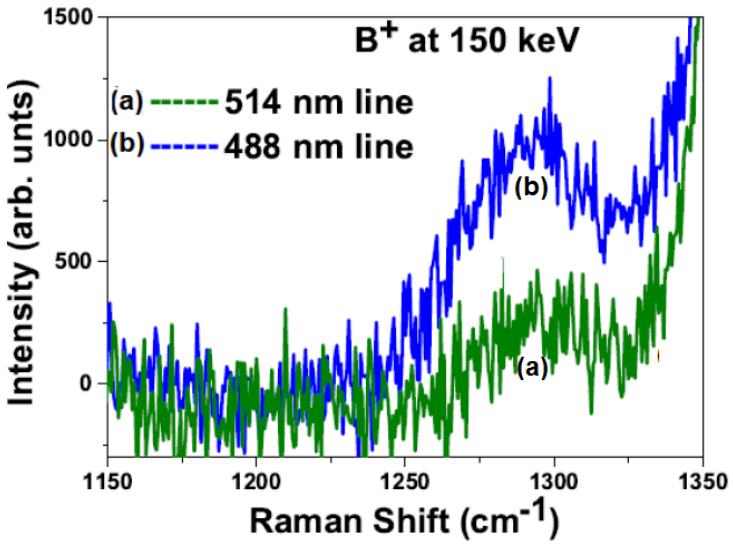

Figure 5.19: *Dependance of the LO c-BN Raman peak with the Raman laser energy (centred in the region of interest)* for h-BN sheets at 150 keV and a fluence of 5×10^{14} ions/cm^2.

Comparing the two spectra, the blue Ar^+ 488 nm line shows a stronger n*c*-BN

LO peak signal for the Raman intensity as compared to the green 514 Ar^+ nm line with a sufficient signal-to-noise ratio for measurements carried out on the same sample under similar conditions. A close comparison shows that the 514 nm line is up to 700 units lower than the 488 nm line. Because of the high intensity, the 488 nm line it is suggested that it better at distinguishing n*c*-BN phonons as compared to the 514 nm line. No nc-BN LO mode was detected with the 700 nm line.

UV-Raman

Ultra-violet Raman spectroscopy with wavelength of 244 nm was also used in the analysis of the sample before and after implantation. It was used in order to determine the effect of increasing laser energy in the analysis of the *h*-BN and *c*-BN nanostructures already observed with the laser of longer wavelengths i .e. the 488 nm and 514 nm laser lines. Figure 5.20 represents the Raman spectrum for samples analyzed by UV Raman. Figure 5.20 (a) is the spectrum for unimplanted sample and 5.20 (b) spectrum for the sample implanted with boron ions at 150 keV and fluence of $5x10^{14}$ ions/cm^2.

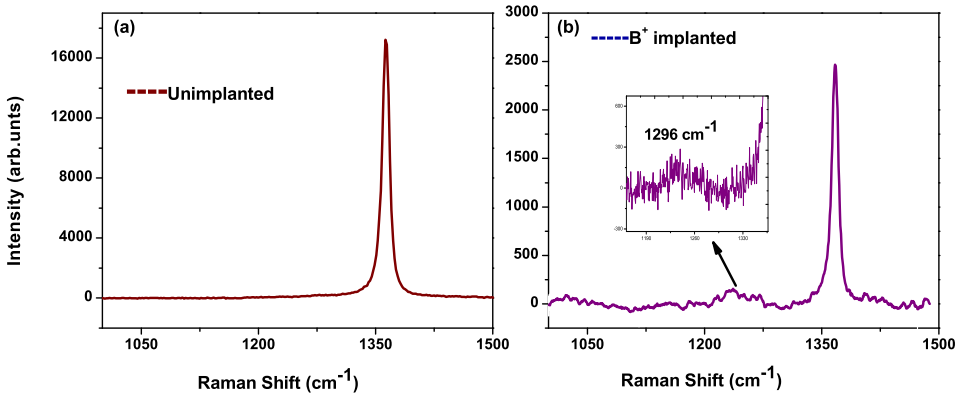

Figure 5.20: *Raman spectra for h-BN sheet samples analyzed by the UV Raman (a) is the unimplanted spectrum (b) spectrum for sample implanted with boron ions at 150 keV and a fluence of* 5×10^{14} *ions/*cm^2.

It is observed that the unimplanted spectrum is similar in linewidth (8.4 cm^{-1})

and position (1366 cm^{-1}) as compared to the other spectra analyzed with the 488 nm and the 514 nm, but with decreased intensity up to about 2000 counts. After implantation, the *h*-BN 1366 cm^{-1} vibrational mode is still dominant with the n*c*-BN LO phonon peak observed previously with visible Raman present, but almost invisible with UV. When zoomed into, the n*c*-BN peak becomes visible but has a low intensity as seen in the inset of figure 5.20 (b).

The penetration depth of the 488 nm and 514 nm Raman lines is about 1 μm below the surface of *h*-BN sample as seen from calculations using the absorption coefficient in equation 5.3.2 and also reported by Reich *et al* [122], as a result analyses with these lines sampled the entire implanted region. The absorption coefficient of *h*-BN in UV is large therefore it will penetrate less ($\approx$0.3 μm) into the material, sampling a small volume of the implanted region before being absorbed. As a result a weaker n*c*-BN signal as observed in UV compared to the two visible Raman lines.

From these observations it is concluded that the Raman spectral lines in the visible light range gave better analyses for *c*-BN nanostructure as compared to the UV Raman, with the 488 nm line being more effective in detecting the n*c*-BN particles as compared to the 514 nm line. The 488 Ar^+ line is well known for the detection of nanosize particles, which has also been observed by Werninghaus *et al* [202]. The UV Raman was ineffective due to its large absorption coefficient in *h*-BN which makes it to get absorbed.

Laser Power Density Dependence

Figure 5.21 represents the Raman spectra for samples implanted with boron at 150 keV, analyzed with objective lenses of different magnifications to determine the effect of varying the incident laser beam power density. The measurements were

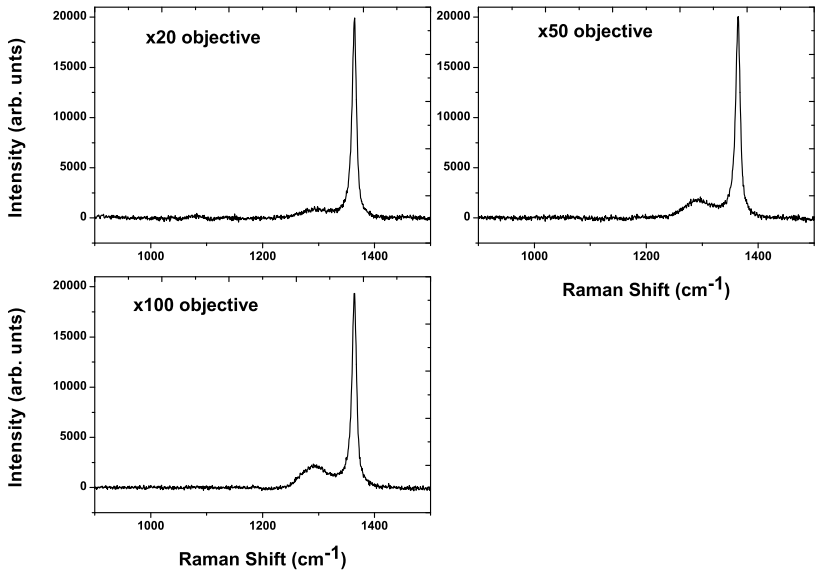

Figure 5.21: *Dependance of the LO c-BN peak with the objective lens for B implanted at 150 keV and fluence of* 5×10^{14} *ions/cm*^{2}.

carried out with 20x objective, 50x objective and 100x objective. The spectrum for 100x objective gave the highest peak intensity followed by the 50x and finally the 20x objective. Generally the higher the magnification the higher the laser power density, as such, the 100x objective concentrated the laser beam to the sample more within a small area, hence increasing the phonon interaction of the material with the laser beam compared to the other two objectives. The lowest magnification gave the weakest phonon signal

This dependence show that high objective/magnification a gave stronger signal. Normally a beam with high power density affects the sample by raising the temperature which in some cases may burn the sample. Besides, the exposure time for the laser beam on the sample was minimized as much as possible to avoid any heating up effect. As such this objective was not used for the measurements in this work. The 50x objective was used throughout.

Annealing Effect

Annealing is a thermal process where a material is exposed to heat or heated to a given temperature in order to change its properties. Annealing is commonly carried out to repair any radiation damage caused after ion irradiation processes. Annealing was carried out on *h*-BN samples in order to determine whether the changes being carried out by implantation were permanent.

The samples were annealed to different temperatures ranging from 80 to 400 ^{o}C. The first set of samples were annealed under argon in the Linkam high temperature cell (TS 1500) microscope furnace located in the Raman Spectroscopy unit.

The annealing was done carefully to remove any moisture that may have been absorbed by the sample. The first measurement was carried out at room temperature (at 23 ^{o}C). The temperature was then raised to 80 ^{o}C and the samples kept at this temperature for 5 minutes and Raman measurements carried out on them. The temperature was again raised to 100 ^{o}C and the sample kept in this temperature for five minutes and analyzed with Raman. Using the same procedure the temperature was raised to 200 ^{o}C, 300 ^{o}C and 400 ^{o}C with the sample maintained at each temperature for 5 minutes, then analyzed with Raman.

The second set of measurements were carried out with the same procedure but the samples annealed for 10 minutes. Finally, the third set of measurements were recorded for each temperature after annealing the sample for 20 minutes.

The n*c*-BN LO mode peaks are present before and after annealing with implying that the damage caused on the material are permanent. To study the annealing effect, the relationship of the Raman linewidth and intensity with annealing temperature was analyzed. The Raman linewidth is usually the measure of phonon lifetime. The variation of the phonon linewidth with temperature was expressed

by [203] given as,

$$\Gamma(T) = \gamma + \Gamma_O(1 + \frac{2}{e^x - 1}) \tag{5.4.1}$$

where γ is temperature independent part of the linewidth and x is given by,

$$x = \frac{\hbar\omega}{2k_B T} \tag{5.4.2}$$

with $\hbar\omega$ is the phonon energy, Γ_o the linewidth for the Raman peak and k_B is the Boltzmann constant.

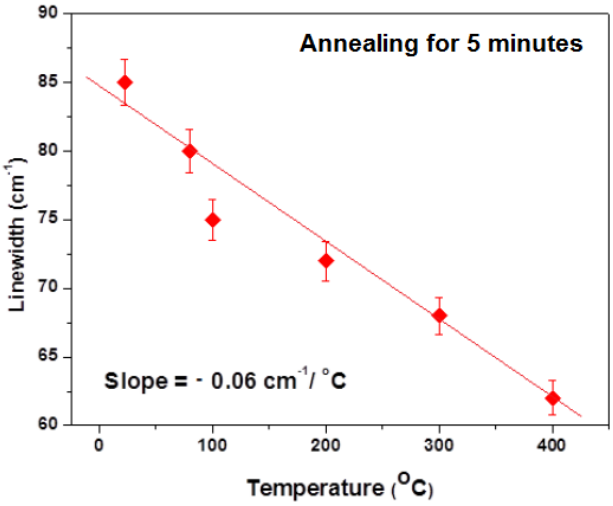

Figure 5.22: *Temperature dependence of the linewidth of the LO c-BN peak for h-BN sheet samples implanted with boron at 150 keV and 5×10^{14} ions/cm^2. The sample was annealed for 5 minutes. The slope of the graph was -0.06 cm^{-1}/^{o}C.*

Figure 5.22 and 5.23 represent temperature dependence of the linewidth of the LO c-B peaks as a function of temperature for polycrystalline *h*-BN sheet samples that were implanted with boron at 150 keV and at the optimum fluence of 5×10^{14} ions/cm^2 and annealed for 5 minutes and 20 minutes respectively.

From both figures, it is clear that the linewidth decreases with increasing annealing temperature. High temperature annealing leads to a decrease in defects in

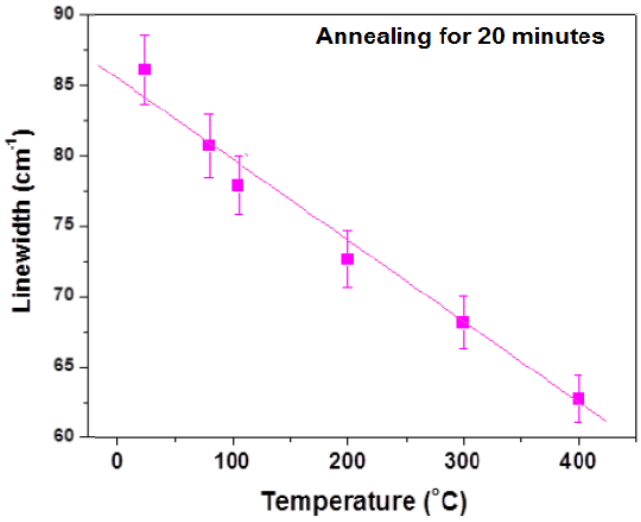

Figure 5.23: *Temperature dependence of the linewidth of the LO c-BN peak for h-BN sheet samples implanted with boron at 150 keV and 5×10^{14} ions/cm^2. The sample was annealed for 20 minutes. The slope of the graph was -0.08 cm^{-1}/^{o}C.*

c-BN produced. This is in good agreement with equation 5.4.1. The integrated intensity of the *c*-BN peak increased with increasing annealing temperature, suggesting an increase in the amount of n*c*-BN produced. Increasing the annealing temperature also causes a shift in the position closer to the *c*-BN LO peak position 1304. Most importantly, the implantation effect associated to the formation of n*c*-BN structure permanent up to the maximum annealing temperature used in this work.

Temperature variation implants

All the results shown thus far have been for implantations done at room temperature. This subsection represents an initial study of varying the implantation temperature. For the low temperature implantation, the *h*-BN sheets were implanted at liquid nitrogen temperature (-196 ^{o}C/77 K) and for high temperature,

implantations were done at 200 ^{o}C and 400 ^{o}C in a temperature controlled chamber. Figure 5.24 represents the *h*-BN spectra after implantation with boron ions at 5×10^{14} ions/cm^2, with an implantation energy of 150 keV and with the implantation temperature varied from liquid nitrogen temperature (LN_2), room temperature (RT), 200 ^{o}C and 400 ^{o}C.

After implantation, the intensities of *h*-BN peaks show a reduction in intensity with increasing temperature for the same fluence and energies. The LN_2 implanted sample shows the least reduction in intensity followed by the RT implanted sample.

Also observed after implantation are the n*c*-BN phonon modes for all the different temperatures at 1296 cm^{-1} for the LN_2 implanted sample, 1295 cm^{-1} for the RT implanted sample, 1290 cm^{-1} for sample implanted at 400 ^{o}C and 1288 cm^{-1} for 400 ^{o}C. The combined Raman spectra, centred around the region of interest, are shown in figure 5.25.

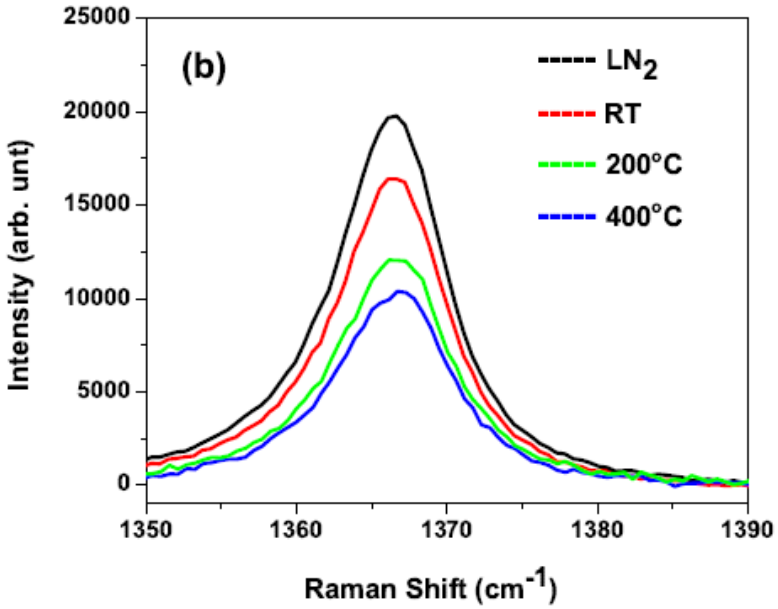

Figure 5.24: *Raman spectra for h-BN peak, for h-BN sheets implanted with boron at various implantation temperatures as indicated at 150 keV and a fluence of* 5×10^{14} *ions/cm*^{2}.

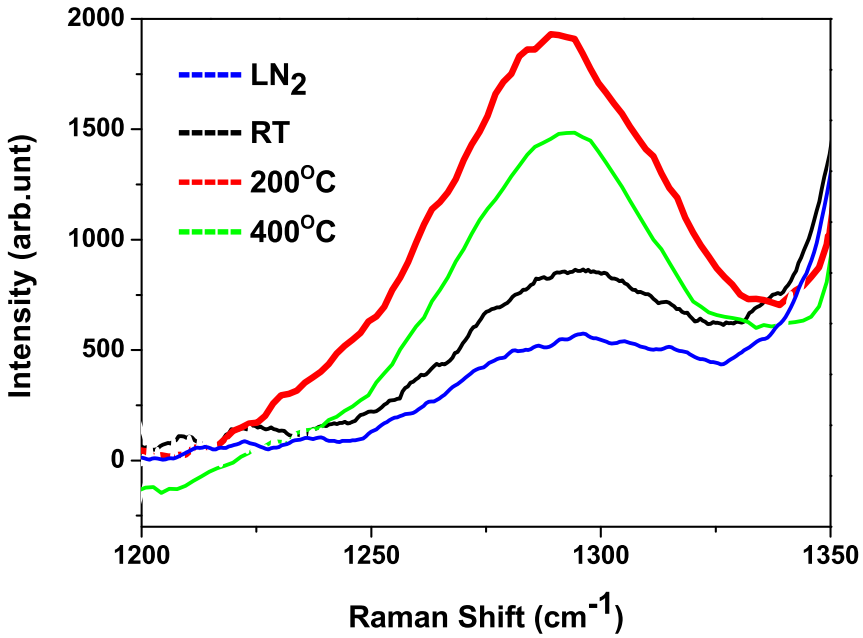

Figure 5.25: *Raman spectra for LO, c-BN peaks for h-BN sheets implanted with boron at 150 keV and a fluence of* 5×10^{14} *ions/cm*^{2} *at various implantation temperatures.*

Discussion

The phonon features in figure 5.25 have already been associated with the LO phonon mode for the n*c*-BN structure created due to strain/stress in the *h*-BN material which is driven by defects introduced after implantation. The analyses also show that the intensity of these n*c*-BN peaks increase with increasing implantation temperature up to 200 ^{o}C and decrease in intensity at 400 ^{o}C.

We presume that at low temperatures (LN_2), the interstitial mobility is greatly suppressed. The knowledge that defect concentration and the subsequent volumetric stress are responsible for *h*-BN to *c*-BN symmetry change, then, at LN_2, if the defects' movement is slowed by the low temperature, then the n*c*-BN formation is also reduced. As the temperature increases the defect mobility is increased resulting in an increased n*c*-BN symmetry. The results suggest that the formation of n*c*-BN symmetry is favoured at 200 ^{o}C which has the highest n*c*-BN LO peak

intensity. At 400 ^{o}C it is possible that the defects created during irradiation are annealed away reducing the amount of nc-BN produced. As a result, a low nc-BN Raman phonon vibration signal is detected as seen in figure 5.25. We predict that at even higher temperatures, beyond 400 ^{o}C the c-BN peak may reduce even further. It is therefore concluded that implantations done with temperatures around 200 ^{o}C may favour the nc-BN production.

5.4.2 Polycrystalline *h*-BN Rod sample

Ion implantation and subsequent Raman analysis were carried out on 99.9% pure polycrystalline h-BN rod samples. These samples were also supplied by the Goodfellow Ceramic company in England with the difference being in the sintering process with the polycrystalline sheets.

The first set of experiments were done by varying the ion fluence, with a single energy of 150 keV, at room temperature. Different fluences, i. e. 1×10^{14} ions/cm^2, 5×10^{14} ions/cm^2 and 1×10^{15} ions/cm^2 were used, and Raman Spectroscopy carried out on them. The details of the Raman spectrum for the sample before implantation is shown in the inset of figure 5.4. Figure 5.26 represents a combination of spectra for h-BN rod samples at 150 keV, with boron at various fluences.

Discussion

After implantation, together with the principal h-BN peak, there are features at frequencies 1301 cm^{-1}, 1303 cm^{-1} and 1301 cm^{-1} for the respective fluences. These peaks had a slightly lower intensity and a wide FWHM as compared to the sheet samples implanted at similar fluences.

These peaks are associated to the LO peaks present in nc-BN also seen in the sheet samples in section 5.3.1, indicating that ion implantation introduced

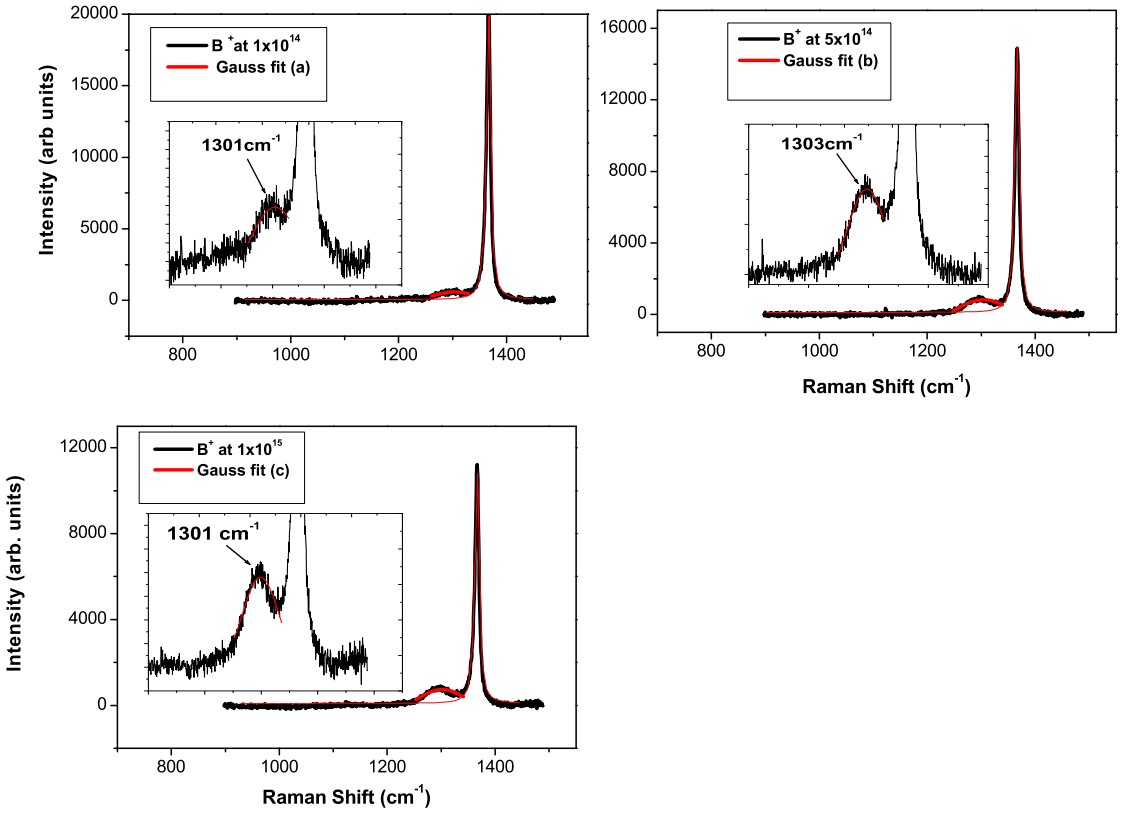

Figure 5.26: *Raman spectra for polycrystalline rod h-BN samples implanted with boron at 150 keV using various fluences.*

defects that led to stress that favoured a symmetry change in the h-BN to c-BN nanostructure for these samples as well.

There was a clear dependence of the nature and extent of the peaks with the ion fluence. The highest fluence gave the lowest intensity with the optimum observed at 5×10^{14} ions/cm^2. This trend is similar to that observed in the sheet h-BN samples, indicating that the sintering process for the sample preparation during pressing does not have any impact on the observed results. The behaviour of the FWHM is also similar to that of the intensity with the narrowest peak with the highest intensity being at 5×10^{14} ions/cm^2. The peaks are however broader as compared to sheet h-BN samples. In these samples however, there were no extra peaks observed in at around 997-1005 cm^{-1} wavenumber that were observed for

the sheet samples (5.7).

5.4.3 Single crystal *h*-BN

Boron ion implantation was carried out on single crystal *h*-BN samples supplied by HQ Graphene company in Netherlands. We used single crystal *h*-BN samples in this section in order to determine whether the possible phase transformation of *h*-BN is influenced by the nature of the crystal and crystal orientation. The samples were approximately 1×1 mm transparent flakes with a thickness approximately 5 μm.

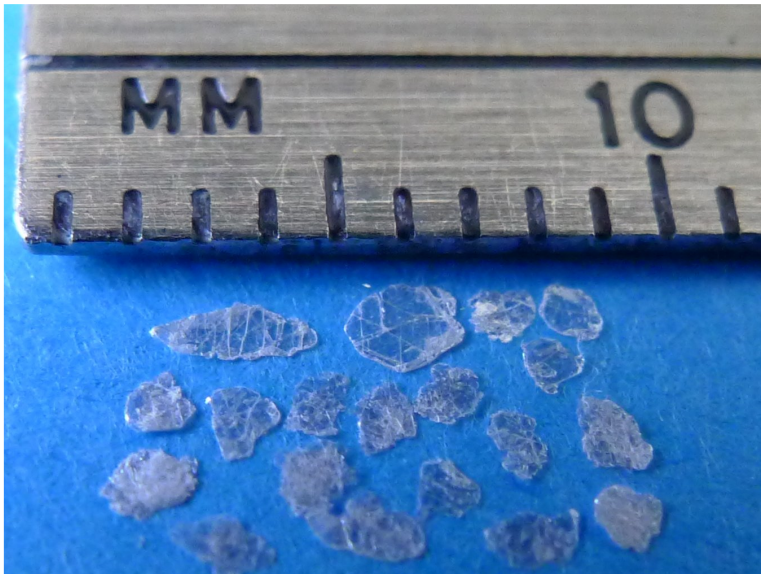

Figure 5.27: *Photograph of single crystal h-BN flakes. Note the millimetre scale.*

Before implantation the samples were cleaved using polydimethylsiloxane (PDMS) in order to obtain a smooth surface. Because of the minute size of the samples, handling them was a challenge, as such, the samples were held onto a sapphire plate using a double sided carbon conducting tape, also supplied by HQ Graphene company to hold them firmly during implantation.

Figure 5.27 represents a photograph of the *h*-BN single crystal samples indicating their dimensions and the transparency aspect. Figure 5.28(a) shows an optical micrograph of a sample at low magnification of 50×. It also shows the sapphire plate and the carbon tape that were used as sample holders.

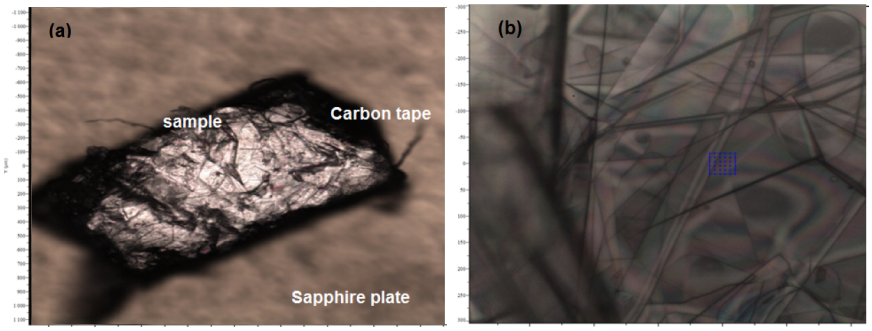

Figure 5.28: *Optical micrograph for h-BN single crystal samples (a) at low magnification (b) at high magnification.*

Figure 5.28(b) represents the micrograph at a high magnification with a 100× objective, while figure 5.29 represents the Scanning Electron Microscopy (SEM) image for samples showing the *h*-BN flakes laying on top of each other.

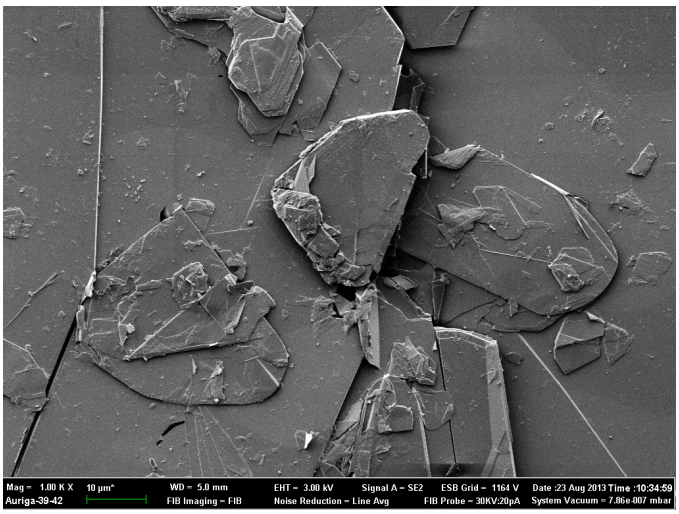

Figure 5.29: *Scanning Electron Microscopy image for h-BN single crystals.*

Figure 5.30 represents the Raman spectroscopy measurements for the single

crystal samples before implantation, carried out point by point on a 200×200 μm square area on the sample using the 514 nm argon line. The spectrum shows an intense Lorentzian peak at 1366.0 cm^{-1} with a FWHM of 8.0 cm^{-1}. This peak represents the phonon vibration for h-BN. There was no other peak present in the spectrum and the spectrum is very similar to the spectra obtained for the two polycrystalline h-BN samples reported before.

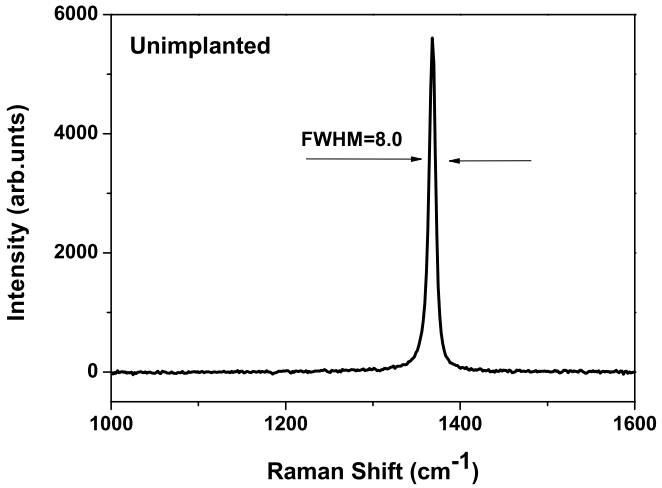

Figure 5.30: *Raman measurements for h-BN single crystal sample before implantation.*

Implantation for these single crystals were carried out perpendicular to the c-axis and at an incident angle of 7^o so as to reduce the effect of ion channelling. Boron was used for implantation at fluence between 1×10^{14} ions/cm^2 and 5×10^{16} ions/cm^2. After implantation the samples' colour changed from transparent to translucent amber crystal with high fluence implants having a darker hue, indicating the effect of radiation damage.

Figure 5.31 represents the spectra for samples implanted at 150 keV using various fluences as shown. Similar to the other samples, the intensity of the h-BN peak

reduced with increasing fluence, with slight increase in linewidth due to concentration of defects and the resultant stress introduced into the material by implantation.

There are new peaks that are observed in the samples' spectra after implantation occurring between 1295 cm^{-1} and 1300 cm^{-1}. The phonon modes are broad with a low intensity as compared to the *h*-BN peak. The position and nature of these peaks have been attributed to the n*c*-BN LO phonon mode peak. It implies that like the polycrystalline implanted sample, the single crystals showed vibrational mode associated with the *c*-BN nanostructure after implantation.

The intensities of these peaks was dependent on the fluence. At the lowest fluence used (1×10^{14} ions/cm^2), the peak's intensity is low and has a broad linewidth. The intensity increases and line narrows down as the fluence increases attaining a maximum at 1×10^{15} ions/cm^2 after which the intensity decreases and the linewidth becomes broader. This observation has also been seen in the polycrystalline samples, showing that there is a fluence dependence for the stress that lead to a *c*-BN symmetry in *h*-BN below and above which the little of no phonon vibration can be detected by Raman as a result of more radiation damage.

Unlike for both rod and sheet samples where the optimum fluence was 5×10^{14} ions/cm^2, the optimum for the single crystal samples was 1×10^{15} ions/cm^2, which is twice as high.

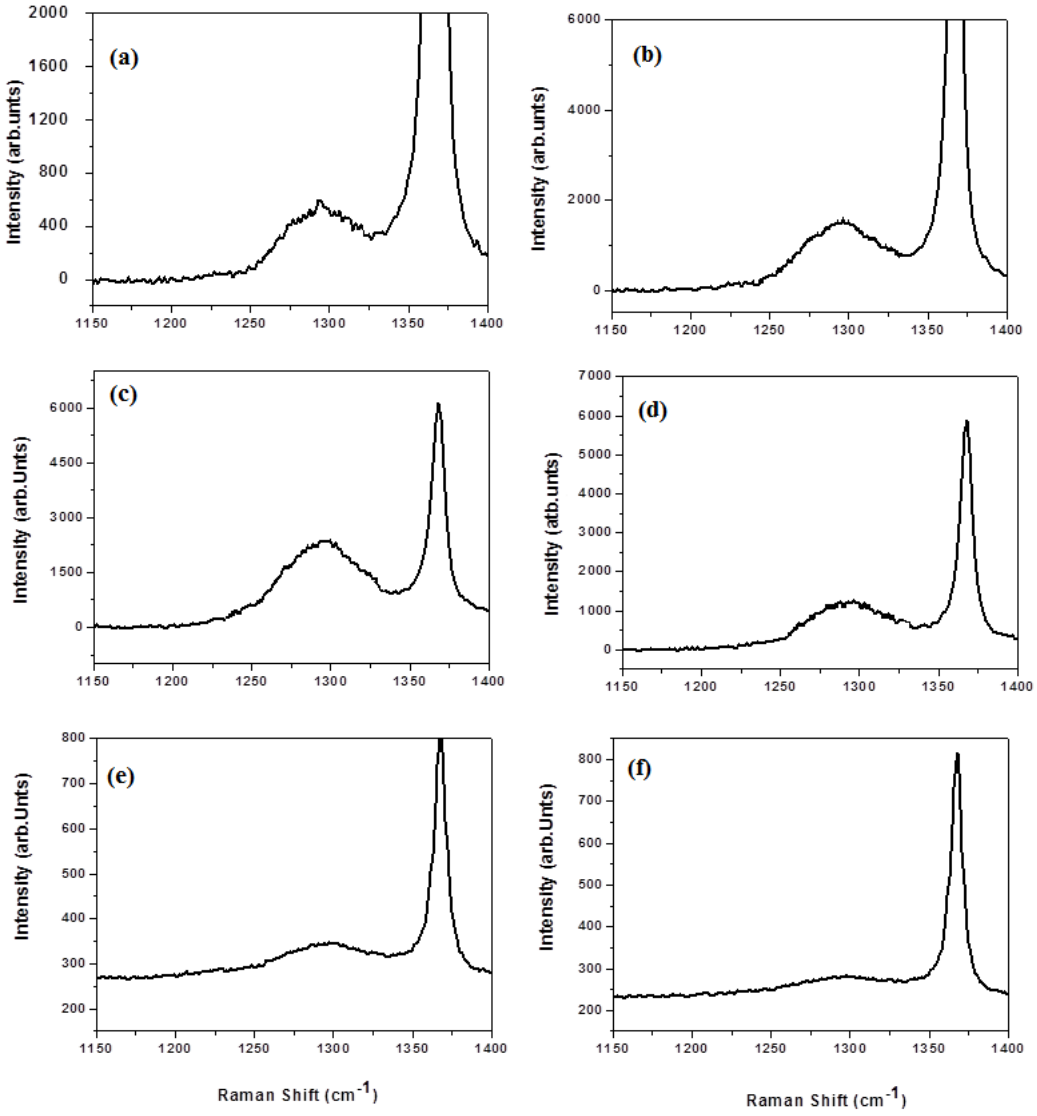

Figure 5.31: *Raman measurements for h-BN single crystal samples after implantation with boron at 150 keV and at various fluences (a) 1×10^{14} ions/cm^2 , (b) 5×10^{14} ions/cm^2 , (c) 1×10^{15} ions/cm^2, (d) 5×10^{15} ions/cm^2, (e) 1×10^{16} ions/cm^2 and (f) 5×10^{16} ions/cm^2. Note the differences in the intensity scale.*

5.5 Helium Ion Implantation

Helium ions were also used for ion implantation carried out in this work. They were the ions with the lowest atomic mass to be used. The results in this section are for polycrystalline sheet samples. Implantations were also carried out with fluence range of 1×10^{14} ions/cm^2 to 1×10^{16} ions/cm^2 at a constant energy of 150 keV. Table 5.2 shows a summary of all the nc-BN peak details for all the He implantations.

Table 5.2: *A summary of the nc-BN peak characteristics for h-BN sheet samples implanted with helium ions at 150 keV.*

Fluence (ions/cm^2)	Peak position (cm^{-1})	FWHM (cm^{-1})	$I_G I_L$
1.0x10^{14}	1260	125	0.015
5.0x10^{14}	1275	122	0.019
1.0x10^{15}	1285	109	0.023
5.0x10^{15}	1298	104	0.032
1.0x10^{16}	1283	112	0.025

Figure 5.33 (i) represents the Raman spectra for all the He implantations implantations at various fluences.

The FWHM for the h-BN peak increases while the intensity reduces with increasing ion fluence, due an increase in stress levels in the h-BN material. The margin of the peak intensity and linewidth reduction is however lower as compared to boron implantation for the same fluence.

Together with the principal h-BN peak, phonon bands, similar to those observed in boron at almost similar positions are observed after implantation. The peaks are located at 1260, 1275, 1285 1298 and 1283 cm^{-1} for the respective ion fluences. The peaks have the characteristic asymmetric broadening and low intensities which we attributed to nc-BN structure after implantation. We therefore suggest that helium ion implantation also induced structural modification of h-BN to nc-BN

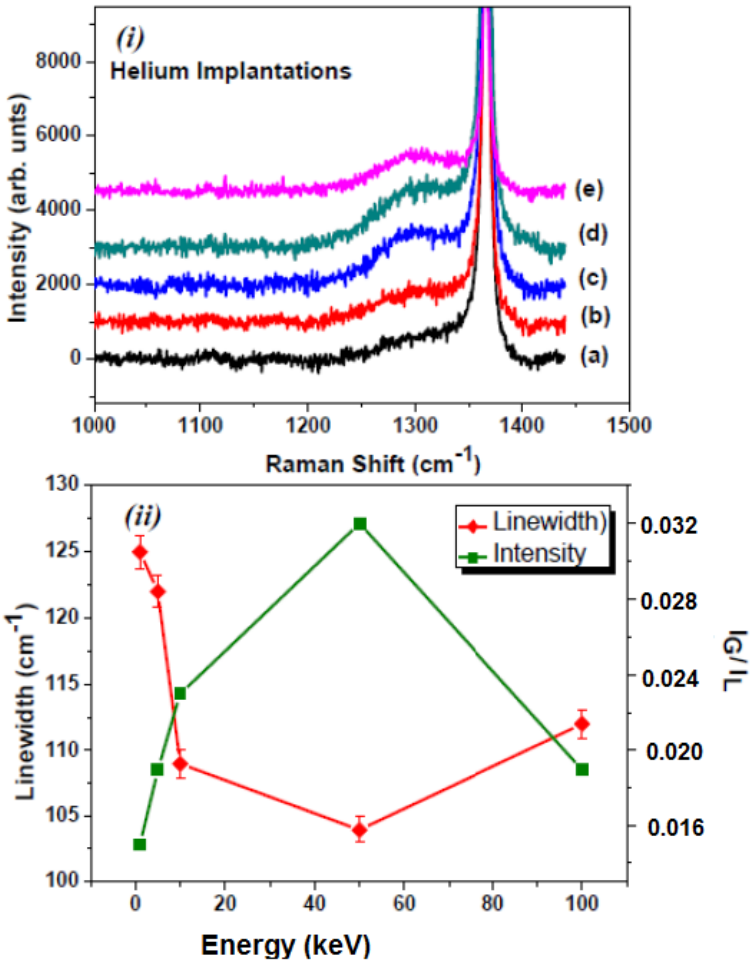

Figure 5.32: *(i)Raman spectra for h-BN sheet samples implanted with helium ions implanted at the energy of 150 keV and fluences (a) 1×10^{14} ions/cm^2, (b) 5×10^{14} ions/cm^2, (c) 1×10^{15} ions/cm^2, (d) 5×10^{15} ions/cm^2 and (e) 1×10^{16} ions/cm^2 (ii) Represents the relationship of the fluence with the linewidth and the integrated intensity of the nc-BN LO peaks.*

symmetry. The most distinctive characteristic for these peaks in contrast to the ones observed in B is the large *c*-BN LO peak shift.

Figure 5.33 (*ii*) shows the relationship for the broad peak linewidth and peak intensity as a function of the fluence. From this relationship, it is deduced that the Raman intensity increases with increasing fluence, attains a maximum at 5×10^{15} ions/cm^2 then decreases with further increase in fluence. On the other hand the linewidth decreases with increasing fluence with the narrowest linewidth obtained

at 5×10^{15} ions/cm^2 and then increases with further increase in fluence.

From this observation and analysis, h-BN to c-BN symmetry change is favoured at relatively high fluences for low mass number ions. A possible explanation is, helium being a light ion requires a high ion concentration to cause a large intrinsic stress that induce the cubic symmetry visible in Raman. At fluences higher than the optimum, the threshold stress is exceeded therefore very little nc-BN Raman active mode are visible because of high radiation damage and stress levels. The reduction in the intensity between 5×10^{15} ions/cm^2 and 1×10^{16} ions/cm^2 for both h-BN and c-BN features indicates that indeed higher fluences damaged the material.

In contrast to boron for all fluences, the cubic symmetry formation in He implantation is favoured towards higher fluence for instance the intensity of the c-BN LO peak at the highest fluence 5×10^{16} ions/cm^2) is almost 100 times more for helium compared to boron. In relation to calculations by SRIM simulations, the damage concentration for helium is far less as compared to boron at similar fluences and energies, therefore at high fluence B ions induce high stress levels beyond the threshold for c-BN formation compared to He. No other peaks were observed in the spectrum after implantation.

5.5.1 Helium Energy variation

An energy variation was carried out on helium implanted samples. The samples were implanted with the optimum helium fluence of 5×10^{15} ions/cm^2 at 40 keV, 80 keV, 120 keV and 150 keV. All implantations were also carried out at room temperature. The c-BN LO peak is clearly visible in all the implanted spectra at 1282, 1289, 1299 and 1301 cm^{-1} for the respective energies, indicating the presence of stress induced nano-cubic symmetry. The intensity and linewidth of these

peaks varies depending on the implantation energy. Like boron implantation, the normalized (normalized with respect to the principal h-BN peak) intensity of the nc-BN LO peaks increase with increasing implantation energy with implantation at 40 keV being almost invisible. The peak at high energy of 150 keV has a wider linewidth as compared at 80 and 120 keV.

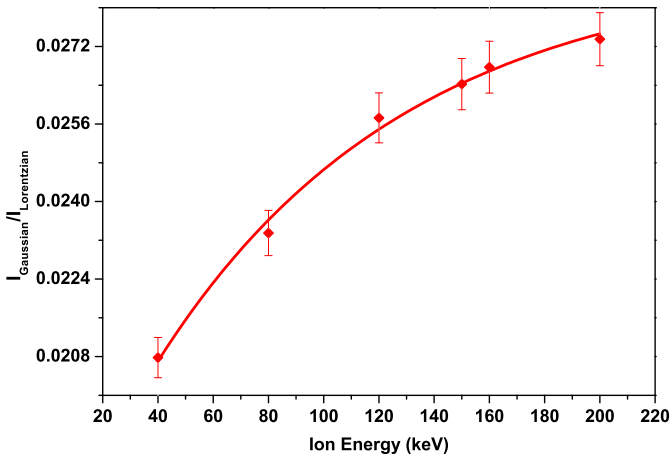

Figure 5.33: *Relationship between the normalized intensity of the LO nc-BN peak and the implantation energy for helium ions implanted in h-BN sheet samples at* 5×10^{15} *ions/cm*^{2}.

Discussion

For the implantation done at He's optimum fluence (5×10^{15} ions/cm^2), low energies did not produce much change to the spectrum after implantation but the important effect is seen at higher energy regimes. The total damage density is higher at high energy as predicted by SRIM and as such high energy implantation leads to large intrinsic stress into the material as compared to implantation at low energy and hence the nc-BN symmetry is favoured at high the highest energy used. Another effect of the increase in stress with implantation energy is seen from the shift of the LO peaks to higher wavenumbers with increasing implant energy.

5.6 Lithium Ion Implantation

Polycrystalline *h*-BN sheet samples were implanted with lithium ions. For lithium ions, different ion fluences were used to determine the optimum Li fluence. Other parameters were also altered such as the Raman laser power.

5.6.1 Varying ion fluence

Polycrystalline hot pressed *h*-BN sheet samples were implanted with lithium ions at various ion fluences ranging from 1×10^{14} ions/cm^2 to 4×10^{16} ions/cm^2. All the implantations were also done at room temperature at the energy of 150 keV. The first Raman scans were measured on 25 points over a 500×500 μm square area with the 514 nm argon ion laser.

Figure 5.34 represents a combination of all the spectra for samples implanted with lithium ions at different ion fluence, using the 514 nm argon ion laser. Figure 5.34 (a) represents the spectrum for the sample before implantation (b) is the spectrum after implantation with lithium ions at 1×10^{14} ions/cm^2, (c) at 5×10^{14} ions/cm^2, (d) at 1×10^{15} ions/cm^2, (e) at 5×10^{15} ions/cm^2 and (f) at 1×10^{16} ions/cm^2. All the Raman analyses were done on the samples under similar conditions as for boron and helium for consistency.

Similar to all the boron and helium implanted spectra, after implantation the *h*-BN peaks are still predominant in the spectra. The peaks' intensity are dependent on the implantation fluence with the highest implanted fluence's intensity having reduced by up to 15000 counts. These *h*-BN peak intensities are higher compared to the boron implants for similar fluence, for instance the intensity of the sample implanted with boron at 1×10^{15} ions/cm^2 is up to 5000 counts lower than that of lithium at this fluence. These peak reductions are due to the effect of implantation

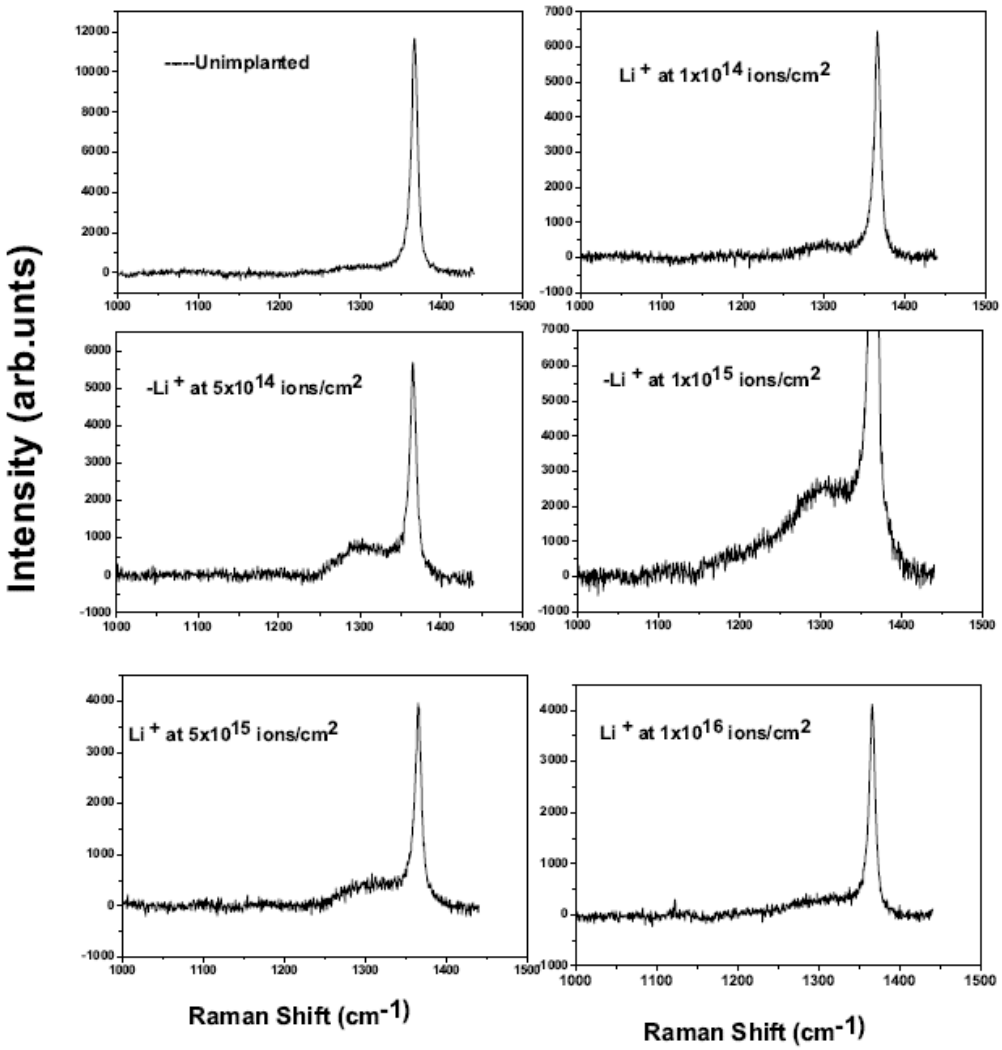

Figure 5.34: *Raman Spectra for h-BN sheet samples implanted with lithium ions at 150 keV and with various fluences.*

stress due to radiation damage in the h-BN matrix.

Together with the h-BN principal peak, similar peaks between 1290 and 1302 cm^{-1} as observed in B and He implants appear in the Raman spectra after Li implantation.

Discussions

For all the lithium implantation, it was found that the spectrum changed after implantation with the nature and extent of the changes being fluence related. The

features are observed to be in similar positions as the LO mode for *c*-BN with nanoscale characteristics observed in boron and helium implantation, and as such it is concluded that lithium implantation also introduced sufficient stress levels into the *h*-BN which in turn led to structural distortion and subsequent bond reconstruction with n*c*-BN symmetry. A summary of all the n*c*-BN LO peak properties for all the different fluences for lithium implants is shown in table 5.3, and a graphical representation os the relationship between the fluence as a function of the intensity and linewidth is shown in figure 5.35

Table 5.3: *A summary of the peak characteristics for h-BN sheet samples implanted with lithium ions at 150 keV.*

Fluence (ions/cm^2)	Peak position (cm^{-1})	FWHM (cm^{-1})	I_G/I_L
1.0x10^{14}	1290	150	0.019
5.0x10^{14}	1296	137	0.033
1.0x10^{15}	1302	92	0.042
5.0x10^{15}	1298	138	0.025
1.0x10^{16}	1290	142	0.018

The fluence of 1×10^{15} ions/cm^2 produced n*c*-BN peak with the highest intensity and narrowest linewidth, above and below this fluence, the intensity of the peaks decrease. It is suggested that the amount of structural transformation increases with increasing fluences up to the optimum and above this fluence any addition of the ion to the substrate's matrix induces stress levels beyond the formation threshold and the Raman signals is observed to attenuate as seen by the decrease in intensity of the n*c*-BN LO peak. No other features are observed in the spectrum after implantation.

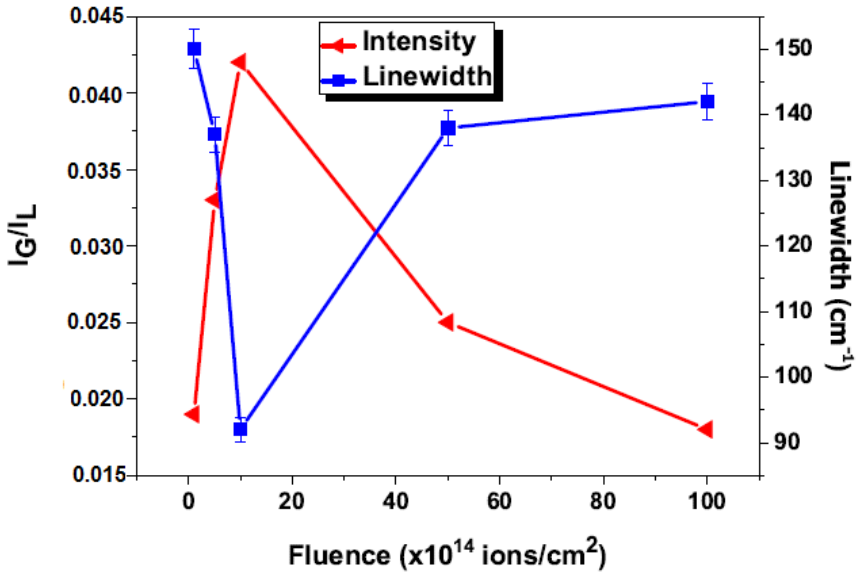

Figure 5.35: *Represents the relationship of the fluence with the linewidth and the integrated intensity of the nc-BN LO peaks for all the Li implants h-BN sheet samples at 150 keV.*

5.7 High Mass Number Implantation

5.7.1 Nitrogen Ion Implantation

After carrying out implantation with boron and comparing it with the implantation of other ions i.e. helium (which is a light and noble gas) and lithium (which is a metal), the data suggested that boron was a better ion species of the three ions in inducing the required intrinsic stress in *h*-BN to create n*c*-BN symmetry at low fluences. It was suggested that this may be due to the fact that a boron atom forms part of the BN compound and making it easier to cause a transformation as compared to the other ions. As a result it was also suggested that nitrogen, also being one of the atoms that form BN material, be used as an implantation species and investigate if the result compared to those of boron implantation.

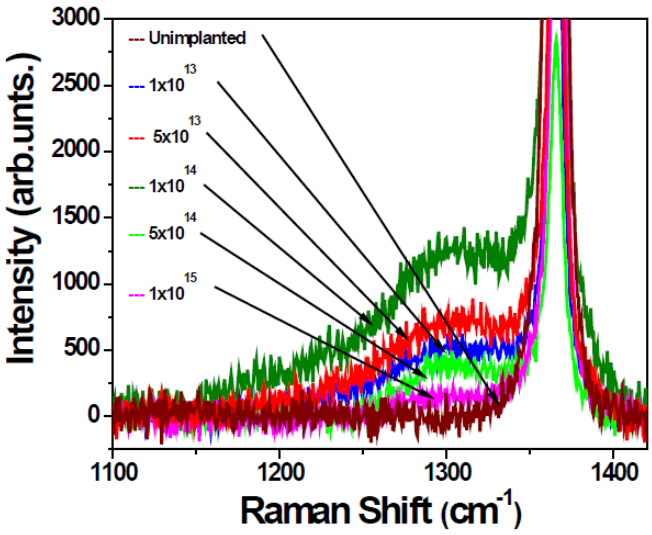

Figure 5.36: *Raman spectra for h-BN sheet before implantation and implanted with nitrogen ions implanted at the energy of 150 keV and fluence of (a) 1×10^{13} ions/cm^2, (b) 5×10^{13} ions/cm^2, (c) 1×10^{14} ions/cm^2, (d) 5×10^{14} ions/cm^2* (e) *1×10^{15} ions/cm^2.*

Implantations were carried out under similar conditions of fluence and energy

Table 5.4: *A summary of the nc-BN peak characteristics for h-BN sheet samples implanted with nitrogen ions at 150 keV.*

Fluence (ions/cm^2)	Peak position (cm^{-1})	FWHM (cm^{-1})	$I_G I_L$
5.0x10^{13}	1295	125	0.043
1.0x10^{14}	1298	100	0.052
5.0x10^{14}	1292	85	0.031
1.0x10^{15}	1285	135	0.024
5.0x10^{15}	1279	142	0.013
1.0x10^{16}	1273	153	0.008

as those used in B, Li and He implantations. The lowest fluence of 1×10^{13} ions/cm^2 was used since an optimum had not been realized even at the 1×10^{14} ions/cm^2, which was the lowest fluence used for the other ions. Figure 5.36 represents the spectra for the samples implanted with nitrogen ions at different fluence. Like boron, nitrogen also induced stress into the *h*-BN matrix to form the n*c*-BN symmetry evident from the LO vibrational phonon mode. The new peaks are observed after at 1295 cm^{-1}, 1300 cm^{-1}, 1302 cm^{-1}, 1289 cm^{-1} and 1270 cm^{-1} for the respective fluences. Table 5.4 gives a summary of the n*c*-BN LO peak details, created after implantation.

Figure 5.37 represents the relationship between the normalized intensity and the linewidth as a function of the implantation fluence for N implants. The normalized intensity for these peaks increases with increasing fluence attains an optimum at 1×10^{14} ions/cm^2 and any increase in fluence lead to a decrease in the normalized intensity. The optimum fluence was found to be lower to that of boron's 5×10^{14} ions/cm^2, however the intensity at this fluence is lower as compared to the peak intensity for boron's optimum fluence at similar energy. The overall comparison also shows that for similar fluences, boron gave better results with higher intensities and symmetric linewidth compared with nitrogen.

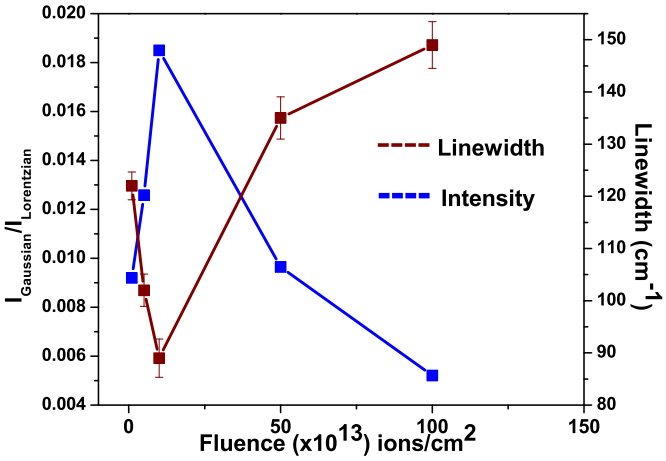

Figure 5.37: *Relationship between the linewidth and normalized intensity for the LO nc-BN Raman peaks as a function of the fluence for samples implanted with nitrogen ions.*

5.7.2 Argon Ion Implantation

Argon ion implantation was carried out in order to determine the effect of much higher mass ion implantation. Implantation was carried out on polycrystalline *h*-BN sheet samples using argon ions at different energies and fluences. The energy range remained the same as for all the other ions i.e. from 40 to 150 keV for consistency. The fluence however was chosen according to the trend seen for the other ions. Since the implantation effect optimum was obtained at lower fluence with increasing ion mass, the fluence for argon was much lower as compared to the other ions. The range was from 1×10^{13} ions/cm^2 to 1×10^{15} ions/cm^2.

Figure 5.38 represents the spectrum for the samples that were implanted with argon ions at various fluences at 150 keV and figure 5.39 represents the Raman spectra for samples that were implanted by argon ions at different energies with a fluence of 1×10^{13} ions/cm^2.

The major observation in both figure 5.38 and 5.39 is the principal *h*-BN peak, still present after implantation also observed for the other implants implying that

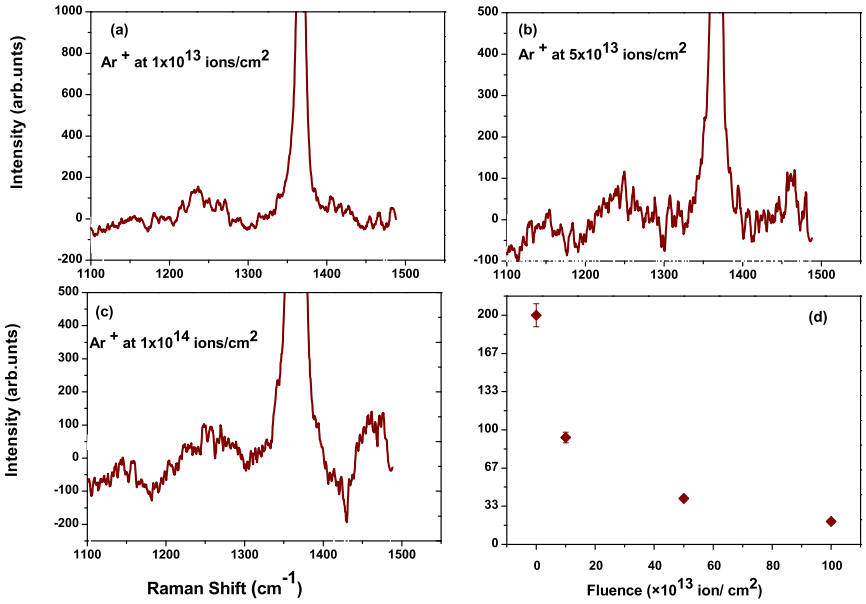

Figure 5.38: *Raman spectroscopy for h-BN samples implanted with argon ions at 150 keV with various fluences (a) 1.0×10^13 (b)5.0×10^13, and (c)5.0×10^14 ions/cm^2 (d) represents the relationship between the intensity of the nc-BN LO peaks with fluence.*

the material remains predominantly *h*-BN after implantation.

Observed in the spectra are broad features at wavenumbers 1236 cm^{-1}, 1249 cm^{-1} and 1247 cm^{-1} after implantation showing a larger shift than previously used ions if we also consider them to be from the LO peak for n*c*-BN vibrational symmetry. The features at these wavenumbers have broad FWHM and with low intensities and large shifts as compared to the other ions used for similar fluences and energies. The broad features observed after implantation with 1×10^{13} ions/cm^2 and 5×10^{13} ions/cm^2 were are consistent with n*c*-BN LO vibrations. Argon being a much heavier ion as compared to the ions used previously is likely to create a large defect concentration and hence more stress to the material at these fluences which is beyond the threshold for the stress that leads to the *c*-BN symmetry. The estimated n*c*-BN amount for argon is found to be extremely low for the fluence levels used in this work. We therefore propose that in order to get the same effect,

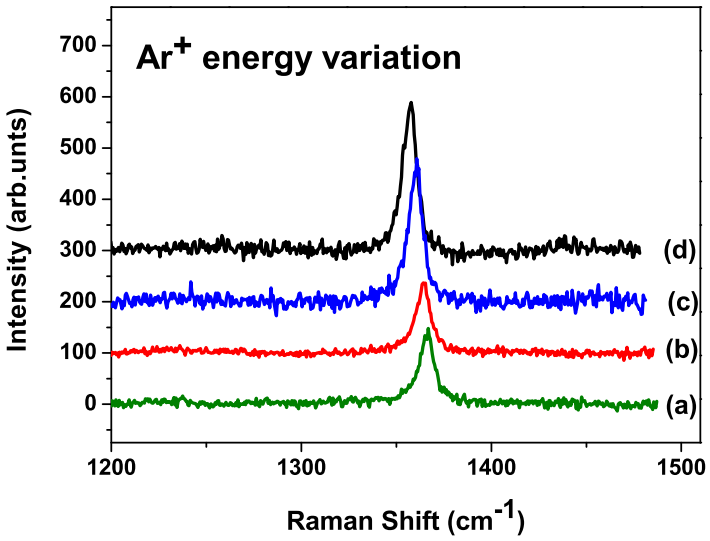

Figure 5.39: *Raman spectroscopy for (a) the unimplanted samples and (b, c, d)implanted with argon ions at various energies (b) 40 keV, (c) 80 keV and (d)150 keV at 1.0×10^{13} ions/cm^2.* The spectra are for the principal h-BN peak

lower fluence implantation should be used in future research. Figure 5.38(d) shows how the intensity of the n*c*-BN LO peak decreases exponentially with increasing fluence.

It is interesting to note the behavior of the *h*-BN peak after Ar implantation. The nature of this peak is dependent on the implantation fluence and energy. To begin with, the intensity of the peak reduces drastically with increasing fluence. At the highest fluence of 1×10^{15} ions/cm^2, the intensity reduces in the order of about 10,000 units compared to the unimplanted sample's spectrum. The peak's linewidth also increases with varying fluence. Similar trends are observed for energy variation with respect to the integrated peak intensity where the intensity of the principal *h*-BN peak which reduces exponentially with increasing energy at a constant fluence. The *h*-BN peaks show frequency shifts of 1 cm^{-1}, 3 cm^{-1} and 5 cm^{-1} for (a) 40 keV, (b) 80 keV and (c) 150 keV respectively.

Argon ions induce a high radiation damage, hence the high stresses influence the h-BN vibration more as compared to the other lighter ions. This agree well with SRIM simulations which show the damage density of argon ions in h-BN being very high as compared to boron for example, of the order of 1000 vacancies/cm ^{3}. From this it is concluded that argon ions introduces too much radiation damage in h-BN at the fluences and energy ranges used in this research. Similar observations were made for polycrystalline rod and single crystal h-BN samples.

5.8 Summary

A summary of all the Raman spectroscopy results are presented herein. Both polycrystalline and single crystal samples were used in this work. Different ions were used in these investigations including helium, lithium, boron, nitrogen and argon which were implanted at different ion energies and fluences. These ions were used to investigate the effect of varying the ion mass during the implantation process. Other parameters that were investigated were the dependence of the Raman peak shifts and intensity with respect to the wavelength and power of the incident Raman light.

The unimplanted Raman spectra always showed that both single crystal and polycrystalline sample were homogenous h-BN with high quality and with insignificant internal stress. After implantation there were changes to the spectra of the samples. First, the h-BN main peak broadened and reduced in intensity as a result of radiation damage that caused stress in the material. Besides the changes in the h-BN peak, new peaks are also observed after implantation. The position of these features have been attributed to the LO peaks found in c-BN indicating that the defect concentration induced a volumetric strain/stress at shallow regions of the

h-BN sample. This intrinsic stress in turn caused the buckling of the interplaner bond and a subsequent reconstruction to the *c*-BN symmetry. The nature and extent (asymmetrically broadened with low intensities and a low frequency peak shift) of these features indicate that they are nanostructures of *c*-BN.

The nature of the LO *c*-BN peak was investigated with respect to the different parameters. This section gives a comparison for all the ions used. Results for argon ions are not presented herein because Ar implanted samples gave very low signal to be compared with the other ions. Figure 5.40 represents the relationship between the integrated intensity *c*-BN LO peak and the ion fluence for the first three ions with lowest ion mass.

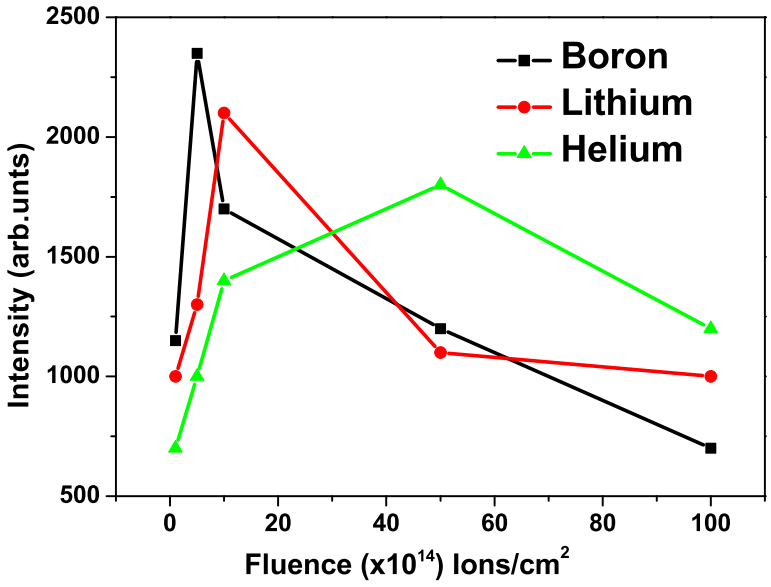

Figure 5.40: *Relationship between the intensity of the nc-BN LO peak with the ion fluence for helium, lithium and boron ions for h-BN sheet samples implanted at 150 keV [204].*

All the three ions show similar trends with varying ion fluence i. e. there is an increase in the intensity with increasing ion fluence, which then attains an optimum for a particular fluence and then reduces further with increasing fluence. The maxima are attained at 5×10^{15} ions/cm^2, 1×10^{15} ions/cm^2, 5×10^{14} ions/cm^2

and 1×10^{14} ions/cm^2 for helium, lithium, boron and nitrogen respectively. There is a shift in the optimum fluence to lower values with increasing mass number. In other words, the maximum sp^3 symmetry production is attained when there is some threshold amount of defect concentration to cause sufficient stress in h-BN sp^2 symmetry which is dependent on the incident ion mass. It is inferred then that with lighter ions more ions are required compared to a heavier ion to produce a close to or similar structural change to the h-BN sample. The ratio I_G/I_L roughly estimates the amount of c-BN in the implanted sample [122] with I_G being the integrated intensity for the c-BN LO mode peak as a Gaussian fit and I_L the integrated intensity for the principal h-BN peak fitted as a Lorentzian fit. All the estimates were calculated for the normalized intensity (normalized with respect to the intensity of the principal h-BN peak sample) at the optimum fluence of each ion. Boron ion at its optimum fluence, gave the highest ratio, followed by nitrogen then lithium and finally helium produced. A summary of all estimations for the amount of c-BN present for each ion at various fluences is given in table 5.5.

Table 5.5: *The relationship between the estimated percentage amount of c-BN and the optimum fluence for the different ions. The values in bold indicate the amount at optimum value.*

Fluence	Estimated Amount (I_G/I_L)			
	He	Li	B	N
5.0x10^{13}	0.008	0.015	0.033	0.043
1.0x10^{14}	0.015	0.019	0.045	**0.052**
5.0x10^{14}	0.019	0.033	**0.062**	0.031
1.0x10^{15}	0.023	**0.042**	0.032	0.024
5.0x10^{15}	**0.032**	0.025	0.020	0.013
1.0x10^{16}	0.025	0.018	0.012	0.008

Figure 5.41 shows the graphical representation for the relationship between the normalized intensity of the LO nc-BN (expressed as percentage) in the sample after

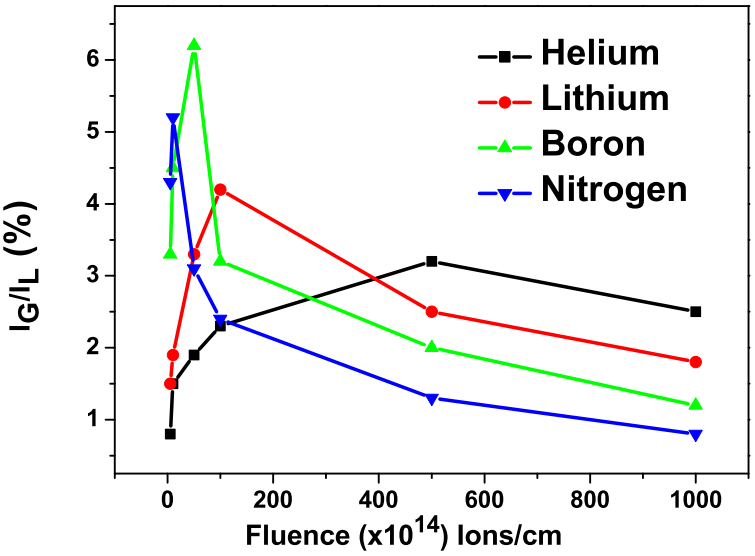

Figure 5.41: *Comparison between the estimated c-BN amount (expressed as %) and the ion fluence for helium, lithium, boron and nitrogen ions.*

implantation with different ions at different fluences. Of all the four ions, boron at the optimum fluence gave the highest amount of about 6.2% followed by nitrogen at 5.2%. Lithium was next at 4.2% while helium had the lowest amount of 3.2%.

The amount of *c*-BN produced is an underestimation. The penetration depth of the laser light is approximately 1 μm while the implanted depth is approximately 0.5 μm for boron for example, therefore the intensity of *h*-BN will always be larger compared to that of *c*-BN.

It is possible to calculate the intensity of the laser light as it penetrates the *h*-BN material using

$$I = I_o exp^{-}\mu x \tag{5.8.1}$$

where I_o is the initial laser intensity , μ the absorption coefficient for *h*-BN and x the penetration depth.

For the penetration depth of 1 μm, with the initial laser intensity being 20 W/m^2 the intensity reduces to 0.0075 W/m^2, while at 0.5 μm, the intensity will

have reduced to 0.012 W/m^2. This intensity at 1 μm still contributes to the Raman scattering seen in the spectra. We cannot consider the intensity at with respect to the implantation depth since other factors such as the ion mass, the fluence and energy have to be considered as well making this method a complex.

Boron and nitrogen ions thus gave the best results as compared to the other ions. One of the reasons may be due to the fact that they are part of the atomic species of boron nitride and as a result they do not alter the composition of the material. Boron defects are is known to have a low formation energy in h-BN to favour the formation of the c-BN structure [13].

Energy variation for all the ions used was also studied. The most common observation for all the ions with regards to energy is the frequency shift to low wavenumbers and the broadening of the c-BN linewidth with increasing energy, and an increase in the integrated intensity with increasing energy. It is found that the nc-BN integrated intensity for all the ions used increases with increasing energy. Implantations carried out at different fluences and energy show that altering the energy does not affect the optimum fluence for any ion.

5.9 Fourier Transform Infrared Spectroscopy (FTIR)

Fourier Transform Infrared Spectroscopy was used in the identification of the local structural order and composition of the samples before and after implantation. The mid infrared spectral region (2500-400 cm^{-1}) was used for all characterization of samples in this work, with all analyses carried out at room temperature. Fourier Transform IR like Raman spectroscopy has the ability of identifying the chemical bonds and functional groups in boron nitride since the hybridization states i.e. sp^2 and sp^3, of B-N atomic bonds can be easily differentiated though a well defined absorption band in a given sample. All FTIR analyses were carried out on polycrystalline *h*-BN sheet samples using the Bruker TENSOR 27 Infra-Red Spectroscope located at the University of the Witwatersrand.

This method was used to determine the change in *h*-BN after implantation with different ions. The IR active mode for *h*-BN is at the center of the Brillouin zone Γ given as,

$$\Gamma = A_{2u} + E_{lu} \tag{5.9.1}$$

where E_{lu} and A_{2u} are the vibrational modes active in the infrared spectral region for *h*-BN.

5.9.1 Unimplanted sample

Figure 5.42 represents the spectrum for *h*-BN samples before implantation. The samples were mechanically polished to thickness of 0.05 mm. The spectrum shows two distinct peaks at 776 cm^{-1} and 1378 cm^{-1}. These peaks represent the transverse optical modes for *h*-BN also reported in literature [205, 206]. The peak at 1378 cm^{-1} represents the E_{lu} mode which corresponds to the in-plane B-N bond

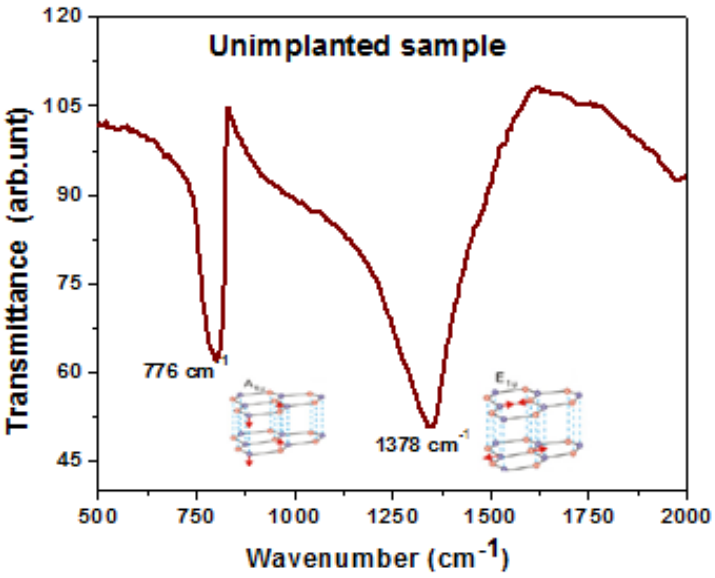

Figure 5.42: *FTIR spectrum for h-BN sheet samples before implantation.*

stretching vibration and the peak at 776 cm^{-1} represents the A_{2u} mode which is due to the out-of-plane B-N-B sp^2 bond bending vibration for BN in equation 5.9.1.

Depending on the synthesis conditions, *h*-BN has shown a range of values in the location of these vibrational modes, i. e. 770-810 cm^{-1} for the A_{2u} mode and 1360-1400 cm^{-1} for the E_{lu} mode [207, 208]. No other vibrational mode was observed in the spectrum and so it was concluded that the sample is purely *h*-BN.

Other phases of BN also exhibit IR vibrational modes at different wavenumbers: for instance, the *r*-BN exhibits a vibrational mode very close to the *h*-BN mode at 1375 cm^{-1} and the *w*-BN has its mode centred at 1267 cm^{-1} [64, 209]. Cubic BN exhibits vibrational mode centres given in equation 5.9.2. The mode represents the Transverse Optical (TO) infrared vibration for *c*-BN that is due to B-N bond stretching at the Brillouin centre at *q=0*.

$$\Gamma = T_2 \tag{5.9.2}$$

The vibrational mode occurs at different frequency positions depending on the purity, grain size and stress level in the c-BN material under investigation. For pure c-BN with minimum internal stress, the vibrational mode occurs at centres between 1000-1010 cm^{-1} [210]. This has been largely seen for samples prepared as thin films by CVD and PVD techniques. For bulk c-BN sample with micro-crystal size, the vibrational mode is centred at about 1050-1070 cm^{-1} [193]. This mostly occurs for c-BN samples prepared by the HPHT technique. The shift is due to the residual compressive stress experienced by the material during the synthesis process. When the c-BN product is nanosized, the vibrational centre occurs at about 1090-1110 cm^{-1}, mostly for samples prepared by techniques such as magnetron sputtering and Low-Temperature Low-Pressure conditions [211, 212].

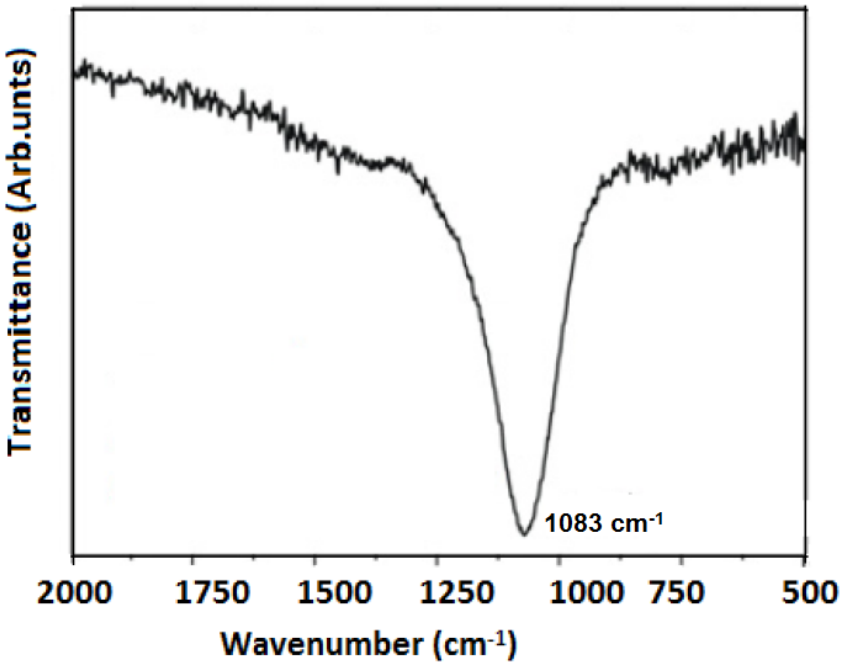

Figure 5.43: *FTIR spectrum for c-BN powder sample.*

Figure 5.43 represents the IR spectra for the c-BN powder sample previously analyzed by Raman. It shows a vibrational mode at 1083 cm^{-1}. Of interest to this

work, are the changes that occur to the *h*-BN spectrum after implantation.

5.9.2 Ion mass variation

Boron Implanted

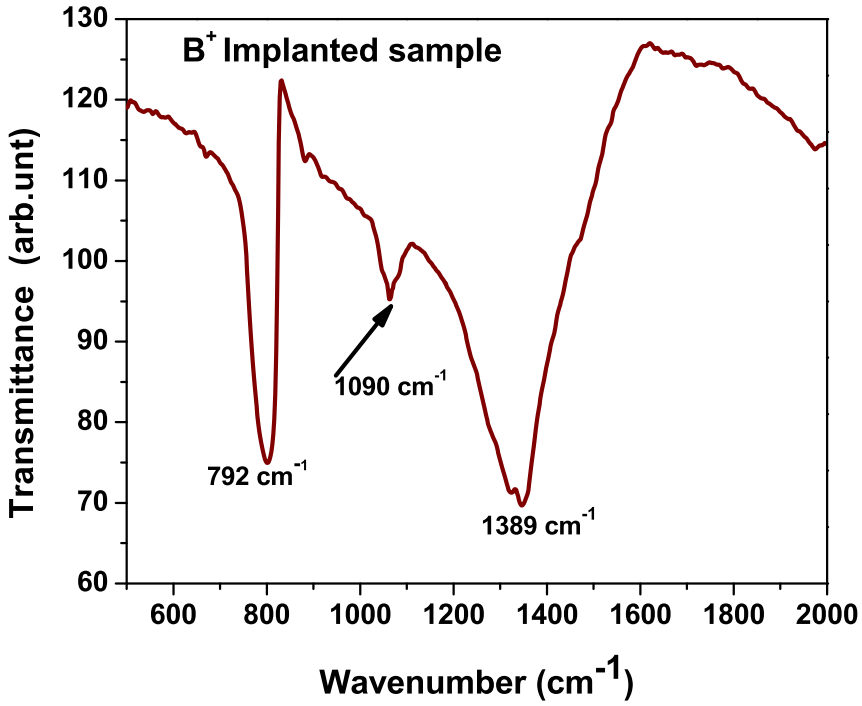

Figure 5.44: *FTIR spectrum for h-BN sheet samples after implantation with boron ions at 150 keV and fluence of* 5×10^{14} *ions/cm*^{2}.

Figure 5.44 shows the infrared transmission spectrum for samples that were implanted with boron ions at fluences of 5×10^{14} ions/cm^2 at 150 keV. This fluence was chosen since it gave the optimum fluence for boron implants with Raman analyses. The spectrum shows two distinct vibrational modes corresponding to the A_{2u} and E_{lu} IR modes for *h*-BN samples also observed in the pristine sample.

A closer look at the *h*-BN peaks indicate that there is a frequency shift to high wavenumbers in the out-of-plane stretching mode from 1378 cm^{-1} to 1389 cm^{-1}

and the in-plane bending mode from 776 cm^{-1} to 792 cm^{-1}. The shift in the in-plane mode is as a result of ion induced hybridization alteration to other crystalline orders as a result of the implantation. The transmission intensity of these peaks shows a high intensity even after implantation showing that the material is still largely *h*-BN.

There also occurs a new peak in the spectrum centred at 1090 cm^{-1}. The peak has a weak intensity as compared to the *h*-BN peaks, and it has a FWHM of 30 cm^{-1}. Considering the vibrational modes for BN, this peak is related to the *c*-BN vibrational mode also seen by [211]. The peak position is shifted by up to 40 cm^{-1} in comparison with the vibrational modes for bulk *c*-BN [193] and it is similar to the mode exhibited by nanosize *c*-BN crystal reported by [212], hence we can attribute it to having originated from n*c*-BN symmetry formed after implantation. There is also a small peak at around 884 cm^{-1}, whose origin is unknown and a split on the *h*-BN peak at 1378 cm^{-1} (discussed later).

Lithium and Helium Implanted

Fourier Transform IR was also carried out on samples that were implanted with lithium and helium ions. Lithium samples investigated were implanted at 150 keV with the fluence of 1×10^{15} ions/cm^2 which was the optimum fluence for all lithium implants as analyzed by Raman. Figure 5.45 represents the FTIR spectrum for lithium implanted sample.

The spectrum shows the A_{2u} and E_{lu} IR *h*-BN features at 780 cm^{-1} and 1385 cm^{-1} having a shift of 4 and 7 cm^{-1} respectively from the unimplanted sample. In addition to these peaks, there is a new feature emerging at 1096 cm^{-1} and 1113 cm^{-1} respectively. The origin of the peak at 1096 is most probably due to *n*c-BN. The origin of the peak at 1113 cm^{-1} is also proposed to be due to *n*c-BN with a

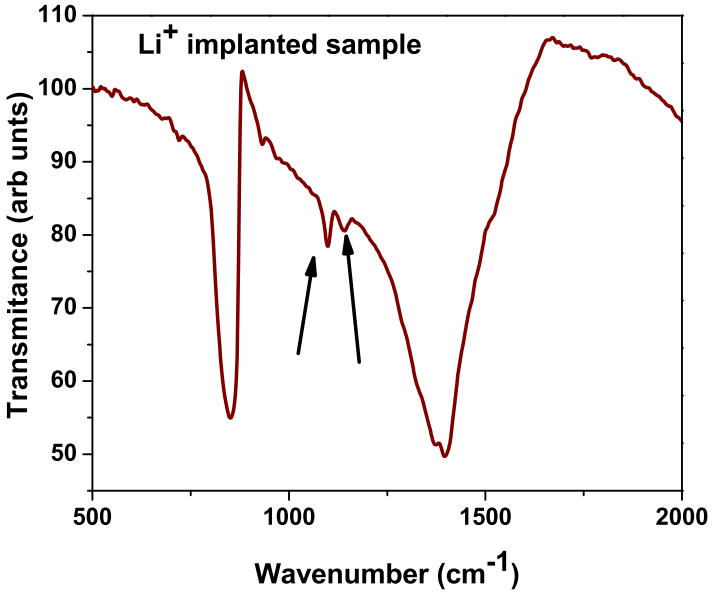

Figure 5.45: *FTIR spectrum for h-BN sheet samples after implantation with lithium ions at 150 keV and fluence of* 1×10^{15} *ions/cm*^{2}.

shift of 10 cm^{-1}. The reason for the split in the *c*-BN vibrational mode in figure 5.45 is not yet known.

Figure 5.46 represents the spectrum for samples that were implanted with helium at 150 keV and fluence of 1×10^{15} ions/cm^2 which was the optimum fluence for all helium implants in Raman. The A_{2u} B-N-B bending and E_{lu} IR B-N bond stretching *h*-BN vibrational features are still visible at 780 and 1382 cm^{-1} respectively having a smaller shift of 6 and 4 cm^{-1} respectively with reference to the unimplanted sample. A new weak feature is also observed at 1113 cm^{-1}.

Discussion

All the *h*-BN peaks show a shift to higher wavenumber almost linearly with increasing implantation ion mass. Since a peak shift is associated with the increase in compressive stress within the material, it implies that B, which has the highest

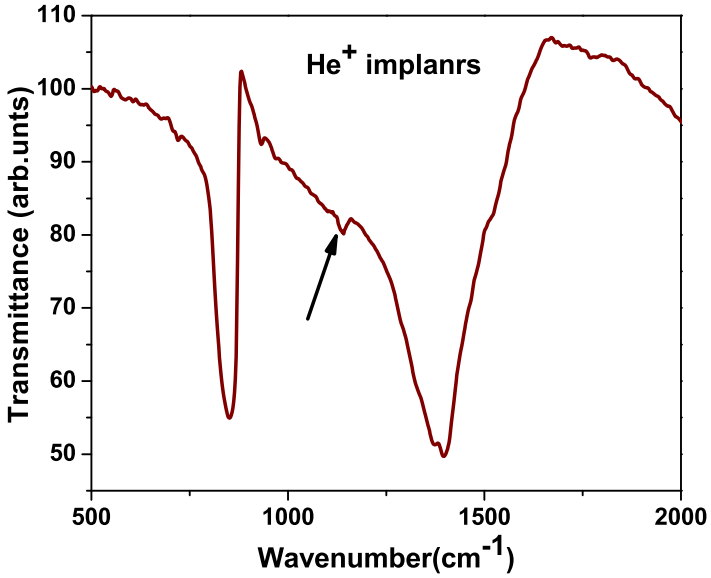

Figure 5.46: *FTIR spectrum for h-BN sheet samples after implantation with helium ions at 150 keV and fluence of* 5×10^{15} *ions/cm*^{2}.

mass introduced more defects and hence large compressive stress into the *h*-BN matrix as compared to lithium and helium.

In all the implanted spectra, it is observed that the *h*-BN at 1380 cm^{-1} has been split into two as seen in the spectra centred around the region of interest in figure 5.47. The new mode is centred at 1362 cm^{-1}. This peak appears as a shoulder with very low intensity and wide linewidth. This work associates the existence of this new peak with the presence of a *r*-BN phase in the sample after implantation. Rhombohedral BN vibrational studies have shown that it exhibits similar modes as those of *h*-BN, as such it will have its peak centred very close to the E_{lu} mode for *h*-BN [64]. The existence of this *r*-BN IR mode, which is due to the vibration of B and N between the planes, has been found to have the same atomic displacement as the E_{lu} IR mode for *h*-BN at 1380 cm^{-1} and commonly occurs close to this position in IR. After implantation we see the new peak at 1362

cm^{-1} and therefore suggest it is due to r-BN phase. Rhombohedral BN normally occurs as a transitional phase during the h-BN to$c$-BN phase transformation and it is possible that traces of it also exist after ion implantation. This phase is however not visible in Raman; this may be due to the fact that, in Raman, it is a challenge to differentiate between the different phases of BN with similar hybridization i.e. r-BN and h-BN (sp^2).

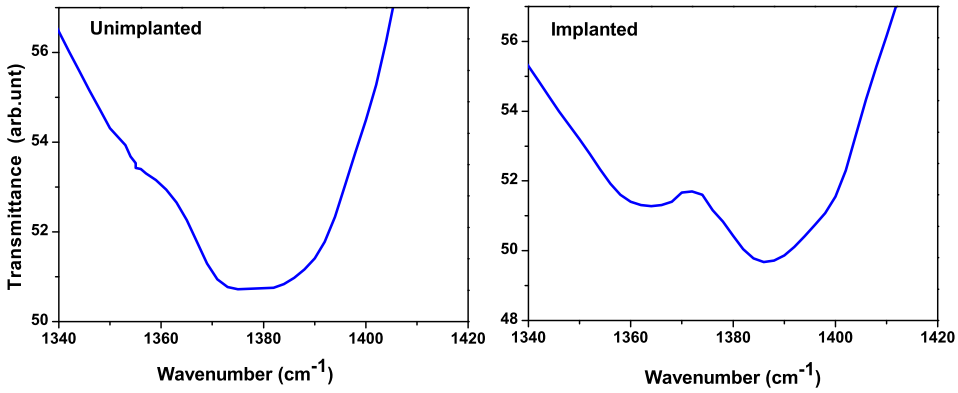

Figure 5.47: *Fourier Transform IR for h-BN sheet sample (a) unimplanted and (b) implanted with boron at 150 keV and fluence of* 5×10^{14} *ions/cm*^{2}.

5.9.3 Fluence dependence

A fluence dependence for the different ions was carried out on the samples and FTIR analyses carried out on them. Figure 5.48 and 5.49 represents FTIR spectra for samples that were implanted with boron and lithium ions at different fluence. A fluence variation graph for helium was not shown however a comparison with the other ions is shown later in this section. For each ion used at different fluences, the nc-BN vibrational mode are observed with the nature and extent of these peaks being dependent on the fluence.

Figure 5.48 represents the spectra for the samples implanted with boron at different fluences. The spectra have been plotted around the region of interest, cutting

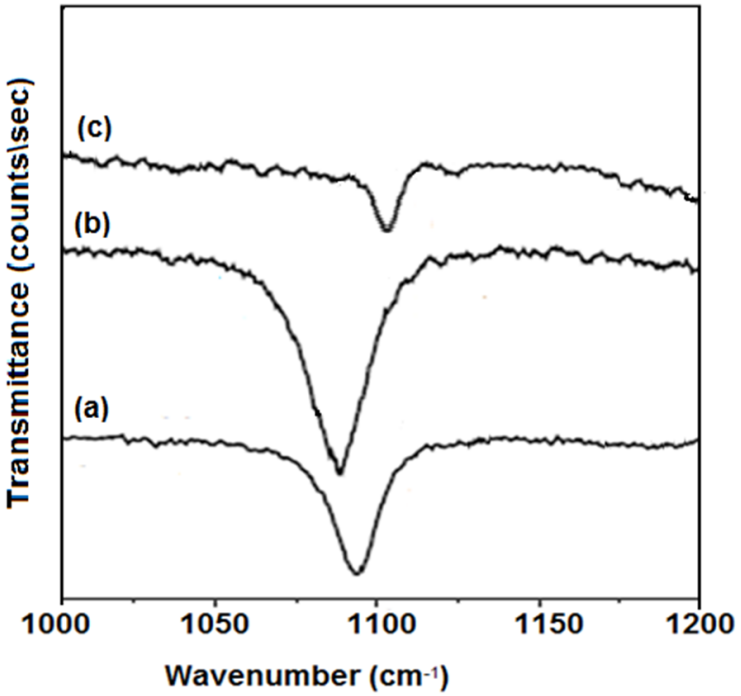

Figure 5.48: *FTIR spectrum for h-BN sheet samples after implantation with boron ions at 150 keV with various fluences (a) 1×10^{14} ions/cm^2, (b) 5×10^{14} ions/cm^2 and (c) 1×10^{15} ions/cm^2*, showing the nc-BN modes.

off the two *h*-BN modes, to clearly view the details of the *c*-BN vibrational mode. The peaks appear at (a) 1095 cm^{-1}, (b) 1090 cm^{-1} and (c) 1103 cm^{-1} for the respective fluences as shown in the diagram. It is clear that the transmittance intensity is highest for implantation carried out at 5x10^{14} ions/cm^2 and lowest for the highest fluence of 1x10^{15} ions/cm^2. The peaks slightly shift to higher wavenumbers moving away from the optimum fluence. This implies that the n*c*-BN symmetry is created in the *h*-BN matrix at a certain optimum stress level related to a specific defect density below and beyond which the *c*-BN nanoparticles created cannot be detected by the IR signal. These results correspond well with the results from Raman spectroscopy with the optimum being 5x10^{14} ions/cm^2 in both analyses.

Figure 5.49 shows the FTIR spectra for lithium ions also implanted at different

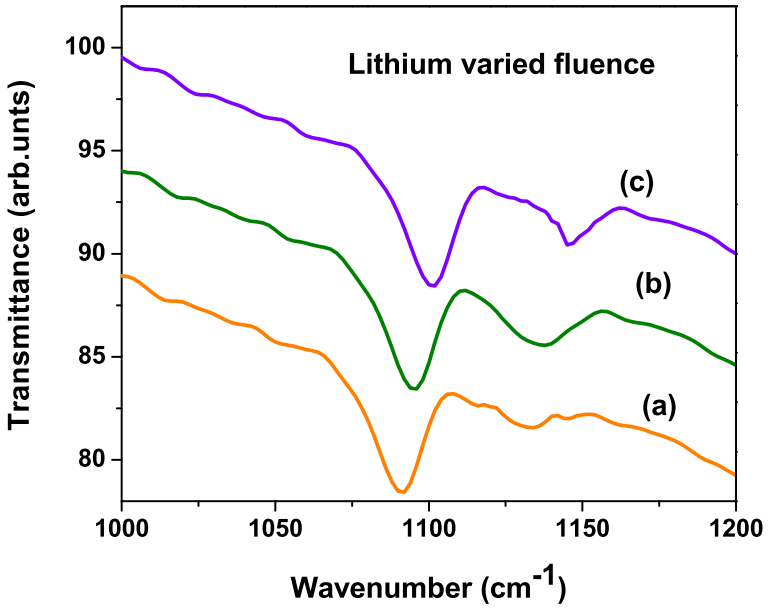

Figure 5.49: *FTIR spectrum for h-BN sheet samples after implantation with lithium ions at 150 keV with various fluences (a) 5x10^{14} ions/cm^2*, (b) 1x10^{15} ions/cm^2 and (c) 5x10^{15} ions/cm^2.

fluences. At the optimum fluence i. e. 1×10^{15} ions/cm^2, the spectrum has a two peak at 1096 and 1113 cm^{-1}, while at low fluence 5×10^{14} ions/cm^2, there is only a single *c*-BN at 1092 cm^{-1}. At 5×10^{15} ions/cm^2, there is a small peak at 1135 cm^{-1} together with the main *c*-BN peak at 1102 cm^{-1}. Also generally observed here is a systematic upward frequency shift with increasing ion fluence.

In summary, figure 5.50(a) represents the relationship between the peak position and the ion mass and while (b) shows the relationship between the intensity and the ion mass for the *c*-BN peaks, all taken at the optimum fluence for each ion (All lithium comparison data were from the intense peak after implantation). For all the three ions used in these experiments, the analyses shows an additional vibrational mode after implantation. The peaks are centred at 1090 cm^{-1} for boron, 1098 cm^{-1} for lithium and 1113 cm^{-1} for helium ions. The position of these peaks correspond to the position of the TO vibration mode for nanocrystalline *c*-BN. The nature

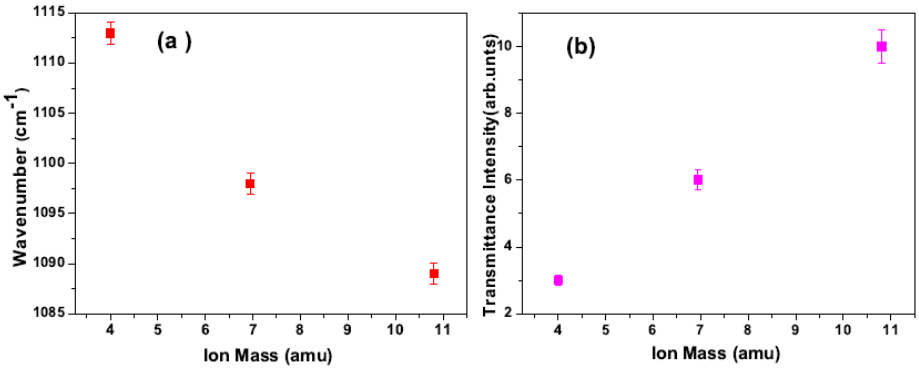

Figure 5.50: *(a) The relationship between the c-BN TO vibrational mode position with the ion mass and (b) the relationship between the transmittance intensity and the ion mass at optimum fluence.*

and extent of the peak depends on the ion mass, with the boron peak being the highest, followed by lithium and then helium. In addition to boron having the highest intensity, its peak is more symmetric with narrow FWHM. Lithium shows another peak at 1130 cm^{-1} whose origin is also likely due to nc-BN with smaller crystallites since this at this wavenumber it lies within the range for nanocrystalline c-BN. The intensity from the sample implanted with helium is quite low with only 10 counts, with the peak being asymmetrical compared to boron and lithium IR spectra.

FTIR analysis has been used to give a quantitative assessment of volume/ amount of individual polymorphs comprised in a mixed sample. To estimate the volume of c-BN in the sample, the relative transmittance intensity, for instance the intensity at 1090 cm^{-1} (for a boron implanted sample) was normalized with respect to the h-BN B-N stretching bond intensity at 1382 cm^{-1} [64]. This volume can be calculated as the ratio of the intensities of the cubic phase and the sum of the cubic phase and the hexagonal phase in the transmitted spectrum, given as

$$\%_{c-BN} = \frac{I_{c-BN}}{(I_{c-BN} + I_{h-BN})} \times 100 \quad (5.9.3)$$

Where I_{h-BN} is taken at the B-N stretching vibrational mode of the principal *h*-BN.

To obtain the normalized peak intensities, the *c*-BN TO peak data were fitted using the Gaussian fit and the estimated volume calculated with respect to the *h*-BN peak for an unimplanted sample fitted using the Lorentzian fit. The results obtained are indicated in table 5.6.

Table 5.6: *The relationship between the estimated amount of c-BN and the optimum fluence for the different ions.*

Ion	Optimum Fluence (Ions/cm^2	Estimated % amount
Boron	5.0x10^{14}	8.3
Lithium	1.0x10^{15}	4.6
Helium	5.0x10^{15}	3.7

These results show that there is an ion mass dependence at optimum fluence for each ion, of the estimated amount of *c*-BN converted in the sample. Boron ions gave the highest % yield of *c*-BN at the lowest fluence, implying that it is the best candidate to be used for the *h*-BN to *c*-BN symmetry change. These results complement the results from Raman in terms of both fluence and ion mass dependence. A graphical representation for FTIR spectra for the amount as a function of the fluence for the three different ions looks very similar to that observed for Raman, as shown in figure 5.51 in terms of the estimated amount, however in FTIR results here not all the fluences used were recorded.

The rod samples FTIR measurements were unsuccessful due to the sample thickness. Reducing this thickness was a challenge due to the nature of the sample.

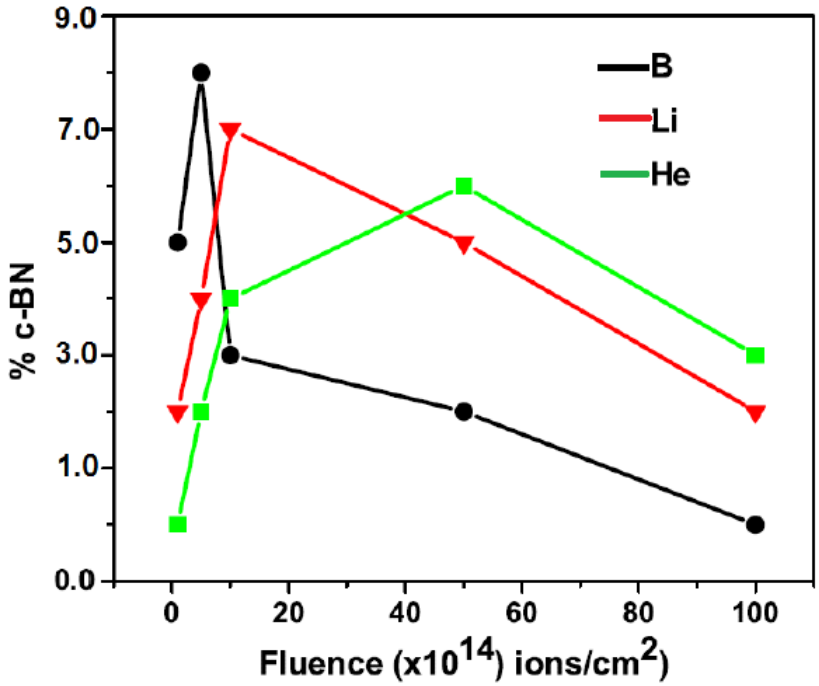

Figure 5.51: *The relationship of the estimated c-BN amount with the implantation fluence for boron, lithium and helium ions at optimum fluence as calculated by 5.9.3.*

Mechanical polishing led to crumbling of the sample below 0.5 mm. The FTIR measurements were also a challenge for the single crystal sue to their small size and the carbon tape used as a holder during implantation.

5.10 Glancing Incident X-Ray Diffraction (GIXRD)

Glancing incident XRD is a technique used to characterize and understand crystal sub-surface structure material. Contrary to the conventional XRD which gives information on the bulk structure of a given material, most of the incident X-rays arrive at a glancing angle (ω) with respect to the surface of the material. These X-rays are then scattered near the surface of the material and depending on the magnitude of the incident angle, i.e when the glancing incident angle is slightly larger than the critical angle for total reflection ($\omega_i > \omega_c$), then the reflected X-rays are able to reveal the sub-surface or buried layer information of the material under investigation [213].

From SRIM calculations, we require information on the implanted layer which is a approximately 0.5μm below the surface of the *h*-BN, therefore GIXRD is a suitable technique as compared to conventional XRD as it is able to carry out a depth profiling on the sample from the surface to the end of range of the implant by varying the glancing angle of the incident X-rays.

The GIXRD data output is given in the form of diffraction peak intensity as a function of the diffraction angle. Any material will reflect X-rays at a specific 2θ angle if the angle of incidence satisfies the Bragg's equation (discussed in appendix 2). Each diffraction peak corresponds to a particular set of Miller indices that are used to identify different planes of material which in turn are used to analyze the crystal structure details such as the lattice parameter, hence assisting in the identification of material under investigation.

The measurements were carried out on *h*-BN before and after implantation using the D8 ADVANCE Bruker X-ray Diffractometer located in the School of Chemistry, University of the Witwatersrand. The diffractometer is equipped with

CuKα radiation of λ=1.504 $\mathring{A}$, operating at a voltage of 40 kV and 40 mA current. The analyses were carried out for various incident angle ranging from ω_i=0.05^o to ω_i=1.50^o, with the recording made step-by-step from 2θ=20^o to 2θ=90^o, in steps of 0.02^o with accumulated time of 5s per step, amounting to a total time of 4 hours for a single run.

5.10.1 Unimplanted *h*-BN Samples

Figure 5.52 (a) represents the GIXRD spectrum for a virgin sheet sample, which was analyzed at an incident angle ω_i=0.1^o. The diffraction pattern reveals several peaks at Bragg angle values 2θ=26.64^o, 41.70^o, 43.89^o, 50.03^o, 55.26^o, 75.96^o, and 82.32^o. These peaks are observed to have very narrow linewidth of 0.3^o with different intensities. The peak at 26.64^o has the highest intensity while the one at 2θ = 43.9^o has the lowest intensity. Figure 5.52 (b) is the GIXRD pattern for the polycrystalline rod sample analyzed at an incident angle of 0.3^o. Similar to the sheet sample the diffraction pattern shows various peaks at 2θ=26.52^o, 41.69^o, 44.11^o, 50.24^o, 55.16^o, 75.96^o, and 82.29^o.

he analyses of both the sheet and rod samples' peaks show diffraction angles for high quality *h*-BN crystals corresponding to the (002), (100), (101), (102), (004), (110), (011) *h*-BN planes respectively. The lattice parameter was calculated to be *a*=0.250 nm and *c*=0.667 nm, similar to the standard lattice parameters for *h*-BN as identified by JCPDS database no. 34-0421 and also seen by Saito *et al* [214] (see table 3.2). There are some other peaks at 36.08^o 39.84^o and 48.48^o present for the sheet samples which are not present in the rod samples. These peaks represent the (202), (003) and (005) planes also identified by the JCPDS database no. 34-0421. The absence of these planes in the rod sample could be as a result of different

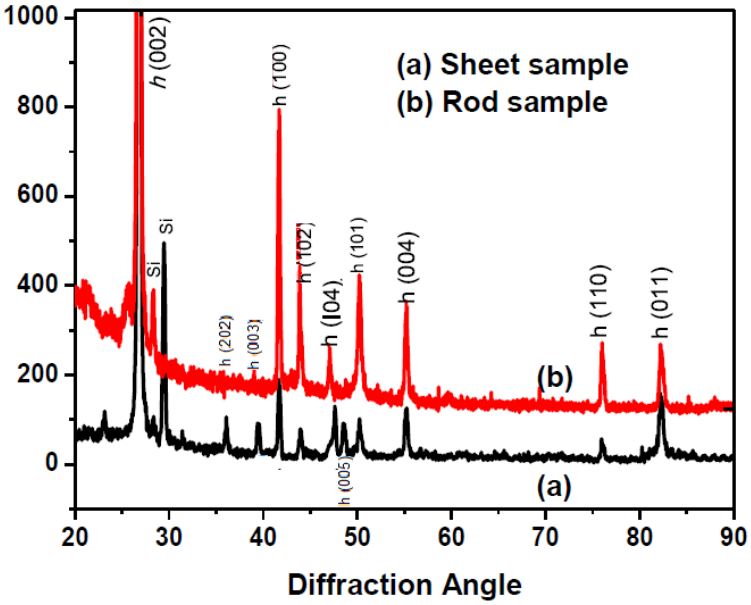

Figure 5.52: *GIXRD diffraction pattern for unimplanted (a) polycrystalline h-BN sheets, (b) polycrystalline h-BN rod sample analyzed using an incident angle of 0.3°.*

texturing between the two material because of the different sintering processes used in the samples' preparation. As such certain orientations are preferred and hence visible in the XRD diffraction pattern for the sheet samples and not in the rod samples.

All the peaks were retained even after using various incident angles indicating that both the surface and the sub-surface part of the crystal were purely *h*-BN. There is also another diffraction peak at 28.50° which is characteristic of silicon (311) diffraction peak, most likely obtained from the glass that was used as a sample holder.

5.10.2 Cubic BN GIXRD

Since we have observed cubic symmetry with the optical spectroscopies after implantation of *h*-BN which we attributed to the n*c*-BN symmetry, it is essential to investigate the XRD pattern for *c*-BN in order to relate it to the pattern after

implantation. Figure 5.53 represents the XRD diffraction pattern for c-BN that has already been analyzed by Raman and FTIR spectroscopies. Since the samples were of powder form, standard X-ray diffraction using the conventional θ- 2θ geometry was used for analysis. The analyses were carried out using the D2 PHASER Bruker X-ray Diffractometer located at the School of Chemistry, University of the Witwatersrand. The measurements were carried out in the θ- 2θ range of values from 20^o to 90^o, for 1 hour in the step size of 0.1^o counts per every 5 seconds to increase precision and consistency.

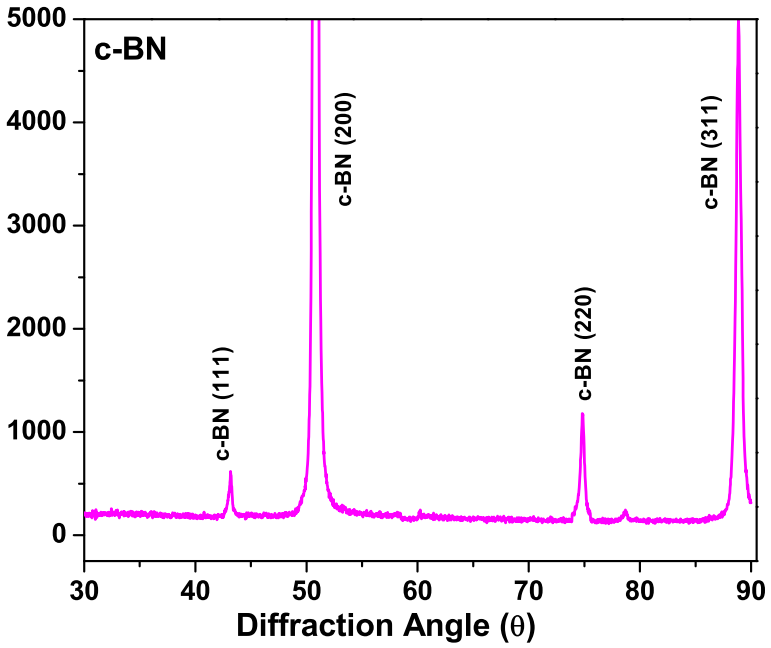

Figure 5.53: *XRD diffraction pattern for c-BN powder supplied by Element Six Company.*

The diffraction pattern shows several peaks at 2θ values of 43.79^o, 50.88^o, 74.82^o and 88.89^o. These peaks correspond to the (111), (200), (202) and (311) planes with lattice parameter calculated to be 0.3615 nm which corresponds to the c-BN lattice parameter identified by the JCPDS database (no. 35-1365). This has also been observed by other researchers [212, 215].

The FWHM of these peaks are relatively wide because of the nanosize particle size of the powder crystals in the sample. it is possible to calculate the particle size for the *c*-BN particles using the Scherrer equation. This equation relates the estimated crystal size ($D_{crystal}$) to the line perpendicular to the (hkl) plane corresponding 2θ angle and the linewidth [216]. It is given as,

$$D_{crystal} = \frac{k\lambda}{\beta_{\frac{1}{2}} \cos\theta} \tag{5.10.1}$$

where λ is the wavelength of the radiation (in this case CuKα with λ=1.504 $\mathring{A}$), k is the Scherrer's constant=0.94, $\beta_{1/2}$ the full width at half maximum of the diffraction peak, and θ the Bragg angle for the specific (hkl) plane. The particle size for the *c*-BN powder was calculated to be 120 nm. This calculations agreed well with the particle size obtained from Scanning Electron Microscopy shown in figure 5.3, showing the crystals to have an average diameter of approximately 100 nm for the smaller crystallites.

5.10.3 Implanted Polycrystalline *h*-BN rod samples

Glancing incident XRD measurements were carried out on the polycrystalline *h*-BN rod sample slice that was implanted with boron ions at 150 keV and fluence of 5×10^{14} ions/cm^2. The measurements were carried out under the same conditions as for the unimplanted, i.e. at voltage of 40 kV and current of 40 mA with 2θ range of 20-90^o in steps of 0.02^o for 5 seconds per step. Figure 5.54 represents the GIXRD diffraction pattern for the implanted sample with measurements done at the incident angle of $\omega = 0.3^o$.

The diffraction peaks for *h*-BN are observed to shift slightly by 0.2^o after implantation as compared to the unimplanted sample. The peaks also show a broadening

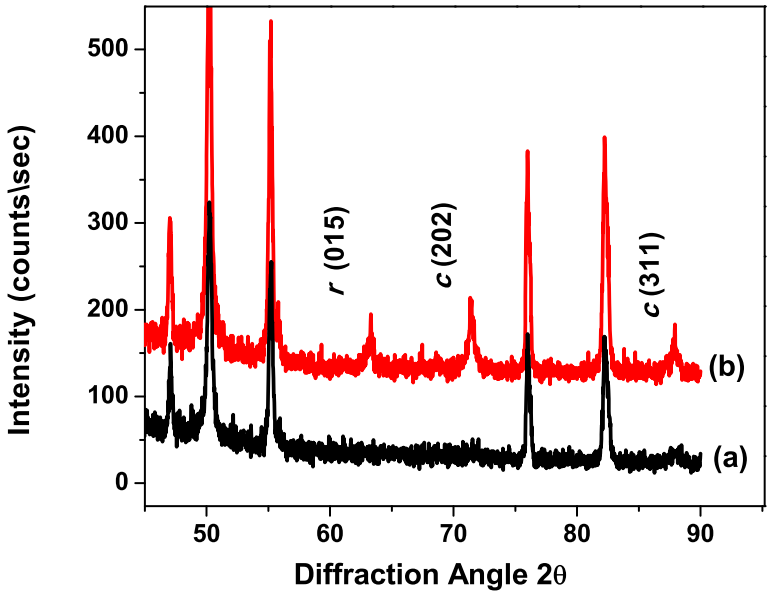

Figure 5.54: *GIXRD diffraction pattern for h-BN rod sample (a) before and (b) after implantation with boron ions at 150 keV and fluence of* 5×10^{14} *ions/cm*^{2} *at* $\omega_i = 0.3^o$.

compared to the ones before implantation. The lattice parameter was calculated to be a=0.251 nm and c=0.668 nm. These slight lattice expansions are attributed to surface stress induced atomic displacement and to point defects in the h-BN lattice as a result of the irradiation. The silicon diffraction line is also present since the same sample holder was used.

Together with these peaks, there occur three new diffraction lines at 63.69^o, 74.37^o and 89.56^o. The first line, at 63.69^o corresponds to Bragg angle values of the (015) plane for r-BN as identified by JCPDS database no. 45-117 suggesting that there are traces of r-BN symmetry induced after ion implantation, confirming a possible h-BN to r-BN symmetry change. The r-BN phase has also been observed during some of the c-BN growth processes from the h-BN phase, for example as an intermediate phase in in HPHT phase transformation [14, 83]. By ion implantation it is suggested that there is sufficient defect concentration and stress level that favoured the formation of rhombohedral symmetry which is observed by GIXRD

in this section. The r-BN vibrational mode has been observed in FTIR spectra after implantation hence the two analyses are complementary. The Raman spectrum for r-BN has been rarely observed because it exhibits a Raman shift very close to that of h-BN [217]. It is therefore difficult to distinguish between the the two spectra by Raman especially for nanocrystalline r-BN and in thin films. work.

The diffraction patterns at 74.37^o and 89.56^o correspond to the (202) and (311) planes for c-BN with the lattice parameter calculated to be a=0.3614 nm and a=0.3616 nm respectively. This corresponds with measurements done in [218], showing that the implanted sample contains the planes associated to c-BN structure. The peak at 89.56^o appears to be broader and with very low intensity compared to the one at 74.37^o. This may be so considering the indexing factor for c-BN, where the (202) plane has a higher factor and will therefore diffract X-rays with a much greater intensity as compared to the (311) plane, as given in JCPDS database no. 35-1365.

The diffraction line broadening is normally attributed to reduction in crystal size and hence the c-BN could be composed of nanoscale particle size crystals. We can calculate the tentative c-BN particles size using the Scherrer equation 5.10.1. The Scherrer equation is based on the assumption that the nc-BN formed are spherical nanoparticles. The particle size for nc-BN for the (202) plane at 74.37^o with a linewidth of 1.4^o is estimated to be 12 nm and for the (311) plane at 89.56^o the crystal size was approximately 9 nm. X-rays diffract from planes in a material, and as such it is plausible that the c-BN symmetry observed may also be as a result of nc-BN aggregated structures within the h-BN matrix formed by stress created in the material as a result of defect concentration after implantation. These results correspond synonymously with results from Raman and FTIR where nc-BN with

nanosized characteristics were observed after implantation.

Glancing incident XRD was further carried out on the same boron optimum implanted sample but with different angles of incidence ω_i from 0.1^o to 1^o. Figure 5.55 represents the diffraction pattern for the samples analyzed at the different incident angles, with (a) being the unimplanted (b) at ω=0.1 ^{o}, (c) at ω=0.2^o (d) at ω=0.3^o (e) at ω=0.5^o. The diffraction patterns for the implanted samples show all the *h*-BN peaks. Together the *h*-BN, the *r*-BN diffraction lines at around 63.50^o, and n*c*-BN peaks at around 74.30^o and 89.50^o are also visible for the four respective incident angles.

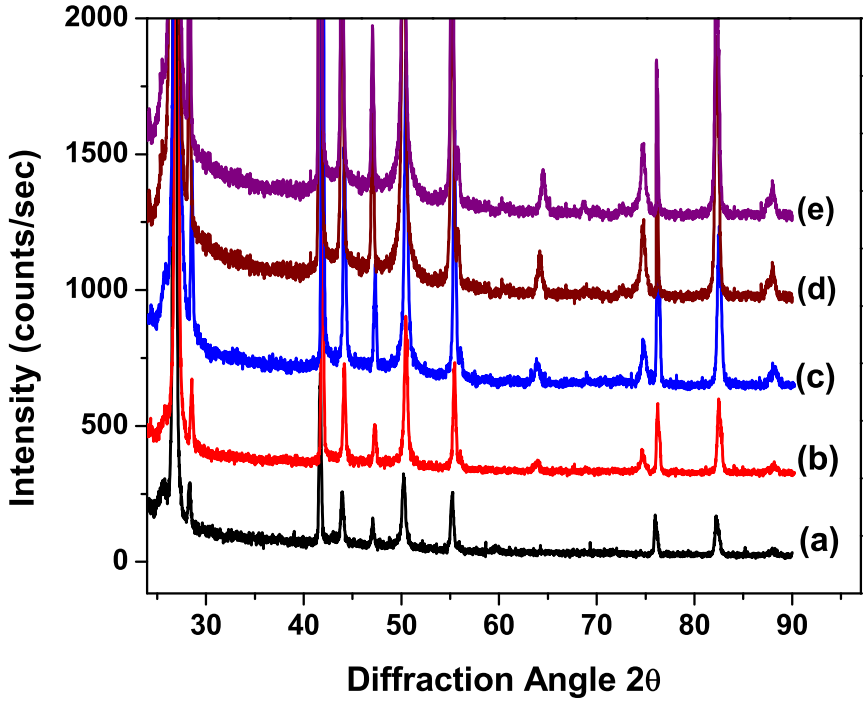

Figure 5.55: *GIXRD diffraction pattern for (a) h-BN rod sample before implantation and (b, c, d and e) after implantation with boron ions at 150 keV and fluence of* 5×10^{14} *ions/cm*^{2}*. (b) is the pattern analyzed at* ω=0.1^o*, (c) at* ω=0.2^o *(d) at* ω=0.3^o *(e) at* ω=0.5^o.

We will focus on the n*c*-BN diffraction peaks at 74.37^o since they are more intense as compared to the (311) peaks at 89.56^o. Figure 5.56 represents a graph

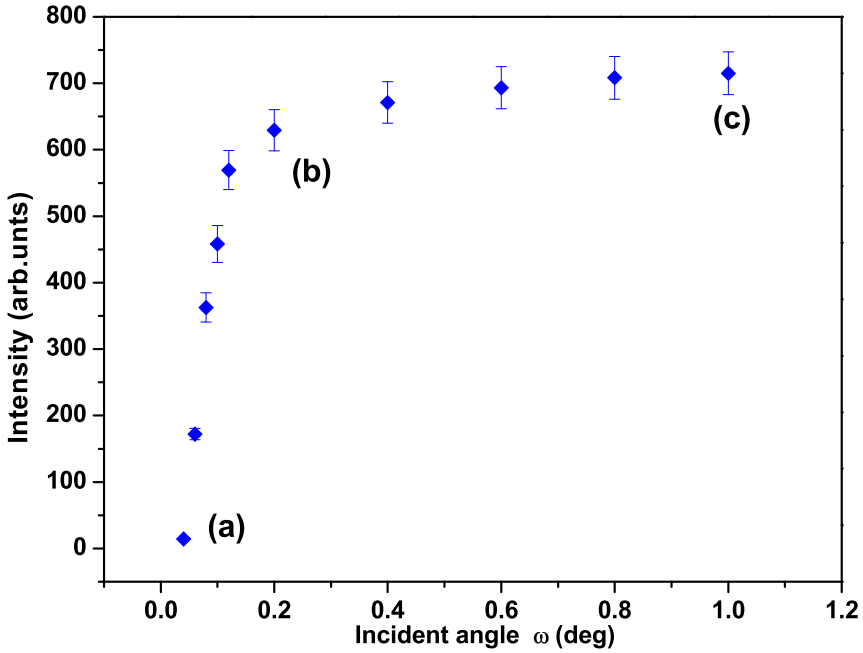

Figure 5.56: *Relationship between the glancing incident angle and the diffraction peak intensity for the c-BN (202) plane peak at 74.37°* for boron implanted samples at 150 keV and at the fluence of 5×10^{14} ions/cm^2.

of the diffraction peak intensity as a function of the incident X-ray angle. The GIXRD information depicted a sequence in the proportional yield (based on the diffraction peak intensity) of c-BN at various angles. At a shallow angle of 0.1^o, which corresponds to position (a) in figure 5.56, the peak intensity is very weak with only about 180 counts per second. The intensity then increases with increasing glancing angle and levels out at 0.3^o corresponding to position (b) in figure 5.56, after which it remains relatively constant up to 1^o as seen in position (c) of 5.56.

To understand this behaviour, we studied the theory on GIXRD, in terms of the relationship between the penetration depth of the X-rays as a function of the incident angle [214, 219] and related this to the ion range of the ions as they settle in the h-BN material using SRIM simulations. The penetration depth of the X-rays ρ can be expressed as a function of the incident angle ω_i as

$$\rho = sin\omega_i/\mu \tag{5.10.2}$$

for $\omega_i > \omega_c$ (i.e. beyond the critical incident angle edge where total reflection occurs with ω_c for h-BN being 0.14^o), μ is the linear absorption coefficient for h-BN [220].

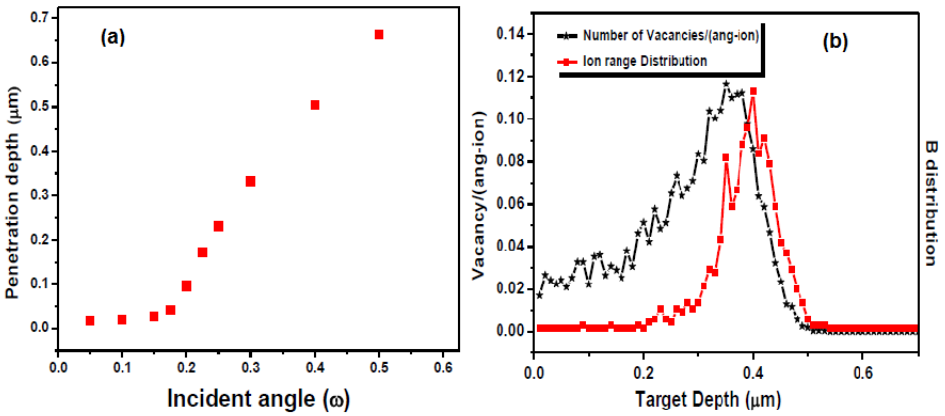

Figure 5.57: *(a) Relationship between the calculated penetration depth ρ in (microns) of incident X-rays and the glancing incident angle ω_i. (b) Is the SRIM simulation for the collision events of boron ions implanted in h-BN at 150 keV.*

Figure 5.57(a) represents the relationship between the penetration depth of the X-rays into the material as a function of the angle of incidence of the X-rays from ω_i=0 (the surface) to ω_i=2^o, calculated using equation 5.10.2. As the incident angle of the X-rays increases, the X-rays penetrate deeper into the material. This was compared with simulations from the SRIM Program as seen in figure 5.57(b). In SRIM, as boron ions come to rest within the h-BN matrix, a damage cascade is formed from the surface of h-BN to the end of range at 0.45 μm, with the projected ion range being 0.4 μm. Comparing the projected range and the X-ray penetration depth, the penetration depth of the X-rays increases rapidly with increasing glancing angle. Of interest are the events that occur from the surface up to the end of the ion range.

At low glancing angle (0.05^o) the c-BN peak has a low intensity as seen in figure 5.56. It increases with increasing glancing angle and reaches maximum at ω=0.3^o after which it remains constant up to 1^o. Comparing this to at the p-ω graph in figure 5.56 (a), at ω=0.3^o, the penetration depth is approximately 0.37 μm which according to SRIM calculations is within the implanted layer which is close to the projected range of the ions as they come to rest within the material. As such, we presume the reason for the diffraction peak intensity reaching maximum is that the diffracting volume in the entire range of the implantation contains the maximum damage where the c-BN symmetry is likely to be formed.

At incident angles greater than 0.3^o, such as at c (in figure 5.56) synonymous to the region beyond end of range of the ions in SRIM, the c-BN and r-BN X-ray diffraction intensity remains fairly constant with increasing incident angle. This is because, at higher incident angles, the sampling volume by the X-ray constitutes the entire volume of the implanted region so, the diffraction peaks originating from c-BN and r-BN will be visible having almost constant intensities even with changing incident angle at depths beyond the implantation range where the material is purely h-BN.

5.10.4 Implanted Polycrystalline *h*-BN sheets

Similar measurements were done on the h-BN sheet samples with measurements recorded form 0.01^o to 0.5^o. The measurements recorded here were obtained using similar parameters as used before.

Figure 5.58 represents the diffraction pattern for polycrystalline h-BN sheets, analyzed at 0.3^o. Figure 5.58 (a) is the pattern for angles between 40^o and 60^o, while (b) is the pattern for angles between 60^o and 85^o, for the same sample.

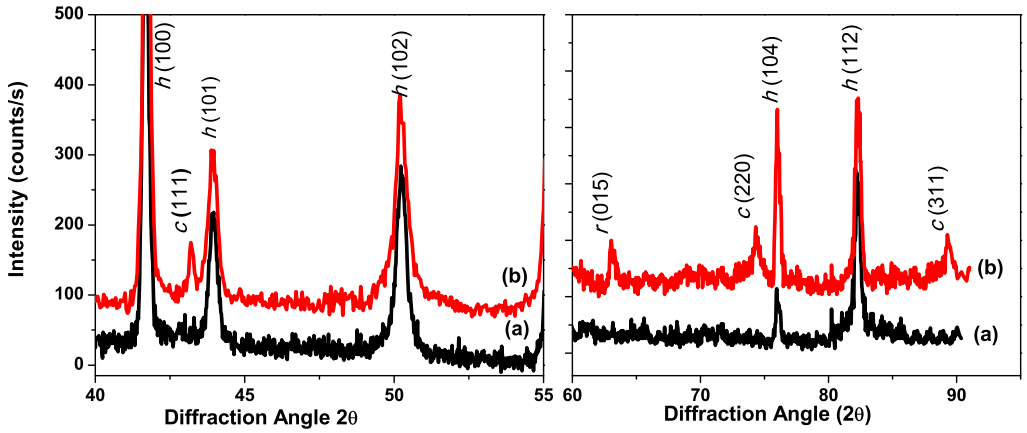

Figure 5.58: *GIXRD diffraction pattern for h-BN sheet sample (a) before and (b) after implantation with boron ions at 150 keV and fluence of* 5×10^{14} *ions/cm*^{2} *at* $\omega_i = 0.3^o$.

We separated the pattern in order to show clearly any features with low intensity centred around the region of interest.

All the h-BN peaks as seen for rod sample are also observed in these samples. Similarly as before, the h-BN diffraction peaks show a slight increase in the linewidth of the h-BN after implantation. We have attributed this line broadening and peak shift to residual stress due to implantation. New peaks are observed in the sample after implantation at Bragg angles of 43.2^o, 63.04^o, 74.32 and 89.2^o. These peaks have a wide linewidth, with low intensities relative to the h-BN peaks. The peak at 63.04^o was associated with the (015) plane for r-BN. The peak at 74.32^o was associated with the (202) plane and the one at 89.2^o is associated it with the (311) plane for c-BN. Similar peaks were also observed in the h-BN rod samples after implantation. The other peak at 43.2^o present in the sheet sample's pattern was not observed in the rod h-BN samples. From JCPDS database no. 35-1365 this peak was identified to represent the (111) reflection for c-BN.

Calculation of the lattice parameter for this plane is a=0.3615 nm, which is the lattice parameter for c-BN (refer to table 3.2). Using the Scherrer equation 5.10.1, and assuming the particles produced are spherical, the approximate crystal size was calculated to be 11.6 nm.

The occurrence of the (111) reflection was significant in verifying the presence of nc-BN since the peak at 74.32^o could have been easily identified by the JCPDS database file no. 49-1327 as the w-BN phase, with lattice parameters a=b=0.255 nm and c=0.42154 nm, which also forms transitionally during the h-BN to c-BN phase transformation process. It was concluded that this peak originated from the c-BN phase as no other w-BN peak was identified here or with the other analyses techniques (Raman and FTIR).

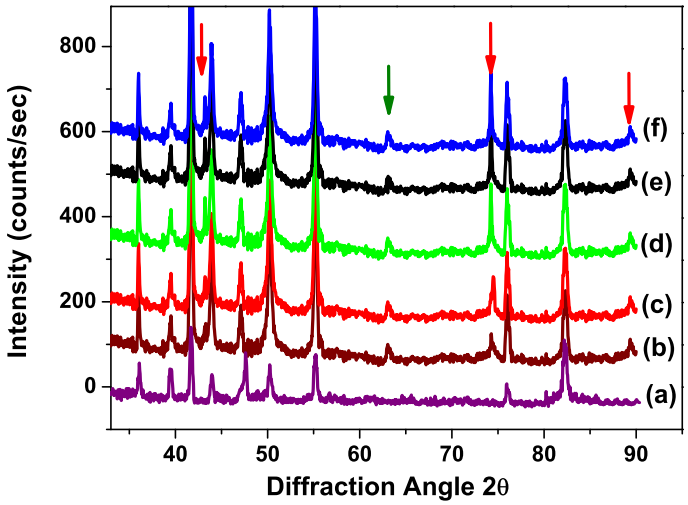

Figure 5.59: *GIXRD pattern for h-BN sheets (a) unimplanted and implanted with 5×10^{14} ions/cm^2 boron ions at 150 keV at glancing angles (b) 0.1^o (c) 0.2^o, (d) 0.3^o (e) 0.4^o and (f) 0.5^o.*

The diffraction patterns for the sheet samples implanted with boron at 5×10^{14} ions/cm^2 and analyzed at different incident angles are shown in figure 5.59. The unimplanted pattern was analyzed at 0.3^o. The red arrows indicate the (111),

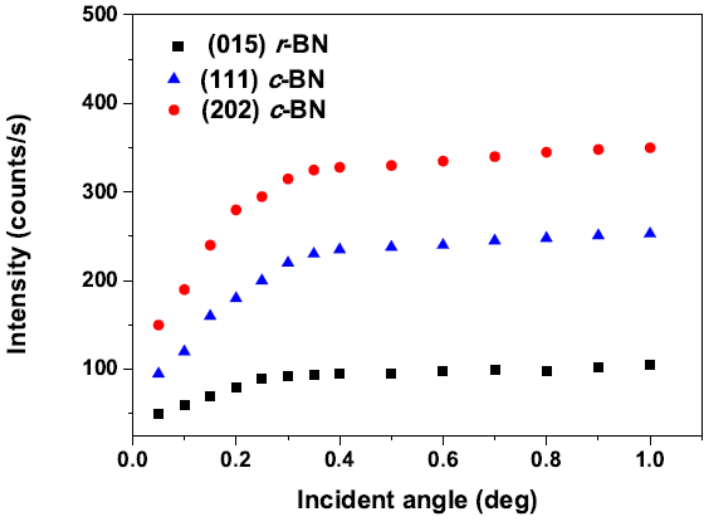

Figure 5.60: *Relationship between the peak intensity for the c-BN and r-BN with respect to the incident glancing angle for h-BN implanted sheets.*

(202) and (311) planes for c-BN while the green arrows represents the (015) plane for r-BN. The intensities of the new diffraction peaks were also dependent on the incident glancing angle with an increasing intensity up to 0.3^o, after which the intensity remains fairly constant as shown in figure 5.60. This also corresponds well with the SRIM results for the penetration depth of ions and the incident angle for the X-ray with similar trend as observed with the rod samples.

5.10.5 Fluence variation

To investigate the dependence of the r-BN and c-BN diffraction peaks on fluence, h-BN sheets were implanted with boron at 1×10^{14} ions/cm^2, 5×10^{14} ions/cm^2 and 1×10^{15} ions/cm^2 were analysed using GIXRD. Figure 5.61 represents the diffraction pattern for implanted samples for the h-BN (004) reflection analyzed at a glancing angle of 0.3^o. (This peak was chosen arbitrarily since the trend was the same for all the h-BN peaks). It shows a shift towards higher angles and line broadening of the diffraction peak with increasing fluence indicating that the higher the fluence

the more the compressive stress in the h-BN material.

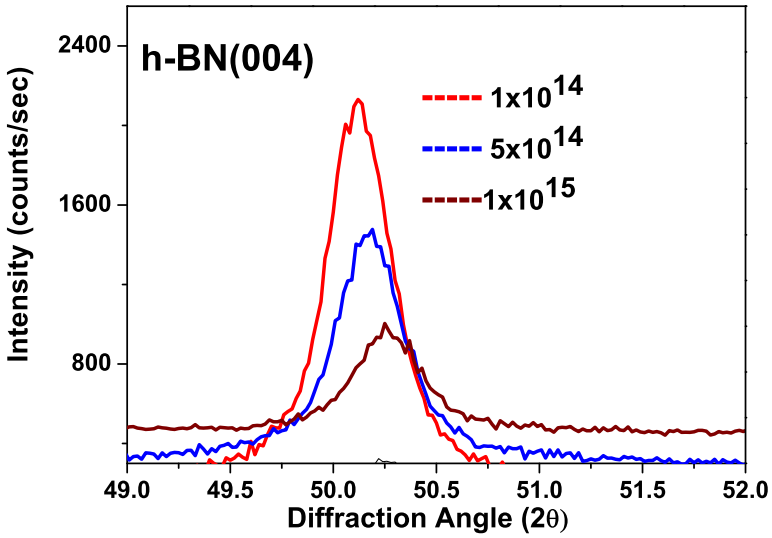

Figure 5.61: *Comparison for the shift of the (004) h-BN for the different fluences at a glancing angle of 0.3°.*

Figure 5.62 represents the diffraction patterns for the respective fluences compared to the unimplanted. All analyses were carried out at 0.3°. After implantation there are new peaks appearing in the GIXRD pattern for all the three fluences as summarized in summary table 5.7. These peaks are associated with the (111), (202) and (311) reflections for c-BN and (015) reflection for r-BN also seen previously.

The r-BN peak is strongest at 1×10^{14} ions/cm^2 and it decreases as the fluence increases. The lattice parameters for these peaks were calculated for the different fluences. At 1×10^{14} ions/cm^2, the r-BN value is a=0.232 nm which corresponds to the lattice constant of the bulk (0.2318 nm) and the constant expands with increasing fluence which suggests there is an increase in compressive stress with increasing fluence. It is suggested that at a lower fluence, the induced stress favours the formation of r-BN in the implanted volume. At higher fluences, the increase in defect concentration and high stress induce a higher cubic symmetry.

Table 5.7: *Summary of peak positions for sheet h-BN samples implanted with different fluence.*

Fluence (ions/cm^2)	c-BN	r-BN
1×10^{14}	43.11	63.67
	74.26	
	89.37	
5×10^{14}	43.12	63.53
	74.37	
	89.56	
1×10^{15}	43.23	63.93
	74.69	
	89.75	

The c-BN peaks' intensities increase with increasing fluence, attain a maximum at 5×10^{14} ions/cm^2 and decrease in intensity with further increase in fluence where a small diffraction signal is detected as shown in figure 5.62. There is also a line broadening of the peaks, and using the Scherrer equation (assuming the particles are spherical) the particle size is largest at 5×10^{14} ions/cm^2 at 11.6 nm. The c-BN lattice parameters are calculated as 0.3613 nm for 1×10^{15} ions/cm^2, 0.3617 nm for 5×10^{14} ions/cm^2 and 0.3616 nm for 1×10^{14} ions/cm^2. The shift and broadening of the nc-BN peaks indicate that by increasing the fluence, more atomic displacements and defect concentration lead to an increased stress which favours c-BN symmetry up to an optimum.

The incident angle dependence is similar for boron ions implanted at 150 keV for all the fluences i.e. the intensity of the diffraction peaks increases with increasing incident angle and beyond 0.3^o the intensity remains constant with increasing glancing angle. These are shown in figure 5.59 for 5×10^{14} ions/cm^2 (previous section) and in figures 5.63 and 5.64 for 1×10^{14} ions/cm^2 and 1×10^{15} ions/cm^2 respectively.

Boron at the energy of 150 keV and at 5×10^{14} ions/cm^2 has shown to have the

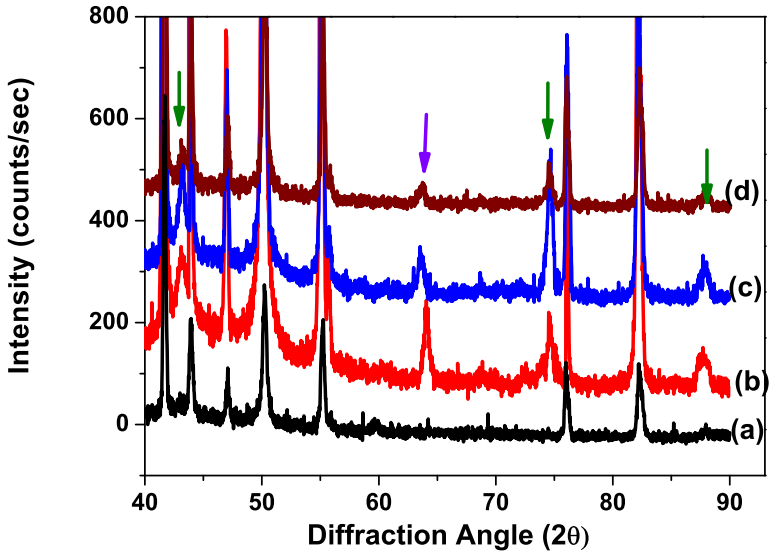

Figure 5.62: *GIXRD pattern for h-BN sheet samples implanted at (b) 1×10^{14} ions/cm^2 (c) 5×10^{14} ions/cm^{2}and (d) 1×10^{15} ions/cm^2 at a glancing angle of 0.3^o*

optimum n*c*-BN symmetry formation from the GIXRD analysis technique used in this section. We therefore suggest that this fluence induces an effective stress into the *h*-BN matrix which drives the material to a region where *c*-BN symmetry is stable.

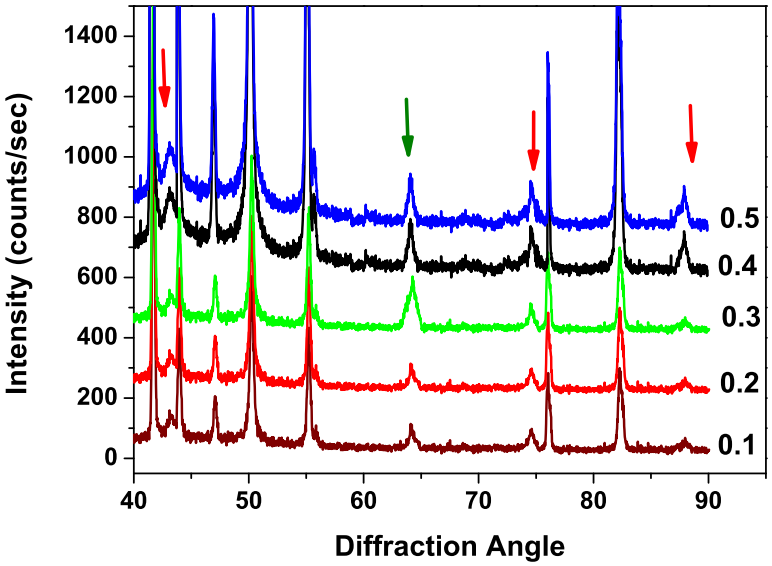

Figure 5.63: *GIXRD pattern for h-BN sheet samples implanted at (b) 1×10^{14} ions/cm^2 analysed at different glancing angles.*

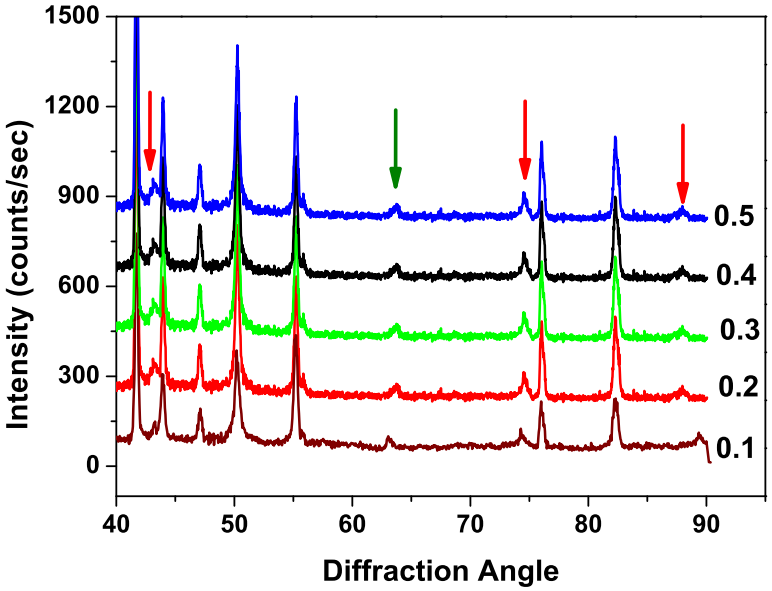

Figure 5.64: *GIXRD pattern for h-BN sheet samples implanted at 1×10^{15} ions/cm^2 analysed at different glancing incident angles.*

5.11 Transmission Electron Microscopy

Transmission Electron Microscopy was used in this work, mainly in cross-section, to investigate the morphology of the h-BN samples before and after ion implantation. The TEM specimens were prepared by Focused Ion Beam (FIB) sectioning to get an electron transparent specimen.

5.11.1 Focused Ion Beam sectioning

The FIB milling process for TEM specimen preparation has gained popularity as one of the best ways to prepare TEM specimens and especially when cross-sectional details of the samples are required. It poses various advantages over the other sample preparation techniques, for instance the specimen can be prepared directly from the bulk material with no other sample preparation like polishing required. The material can be thinned down to electron transparency with acceptably low level of radiation damage. It is a relatively quick process that is suitable in preparing both superhard materials and the very soft ceramics since all the parameters are controlled. This method has become successful since there is less degradation of finer details of the specimen as the final polishing is done at very low currents and voltages. The nature of the samples motivated the use of FIB sectioning in this work.

All the FIB sample preparations were carried out at the Council for Scientific and Industrial Research (CSIR) in Pretoria using the Auriga Cobra FIB-SEM. In the FIB process, the entire sample was first lightly coated with gold in order to reduce the charging effect and beam drift during milling and imaging of h-BN. An area of interest was identified on the surface of the bulk sample and a platinum "strap" deposited on this section with a surface area of 10 μm by 5 μm and 4 μm

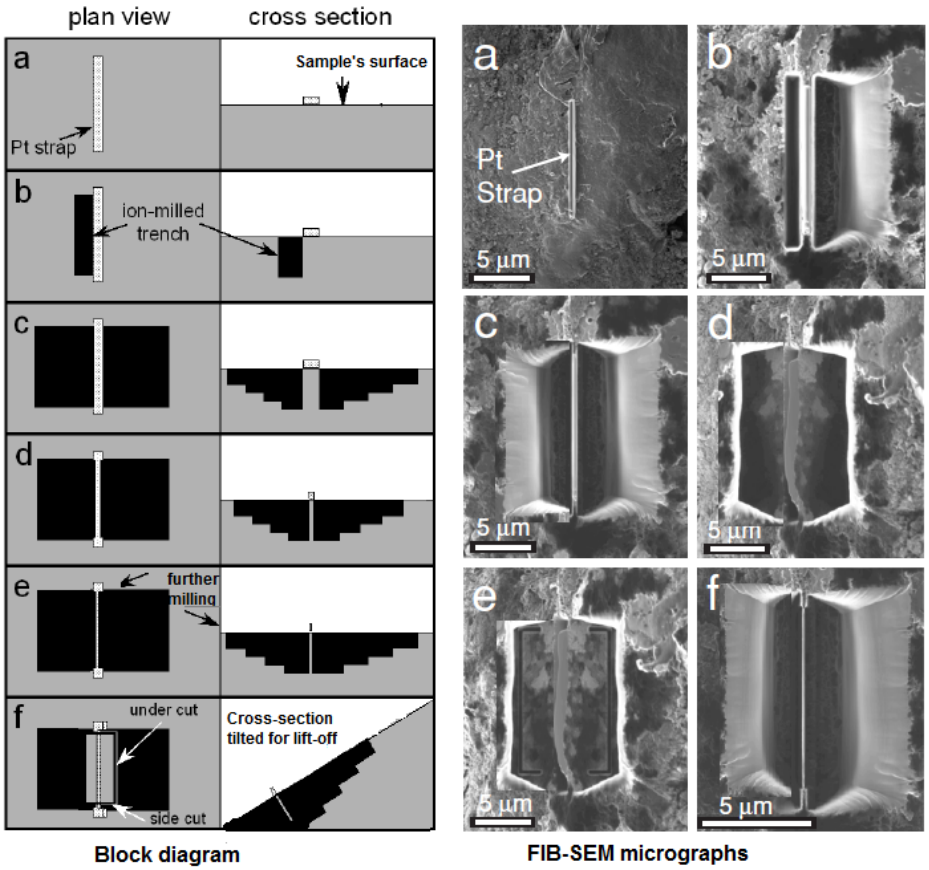

Figure 5.65: *Block and micrographic representation of the processes that take place during the FIB milling sample preparation. The micrograph represent the actual FIB-SEM images obtained during the sectioning process. In both figures (a) deposition of the Pt coating (b) initial milling process on one side of the strap (c) milling of the other side of the strap (d, e) further milling at low beam currents (f) the undercut.*

thickness to further minimize charging, and as a protective layer to the sample during the milling process.

The FIB ion source is fed with liquid gallium that is ionized to produce a beam of Ga ions. These ions are accelerated at an energy of 30 kV then manipulated with a nanometer precision to the target material at a current of 20 nA, and directed to the sample using electrostatic lenses. The beam excavates the material (by sputtering) from both sides of the strap with a step-cut geometry to allow for the last step cutting up to a depth of about 4 μm. The entire FIB sectioning process

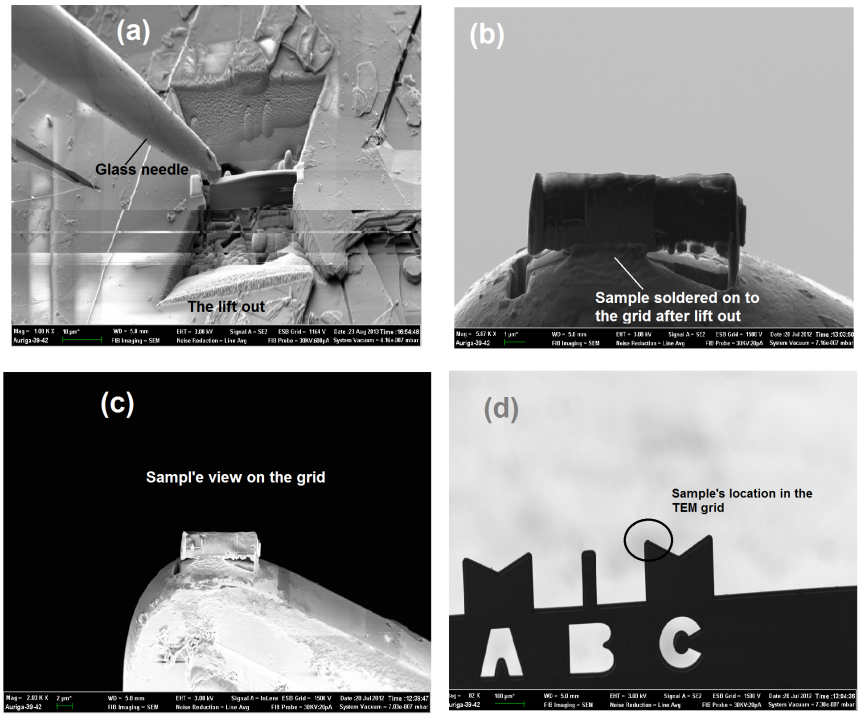

Figure 5.66: *FIB-SEM micrographs showing the final stages of (a) "lift out" (b,c) mounting of the specimen into the TEM grid. (d) shows the image of the grid with the specimen barely visible at low magnification.*

is shown in figure 5.65.

After the excavation process, the ion beam perforation procedure follows, which involves the undercutting of the specimen. The removal of the specimen is done using a hydraulic micromanipulator and a stereomicroscope where a drawn glass needle is directed to the excavation site and the thin specimen extracted by electrostatic attraction to the needle as shown in figure 5.66 (a).

The sample is then soldered/attached on to a 3 mm copper TEM grid as shown in figure 5.66 (b and c) using platinum. A low beam current of approximately 100 pA is used for the final polishing to a thickness of about 50 nm. This sample is electron transparent as shown in 5.66 (c) with dimensions of 10 μm $\times$5 μm with a thickness of 50 nm and ready for TEM analyses.

5.11.2 Energy Dispersive X-ray Spectroscopy

Energy dispersive X-ray spectroscopy (EDS) is an analysis technique used to identify the elemental composition of a given sample under investigation. It gives the qualitative and quantitative information of the elements present in the material. The EDS system analyses the materials by the use of the characteristic X-rays that are produced when a beam of electrons strikes a material.

The EDS system is normally an integral part of the Transmission Electron Microscope the (FEI Quanta F20 TEM used in this study). It is composed of an X-ray Si detector cooled by liquid nitrogen a pulse processor and an analyzer.

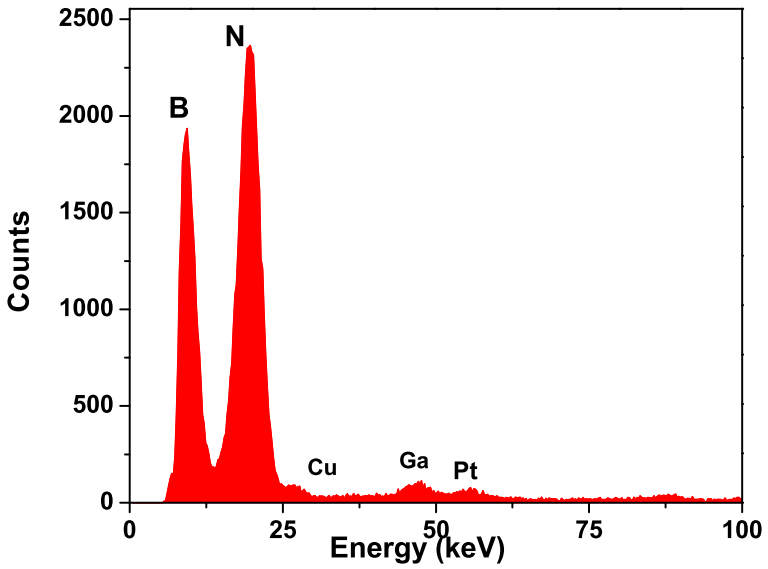

Figure 5.67: *EDS spectrum for h-BN sheet sample.*

All the EDS measurements were carried out on an *h*-BN sample that was implanted with boron ions at 150 keV and a fluence of 5x10^{14} ions/cm^2. Figure 5.67 represents the EDS spectrum for the *h*-BN sample with measurements collected from the sample. The spectrum indicates a high amount of boron and nitrogen in the sample with their dispersive peaks being close to each other.

Other elements including copper, gallium and platinum were also detected.

Copper was observed to have a high count as it originated from the copper grid that was used as a sample holder. Gallium counts observed were obtained from gallium ions that were used during the Focused Ion Beam (FIB) slicing of the *h*-BN to obtain an electron transparent specimen. Platinum observed was obtained from the platinum that was used as a coating and protective layer during FIB sectioning.

5.11.3 Polycrystalline samples

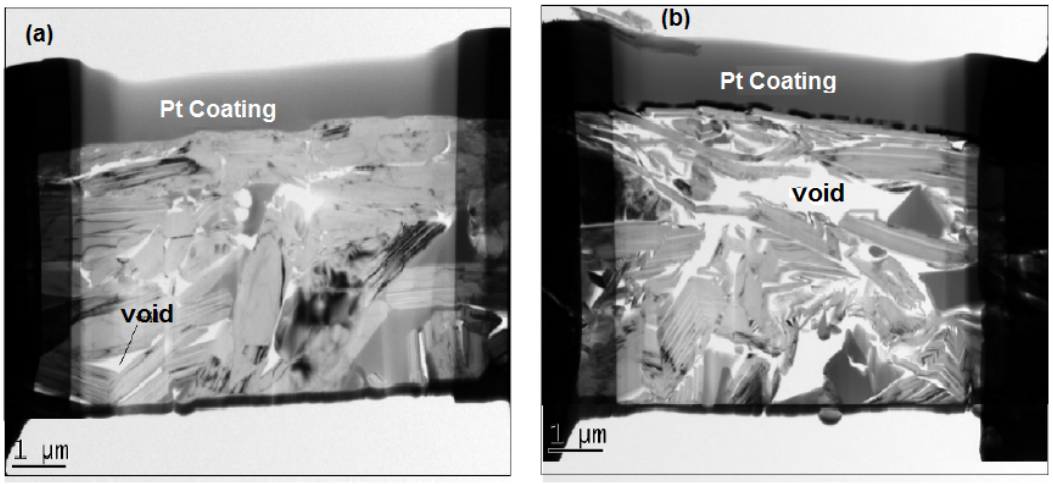

Figure 5.68: *TEM micrograph for (a) h-BN sheet and (b) h-BN rod sample at low magnification showing the overall view of the sample after FIB sectioning.*

Conventional TEM employs diffraction contrast or mass thickness to measure the intensity of the diffracted electrons in the imaging process. In this process, the microscope is operated at low to medium magnification. The TEM measurements were carried out on the polycrystalline *h*-BN sheet implanted by boron ions at 150 keV and fluence of $5x10^{14}$ ions/cm^2. Figure 5.68(a) and (b) represent the TEM micrographs for FIB lamella of *h*-BN sheets and rod samples respectively. After preparation, TEM images show that the FIB sectioned specimen contains a number of voids. Because the original sheets were prepared by hot press sintering, voids present in the specimen will grow as a result of preferential etching along the

boundaries of the voids. The voids present in the lamellae may be a contributing factor for Pt diffusion into the material observed by EDS.

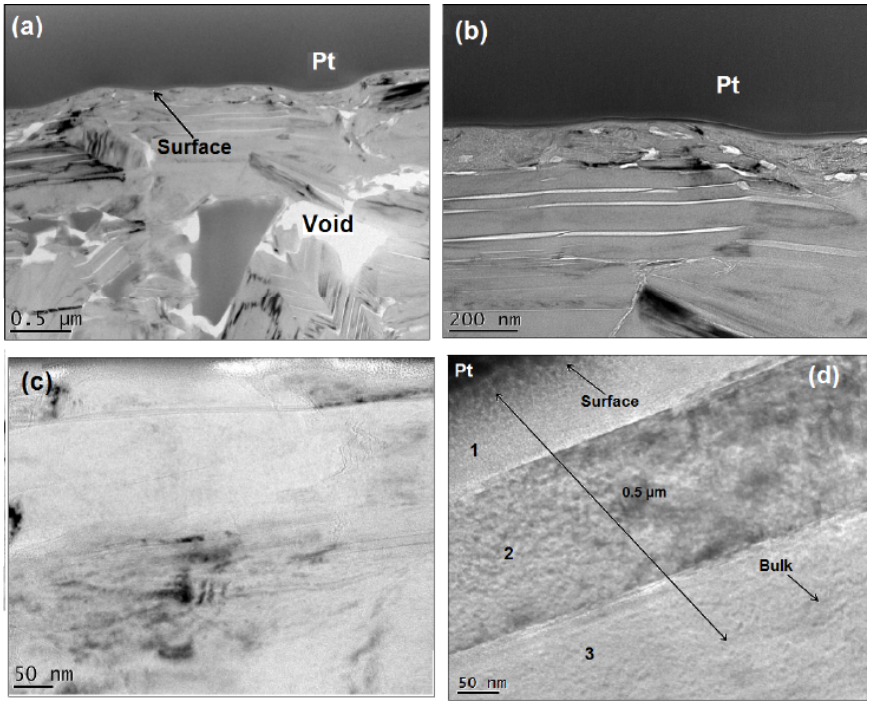

Figure 5.69: *TEM micrographs for sheet sample implanted with boron ions at* 5×10^{14} *ions/cm*^{2} *and 150 keV. The images are taken at different magnifications .*

Figure 5.69 represent TEM micrographs for the polycrystalline *h*-BN sheet sample, prepared by FIB sectioning, at different magnifications. Figure 5.69 (a) shows the TEM micrograph for the region of the sample from the surface to about 4 μm below the surface of the sample, (b) 600 nm below the surface and (c) 300 nm below the surface of the material. In figure 5.69 (d), the region is composed of the surface coated with the platinum, an intermediate layer between the platinum coating and the implanted region labeled 1, region labeled 2, which coincided with the implantation range and the substrate's bulk labeled 3 which is about 0.6 μm below the surface. The contrast seen in section 2 coincides with the implanted range but no imaging has shown a clear difference in the composition with section 3 and therefore may not necessarily represent the implanted layer. Platinum can

be seen clearly having diffused into the material. Because of the poor quality of the samples efforts to image the nanoparticles was unsuccessful with conventional TEM.

5.11.4 High Resolution TEM

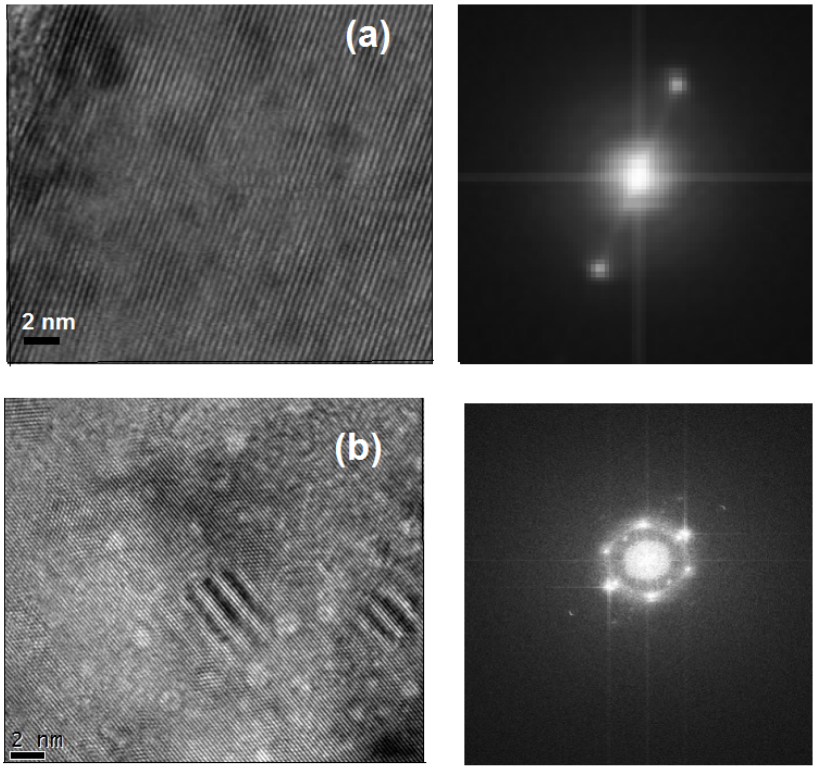

Figure 5.70: *HRTEM micrograph for B implanted sheet sample (a) unimplanted region (1 μm deep into the substrate). Image on the right is an FFT pattern for the sample taken from the region (a). (b) HRTEM taken from the a region 0.35 μm from the surface. Image on the right is an FFT pattern taken from region (b).*

High Resolution TEM involves imaging of the specimen at high magnification $>$ 200,000x. The method involves the use of phase contrast to image atomic lattice fringes from which the lattice parameter can be measured and the specimen can be identified. A Fast Fourier Transform (FFT) image can be collected within small regions to determine the diffraction planes for the particular material that

form the lattice pattern. Figure 5.70 (a) is the region, 1 μm below the surface, which represents the bulk/unimplanted region. The lattice fringes are clearly seen indicating that the material is crystalline. The FFT micrograph represents the diffraction pattern of the sample showing the (0002) planes for h-BN. The atomic spacing was found to be 0.2504 nm which is the lattice parameter for h-BN. Figure 5.70(b) represents the HRTEM image collected 0.35 μm from the surface. The FFT image in this region shows a (111) planes which are associated to the c-BN [221] implying there are traces of the c-BN in this region.

5.11.5 Single crystal *h*-BN

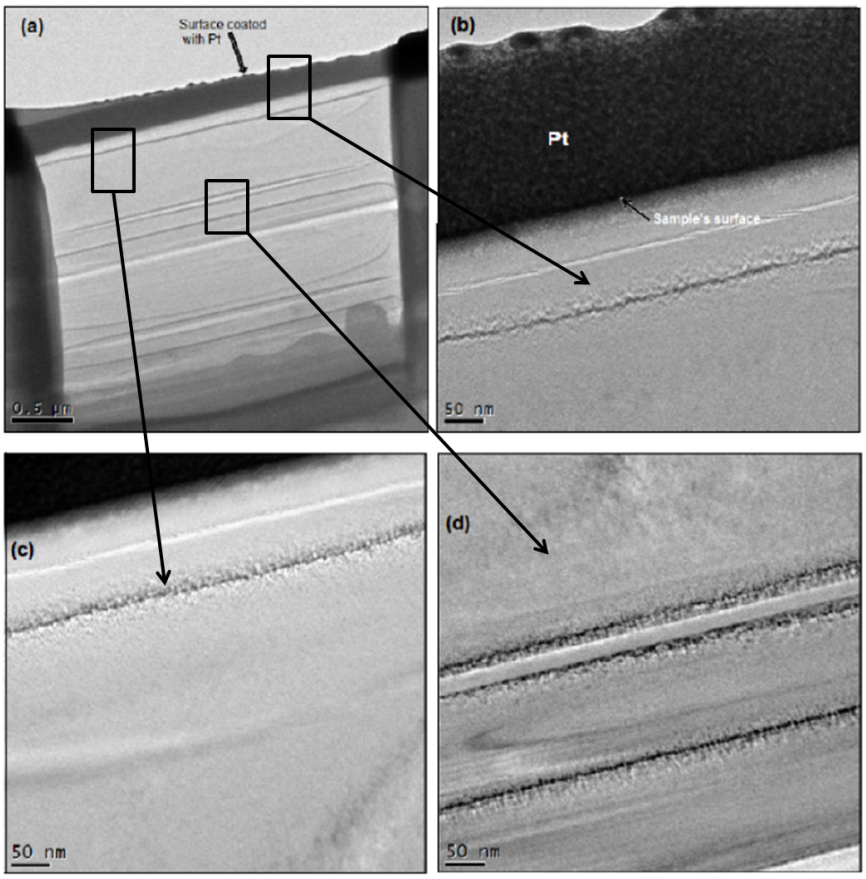

Figure 5.71: *Cross-sectional TEM micrograph for single crystal h-BN sample implanted with boron ions at 5×10^{14} ions/cm^2 and 150 keV. Regions (b,c,d) represent the different sections as enclosed in figure (a).*

Figure 5.71 represents the cross-section TEM micrographs for boron implanted *h*-BN single crystal specimen prepared by FIB sectioning. Figure 5.71(a) shows the micrograph for the entire sample at low magnification, (b and c) shows the regions close to the surface and (d) the region where most of the implanted region is expected to be according to SRIM simulations in figure 5.72. Boundaries are seen in the micrographs which are as a result of small crystals which are attached by van der Waals force on the large size crystal during the growth process. With this scenario, it was challenging to view the implanted layer using TEM imaging for the single crystal samples. Note that there was no Pt diffusion into this single crystal sample. Apart from these, there is no visible difference in the entire specimen from the surface to about 0.6 μm.

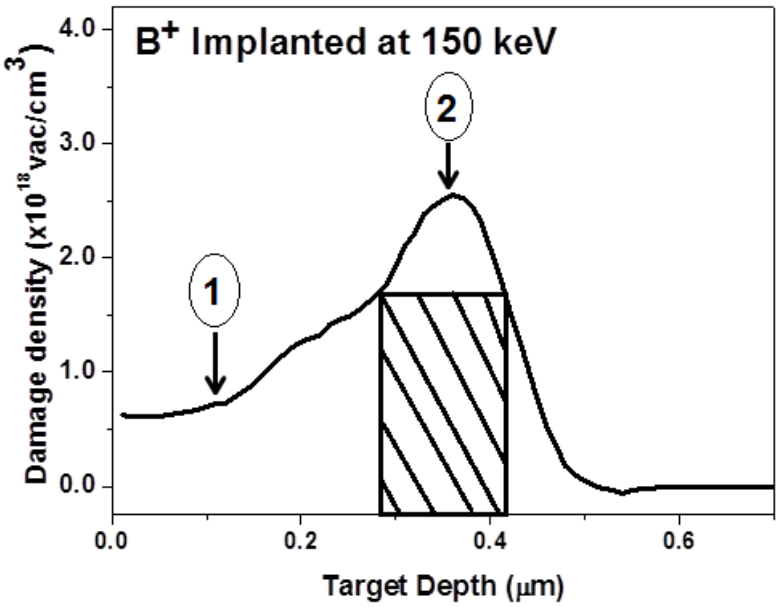

Figure 5.72: *SRIM simulation for h-BN single crystal sample implanted with boron ions at 5×10^{14} ions/cm^2 and 150 keV. The highlighted region represents region of maximum damage.*

5.11.6 HAADF-STEM

Due to low fluences that have been used in ion implantation for the samples here, the sp^3 coordinated regions may be sparingly distributed within the h-BN matrix making TEM analysis challenging. The High-Angle Annular Dark-field (HAADF) analysis that operates in the Scanning Transmission Electron Microscopy (STEM) mode was employed to study the microstructure of the sample since the contrast of the image correlates strongly with the sample's density [222]. This method is important as it helps visualize stress regions and identify defects, ad-atoms and impurities with different masses from the surrounding pristine material. The regions in the material with high density have a lower contrast (will appear brighter) as compared to the low density regions which appear dark.

The HAADF detector consists of a scintillator-photomultiplier that is placed in a housing above the projection chamber of the FEI Quanta F20 TEM. The HAADF-STEM uses highly incoherent, elastically scattered electrons to record images with different atoms giving different Z contrast/intensity.

Figure 5.73 represents an HAADF-STEM image for single crystal sample that was implanted with boron ions at 150 keV and fluence of 5×10^{14} ions/cm^2. The micrograph represents a cross-sectional length of about 0.5 μm from the sample's surface, which according to SRIM is the region where most of the nuclear stopping process takes place. In region 1, about 0.1 μm from the surface, there is a high intensity contrast as compared to region 2 about 0.4 μm from the surface. We know high contrast represents regions with low density and as such we suggest that region 1 is composed of the low density sp^2 bonded h-BN.

The low contrast region 2 is attributed to regions of high density in the material and as such we attribute this region to contain sp^3 bonded high density c-BN lattice.

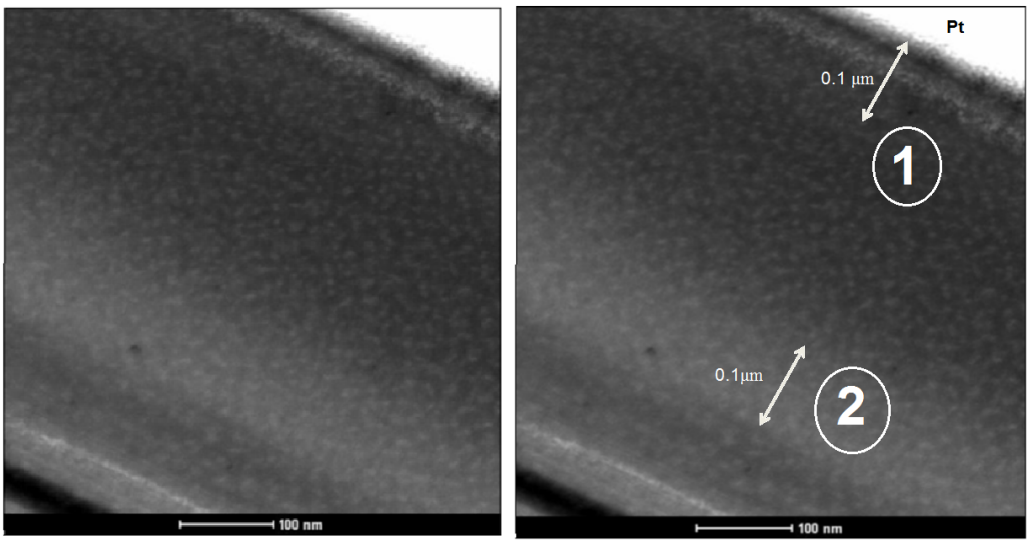

Figure 5.73: *HAADF STEM micrograph for single crystal h-BN sample implanted with boron ions at 5×10^{14} ions/cm^2 and 150 keV.*

The width of this region is about 0.1 μm which corresponds to that part of the range of the implantation in SRIM highlighted as the area under the curve as shown in figure 5.72.

All the TEM results presented in this section are preliminary. The main challenge has been to get a sample in which we can distinguish between the implanted and unimplanted regions using TEM imaging, because of either plate boundaries or voids in the material which are seen after FIB sectioning. In the analyses carried out here this was difficult.

This work recommends that a multiple energy implantation be carried out, where an entire region from the surface to the end of range that will represent the implanted region, as shown in the SRIM simulation in figure 5.74. This will be useful since the entire region is implanted even if there are plate boundaries and voids between the surface and the end of range.

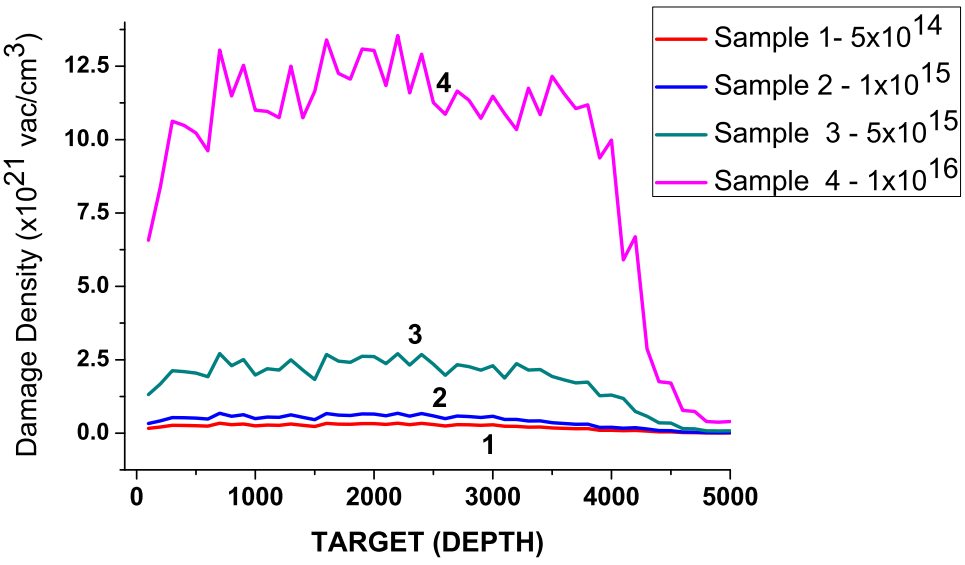

Figure 5.74: *SRIM simulation for multiple energy implantation from 37 keV to 170 keV, for h-BN samples implanted with boron ions at different fluences to create a uniform distribution of damage from the surface to the end of range.*

Chapter 6

Spatial Correlation model

6.1 Introduction

In the previous chapter, Raman spectroscopy was employed as one of the techniques to determine the effect of implantation on *h*-BN by observing and analyzing the changes in the phonon spectra before and after implantation. It was shown that nanostructured *c*-BN symmetry was induced after ion implantation of *h*-BN. This chapter seeks to correlate the experimental information analyzed by Raman spectroscopy with the Spatial Correlation Model/Phonon Confinement Model calculations in order to understand the changes in the Raman line with changes in the crystal size. This study also aims at determining the approximate crystal size for n*c*-BN produced and correlate it with calculation obtained using GIXRD.

In the n*c*-BN experimental Raman results in Chapter 5, the Raman spectra are broad and shifted with respect to the bulk value of approximately 1304 cm^{-1} to lower frequencies, which was mainly attributed to the lateral compressive strain caused by ion implantation in *h*-BN. The Spatial Correlation Model (SCM) or the Optical Phonon Confinement Model (OPCM) study is fundamental in our current research as we observe changes in the Raman peak after introducing disorder

in h-BN by ion implantation. The main purpose is to understand the characteristics of the strain and the optical phonon confinement in self-assembled c-BN nanoparticles. The experimentally observed optical phonon frequency shift values are analyzed with quantitative calculations.

6.1.1 Theory of Phonon Peak

Normally in an ideal infinite crystal, the momentum conservation selection rule for phonons near the Brillouin zone centre $q=0$ are allowed to contribute to the first order Raman spectrum. When the crystal lattice periodicity of the material is interrupted such that the size of crystallites in the material is decreases to nanoscale, due to extended defects and stress in the material, this selection rule is violated and as such phonons at Brillouin centre $q\neq 0$ are now allowed to contribute to the Raman first order spectrum [202]. This results in changes to the Raman line characteristics including (1) the asymmetric broadening of the linewidth (2) Reduction in intensity and (3) A shift of the phonon line toward lower frequencies.

The Spatial Correlation Model was first developed by Parayanthal *et al* [183] and later developed by Richter-Wang *et al* [223] whose work was based on quantifying the relationship of the Raman first-order peak shift, asymmetric broadening and change in the intensity with respect to the disorder in semiconductor alloys. This model correlates quantitatively the crystal size and quality and the Raman spectrum. The model is based on a Gaussian function exp $(q^2L^2/4)$ which has been used to account for the contribution of phonons away from the Brillouin zone centers. It calculates the intensity $I(\omega)$ of the phonon dispersion of the Raman peak at frequency ω given as

$$I(\omega) \propto \int \exp(\frac{-q^2L^2}{4}) \times \frac{d^3q}{[\omega - \omega(q)]^2 + (\frac{\Gamma_o^2}{2})^2} \tag{6.1.1}$$

where L is the correlation length, q has units of $(2\pi/a)$ with a being the lattice parameter (in this case a=3.616 $\mathring{A}$ for c-BN), and Γ_o is the estimated full width at half maximum of the Raman line determined from the experimental spectrum of the c-BN LO mode. The dispersion relation of optical phonons is derived from a one-dimensional linear chain model assumed to be isotropic [168, 224] and is approximated to be of the form

$$\omega^2(q) = A + \sqrt{[A^2 - B(1 - \cos(\pi q)]} \tag{6.1.2}$$

with A and B being constants specific to the material under investigation.

Raman scattering studies have appeared in the literature on the modifications to the original Richter-Wang-Ley's model. Today the Raman line-shapes of nanostructures (nanowire [225], quantum dots, quantum wells [223], thin films [226]) can be modeled successfully using the modified Richter-Wang-Ley Phonon Confinement Models. For the phonon dispersion relation of the bulk material, $w(q)$ of the LO mode used in our model is assumed to be isotropic and also based it on a theoretical calculation reported by Zhang *et al* [215], where

$$\omega^2(q) = 1284.2 - 0.1q - 147.94q^2 + 81.39q^3 + 726.79q^5 - 1870.3q^5 + 1074.72q^6 \tag{6.1.3}$$

From the calculations, w(q) at q=0 is 1284.2 cm^{-1} which is 19.8 cm^{-1} wavenumbers from the bulk c-BN LO phonon peak at 1304 cm^{-1}.

Figure 6.1 (a) represents the Raman spectra for c-BN with different crystal sizes as measured by [184] and figure 6.1 (b) shows an example of the Raman spectrum

for GaAs with different particle sizes as calculated by Arora *et al* in their study on "Phonon Confinement in Nanostructured Materials" [227], in both cases using the Spatial correlation model. The bulk material was used for comparison and it is observed that as the crystal size reduces from the bulk material, there is an asymmetric line broadening and a shift to lower wavenumbers.

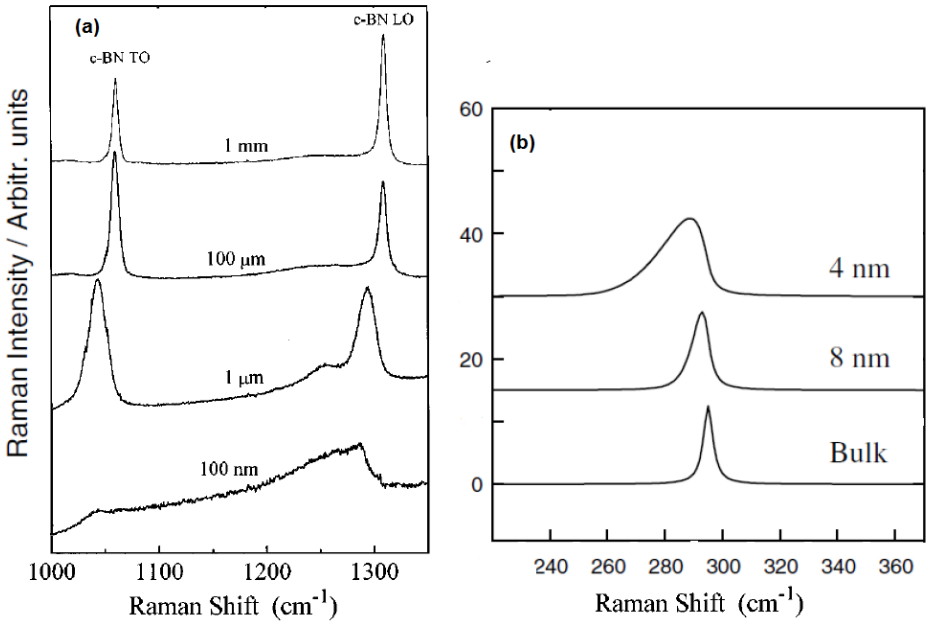

Figure 6.1: *(a) Calculated Raman Spectrum of confined LO phonon in c-BN [184] and (b) GaAs particles with different crystal sizes [227].*

Before fitting our experimental data, our custom-design OPCM was calibrated against simulated Raman lineshapes presented by Zhang and Matsumoto in [215]. This report was chosen mainly because our work employed a phonon dispersion relation similar to the one reported therein but for *c*-BN prepared by HPHT method. Zhang and Matsumoto also, in that same report, present Raman lineshapes simulated from a wide range of correlation lengths. In this work, different values of correlation length (L = 10 $\mathring{A}$, 20 $\mathring{A}$, 50 $\mathring{A}$, and 100 $\mathring{A}$) were used to fit Raman line shapes calculated in [194]. The values of Γ_o=4 cm^{-1} and a_o=0.36157 nm [184] were

used in this work. The natural width of the phonon at 1299 cm^{-1} is 4 cm^{-1} at room temperature [203].

Figure 6.2 represents Raman measurement for the polycrystalline *h*-BN sheet samples that were implanted with boron ions at 5x10^{14} ions/cm^2, at 150 keV, and the spectrum generated from calculations using the SCM Model in equation 6.1.1. The filled symbols represents the experimental data after background subtraction while the continuous line represents a fit of the calculated data. The peak position for the experimental measurements is 1299 cm^{-1}, while the calculated peak position is 1301 cm^{-1} in good agreement with each other. The correlation length from this calculation, which relates to the crystal size of the *c*-BN was obtained to be 15.2 nm. Considering this correlation length (and also assuming the crystals are spherical), the nanocrystalline nature of *c*-BN formed was confirmed. These calculations for the crystal size Correlates well with the GIXRD measurements in Chapter 5 which also show that the estimated crystal size for n*c*-BN created is between 9 and 15 nm.

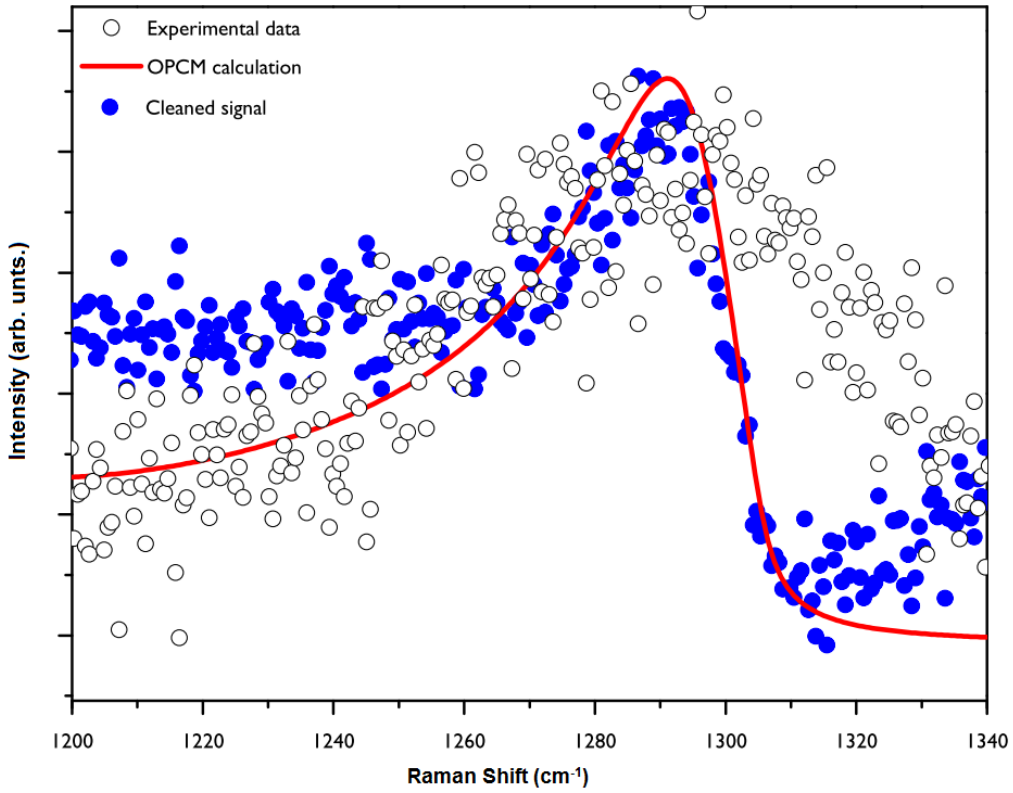

Figure 6.2: *Raman experimental measurements for boron optimum fluence (open symbols), the cleaned experimental data after background subtraction (filled symbols) and the calculations (continuous line) using the Spatial correlation model in equation 6.1.1 for the c-BN LO mode.*

Chapter 7

Summary and Conclusions

7.1 Summary

The work presented herein focused on selectively introducing defects into sp^2 h-BN with an aim of inducing an sp^3 bonded cubic BN structure. Ion implantation was the major process used to modify different h-BN substrates including sliced polycrystalline rods, recrystallized sheet and single crystal sample types. Different ions including helium, lithium, boron, nitrogen and argon were used. The ion fluence, ion energies and substrate temperatures were varied.

The samples were analyzed by various techniques including Raman spectroscopy (which was the main analysis technique), Fourier transform Infrared spectroscopy, and Glancing incident X-ray diffraction. Transmission electron microscopy, Energy dispersive spectroscopy and scanning electron spectroscopy were also used with moderate success.

The simulation and experimental results obtained show that ion implantation introduced a substantial number of point defects into the surface and sub-surface of an h-BN substrate. These defects led to an increase in stress levels in the material, increasing the local density to favour the formation of the high density cubic symmetry. Different analyses have shown that the defect concentration was

found to be controlled by and depend on factors such as ion mass, the implantation energy, the ion fluence and implantation temperature.

Raman spectroscopy done on the material show that the initial material has a Lorentzian peak centred at 1366 cm^{-1} assigned to the *h*-BN material. After implantation, new phonon vibrational mode peaks were introduced, centred between 1290 cm^{-1} and 1303 cm^{-1} depending on the ion mass, the implantation energy and the implantation temperature. These were associated with the formation of *c*-BN symmetry after implantation. Using the Phonon Confinement Model, based on the characteristics of the Raman spectra i.e. asymmetric broadening, low intensities and shift to lower wavenumbers compared to the *c*-BN peak for bulk material (1304 cm^{-1} cm), it was suggested these peaks originated from the implanted region which consisted of the nanostructured *c*-BN symmetry (n*c*-BN).

The extent of the occurrence of the n*c*-BN mode depicted a sequence in the yield of the *c*-BN with respect to the implantation parameters on basis of the intensity and linewidth. For a fixed ion mass and implantation energy of 150 keV, each ion used had an optimum fluence that gave the highest intensity for the LO n*c*-BN phonon peak. Helium ions had an optimum at a fluence at 5×10^{15} ions/cm^2, lithium at 1×10^{15} ions/cm^2, boron at 5×10^{14} ions/cm^2 and nitrogen at 1×10^{14} ions/cm^2, implying that for each ion, there is a critical defect concentration, hence stress level required to induce the cubic symmetry below and above which much less n*c*-BN LO Raman signal was detected. Above these fluences, radiation damage overwhelms the conversion process.

With respect to the ion mass, boron ions at 5×10^{14} ions/cm^2 gave the highest n*c*-BN yield followed by nitrogen, lithium, helium and argon respectively for the same energy of 150 keV. The reason was suggested to be because B is one of the

atoms that constitute the BN compound and it has a high formation energy in BN. The formation energy for N ions, also a constituent of BN, is lower than B most likely because it has a higher mass number and hence caused more damage to the material. Argon ions showed the lowest yield of all the ions within the energy and fluence ranges used.

Energy variation analysis revealed that an increase in energy caused an increase the yield of nc-BN symmetry for the energy range used in this study. SRIM simulations showed that for the same ion with similar fluence at variable energy, the integrated damage concentration increases at higher energies and hence increasing the stress levels responsible for c-BN formation.

Annealing the samples after implantation caused a reduction in the linewidth of the nc-BN LO peak, which was associated with the relaxation of crystal strain created during implantation. Boron implantation at 200^{o}C showed a favorable increase to the nc-BN Raman intensity.

Results from FTIR also showed a change in the structure of the h-BN material after implantation. New vibrations were observed at wavenumbers between 1090 and 1114 cm^{-1} depending on the ion type and the fluence which were attributed to the vibrational modes for nanocrystalline c-BN. Using the FTIR formula an estimated amount (6%) for c-BN in the sample was determined. The samples implanted with boron at 150 keV gave the highest estimated amount followed by lithium and finally helium. The estimated amount for c-BN produced was also fluence dependent with the same optimum fluence obtained for each ion as the ones using Raman.

Traces of r-BN were also observed using FTIR showing that there existed a multi-symmetry in the samples' matrix after implantation.

Glancing incident XRD results were also reported for boron implanted samples. The diffraction patterns after implantation showed diffraction peaks at 43^o, 74^o and 89^o which were associated with the (111), (202) and (311) planes for c-BN. There were also diffraction patterns at 63^o associated with the (015) plane of the rhombohedral BN.

Finally TEM results were recorded. FIB sample preparation was used as the major sample preparation technique. Both polycrystalline and single crystals were analyzed with the single crystals being easier to work with. Imaging did not yield very positive results primarily due to the nature of the samples after FIB sectioning. There was also no contrast between the unimplanted and the implanted regions because the nc-BN structure is burred within a matrix with the same atomic number.

HAADF-STEM analyses proved to be fairly successful of all the microscopy analyses. There was an indication of regions of high density in the implanted specimen which were associated with the cubic symmetry since this technique uses density contrast to differentiate between materials with different densities.

7.2 Conclusion

•Cubic BN symmetry was successfully induced by ion implantation of *h*-BN evident from the various complementary analyses, with the particle size of the n*c*-BN particles estimated to be between 9 nm and 15 nm. The occurrence of the *c*-BN structural symmetry was attributed to point defects (interstitials) introduced into the samples by ion implantation. The aggregation of these point defects caused compressive strain/stress into *h*-BN. This stress in *h*-BN drives it into a region where the *c*-BN formation begins to take place. The defect concentration and the subsequent volume strain scaled up with threshold for the formation of *c*-BN structure which was found to depend on the implantation parameters such as the ion mass, ion fluence, the implantation energy and the substrate temperature. Low ion mass species required higher defect concentration to cause the same effect as for high mass number ions. Higher mass number species such as Ar used here caused large compressive stress and as a result very little signal was detected by the different analyses techniques.

•Glancing Incident XRD showed n*c*-BN structures within the h-BN lattice.

•An increase in the annealing temperature led to reduced stress, with the LO n*c*-BN mode still present after annealing to 400 ^{o} C.

•Rhombohedral BN symmetry was also formed during the implantation process.

•The nature of the starting material did not have any effect on the occurrence of the *c*-BN symmetry as all the samples used showed the same change after implantation. The nature of the material only affected the analyses techniques used, i.e. both the polycrystalline samples' preparation was challenging for TEM measurements. The FTIR measurements for implanted rods also proved difficult as it was difficult to polish the samples down to suitable thickness being a challenge,

while the single crystals were not suitable for GIXRD measurements because of their small size.

7.3 Recommendations

Transmission EM analyses posed a big challenge especially due to the nature of the sample. Due to either voids or plate boundaries in the polycrystalline samples it was difficult to determine the actual implanted layer which is buried between the *h*-BN layers for single energy implants done in this study. This work suggests that a multiple energy implantation be carried out on these samples in order to get a uniformly implanted layer from the surface to the end of range.

Varying the implantation temperature and annealing was preliminary in this work and therefore more studies with these variables should be carried out.

APPENDIX

A1: Instruments

Figure 1: *Photograph of the Varian 200-20A2F ion implanter located at iThemba LABS Gauteng, Johannesburg.*

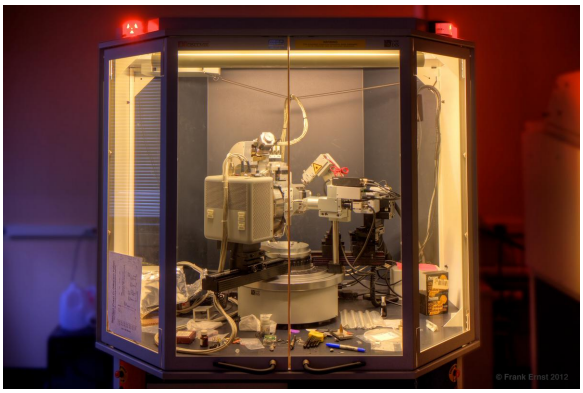

Figure 2: *Photograph of the D8 ADVANCE Bruker X-ray diffractometer located at the school of Chemistry, University of the Witwatersrand.*

Figure 3: *Photograph of the Auriga Cobra FIB-SEM located at Council of Science and Industrial Research (CSIR) in Pretoria.*

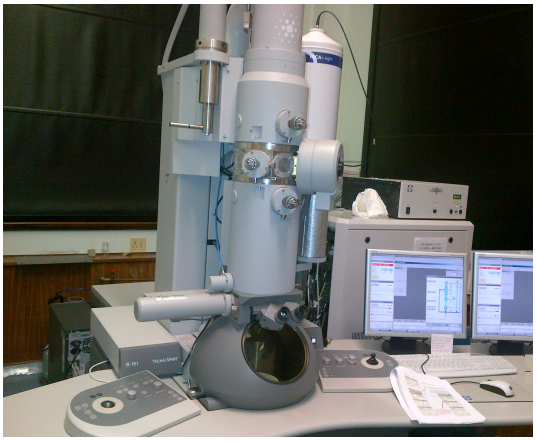

Figure 4: *Photograph of the FEI Quanta F20 TEM located at the University of Western Cape, South Africa.*

A2: List of Publications

1. E. Aradi, S. R Naidoo, R.M. Erasmus, T. E. Derry, *Raman Characterization of Ion Implanted Hexagonal Boron Nitride*, S. A. Inst. Phys. **978**-1-8688-3 (2011) 672-676.

2. E. Aradi, R. M. Erasmus, T. E. Derry, *Formation of Cubic Boron Nitride Nanocrystals by Helium, Lithium and Boron Ion Implantation*, J. Nucl. Instr. Method, B, **257**, (2012) 57-60.

3. E. Aradi, S. R. Naidoo, R. M. Erasmus, B. Julies, T. E. Derry, *Investigations on the Characterization of Ion Implanted Hexagonal Boron Nitride*, J. Nucl. Instr. Method, B **307** (2013) 214-217.

4. E. Aradi, S. R. Naidoo, T. E. Derry, D. G. Billing, D. Wamwangi, *Ion beam Modification of the Structure and Properties of Hexagonal Boron Nitride: X-Ray Diffraction and Fourier Transform Infrared Spectroscopy Analysis*, J. Nucl. Instr. Method, B, **331** (2014) 140-143.

5. E. Aradi, S. R. Naidoo, R.M. Erasmus, T. E. Derry, *Raman Studies on the Effect of Multiple Energy Ion Implantations on Hexagonal Boron Nitride*, Radiation Effects and Defects Solids. Accepted manuscript(2014).

6. E. Aradi, R. Machaka, S. R. Naidoo, R.M. Erasmus, T. E. Derry, *Size Effect Investigations of c-BN Nanocrstals Studied by the Spatial Correlation Model of Raman Scattering*, J. Raman Spectros. In preparation (2014)

A3: Conferences Attended

1. **July 13-18, 2014**: The 26^{th} International Conference on Atomic Collisions in Solids (ICACS) Debrecen, Hungary.

2. **July 9-12, 2014:** The 7^{th} international meeting on Recent Developments in the study of Radiation Effects in Matter (REM7), Budapest, Hungary.

3. **Oct 19-25, 2013:** International Conference on Adaptive Optics, Cape Town, South Africa

4. **July 8-12, 2013:** The 58^{th} South African Institute of Physics (SAIP2013) Conference, Zulu Land, South Africa.

5. **Sept 2-7, 2012:** The 18^{th} International Conference for Ion Beam Modification of Materials (IBMM2012), Qingdao, China.

6. **July 9-13, 2012:** The 57^{th} South African Institute of Physics (SAIP2012), University of Pretoria, South Africa

7. **Nov 13-20, 2011:** The International Conference on Radiation Damage in Nuclear Materials, at the International Centre for Theoretical Physics, Trieste, Italy.

8. **Sept 4-6, 2011:** International Conference on the Advancement of Women in Science and Technology, Johannesburg, South Africa

9. **July11-16, 2011:** The 56^{th} South African Institute of Physics (SAIP2011) Conference, Pretoria, South Africa

10. **April 4-9, 2011:** International Conference for Women in Physics (ICWIP 2011), Cape Town, South Africa

11. **Oct 23-36, 2010:** Post Graduate cross faculty Symposium University of the Witwatersrand, South Africa

12. **Sept 11-16, 2010:** South African Institute of Physics (SAIP2010) Conference, Council of Scientific and Industrial Research Institute, Pretoria, South Africa.

13. **Aug 22-27, 2010:** The 17^{th}International Conference for Ion Beam Modification of Materials (IBMM2010) in Montreal, Canada.

14. **Dec 4, 2009:** Annual Postgraduate Seminar, Moi University Eldoret, Kenya.

15. **Sept 20-23, 2009:** Annual Postgraduate Cross Faculty Symposium, Wits University.

16. **July 7-13, 2009:** The 55^{th} South African Institute of Physics (SAIP2009) Conference, Durban, South Africa.

References

[1] R. Machaka, R. M. Erasmus, and T. E. Derry, *Formation of c-BN Nanocrystals by Helium Ion Implantation*, Diam. Relat. Mater., **19** pp. 11331–1134, (2010).

[2] I. Bello S. T. Lee W. J. Zhang, Y. M. Chong, *Nucleation, Growth and Characterization of Cubic Boron Nitride (c-BN)*, J. Phys. D Appl. Phys, **40** pp. 6195–6174, (2007).

[3] Y. M. Chong, W. J. Zhang, Y. Yang, Q. Ye, I. Bello, and S. T. Lee, *Deposition of cubic boron nitride films on diamond-coated WC:Co inserts*, Diam. Relat. Mater., **18**(11) pp. 1387 – 1392, (2009).

[4] T. E. Mosuang. *Defects and Defect Processes in some Ultra Hard Nitrides*. PhD thesis, University of the Witwatersrand, Johannesburg, (2003).

[5] D. A. Neumayer and J. G. Ekerdt, *Growth of Group III Nitrides, Review of Precursors and Techniques*, Chem. Mater, **8** pp. 9–25, (1996).

[6] I. Takanori, M. Toshihiro, and Y. Toyonobu, *Effects of the substrate bias on the formation of cubic boron nitride by inductively coupled plasma enhanced chemical vapor deposition*, J. Appl. Phys., **75**(3) pp. 1330–1334, 1994.

[7] R. H. J Wentorf, *The Cubic Form of Boron Nitride*, J. Chem Phys., **26** pp. 956–968, (1957).

[8] R. H. J Wentorf, *Sythesis of the Cubic Form of Boron Nitride*, J. Chem Phys., **4**(3) pp. 3812–3820, (1975).

[9] C. B. Samantaray and R. N. Singh, *Review of Synthesis and Properties of Cubic Boron Nitride (c-BN) Thin Films*, International Materials Review, **50** (6) pp. 313–344, (2005).

[10] W. J. Yu, M. W. Lau, S. P. Chan, Z. F. Liu, and Q. Q. Zheng, *Ab initio Study of Phase Transformations in Boron Nitride*, Phys. Rev. B, **66** pp. 014108–0141017, (2003).

[11] I. Jiménez, A. F. Jankawsk, L. J. Terminello, and D. G. J. Sutherland, *Core-Level Photoabsorption Study of the Defects and Metastable Bonding Configuration in Boron Nitride*, Phys. Rev. B, **55**(18) pp. 10225–10237, (1997).

[12] A. Klett, R. Freudenstein, and W. Kulisch, *Dependence of the Stress of c-BN Films on the Major Deposition Parameters: Theoretical andExperimental Studies*, Thin Solid Films, **398-399** pp. 130–136, (2001).

[13] T. E. Mosuang and T. Lowther, *Influence of Defects on the h-BN to c-BN Phase Transformation*, Phys. Rev B, **63** pp. 014112–014117, (2002).

[14] R. Machaka. *Ion Beam Modification of Boron Nitride by Ion Implantation.* PhD thesis, University of the Witwatersrand, Johannesburg, South Africa, (2006).

[15] J. F. Ziegler, *Stopping of Energetic Ions in Elemental Matter*, J. App. Phys, **85**(3) pp. 1–24, (1999).

[16] P. Sigmund, *Stopping power in perspective*, Nucl. Instr. and Meth. Phys. Res. B, **135**(1-4) pp. 1–15, 1998.

[17] D. Fink and L. T. Chadderton, *Ion-solid interaction: Current Status and Perspectives*, Brazilian Journal of Physics, **35**(3B) pp. 734–740, (2005).

[18] Y. Yamamura, T. Kenmotsu, K. Yorizane, and T. Muromoto, *Progress in Computer Simulation for Ion-Solid Interaction*, Ion Impt. Techno. Proceedings, **2** pp. 672–677, (1999).

[19] M. Nastasi, and J. M. Mayer, and J. K. Hirvonen. *Ion Solid-Interaction: Fundamentals and Applications.* Cambridge Solid State Science Series, Cambridge University Press, (1996).

[20] A. Orbán and S. Hagmann, *Developments for Ion-Solid Interaction Studies*, The commission of an electrostatic deflector unit, **1**, (1997).

[21] Sybil Parker. *Dictionary for Scientific and Technological Terms.* The McGraw- Hill Companies Inc. 6^{th}edition, Cambridge University Press, (2003).

[22] G. Amsel and G. Battisstig, *The Impact on Material Science of Ion Beam Analysis with Electrostatic Accelerators*, Nucl. Instr. and Methods, Physics Research, B, **240** pp. 1–12, (2005).

[23] J. F. Prins, *Ion -Implanted Structures and Doped Layers in Diamond*, Mater. Sci. Rep., **7**(217), (1992).

[24] W. E. Bacham. *Elements of Nuclear Physics.* Longman New Yolk, USA, (1999).

[25] P. D. Townsend, *Optical Effect of Ion Implantation*, Rep. Prog. Phys., **50** (5) pp. 501–558, (1987).

[26] G. O. Amolo. *Optical and Electrical Properties of Ion Beam Modified Materials.* PhD thesis, School of Physics, University of the Witwatersrand, Johannesburg, South Africa, (2007).

[27] N. Cheung. *Ion Implantation.* U. C. Berkley, EECS143, China, 7, (2005).

[28] J. R. Conrad, J. L. Radtke, R.A. Dood, J.F. Worzala, and N. C. Tran, *Plasma Source Ion-Implantation Technique for Surface Modification of Materials*, J. Appl. Phys., **62**(11) pp. 4591–4596, (1987).

[29] L.A. Giannuzi, B.I. Prenitzer, and B.W. Kempshall. *Introduction to Focused Ion Beams, Instrumentation, Theory techniques and Particles.* Springer, Chapter 2, USA, (1976).

[30] E. J. Veldhuizen, C. G. Granquivist, G. Niklasson, and L. Nillson, *Material Science Application of Heavy Ion Beams from the Gugtaf Werner Cyclotron*, Nuclear and Engineering Physics, **2**, (1987).

[31] R. Hellborg, H. J. Whitlow, and Y. Zhang. *Ion Beam in Nanoscience and Technology.* Springer- Verlag Berlin Heidenberg, Cambridge University, (2009).

[32] E. K. Nshingabingwi. *Cross section Transmission Electron Microscopy of Radiation Damage in Diamond.*

[33] W. Moller. *Fundamentals of in Surface Interactions.* Kluwer Academic Publisher, New York, (2004).

[34] J. Lindhard and M. Scharff, *Energy Dissipation in the keV Region*, Phys. Rev., **124**, (1961).

[35] G. J. Phelps, *Dopant ion implantation simulations in 4h-silicon carbide*, Modelling Simul. Mater. Sci. Eng.1139, **12** pp. 1139–1146, 2004.

[36] K. Nordlund, *Molecular Dynamics Simulation of Ion Ranges in the 1-100 keV Energy Ranges*, Computer Material Science, **3** pp. 448–456, (1995).

[37] D. K. Avasthi and G. K. Mehta. *Swift Heavy Ions for Material Enginnering and Nanostructuring*, volume 1. Springer-New Delhi, Capital Publishing Company, New York, (2011).

[38] J. F. Ziegler. *The Stopping Range of Ions in Matter*, volume 1. Pergmon Press, New York, (1985).

[39] P. Sigmund, *Reciprocity in Electronic Stopping of Slow Ions in Matter*, Eur. Phys. Journal D, **47**, (2008).

[40] G. Dearnaley, *Ion Bombardment and Ion Implantation*, Rep. Prog.Phys., **32**, (1969).

[41] P. Sigmund. *Stopping of Heavy Ions: a Theoretical Approach*, volume 204. Springer Tracts in Modern Physics, (2004).

[42] O. Kabadayi, and H. Gümüs, Z_2 *of the Stopping Power for Electron Beams, Nuclear Instrumentation and Methods in Physics*, Nucl. Instum. Method B, **267** pp. 299–301, (2009).

[43] M. Nastasi, and J. M. Mayer, and J. K. Hirvonen. *Ion Implantation and Synthesis of materials.* Springer -Verlag Berlin Heidelberg, Cambridge University Press, (2006).

[44] K.D. Hirshman, *Ion Implantation Notes*, Roster Institute of Technology, **20** pp. 1–9, (2002).

[45] Wikipedia, *Stopping Power Particle Radiation*, http://en.wikipedia.org/wiki/stoppingpower(particleradiation)(14/06/2011), .

[46] D. S. Gemmell. *Channeling and Related Effects in the Motion of Charged Particle in Crystal*, volume 1. Rev. Mod. Phys, (1978).

[47] A. Seppala. *Ion Beam Channeling Studies of Compound Semiconductor Materials* . PhD thesis, Department of Physics, University of Helsinki, Finland, (2001).

[48] G. B. Gelmimi, *Relevance of Ion Channeling for Direct DM Detection*, Journal of Physics, Conference Series, **203** pp. 012042–012047, (2010).

[49] M. S. Dresselhaus and R. Kalish. *Ion Implantation in Diamond, Graphite and Related Materials*, volume 1. Springer, (1992).

[50] Y. N. Osetsky, D. J. Bacon, B. N. Singh, and B. Wirth, *Atomistic Study of the Generation, Interaction, Accumulation and Annihilation of Cascade Induced Defect Cluster*, J. Nucl. Mat., **307** pp. 852–861, (2002).

[51] Yang-Tse Cheng, *Thermodynamic and Factual Geometry Aspects of Ion-Solid Interaction*, Material Science report, **5** pp. 45–57, (1990).

[52] J. F. Ziegler, *Particle Interaction with Matter*, http://www.srim.org, , (18/07/2013).

[53] A. Sorkin, J. Adler, and R. Kalish, *Computer Simulation of Damage due to Fast Ions Through Matter*, Phys. Rev. B, **70** p. 064110, (2004).

[54] W. Eckstein. *Computer Simulation of Ion Solid Interaction*. Springer, Verlag, Belin, (1991).

[55] J. F. Ziegler, *TRIM: Output Files*, http://www.srim.org/SRIM/2009.pdf, pp. 11–12, (10/09/2013).

[56] S.O. Kucheyeva, J.S. Williamsa, and S.J. Pearton, *Ion implantation into GaN*, Mater. Sci. Engin., **33** pp. 51–107, (2001).

[57] B. Mårlid, K. Larsson, and J. O. Carlsson, *Theoretical Investigation of Hydrogen and Halogen- Terminated c-BN (111) Clusters*, Phys. Rev. B, **60**(23) pp. 16055–16072, (1999).

[58] Otfried Madelung. *Semiconductor:Data Handbook,Third Edition.* Springer-Verlag, Berlin Hedenburg, (1974).

[59] J. Zhang, Q. Cui, X. Li, Z. He, W. Li, Y. Ma, Q. Guan, W. Gao, and G. Zou, *Plasma Induced sp^2 to sp^3 Transition in Boron Nitride*, Phys. Rev. B, **399** (4-6) pp. 451–455, (2004).

[60] L. Wang, X. Wang, Q. Yao, G. Chen, and X. Zhang, *Phase Transformation in BN by Nitrogen Protected Annealing at Atmospheric Pressure*, Appl. Surf. Sci., **254**(1) pp. 7109–7113, (2008).

[61] Z. Y. Nain, Z. G. Tian, and Z.P. Wen, *Cubic Boron Nitride with no Stresses*, Chin. Rev. Lett., **16**(2) p. 155, (1999).

[62] J. D. Kester and R. Messier, *Phase Control of Cubic Boron nitride Thin Fils*, J. Appl. Phys., **72**(2) pp. 504–513, (1992).

[63] R. Ahmed, F. Aleem, S. J. Hashemifar, and H. Akbarzadeh, *First principles study of structural and electronic properties of different phases of boron nitride*, Phys. B: Cond. Matter, **400**(12) pp. 297 – 306, (2007).

[64] P. B. Mirkarimi, K. F. McCarthy, and D. L. Medlin, *Review of the Advances in Cubic Boron Nitride Film Synthesis, Material Science and Engineering*, Review Journal, **21** pp. 47–100, (1997).

[65] Karsten Albe, *Theoretical study of Boron Nitride Modifications at Hydrostatic Pressures*, Phys. Rev. B, **55**(10) pp. 6203–6210, (1997).

[66] G J Ackland, *High-pressure Phases of group IV and III-V Semiconductors*, Prog. Phys. 64, **64** pp. 483–516, (2001).

[67] J. Guo, H.Wang, K. Zheng, H. Yan, and M. Yoshimura, *Boron Synthesis at Ambient Pressure and Room Temperature by Plasma Electrolysis*, Electrochemistry communication, **9** pp. 1824–1827, (2007).

[68] L. Liu, Y. P. Feng, and Z. X. Shen, *Structural and Electronic Properties of Hexagonal Boron Nitride*, Phys. Rev. B, **68**(10) p. 104102.1, (1991).

[69] Q. Guo, Y. Xie, C. Yi, L. Zhu, and P. Gao, *Synthesis of ultraviolet luminescent turbostratic boron nitride powders via a novel low-temperature, low-cost, and high-yield chemical route*, J. Solid State Chem., **178**(6) pp. 1925 – 1928, (2005).

[70] H. Yasuda, Y. J. Huang, and H. Mori, *HRTEM and EELS Studies on the Amorphization of the Hexagonal Boron Nitride Induced by ball milling*, J. Am. Ceram. Soc., **83**(2) pp. 03–409, (2000).

[71] G. H.Lee, Y. J. Yu, X. C. N. Petrone, C. H. Lee, M. S.Choi, D. Y. Lee, C. anggu Lee, J. Yoo, K. Watanabe, T. T, C. Nuckolls, P. Kim, , and James Hone, *Flexible and Transparent MoS^2 Field-Effect Transistors on Hexagonal Boron Nitride-Graphene Heterostructures*, NCS Nano, **7**(9) pp. 7931–7936, (2013).

[72] E. Kresten, S.K. Klitgard, M. Brorson, K. Harbst, and C. H. Christensten, *Turbostratic Boron Nitride Coated on High-surface Metal Oxide Templete*, Eur. J. Inor. Chem, **33** pp. 4873–4876, (2007).

[73] J. H. Edgar. *Properties of Group III Nitrides*. INSEPC, London, (1994).

[74] C. Ronning, H. Feldermann, and H. Hofsass, *Growth, Doping and application of Cubic Boron Nitride Thin Films*, Diam. Relat. Mater., **9**(9-1) pp. 1767–1773, (2000).

[75] L. G. Wood, M. Z. Visi J. F. Janik, D. M. Schubert, and P. T. Paine, *New Borate Precarsor for Boron Nitride synthesis*, Chem. Mater., **17**(2) pp. 1855–1857, (2005).

[76] S. Alkoy, C. Toy, T. Gnl, and A. Tekin, .

[77] K. A. K. Basu and J. Mukerji, *Synthesis of Boron Nitride*, J. Mater. Sci., **15** (1) pp. 165–171, (1990).

[78] L. Kleinman and D. M. Bylander, *Efficacious Form for Model Pseudopotentials*, Phys. Rev. Lett, **48** p. 1425, (2008).

[79] Y. Al-Douri, *Structural Phase Transition of Boron Nitride Compound*, Solid State Comm., **132**(7) pp. 465–470, (2004).

[80] T. Soma, A. Sawaoski, and S. Saito, *Characteristics of Wurtzite type of Boron Nitride by Shock compression*, Mater. Research Bull., **9**(6) pp. 755–762, (1974).

[81] G. Lian, X. Zhang, L. Zhu, D. Cui, Q. Wang, and X. Tao, *Phase Transformation of Boron Nitride Under Hypothermal Conditions*, J. Solid State Chem., **182**(6) pp. 1326 – 1330, (2009).

[82] Y. Zhang C. Chen Z. Pan, H. Sun, *Harder than Diamond, Superior Indentation Strength of Wurtzite Boron Nitride and Lonsdalite*, Phys. Rev. Lett, **102**(4) p. 055503, (2009).

[83] Z. T. Chen, Y. Sun, L. Dong, and W. Guo, *Wurtzite Boron Nitride Crystal Growth in the Region of Cubic Boron Nitride Crystal Synthesis*, Chin. Phys. Lett., **50**(1) p. 70, (1998).

[84] L Bourgeois, Y Bando, and T Sato, *Tubes of Rhombohedral Boron Nitride*, J. Phys. D: Appl. Phys., **33**(15) p. 1902, (2000).

[85] T. Ishii, T. Sato, Y. Sekikawa, and M. Iwata, *Growth of Whiskers of Hexagonal Boron Nitride*, J. Crystal Growth, **52, Part 1**(0) pp. 285 – 289, 1981.

[86] S. Cui, W. Feng, H. Hu, and Z. Feng, *First Principle Study of Zinc-Blend to Rocksalt Transition of BN*, Cent. Eur. J. Phys., **8**(4).

[87] E. J. Hamilton, S. E. Dolan, C. M. Mann, H.O. Colijn, and C. A. McDonald, *Preparation of the Amorphous Boron Nitride and its Conversion to the Turbostratic Tubular Form*, J. Science, **260** pp. 659–661, (1993).

[88] T. Oku, K. Haraga, T. Matsuda, T. Harai, and M. Tarabayashi, *Twin Structure of the Rhombohedral and the Cubic Boron Nitride, Prepared by Chemical Vapour Deposition Method*, Diam. Relat. Mater, **12** pp. 1138–1145, (2003).

[89] Y. Chen, J. F.Gerald, J. S. Williams, and S. Bulcock, *Synthesis of Boron Nitride Nanotubes at low Temperatures using Reactive Ball Milling*, Chem. Phys. Lett., **299** pp. 260–264, (1999).

[90] Gérard Demazeau, *High Pressure Diamond and Cubic Boron Nitride Synthesis*, Diam Relat. Mater., **4**(4) pp. 284–287, (1995).

[91] J. Myres and R. D. Kriz, *Thermodynamics of Phase Diagrams, The Analytical Approach*, Mater. Sci. Eng., **2094** pp. 284–287, (1994).

[92] R. H. Wentorf Jr.and A. J. De Lai and N. Y. Schenectary, *Cubic Boron Nitride; Compact and Method for Its Production*, U. S. Patent, **51-307**(368) pp. 547–550, (1966).

[93] C. X. Wang, Y. H. Yang, and G. W. Yang, *Nucleation Thermodynamics of the Cubic Boron Nitride upon High Pressure High Temperature Supercritical Fluid System in Nanoscale*, J. Phys. Chem. B, **108** pp. 728–731., (2004).

[94] M. M. Attalla and M. N zeid. *Boron in Material Technology Based on its Application in Ceramic Industry.* PhD thesis, Engineering department, The American University- Cairo, (1997).

[95] G. Will, G. Nover, and J. von der Gonna, *New Experimental Results on the Phase Diagram of Boron Nitride*, J. Solid State Chem., **154**(1) pp. 280 – 285, (2000).

[96] F. R. Corrigan and F. P. Bundy, *Direct Transition among the Allotropic Phases of Boron Nitride*, J. Chem. Phys., **63** p. 3812, (1975).

[97] V.L. Solozhenko, *New concept of BN phase Diagram: an applied aspect*, Diam. Relat. Mater., **4**(1) pp. 1–4, (1994).

[98] R. H. Wentorf Jr., *Synthesis of the Cubic form of Boron Nitride*, J. Chem. Phys., **34**(3) pp. 809–812, (1961).

[99] V. L. Solozhenko and K. S. Gavrichev, *Boron nitride phase diagram; state of art*, Condensed Matter Physics, **13**(4) pp. 199–214, (1995).

[100] V. L. Solozhenko and K. S. Gavrichev, *Refined Phase Diagram of Boron Nitride*, J. Phys. Chem. B, **103** pp. 2903–2905, (1999).

[101] V. Z. Turkevich, *Phase Diagram and Synthesis of Cubic Boron Nitride*, J. Phys.: Cond. Matter Phys, **14** pp. 10963–1068, (2002).

[102] C. Oshima and A. Nagashima, *Ultra-thin Epitaxial Films of Graphite and Hexagonal Boron Nitride on Solid Surfaces*, J. Phys.: Cond. Matter Phys, **9** pp. 1–20, (1997).

[103] R. Geich, C. H. Perry, and G. Rupprecht, *Normal Modes in Hexagonal Boron Nitride*, Phys. Rev., **146**(2) pp. 543–547, (1966).

[104] N. Ooi, A. Rairkar, L. Lindsey, and J. B. Adams, *Electronic Structure and Bonding in Hexagonal Boron Nitride*, J. Phys.: Cond. Matter Phys, **18** pp. 97–115, (2006).

[105] T. E. Mosuang and J. E. Lowther, *Relative Stability of Cubic and Hexagonal Boron Nitride Forms of Boron Nitride*, J. Phys. Chem. of Solids, **63** pp. 363–368, (2002).

[106] B. Napoleon and Q. L. Williams, *Ab-initio Calculations on the Structure and Properties of Hexagonal Boron Nitride*, Phys. Chem. Lett., **490** pp. 210–215, (2010).

[107] Y. Huang, Y. Bando, C. Tang, C. Zhi, T. Terao, B. Dierre, T. Sekiguchi, and D. Golberg, *Thin-walled Boron Nitride Microtubes Exhibiting Intense Band-edge UV Emission at Room Temperature*, J. Nanotechnology, **20** pp. 085705–085713, (2009).

[108] S. Watanabe, S. Miyake, and M. Murakawa, *Tribological Properties of Cubic, Amophous and Hexagonal boron nitride*, Surf. Coat. Techno., **49** pp. 406–410, (1991).

[109] S. Saha, D.V.S. Muthu, D. Golberg, C.Tang, C. Zhi, Y. Bando, and A.K. Sood, *Comparative High Pressure Raman Study of Boron Nitride Nanotubes and Hexagonal Boron Nitride*, Chem. Phys. Lett., **421**(1-3) pp. 86 – 90, (2006).

[110] G. Will and P. G. Perkins, *Is there a new form of boron nitride with extreme hardness*, Diam Relat Mater., **10**(11) pp. 2010 –2017, (2001).

[111] F. Tian, Z. Liu, Y. Ma, T.Cui, B. Liu, and G. Zou, *Ab initio study of vacancies in cubic bn under pressure*, Solid State Comm., **143**(11-12) pp. 532– 536, (2007).

[112] Haris Division, *Cubic Boron Nitride Products*, http://www.harisdiamond.com/cbn.html, pp. 1–3, (4/19/2012).

[113] G. Will, A. Kirfel, and B.Josten, *Charge density and chemical bonding in cubic boron nitride*, J. Less Common Metals, **117**(1-2) pp. 61–71, (1986).

[114] R. F. Zhang, S. Veprek, and A. S. Argon, *Anisotropic ideal strengths and chemical bonding of wurtzite bn in comparison to zincblende bn*, Phys. Rev. B, **77**(17) p. 172103, (2008).

[115] G. P. Perkins, A. K. Marwaha, and J. J. Stewart, *An improved LCAP SCF Method for three Dimensional Solids and its Application to Polyethylene, Graphite, Diamond and Cubic Boron Nitride*, Theoretic. Chim. Acta, **57** pp. 1–23, (1980).

[116] R. M. Erasmus, J. D. Comins, and M. L. Fish, *Raman and photoluminescence spectra of indented cubic boron nitride and polycrystalline cubic boron nitride*, Diam. Relat. Mater., **9**(3-6) pp. 600 – 604, (2000).

[117] J. Karlsson and K. Larsson, *Hydrogen induced de/reconstruction of c-bn (100) surface*, J. Phys. Chem, **2**(114) pp. 3516–3525, (2010).

[118] L. Vel, G. Demazeau, and J. Etourneau, *Cubic boron nitride: Synthesis, physicochemical properties and applications*, Mater. Sci. Engi.: B, **10**(2) pp. 149 – 164, (1991).

[119] H. Takashima and Y. Kanno, *Evaluation by extended Hückel method on the hardness of the BCN materials*, Sci. Techno Adv. Mater., **6**(8) pp. 910–914, (2005).

[120] E. Betranhandy, L. Capou, S. F. Matar, and C. El-Kfoury, *First Principles search of superhard material with the Si-C-N ternary system*, Solid State Science, **6**(4) pp. 315–323, (2004).

[121] G. Kern, G. Kresse, and J. Hafner, *Ab initio Calculation of the Lattice Dynamics and Phase Diagram of Boron Nitride*, Phys. Rev. B, **59**(13) pp. 8551–8559, (1999).

[122] S. S. Reich, A. C. Ferrari, R. Arenal, A. Loiseau, I. Bello, and J.Robertson, *Resonant raman scattering in cubic and hexagonal boron nitride*, Phys. Rev. B, **71**(20) p. 205201, (2005).

[123] W. R. L. Lambrecht and B. Segall, *Anomalous band-gap behavior and phase stability of c-bn-diamond alloys*, Phys. Rev. B, **47**(15) pp. 9289–9296, (1993).

[124] W. Sekkal, B. Bouhafs, H. Aourag, and M. Certier, *The Molecular Dynamics simulation of Structural and Thermodynamic Properties of Boron Nitride*, J. Phys. Condens. Matter, **10** pp. 4975 – 4984, (1998).

[125] X.W. Zhang, *Doping and electrical properties of cubic boron nitride thin films: A critical review*, .

[126] Y. Zou, Y. Chong, L. Ji, Q. Ye, B. He, W. J. Zhang, I. Bello, and S.T. Lee, *The Fabrication of the Cubic Boron Nitride Nanocone and Nanopillar Array Via Reactive Ion Etching*, Nanotechnology, **20** p. 155303(5pp), (2009).

[127] V. L. Solozhenko, O. O. Kurakevych, D. Andrault, Y. Le Godec, and M. Mezouar, *Ultimate Metastable Solubility of Boron in Diamond: Synthesis of Superhard Diamondlike BC_5*, Phys. Rev. Lett., **102**(1) p. 015506, (2009).

[128] F. P. Bundy and R. H. Wentorf Jr., *Direct Transformation of Hexagonal Boron Nitride to Denser Forms*, J. Chem. Phys., **38**(5) pp. 1144–1149, (1963).

[129] Sumitomo Electrical Industries, *Development and Release of New-Non-Coated Grade "Submicron c-BN2000" for general machining of Hardened Steel*, Patent, **EP 0 386 338 AL**, (2010).

[130] V. L. Solozhenko, A. G. Lazarenko, J. P. Petitet, and A. V. Kanaev, *Bandgap Energy of Graphite-like Hexagonal Boron Nitride*, Journal of Physics and Chemistry of Solids, **62**(7) pp. 1331 – 1334, (2001).

[131] M. Wakatsuki, K. Ichinose, and T. Aoki, J. Chem. Eng., **68** p. 177, (1999).

[132] M. Wakatsuki, K. Ichinose, and T. Aoki, .

[133] O. Fukunaga S. Nakano, H. Ikawa, *New Scope, High Pressure High temperature Formation of Cubic Boron Nitride*, Diam. Relat Mater, Volume 2, Issue 8, 15 May 1993, Pages 1168-1174, **2**(8) pp. 1168–117.

[134] T. Endo, Tadashi, O. Fukunga, and M. Iwata, *The synthesis of c-BN using* $Ca_4B_2N_4$, J. Mater. Sci., **16**, (1981).

[135] R. C DeVries and J. F Fleischer, *Phase Equilibria Pertinent to the Growth of Cubic Boron Nitride*, Journal of Crystal Growth, **13-14** pp. 88 –92, (1972).

[136] T. Sato, H. Hiraoka, T. Endo, Tadashi, O. Fukunga, and M. Iwata, *Effect of Oxygen on the Growth of Cubic Boron Nitride by High Pressure High Temperature*, J. Mater. Sci., **16**, (1981).

[137] H. Hofsäss, H. Feldermann, M. Sebastian, and C. Ronning, *Thresholds for the phase formation of cubic boron nitride thin films*, Phys. Rev. B, **55**(19) pp. 13230–13233, (1997).

[138] T. Wada and N. Yamashita, *Formation of c-BN Films by Ion Beam Assisted Deposition*, J. Vacuum Sci. Techno., **10**, (1992).

[139] A. Twardowsa, B. Rajchel, and L. Jawarska, *Ion Beam Assisted Deposition of Ti-Si-C T Thin Films*, J. Achi. Mater. Manuf. Eng., **37**, (2009).

[140] A. F. Jankowski, J. P. Hayes, D. M. Makowiecki, and M. A. McKernan, *Formation of Cubic Boron Nitride by the Reactive Sputter Deposition of Boron*, Thin Solid Films, **308-309** pp. 94 – 100, (1997).

[141] J. Robertson, *Deposition Mechanism of Cubic Boron Nitride*, Diam. Relat. Mater., **5**(3-5) pp. 519 – 524, (1996).

[142] H. Uchida, M. Yamashita, S. Hanaki, and A. Kurihara, *Synthesis of c-BN Films by Ion Mixing and Vapour Deposition Technique*, Mater. Sci. Eng.: A, **483-484** pp. 695 – 697, (2008).

[143] D. Ila, *Ion Beam Assisted Deposition*, Material Processing, **4** p. 695, (2008).

[144] P. A. Molian, *Laser Physico-chemical Vapour Deposition of c-BN Thin Films*, J. Mater. Sci., **29** pp. 5646– 5656, (1994).

[145] M. Z. Karim, D. C. Cameron, and M. S. J. Hashmi, *Vapour Deposited Boron Nitride Thin Films*, Material and Design, **13**(4) pp. 207–214, (1992).

[146] V. S. Kharlamov, D. V. Kilivov, and Y. V. Trushin, *Computer Simulation of Transition from h-BN to c-BN During Ion Beam Assisted deposition*, Vacuum, **6**(4) pp. 407–427, (1999).

[147] Q. Li, S. F. Wong, W. M. Lau, and C. W. Ong, *Study of the Surface Layer in Cubic Boron Nitride Growth by PVD Method*, Diam. Relat Mater., **16** pp. 421–424, (2007).

[148] S. Minda, M. Kohata, N. Yasunga, and Y. Kikuta, *Preparation of c-BN Films by CO_2 Laser PVD with Simultaneous Nitrogen ion Supply*, Thin Solid Films, **189** pp. 125–138, (1990).

[149] PSPSA, *Chemical Vapour Deposition-An Introduction*, J. Mater., **1**, (2002).

[150] S. Matsumoto, N. Nishida, K. Akashi, and k. Sugai, *Preparation of BN Films by r. f. Thermal Plasma Chemical Vapour Deposition*, J. Mater. Sci., **31**(3) pp. 713–720, (1996).

[151] H. Hofsass, S. Eyhusen, and C. Ronning, *On the Mechanisms of Cubic Boron Nitride Film Growth*, Diam.Relat. Mater., **13**(4-8) pp. 1103 – 1110, (2004).

[152] J. Yu, Z. Zheng, H. C. Ong, K. Wong, S. Matsumoto, and W. M. Lau, *Thermal Stability of Cubic Boron Nitride Film Deposited by Chemical Vapour Deposition*, J. Phys. Chem. B, **110** pp. 21073–21076, (2006).

[153] W. J. Zhang, C. Y. Chan, K. M. Chan, I. Bello, Y. Lifshitz, and S. T. Lee, *Deposition of Large-Area , High-Quality Cubic Boron NitrideFilms by ECR-enhanced Microwave Plasma CVD*, J. Appl. Phys. A, **76**(123) pp. 952–955, (2003).

[154] C. Hu, Q. M. J. Wu, J. Shen, S. Kotake, and Y. Suzuki, *Cubic Boron Nitride Formation by Ion Implantation*, Thin Solid Films, **402**(1-2) pp. 117 – 120, (2002).

[155] A. Bidiville, K. Wasmer amd R. Kraft, and C. Ballif, *Diamond Wire-sawn Silicon Wafers - from the Lab to the Cell Production*, 24th European Photovoltaic Solar Energy Conference and Exhibition, Hamburg Germany, (29 July 2011) pp. 439–442, (2009).

[156] A. Holt, A. Thøgersen, C. Rohr, J. Bye, G. Helgesen, Ø. Nordseth, S. A. Jensen, and L. Ø. Norheim, *Surface Structure of Mono-Crystalline Silicon Wafers Produced by Diamond Wire Sawing and by Standard Slurry Sawing before and after Etching in Alkaline Solutions*, Photovoltaic Specialists Conference (PVSC), 2010 35th IEEE, pp. 003501 –003504, (2010).

[157] http://www.welldiamondwiresaws.com/product/Series3032000.html, *The Well model 3032 Series Diamond Wire Saws*, Wikipedia, , (20/11/2010).

[158] S. Guanquing, L. Zhongyang, Z. Sioxiao, W. B. Liau, and X. J. Jinyun, *An Implantation Facility for Surface Modification of Metals*, Inst. Nucl. Sci. Techno., **1** p. 610064, (2011).

[159] Willem Koenraad Hofker. *Ion Implantation Boron in Silicon.* Philips Res. Rep. Suppl. Volume 8, Verlag, Belin, (1975).

[160] http://www.casetechnology.com/implanter/intro.html, *The Ion Implanter*, Case Technology, , (26/07/2011).

[161] P. H. Rose and G. Ryding, *Concept and Design of Ion Implantation Equipment for Semiconductor Processing*, Rev. Sci. Inst., **77** p. 111101, (2006).

[162] Y. Nishi and R. Doering. *Handbook of Semiconductor Manufuturing Technology.* Boca Raton; CRC Press, 2^{nd} Edition, Verlag, Belin, (2008).

[163] L. Rubin and J. Poate, *Ion Implantation in Silicon Technology*, American Inst. Phys., **1** pp. 12–15, (2003).

[164] E. Woolley, *Surface Hardening by Ion Implantation*, Material World, **5**(10) pp. 515–516, (1997).

[165] I. M. Current, *Ion Implantation for Silicon Device Manufacturing: A Vacuum Perspective*, J. Vac. Sci. Techno. A: Vacuum, Surfaces, and Films, **14**(3) pp. 1115 –1123, (1996).

[166] D. J. Hucknull and M. Kuhn, *Vacuum System Design for the Ion Implanter*, Nucl. Inst. Meth. Phys researrch B, **55** pp. 439–442, (1991).

[167] James R. Treglio, Alexander Elkind, Robert J. Stinner, and Anthony J. Perry, *Advanced Vacuum Arc Metal Ion Implantation Systems*, Surface and Coatings Technology, **96**(1) pp. 1 – 8, (1997).

[168] C.Kittel. *Introduction to Solid State Physics*. Wiley, New York, 3rd ed. Chap 5, USA, (1967).

[169] J. R. Ferraro, K. Nakamoto, and C. W. Brown. *Introductory Raman Spectroscopy*. Academic Press, Elsevier Science 2^{nd} Edition, London, (2003).

[170] N. S. White, K. Kirkwood, A. Sherman, M. Brown, R. Henthorn, K. Salamy, and E. Pertzer, *Laser Raman Spectroscopic Instrumentation for Insitu Geochemical Analyses in the Deep Ocean*, Monterey Bay Aquarium Research Institute, **1** pp. 1–12, (2004).

[171] Michael J. Pelletier. *Analytical Applications of Raman Spectroscopy*. Library of Congress, Berlin, Germany, (1999).

[172] L. Hecht, D. L . Barron, . E.W Blanch, B. F. Alasdair, and D. A. Loren, *Raman optical activity instrument for studies of biopolymer structure and dynamics*, J. Raman Spectrosc, **30**(9) pp. 815–825, 1999.

[173] Richard A. Nyquist. *Infrared and Raman Spectra and Coordination Compounds*. Academic Press Limited, Massachusetts USA, (1997).

[174] G. Dent E. Smith. *Front Matter, in Modern Raman Spectrosopy: A Practical Approach*. John Wiley and Sons LTD, Chichester, UK, (2005).

[175] P. R. Shiri. *Raman Scattering in Carbon Nanotubes*. Master's thesis, School of Physics, University of the Witwatersrand, (2007).

[176] D. A. Long, *Introduction to Raman Spectroscopy*, J. Raman Spectroscopy, **36**(10) p. 1012, (2005).

[177] S. Morel and F. Adar, *Refined Raman Spectroscopy: Bringing New Insight into Industrial Processes*, Optics and Photonics News, **19**(6) pp. 42–46, (2005).

[178] R. I. Lewis and H. Edwards. *Handbook for Raman Spectrosopy (A Practical Appoach).* Marcel Dekker Inc. Volume 28, New Yolk usa, (2001).

[179] M. Kirlik, *Lattice Imaging in Transmission Electron Microscopy*, Mater. Struc., **8**(1) pp. 3–16, (2001).

[180] D. B. William and C. B. Carter. *Transmission Electron Microscopy; A Textbook for Material Science.* Springer Science, Volume 2, New Yolk, USA, (2009).

[181] L. Reimer and H. Kolh. *Transmission Electron Microscopy.* Springer Science, Volume 5, New Yolk, USA, (2008).

[182] B. Fultz and J. M. Howe. *Transmission Electron Microscopy and Diffractometry of Materials.* Springer Verlag, Volume 3, Berlin, Berlin, (2008).

[183] P. Parayanthal and F. H. Pollack., *Raman Scattering in Alloys Semiconductor"Spatial Correlation Model"*, Phys.Rev. Lett., **52**(20) pp. 1822–1825, (1984).

[184] T. Werninghaus, J. Hahn, F. Richter, and D. R. T. Zahn, *Raman Spectroscopy Investigation of Size Effects in Cubic Boron Nitride*, Appl. Phys. Lett., **70** (8) pp. 958 –960, (1997).

[185] S. Hidetoshi, H. Takeshi, O. Tomoo, and I. Yukio, *Nucleation of Boron Nitride on Cubic Boron Nitride Microcrystallites using Chemical Vapor Deposition*, Appl. Phys. Lett., **64**(13) pp. 1638 –1640, (1994).

[186] R. J. Nemanich, S. A. Solin, and Richard M. Martin, *Light Scattering Study of Boron Nitride Microcrystals*, Phys. Rev. B, **23**(12) pp. 6843–6355, (1981).

[187] K. Nakamura, M. Fujitsuka, and M. Kitajima, *Disorder-Induced Line Broadening in First-Order Raman Scattering from Graphite*, Phys. Rev. B, **41** pp. 12260–12263, (1990).

[188] R. M. Erasmus, J. D. Comins, and T. Kubeka, *Optical Spectroscopy Techniques for the NDT of Hard Materials*, 18th World Conference on Nondestructive Testing,, pp. 1–16, (2012).

[189] H. Hofsäss, H. Feldermann, S. Eyhusen, and C. Ronning, *Fundamental Role of Ion Bombardment for the Synthesis of Cubic Boron Nitride Films*, Phys. Rev. B, **65** p. 115410, (2002).

[190] F Banhart and P. M Ajayan, *Carbon Onions as Nanoscopic Pressure Cells for Diamond Formation*, Nature, **382** pp. 3453–3458, (1996).

[191] M. Chaigneau, G. Picardi, H. A. Girard, J. C. Arnault, and R. Ossikovski, *Laser Heating Versus Phonon Confinement Effect in the Raman Spectra of Diamond Nanoparticles*, J. Nanopart. Resear., **14**(6) pp. 1–8, (2012).

[192] W. J. Evans J. M. Lipp. V. G. Baonza and H. E. Lorenzana, *Nanocrystalline Diamond: Effect of Confinement, Pressure, and Heating on Phonon modes*, Phys. Rev. B., **56**(10) pp. 5978–5984, (1997).

[193] P. M. Ossi and A. Miotello, *Structural and Mechanical Properties of Nanocrystalline Boron Nitride Films*, Appl. Orgnometal. Chem, **15** pp. 430–434, (2001).

[194] T. Werninghaus, J. Hahn, F. Richter, and D. R. T. Zahn, *Raman Spectroscopy Investigation of Cubic Boron Nitride Single Crystals and Layer on Si(100)*, Diam. Relat. Mater., **6** pp. 612–616, (1997).

[195] P.V. Zinin, I. Kudryashov, N. Konishi, L.C. Ming, V.L. Solozhenko, and S.K. Sharma, *Identification of the Diamond-like BC Phase by Confocal Raman Spectroscopy*, Spectroc. ActaA: Mole.Biomole. Spectro., **61**(10) pp. 2386 – 2389, (2005).

[196] K. Krystian and B. Friedhelm, *Ab initio Lattice Dynamics of BN and AlN: Covalent versus Ionic Forces*, Phys. Rev. B, **56** pp. 7404–7415, (1997).

[197] H. Sachdev, *Influence of Impurities on the Morphology and Raman Spectra of Cubic Boron Nitride*, Diam. Realt. Mater, **12** pp. 1275–1286, (2003).

[198] O. Kutsay, C. Yan, Y.M. Chong, Q. Ye, I. Bello, W.J. Zhang, J.A. Zapien, Z.F. Zhou, Y.K. Li, V. Garashchenko, A.G. Gontar, N.V. Novikov, and S.T. Lee, *Studying Cubic Boron Nitride by Raman and Infrared spectroscopies*, Diam. Relat. Mater., **19**(79) pp. 968 – 971, (2010).

[199] H. Werheit, V. Filipov, U. Kuhlmann, U. Schwarz, M. Armbrster, A., L. Jasper, T. Tanaka, I. Higashi, T. Lundstrm, V. N Gurin7, and M. M. Korsukova, *Raman Effect in Icosahedral Boron-rich Solids*, Sci. Technol. Adv. Mater., **11** p. 023001, (2010).

[200] V. Paillard, P. Puech, and P. R. Cabarrocas, *Measurement of Stress Gradients in Hydrogenated Microcrystalline Silicon Thin Films using Raman Spectroscopy*, J. Non-Crystal. Sol., **299302** p. 280283, (2002).

[201] M. Backman, F. Djurabekova, O. H. Pakarinen K. Nordlund, Y. Zhang, M. Toulemonde, and W J Weber, *Cooperative Effect of Electronic and Nuclear stopping on Ion Irradiation Damage in Silica*, J. Appl Phys. D, **45** pp. 505385–92, (2012).

[202] T. Werninghaus. *Micro Raman Spectroscopy Investigations of Thin Hard Coatings*. PhD thesis, Institut fiir Physik, TU Chemnitz-Zwickau, (2006).

[203] M. N. Iliev, A. P. Litvinchuk, H. G. Lee, C. W. Chu, A. Barry, and J. M. D. Coey, *Raman spectra of the half-metallic ferromagnet cro2*, physica status solidi (b), **215**(1) pp. 643–646, 1999.

[204] E. Aradi, R. M. Erasmus, and T. E. Derry, *Formation of c-BN Nanoparticles by Helium, Lithium and Boron Ion Implantation*, Nucl. Instrum. Meth. Phys. Res. B:, **272**(0) pp. 57 – 60, (2012).

[205] Y. H. Sheng, Z. J. Ying, N. A.-Min, and Z.X.Bin, *In situ infrared spectroscopic study of cubic boron nitride thin film delamination*, Chin. Phys. B, **17**(9) pp. 3453 –3458, (2008).

[206] Y. Liu, P. Jin, A. Chen, H. Yang, and Y. Xu, *Residual Compressive Stress Induced Infrared-Absorption Frequency Shift of Hexagonal Boron Nitride in Cubic Boron Nitride Films Prepared by Plasma-Enhanced Chemical Vapor Deposition*, J. Appl. Phys, **112** pp. 053501–2 – 05352–5, (2012).

[207] M. Zheng, Y. Gu, Z. Xu, and Y. Liu, *Synthesis and Characterization of Boron Nitride Nanoropes*, Mater Lett., **61**(89) pp. 1943 – 1945, (2007).

[208] B. Fakrach and A. Rahmani. and H. Chadli and K. Sbai and M. Bentaleb and , J. L. Bantignies. and, J. L. Sauvajol., *Infrared spectrum of single-walled boron nitride nanotubes*, Phys. Rev. B, **85** p. 115437, 2012.

[209] Y. Cai, L. Zhang, Q. Zeng, L. Cheng, and Y. Xu, *Infrared Reflectance Spectrum of BN Calculated from First Principles*, Solid State Communications, **141**(5) pp. 262 – 266, (2007).

[210] P.W. Zhu, Y.N. Zhao, B. Wang, Z. He, D.M. Li, and G.T. Zou, *Prepared Low Stress Cubic Boron Nitride Film by Physical Vapor Deposition*, J. Solid State Chem., **167**(2) pp. 420 – 424, (2002).

[211] X. P. Hao, Y. Q. Yin X. G. Xu D. L. Cui, G. X. Shi, J. Y. Wand, M. H. Jiang, X. W. Xu, Y. P. Li, and B. Q. Sun, *Synthesis of Cubic Boron Nitride at Low-Temperatire and Low-Pressure Conditions*, Chem. Mater, **13**(8) pp. 2457–2459, (2001).

[212] W. Gissler, J. Haupt, A. Hoffmann, P.N. Gibson, and D.G. Rickerby, *Mixed phase nanocrystalline boron nitride films: Preparation and Characterization*, Thin Solid Films, **199**(1) pp. 113 – 122, (1991).

[213] W. C Marra, P. Eisenberger, and A.Y. Cho, *X-ray total external reflection-Bragg diffraction: A structural study of the GaAsAl interface*, J. Appl. Phys., **50**(11) pp. 6927–6933, (1979).

[214] H. Saitoh and W. A. Yarbrough, *Preparation and Characterization of Nanocrystalline Cubic Boron Nitride by Microwave Plasma; Enhanced Chemical Vapor Deposition*, Appl. Phys. Lett., **58**(20) pp. 2228–2230, (1991).

[215] W. J. Zhang and S. Matsumoto, *Investigations of Crystallinity and Residual Stress of Cubic Boron Nitride films by Raman Spectroscopy*, Phys. Rev. B, **63** pp. 073201–07205, (2001).

[216] A. Taylor. *X-ray metallography.* J. Chem. Educ Vol 39, USA, (1962).

[217] E. Aradi, S.R. Naidoo, R.M. Erasmus, B. Julies, and T.E. Derry, *Investigations on the characterization of ion implanted hexagonal boron nitride*, Nucl. Instr. Meth. Phys. Resear. B:, **307**(0) pp. 214 – 217, (2013).

[218] A. V. Kurdyumov, V. L.Solozhenko, and W. B Zelyavski, *Lattice Parameters of Boron Nitride Polymorphous Modifications as a Function of Their Crystal-Structure Perfection*, J. Appl. Crystal., **28**(5) pp. 540–545, (1995).

[219] J. Li, S. Majety, R. Dahal, W. P. Zhao, J. Y. Lin, and H. X. Jiang, *Dielectric Strength, Optical Absorption, and Deep Ultraviolet Detectors of Hexagonal Boron Nitride Epilayers*, Appl. Phys. Lett, **101**(17) pp. 171112–5, (2012).

[220] N. Takashi, M. Takayuki, and N. Katsuhiko, *Surface Structure of Isotactic Polypropylene by X-ray Diffraction*, Poly. Eng. Sci., **40**(2) pp. 336–343, (2000).

[221] G. Lian, X. Zhang, M. Tan, S. Zhang, D Cui, and Q. Wang, .

[222] S Utsunomiya, M Kogawa, E. Kamiishi, and R C. Ewing, .

[223] Y. Zheng, L S. Yi, Jian-Lin, Y Bo, H Zhuang-Xiong, P. Lin, Z You-Dou, and W Kang-Long, *Strain and Phonon Confinement in Self-Assembled Ge Quantum Dot Superlattices*, Chin.Phys. Lett, **20** pp. 1–3, (2001).

[224] D. Baron M. Havel, *Smart Raman/Rayleigh imaging of nanosized SiC materials using the spatial correlation model*, J. Mater. Sci., .

[225] R.Jalilian, G.U. Sumanasekera, H. Chandrasekharan, and M. K. Sunkara, *Phonon Confinement and Laser Heating Effects in Germanium Nanowires*, Phys. Rev. B, **74** p. 155421, (2006).

[226] Z. C. Feng, W. Wang, S. J. Chua, P. X. Zhang, K. P. J. Williams, , and G. D. Pitt, *Raman Scattering Properties of GaN Thin Flms Grow on Sapphire Under Visible and Ultraviolet Excitation*, J. Ram. Spectros, **32** pp. 840–846, (2001).

[227] A. K. Arora, M Rajalakshmi, T. R. Ravindran, and V. Sivasubramanian, *Raman spectroscopy of optical phonon confinement in nanostructured materials*, J. Raman Spectros., **38**(6) pp. 604–617, (2007).